A Contribution to Beam Scanning with Array Antennas

Vom Promotionsausschuss der
Technischen Universität Hamburg

zur Erlangung des akademischen Grades

Doktor-Ingenieur (Dr.-Ing.)

genehmigte Dissertation (Monografie)

von

Benjamin Rohrdantz

aus

Hamburg

2024

1. Gutachter:	Prof. Dr.-Ing. Arne F. Jacob
2. Gutachter:	Prof. Dr.-Ing. Matthias Geissler
Prüfungsvorsitz:	Prof. Dr.-Ing. habil. Alexander Kölpin

Tag der mündlichen Prüfung: 12. September 2023

DOI
https://doi.org/10.15480/882.13234

ORCID iD
https://orcid.org/0000-0001-7825-2767

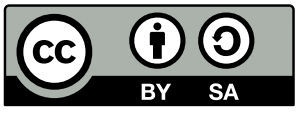

Abstract

Electronically scannable antennas are advanced electronic systems with a unique feature set. One of their most prominent capabilities is the ability to change the beam direction without physically moving the antenna. Since the limitations of mechanical drive systems do not apply, instantaneous direction changes are possible. Additionally, an array antenna allows for the adjustment of critical beam properties, such as sidelobes, beamwidth, or null positions, during operation. It is even possible to excite multiple beams simultaneously from a single aperture. Arrays typically form the basis for electronic beam scanning.

The high scanning performance and wide functional range of these systems are unmatched, but they ultimately lead to complex circuits and high costs. As a result, phased arrays are primarily used in military (radar) applications. However, technological progress and new concepts may change the status quo, leading to broader use.

This thesis discusses various aspects of electronically scannable antennas, beginning with the basics and concluding with innovative solutions. Satellite communication in Geostationary Earth Orbit (GEO) and Low Earth Orbit (LEO) is used as reference application scenario. An overview of current technology, recent advances, and new concepts focusing on efficient designs to reduce cost and complexity is presented. These concepts include 3D-printed waveguides and reconfigurable antennas.

In addition to technology and components, two beamforming arrays are presented. Arrays often utilize planar apertures with a wide scanning range to offer flat, high-performance, but expensive solutions. In many applications, the system's build size is not a significant issue, and the occurring angular changes are minor. For these use cases, hybrid solutions can be an ideal fit. Therefore, a high-gain reflector is combined with an electronically controllable array to enable fast scanning with a limited field of view. A comprehensive study of various rotationally symmetric reflectors allows for determining an optimal reflector shape based on the required beam properties. The feed consists of a custom-designed 30 GHz transmit array with 49 elements, enabling two-dimensional scanning in a $\pm 6^\circ$ conical sector. It includes a wideband signal distribution network and frontend electronics.

Another challenge in phased array designs is the phase shifters or RFICs (core chips) needed to control the excitation of the array elements. These components are often unavailable, bulky, or expensive across many frequency bands. Therefore, the development of a different type of phase-shifting network is of paramount importance. The proposed "heterodyne beamforming" solution combines the frequency-dependent phase response of components with a simple network of mixers. An 8-element dual-polarized linear array based on Substrate Integrated Waveguide (SIW)-technology is developed to validate the concept. Distributed and lumped components form the core of the beamformer at 20 GHz. The heterodyne principle provides an effortless way to scan the beam without high requirements on components or digital circuitry. Finally, an advanced heterodyne beam scanning concept is proposed to extend the principle from linear arrays to planar arrays.

Acknowledgments

Completing my doctorate at the Institute for High-Frequency Technology has been a profound and rewarding experience. It provided me with a platform for creative expression, the realization of my ideas, and the privilege of being part of a unique community. This journey would not have been possible without the support and encouragement of many exceptional individuals, who deserve my deepest gratitude.

First and foremost, I would like to express my sincere thanks to my doctoral advisor, Prof. Dr.-Ing. Arne F. Jacob, for his continuous support and unwavering belief in me. Arne, your approachable nature and trust were crucial in guiding me along my path to the PhD. I am also grateful to Prof. Matthias Geissler for serving as my co-examiner and to Prof. Dr.-Ing. habil. Alexander Kölpin for chairing the examination committee.

My research within the SANTANA projects was generously funded by the German Aerospace Center (DLR), and I had the honor of collaborating with an outstanding team and partners. I am particularly indebted to Dr. Siegfried Voigt for his continuous support and long-term vision, both of which greatly contributed to the success of my research.

The Institute for High-Frequency Technology became a truly special place because of the diverse and remarkable people I was fortunate to meet. I always felt supported by Martin Jenett and Claudia Bredehöft, and the successful completion of numerous lab demonstrations would not have been possible without the active assistance of Anja-Maria Doobe-Jöstingmeier, Werner Thun, and Jürgen Winkelmann. I would like to extend my heartfelt thanks to my long-time office colleague, Carmen Hajunga, with whom I spent countless hours working under yellow light, soldering, and bringing our demonstrators to life. Your dedication and collaboration were invaluable.

Working with students has been a source of great joy for me, and I have been privileged to supervise many remarkable projects. I would like to particularly recognize Torsten Reuschel, Vincent Schmidt, and Anton Sieganschin for their outstanding technical achievements, several of which are featured in this thesis. Hans Mitto and Kirstin Feuerschütz, your moral support and the moments of lightness we shared were invaluable during challenging times.

To my fellow PhDs at the institute, many of whom I am proud to call friends: the collaboration and camaraderie we shared have been extraordinary. I greatly value the time spent with you and look forward to future opportunities to explore and share experiences together. Special thanks are due to Thomas Jaschke for his unparalleled support in our joint endeavors, and to Christian Friesicke, Frauke Gellersen, and Christian Rave – our time together at the institute was truly unforgettable.

Finally, I want to extend my deepest gratitude to my family. To my mother, Doris, for her love and encouragement throughout my life, and to my wife, Dorothea, for her support, understanding, and patience throughout this journey. Your belief in me has been a great source of strength. To my children, who have brought immense joy and perspective into my life – thank you for your love and for reminding me of what truly matters.

Contents

Chapter 1

Introduction

Technological progress has steadily impacted our way of living in the past decades. Marked by the invention of the computer, the mobile phone, and the internet, the so-called digital revolution has significantly changed our way of learning, working, and, most notably, communicating. Data transmission has become a cornerstone of the global community, illustrated by the yearly global internet traffic development. Data traffic has increased from 1 TB (terabyte, 10^{12} bytes) per month in the year 1990 to roughly 122 EB (exabyte, 10^{18} bytes) per month in 2017 [1], [2]. Cisco projected a growth of up to 396 EB per month in 2022. The so-called *Nielsen's Law of Internet Bandwidth* reflects this continuous growth by predicting a high-end user's connection speed to grow by 50% per year (similar to Moore's Law for semiconductors). This rapid development is confirmed by the International Telecommunication Union (ITU) [3]. The estimated percentage of the world population using the internet has risen from 20% in 2005 to 70% in 2022. The ITU states that "Unrelenting global consumption of Internet data continues to drive demand for international bandwidth usage", which is underlined by an increase of the available bandwidth from 300 Tbit/s in 2017 to 1200 Tbit/s in 2022.

Such rapid development is only possible due to technological advances such as faster fiber optical communication backbones and high-speed solutions for the "Last Mile" from the Internet Service Provider (ISP) to the end-user such as Digital Subscriber Line (DSL) or Fiber to the Home (FTTH) in a fixed-broadband scenario.

Starting around 2005, the availability of smartphones and tablet computers in combination with new high-speed wireless technologies caused a rapid increase in global mobile internet subscriptions from less than 5 per 100 inhabitants in 2007 to more than 80 in 2022 [3]. Today, Wi-Fi, 4G, and the upcoming 5G networks are omnipresent in urban areas and offer steadily increasing data rates during all phases of urban lives. Daily routines rely on internet services such as communication (e-mail, messaging), information (news, searching), cloud storage, navigation, and social networks. Staying connected to the internet has become so essential that a lack of high-speed coverage is more than an annoyance for many. However, no or only sparse terrestrial communication infrastructure is available in many areas of our planet, such as in war and conflict zones, the oceans, polar regions, deserts, and other remotely located or undeveloped areas.

From an engineering point of view, the rapidly increasing demand for wireless access poses an enormous challenge: the available bandwidth is scarce, and technology needs constant updates every few years. Spectrally more efficient higher-order modulation schemes help enable higher data rates, but the achievable Signal-to-Noise Ratio (SNR)

limits the approach. It is hence primarily useful for short-range communication. Higher bandwidth, on the other hand, requires the exploitation of new frequency bands to avoid interference with existing services or a change of priorities of spectral allocations. Most wireless services today rely on frequencies below 6 GHz, which do not require a Line-of-Sight (LOS) for short ranges (e.g., indoors or in street canyons). A move to higher frequencies causes higher losses and more blockage, which results in a greater sensitivity to propagation path obstruction, necessitating the development of new higher power and lower noise components for base stations and mobile devices.

Another approach to increasing the average available data rate is spatial multiplexing. Decreasing the cell size of a terrestrial network or the spot beam size of a satellite reduces the number of users per cell and thus maximizes the available data rate per user. Directive antennas allow for segmenting the area surrounding a base station in many sectors. Additionally, beamforming reshapes the sectors according to current demands adaptively. Beamforming is achieved mechanically by moving a directive antenna or electronically utilizing an array of antennas. Such an Electronically Scanned Antenna (ESA) or phased array requires some control at each element to adaptively shape the radiation pattern according to current need, e.g., to point the antenna beam in the desired direction and suppress unwanted signals.

1.1 Brief History of Phased Arrays

The basic principle of phased arrays is well known in physics: If propagating waves superimpose, they either constructively or destructively interfere, thus forming maxima and minima. This phenomenon applies to all types of waves, including water, acoustic, and electromagnetic waves, such as light and radio waves. If the wave sources are coherent, i.e., they have the same frequency and a constant phase relation, the interference pattern is constant and depends only on the phase and amplitude relation of the wave sources. Changing the phase relation between sources changes the position of maximal and minimal interference, hence their “direction”. This direction change is exploited in phased arrays to scan antenna beams.

The first antenna arrays date back to the early 20$^{\text{th}}$ century, when multiple antennas were combined to enhance the gain [4]. Karl Ferdinand Braun learned from such experiments conducted by Marconi [5] and built the first phased array [6]. Braun was the first to use the signal phase to scan the beam and is thus often considered the inventor of the phased array [4].

Phased arrays have developed rapidly from the early days, mainly for direction finding and Radio Detection and Ranging (Radar). In 1927 the famous binomial taper was patented in [7]. Starting with World War II, the military requirement to detect aircraft became a driving force in the development. Many countries deployed arrays such as the Wullenweber type shown in Fig. 1.1b, which is still used today [8]. In 1946 the Dolph-Chebychev amplitude taper was developed and allowed an efficient reduction of the sidelobes [9].

The development of computers enabled the design of more complex planar arrays, which allow scanning in both azimuth and elevation. Such arrays were experimentally shown in 1966 [10]. At the same time, solid-state components were also successfully used in phased arrays [4], starting the transformation from a powerful central transmitter to a

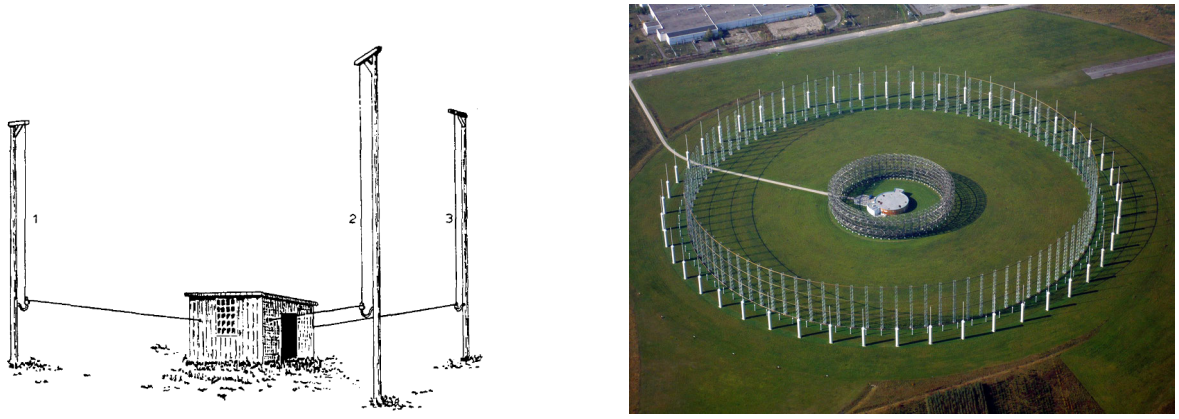

(a) (b)

Figure 1.1: (a) Three monopole antennas constitute the basis of the first phased array by Ferdinand Braun in 1905 on [6]. (b) Modern Wullenweber array antenna in Gablingen [8].

distributed system. Planar arrays based on patch antennas [11], and Wilkinson dividers [12], became popular from the early 1970s [13]. Patch antennas can be mass-produced and are very flat. Developments are ongoing, and phased arrays are steadily becoming faster and more powerful.

1.2 State of the Art

The main driver behind the historical development of phased arrays was the military. Phased arrays have always been very sophisticated, complex, and extremely expensive. For high-gain applications, reflector antennas are a widely used low-cost alternative. However, high-speed scanning without mechanically moving the antenna, generating multiple beams, graceful degradation, and adaptive beamforming are capabilities that are unique to arrays. Hence, they have attracted wide attention beyond the military community or even electromagnetics.

In acoustics, beamforming techniques are used for loudspeaker and microphone arrays to obtain directive characteristics. These are particularly useful in cars to focus a microphone on passengers and reduce the surrounding noise.

Electronic beam scanning even benefits medical ultrasound. A single ultrasonic probe only provides depth information. A steering mechanism of the ultrasonic beam allows for obtaining a 2D image. Ultrasound steering conventionally relies on a mechanically movable lens-based system. Modern systems use phased arrays and beamforming techniques to change the beam direction and depth of focus. Using planar arrangements enables the acquisition of 3D images, e.g., from organs.

An enormous phased array is the Atacama Large Millimeter/submillimeter Array (ALMA) [14] for radio astronomy. It is a prime example of the civil use of a phased array. However, other lower-cost applications exist as well. Some base stations of cellular networks utilize arrays to adjust cells adaptively based on current requirements. Even some consumer electronics such as Wi-Fi routers operate similar so-called Multiple-Input

and Multiple-Output (MIMO) techniques. However, due to the high cost, larger phased arrays with high gain and fast scanning requirements did not have breakthroughs in the communication industry yet.

Many institutes are working on reducing the required technology (primarily electronics) cost to allow broader use of phased array technology. In the industry, some new ideas are also under development by *Kymeta Corporation*, *Hanwha Phasor*, and others [15]. The technically more advanced concept of Digital Beam Forming (DBF) has recently attracted considerable attention even for communication at Ka-band frequencies, and various solutions have been proposed [16]. In DBF, software functions as the beamformer, which allows even greater flexibility.

1.3 Overview of Thesis

The thesis focuses on the ongoing challenge of electronic beam scanning technology. It aims to contribute to the rich history of designs and specifically investigates how to adapt beam scanning with array technology to enable a broader range of (civil/consumer) applications. High system cost has hampered the development of solutions even in the communication industry. However, mobile communications are one of the prime potential use cases for phased array systems. Providing terrestrial internet access gets increasingly complex in rural and remote areas and ultimately fails on the oceans. Here, satellite communication or long-distance microwave links are an alternative to a dense base station network. High-gain antennas are required when communicating with such systems. However, operating high-gain antennas on mobile platforms such as airplanes, ships, or cars requires constant beam adjustments to maintain the communication link. Electronically scannable antennas could be a well-suited solution for such cases.

The thesis is organized as follows. First, Chapter 2 introduces beam scanning and array technology basics. The array principle, beam scanning, its limitations, and different architectures are discussed and analyzed in this chapter, which concludes with an introduction to using phased arrays for (satellite) communications. Chapter 3 focuses on concepts to allow more efficient phased array designs. It includes some technological advancements but also component designs and architectures.

Chapter 4 introduces a hybrid beamforming approach, which combines a high-gain reflector and a planar array for electronic beam scanning. The approach offers a practical solution for applications with limited scanning requirements. The chapter comprehensively analyzes the reflector shape and the necessary tradeoffs. Next, the feed design, including innovative components such as a wideband radial divider, is presented. The feed has to be customized for the reflector to maintain beam properties when scanning. The chapter concludes with simulation and measurement results from the integrated hybrid system.

The required components for phased arrays, such as phase shifters or T/R-modules, are unavailable in many frequency bands. Thus, an innovative heterodyne beamformer concept constitutes the core of Chapter 5. This 2D-beamforming concept uses mixers in combination with adjustable signal sources to scan the beam. No electric or digital control is required, which allows a relatively simple array design. A manufactured linear 8-element array design allows for validating the concept. The thesis concludes in Chapter 6 with a summary of the results and an outlook.

Chapter 2

Phased Array Design Aspects

2.1 Antenna Fundamentals

Antenna theory is a broad field, and a significant amount literature exists on the topic [17]–[20] with partially deviating definitions and notations of essential parameters. This section briefly introduces and defines important antenna parameters used in this work.

2.1.1 Directivity and Gain

Directivity D is an important property for describing antennas. "The ratio of the radiation intensity in a given direction from the antenna to the radiation intensity averaged over all directions" [21] defines the directivity. It compares the radiation intensity in a certain direction to an isotropic radiator:

$$D(\theta, \phi) = \frac{4\pi * U(\theta, \phi)}{P_{\text{rad}}}\,, \tag{2.1}$$

where U is the radiant intensity (power per unit solid angle), P_{rad} is the total radiated power, and θ and ϕ refer to angles in spherical coordinates [22] as illustrated in Fig. 2.1a. D refers to the maximum observed directivity if no angles are specified.

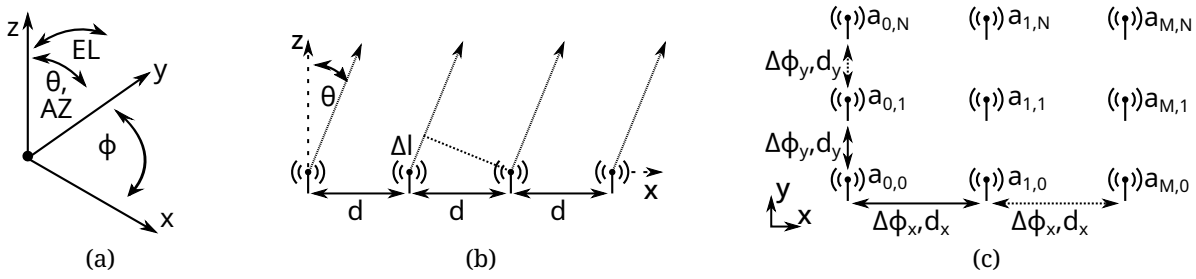

Figure 2.1: (a) Spherical coordinate systems θ, ϕ and elevation (EL), azimuth (AZ) for antenna pattern. (b) Linear array with four elements along the x-axis. (c) Planar array along the x- and y-axis.

To include conductor and dielectric losses occurring in the antenna, an efficiency η is defined. The antenna gain G includes these losses and is thus defined as:

$$G(\theta,\phi) = \eta D(\theta,\phi) = \frac{4\pi\eta * U(\theta,\phi)}{P_{\text{in}}}. \tag{2.2}$$

P_{in} is the incident power at the antenna terminals. An efficiency definition including the mismatch $\eta_0 = \eta(1-|\Gamma|^2)$ is useful if significant input reflections occur at the ports. Using this expression, the realized gain G_{r} can be defined:

$$G_{\text{r}}(\theta,\phi) = (1-|\Gamma|^2) * G(\theta,\phi) = \eta_0 D(\theta,\phi)\ . \tag{2.3}$$

The realized gain is beneficial for characterizing an antenna since it includes all occurring losses. It is the standard definition of gain in this work. Boresight refers to the direction with the maximal gain. A high gain implies a narrow beam required to obtain a high angular resolution to differentiate between closely spaced sources or minimize interference. The Half-Power Beamwidth (HPBW) [17, pp 15-16] is the standard metric to characterize the width of the beam.

2.1.2 Polarization

The time-varying direction of the magnetic and electric field vectors of a Transverse ElctroMagnetic (TEM) wave is an important property called polarization. To measure polarization, the direction of the electric field vectors is tracked over time in a plane perpendicular to the propagation direction. In the most general case, the direction will vary and form an ellipse. Fig. 2.2a depicts such a polarization ellipse. An ellipse is well-defined using the major and minor axes and the tilt angle τ. Two special cases can occur. If the ellipse is only a straight line (minor axis = 0), the field oscillates in a single plane along the propagation direction (linear polarization). Horizontal linear polarization occurs when the major axis is aligned with the x-axis ($\tau = 90°$) and vertical polarization occurs if τ is 0°. If both axes are equal, the ellipse turns into a circle, and the polarization is circular.

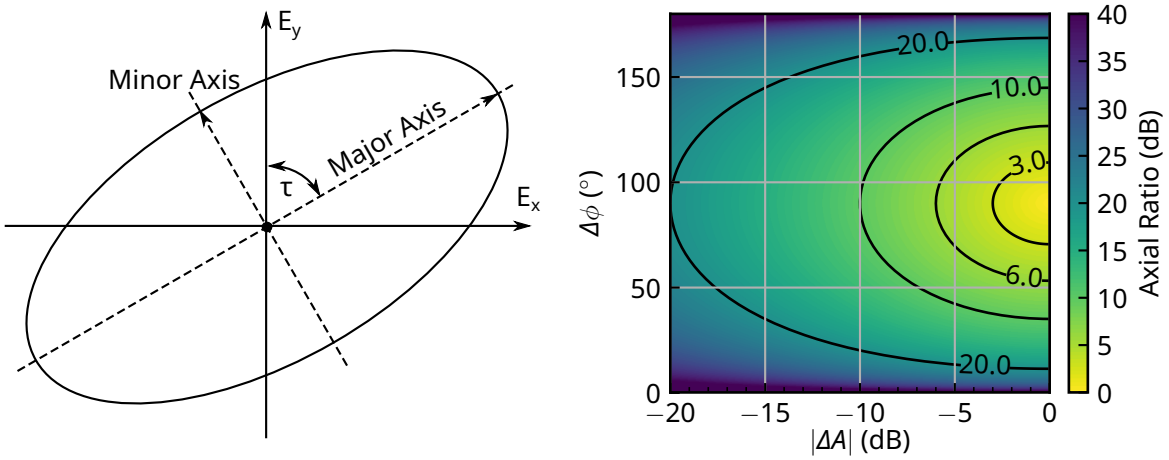

(a) (b)

Figure 2.2: (a) Polarization ellipse and (b) axial ratio of two linear sources with varying relative phase and amplitude.

The polarization of a plane wave can be decomposed into two orthogonal components, e.g., two linear polarizations or two circular ones. Often only one of those components is wanted at a time. This component is said to be the co-polarization, whereas the unwanted part is the cross-polarization. Two orthogonal polarizations can be transmitted simultaneously without interference. Thus, doubling the channel capacity is possible using polarization multiplexing. To make use of this technique, the Transmit (Tx)- and Receive (Rx)-antennas must be able to separate the components, i.e., they must have two channels, each with a high Cross-polar Discrimination (XPD):

$$XPD = \frac{|E_{\text{co}}|}{|E_{\text{cross}}|} \,. \tag{2.4}$$

Circular polarization is particularly useful for mobile applications since it does not require an alignment between the Tx- and Rx-antennas. Circular polarization is either Right-Handed Circular Polarization (RHCP) (clockwise rotating in the propagation direction) or Left-Handed Circular Polarization (LHCP) (counterclockwise rotating) based on the orientation of the field vectors. A good figure of merit for the quality of circular polarization is the axial ratio:

$$AR = \frac{E_{\text{max}}}{E_{\text{min}}} = \frac{|E_{\text{RHCP}}| + |E_{\text{LHCP}}|}{|E_{\text{RHCP}}| - |E_{\text{LHCP}}|} = \frac{XPD + 1}{XPD - 1} \,, \tag{2.5}$$

where E_{max} and E_{min} are the field components in the direction of the major and minor polarization ellipse axes, respectively. The axial ratio is commonly expressed in decibels: 0 dB represents ideal circular polarization. In this work, an AR of less than 3 dB is considered circular, and an AR of less than 6 dB is quasi-circular. These values correspond to an XPD of about -15 dB and -10 dB, respectively. Circular polarization can be excited using two orthogonal linearly polarized sources E_1 and E_2 using equal amplitudes and a 90° phase shift. Realistic sources cannot fulfill this requirement (or at least not for a wide frequency range) since amplitude variation (ΔA) and phase errors ($\Delta\phi$) occur ($E_2 = |\Delta A| E_1 e^{j*\Delta\phi}$). Fig. 2.2b shows the influence of such errors on the axial ratio and hence the polarization purity.

2.1.3 Bandwidth

According to [17, p. 26], antenna bandwidth is “the range of frequencies within which the performance of the antenna, with respect to some characteristic, conforms to a specified standard.” This definition is helpful for a wide variety of application requirements.

The focus here is on two major parameters: the antenna input impedance and the polarization. The impedance bandwidth is defined as the frequency range within which the return loss is better than 10 dB (Voltage Standing Wave Ratio (VSWR) > 2). The polarization bandwidth is harder to define since polarization is direction-dependent in the antenna pattern. Assessing the axial ratio in only the boresight direction helps to calculate a good figure of merit. The frequency range where the boresight axial ratio is below 6 dB defines the polarization bandwidth.

2.2 Array Principle

An array consists of antenna elements specifically arranged and excited to obtain a predefined radiation pattern. In the simplest case, all elements are purely passive. While single antennas typically have relatively wide beams, the array allows to focus the element patterns and creates a more directive beam.

This principle helps to form large, very directive antennas based on simple elementary radiators, thus reducing complexity and build size. The array pattern can be actively modified using control circuitry at each element. Phase adjustments, for example, allow scanning of the focused beam to a desired angle. In this thesis, the transmit and receive case are not separately evaluated since reciprocity applies as long as no active circuitry is involved.

2.2.1 Array Fundamentals

The working principle is best understood using a linear array of isotropic antennas as depicted in Fig. 2.1b. The emitted plane waves from each element superimpose, causing maxima (constructive interference) and minima (destructive interference) in the resulting pattern. A global maximum (i.e., a main lobe) occurs if the path length difference Δl between adjacent elements is a multiple of the wavelength λ. Usually, only a single main lobe is desired. Other occurring main lobes are unwanted grating lobes. All other (nonglobal) maxima in the pattern are called sidelobes.

If the antenna elements are not only placed along one but along two axes, the array is called planar (Fig. 2.1c). The same principle applies, but a focused beam in elevation and azimuth is possible. The pattern of the array

$$\begin{aligned} E(\theta,\phi) &= R(\theta,\phi) * F(\theta,\phi) \\ &= R(\theta,\phi) \sum_{\mathrm{m,n}} |a_{\mathrm{m,n}}| \exp(j2\pi(m d_{\mathrm{x}}(\sin(\theta)\cos(\phi) - \sin(\theta_0)\cos(\phi_0)) + \\ & n d_{\mathrm{y}}(\sin(\theta)\sin(\phi) - \sin(\theta_0)\sin(\phi_0)))) \end{aligned} \tag{2.6}$$

can be determined using the element pattern $R(\theta,\phi)$ and the so-called *Array Factor* $F(\theta,\phi)$. The element weighting coefficient $a_{\mathrm{m,n}} = |a_{\mathrm{m,n}}| \exp(-j(m\Delta\phi_{\mathrm{x}} + n\Delta\phi_{\mathrm{y}}))$ shapes the pattern. Scanning the beam to the desired direction (θ_0, ϕ_0) is possible by adjusting the progressive phase $\Delta\phi_{\mathrm{x}}$, $\Delta\phi_{\mathrm{y}}$ between adjacent antennas along the principal axes of the array:

$$\Delta\phi_{\mathrm{x}} = \frac{2\pi f d_{\mathrm{x}}}{c_0} \sin(\theta_0)\cos(\phi_0), \qquad \Delta\phi_{\mathrm{y}} = \frac{2\pi f d_{\mathrm{y}}}{c_0} \sin(\theta_0)\sin(\phi_0)\,. \tag{2.7}$$

From Eq. (2.7), it is evident that the phase and beam direction depend on the signal frequency f. Typical phase shifters exhibit a constant, frequency-independent phase, inducing a frequency-dependent scan angle. The severity of this so-called beam squint depends on the maximal scanning angle $\theta_{0,\mathrm{max}}$ and the bandwidth Δf. If a $3\,\mathrm{dB}$ reduction in the desired beam direction is acceptable, the maximal tolerable fractional bandwidth is

$$\frac{\Delta f}{f} = \frac{\theta_{\mathrm{BW}}}{\sin\theta_{0,\mathrm{max}}}\,, \tag{2.8}$$

where θ_{BW} denotes the half power beamwidth. It is not critical for systems with a low fractional bandwidth Δf, broad beams, or without scanning requirements. Simple delay

lines of length l are one option to prevent beam squint. Their phase changes constantly with frequency

$$\Delta\phi = \frac{2\pi}{\lambda} l = \frac{2\pi f}{c_0} l \,. \tag{2.9}$$

Hence, if Eq. (2.7) is applied, the scan angle depends on l only.

θ_{BW} depends on the total array size: A large array generates a narrow pencil shape beam. A large linear array with N_{el} elements has a broadside beamwidth of

$$\theta_{\mathrm{BW}} \simeq 0.866 \frac{\lambda}{N_{\mathrm{el}} d} B_{\mathrm{b}} \,, \tag{2.10}$$

where B_{b} is a beam broadening factor [18, p. 19]. In the case of a planar array, the effective area, i.e., the observed array surface size from a non-broadside angle, is reduced for higher scanning angles causing a beam broadening. For a large array, the projection of the area allows one to estimate the beam widening [18, p. 22]:

$$\theta_{\mathrm{BW}}(\theta_0) = \frac{\theta_{\mathrm{BW}}(\theta_0 = 0)}{cos(\theta_0)} \,. \tag{2.11}$$

Adjusting the amplitude of the weighting coefficients $|a_{\mathrm{m}}|$, helps to suppress unwanted sidelobes. The Sidelobe Level (SLL) describes the gain ratio of the main lobe and the highest sidelobe. A uniform amplitude taper leads to a minimal SLL of 13 dB, whereas a binomial taper can completely suppress side lobes for $d = \lambda/2$ [17, p. 540]. In contrast, a uniform amplitude taper leads to the narrowest beam ($B_{\mathrm{b}} = 1$) and the binomial taper to a high beam broadening and hence a low directivity. A Dolph-Chebychev taper yields the minimal achievable beamwidth for a given SLL. All three amplitude distributions and resulting array factors of a 16-element linear array are shown in Fig. 2.3a and Fig. 2.3b, respectively.

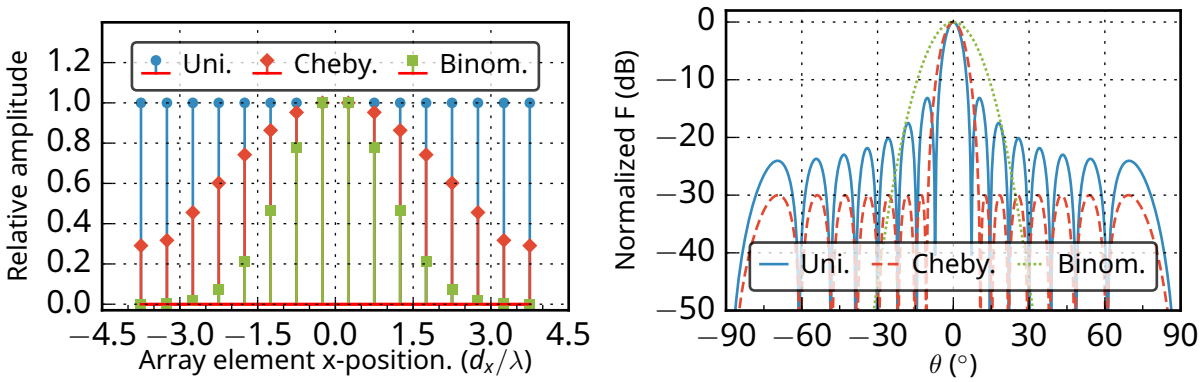

(a) (b)

Figure 2.3: (a) Amplitude distribution for different tapers and (b) resulting patterns of a 16-element linear array.

Grating lobes may significantly deteriorate the array pattern since their gain is similar to that of the main beam. Based on Eq. (2.6) grating lobes in the upper hemisphere ($\theta \in [-\pi/2, \pi/2]$) can be avoided, if the element spacing d and the maximal scanning angle $\theta_{0,\mathrm{max}}$ are chosen such that

$$\frac{d}{\lambda} < \frac{1}{1+\sin(\theta_{0,\max})} \tag{2.12}$$

is fulfilled. Another way to reduce grating lobes is to adapt the element pattern $f(\theta, \phi)$ to minimize radiation in potential grating lobe ranges.

2.2.2 Array Gain

The directivity of a planar array depends on the wavelength and the total array area A, which in turn depends on the element area A_{el} and the number of elements N_{el}. From Eq. (2.11), it is evident that a scanned beam reduces the directivity:

$$D = \frac{4\pi A}{\lambda^2}\cos(\theta_0) = D_{\text{s}} N_{\text{el}}\cos(\theta_0) = \frac{4\pi A_{\text{el}}}{\lambda^2} N_{\text{el}}\cos(\theta_0)\,, \tag{2.13}$$

where D_{s} is the directivity of a single array element. According to Eq. (2.3), the realized gain depends on the directivity, the input reflection, and the efficiency. In contrast to a single antenna, the input matching of an array is scan-angle-dependent due to the interelement coupling of neighboring antennas. Nevertheless, the gain still improves directly with the number of elements.

2.2.3 EIRP and G/T

The properties Equivalent Isotropic Radiated Power (EIRP) for the transmitter and Antenna Gain-to-Noise-Temperature (G/T) for the receiver are often used to compare the performance of antenna systems.

The EIRP is a measure of the power density an antenna system radiates in the direction of the main lobe. It is the product of the antenna gain and the incident power and is hence valuable for system-level analysis:

$$\text{EIRP} = G_{\text{r}} * P_{\text{in}}\,. \tag{2.14}$$

The G/T is an important figure of merit for an Rx antenna. It relates the antenna gain G (usually in dB) to the receiver system's noise temperature T_{Sys}. T_{sys} is the sum of the antenna noise temperature T_{Ant} originating from the (atmospheric) background and the additional noise introduced in the RF signal path T_{Rx}. Noise temperature depends on the received noise power N:

$$T_{\text{Sys}} = \frac{N}{B * k_{\text{B}}}\,, \tag{2.15}$$

where B is the receiver bandwidth and k_{B} the Boltzmann constant. It can be converted to a noise figure $F = \frac{T_0+T_{\text{Sys}}}{T_0}$, where T_0 is the environment temperature [18, pp 6-7]. For practicality, a "standard" environment temperature close to the typical room temperature is often assumed ($T_0 = 290\,\text{K}$). For the receiver, the transmission line losses between the antenna and the first amplifier (so-called Low Noise Amplifier (LNA)) and the LNA performance are crucial. Indeed, in well-designed Rx systems, the noise temperature T_{Rx} is close to the equivalent temperature of the LNA's noise figure.

2.2.4 Number of Controls

The number of controls in an array significantly influences the total cost and complexity. A control in this context is a means to adjust a signal, such as a phase shifter or a controllable attenuator. In the case of suppressed grating lobes, the desired beamwidth θ_{BW} and the maximal scanning angle $\theta_{0,\mathrm{max}}$ determine the minimal number of required controls $N_{\mathrm{el,min}}$ [18, p. 42]:

$$N_{\mathrm{el,min}} \simeq 2 * \frac{\sin(\theta_{0,\mathrm{max}})}{\sin(\theta_{\mathrm{BW}})} \,. \tag{2.16}$$

The equation is valid for large arrays with scanning in one direction. For 2D scanning, $N^2_{\mathrm{el,min,1D}}$ controls are necessary. The realization of such a minimal array is complex. Indeed, the minimal number of controls does not mean the smallest size or simplest design. However, $N_{\mathrm{el,min}}$ is a good figure of merit to compare designs. If a planar array is considered, Eq. (2.10) and Eq. (2.11) can be used to determine the number of elements:

$$N_{\mathrm{el,min}} \simeq 0.866 * \frac{\lambda}{d} * \frac{B_{\mathrm{b}}}{\theta_{\mathrm{BW}} \cos\left(\theta_{0,\mathrm{max}}\right)} \,. \tag{2.17}$$

Grating lobes are suppressed if the element spacing d is smaller than $\lambda/2$ or the maximal scan angle is limited (cf. Eq. (2.12)). The plot in Fig. 2.4 shows the number of controls for a desired beamwidth of $\theta_{\mathrm{BW}} = 2°$. Due to the grating lobe suppression, the planar array with $d = \lambda/2$ requires a high number of elements and controls, even for small scan angles. The planar array with variable element spacing is closer to the ideal minimum for scan angles $\theta_{0,\mathrm{max}} < 50°$. The results are inaccurate for a low element count since the approximation in Eq. (2.10) is only valid for larger arrays. Both planar arrays show an asymptotic behavior for scan angles above 60° since the effective aperture decreases significantly. Furthermore, amplitude tapering is necessary for practical use, decreasing aperture efficiency and widening the beam. In Fig. 2.4, the results for an exemplary beam broadening of $B_{\mathrm{b}} = 1.2$ are also included. All these planar designs are not well suited for applications with high scan angle requirements.

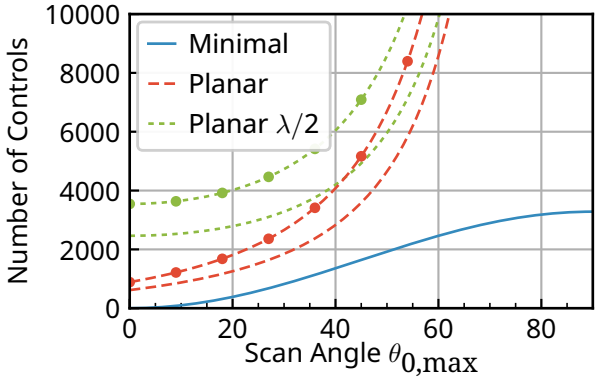

Figure 2.4: The minimal number of controls to obtain a phased array with scanning capability up to $\theta_{0,\mathrm{max}}$ at a given beamwidth (here: $\theta_{\mathrm{BW}} = 2°$). The beam broadening factor is $B_{\mathrm{b}} = 1$, except for the cases marked —●—, where $B_{\mathrm{b}} = 1.2$.

The significant deviation between the ideal minimum and the actual number of controls for the plotted planar arrays at high scan angles exposes the inherent problems. Several

design approaches exist to reduce the gap, including planar arrays consisting of larger sub-arrays or 3D-conformal arrays.

2.2.5 Performance Limitations

Several effects limit the performance of array antennas. One very critical factor is inter-element or mutual coupling. Many simplifications, such as the array factor F, are only valid in the case of independent or weakly coupled array elements. Coupling leads to a change in the reflection coefficient for scanned beams. In the worst case, all incident power is reflected. This effect is called scanning blindness and must be avoided in the desired scanning range.

Another significant limitation is the accuracy of the phase shifters. They are commonly digital and thus have a “stepped” phase response limiting the accuracy and increasing the SLL. Furthermore, amplitude and phase variations might occur in the feed networks, the phase shifters, or the amplitude controls due to production or environmental changes. If not fully calibrated, these effects can deteriorate the beam pattern as well.

2.3 Architectures

A phased array generally consists of the antenna elements, the feed network to distribute signals to the antennas, and the control circuitry to adjust each element’s phase and amplitude. The interconnection of these three building blocks is fundamental to the design of the array. A great variety of different topologies are possible and are chosen according to the application requirements. This section presents important beamforming architectures for later reference.

2.3.1 Feed Network

The feed network is required to distribute a signal to or collect it from each antenna. The two most common designs are the serial and the parallel feeds as depicted in Fig. 2.5a and Fig. 2.5b, respectively.

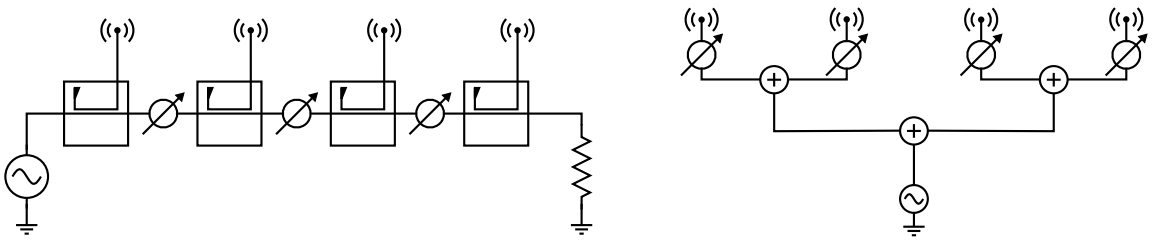

(a) (b)

Figure 2.5: Array topologies using (a) a serial (b) a parallel feed design.

In the serial feed design, all array elements are connected in series, and the signal progresses along the elements from the feed point. As illustrated in Fig. 2.5a, this can be realized using couplers. Phase shifters can be either placed in the signal path, leading to accumulating losses, or at each antenna element.

In contrast, the parallel feed uses a cascading design to split the signal evenly to all elements. Ideally, the amplitude and phase response of each branch are equal. Typical designs are symmetric and use power dividers to split the signal as shown in Fig. 2.5b. Hence, such designs often use 2^N_{el} elements.

The main advantage of the serial feed is a very compact feed network with low losses in the transmission lines. The required total phase shift between elements is also low in a design such as in Fig. 2.5a, where the phase shifters are positioned between elements. Due to the accumulating losses and inaccuracies along the network, this design is challenging for larger arrays. Furthermore, the electrical length of the transmission lines between elements is crucial since the resulting phase shift is frequency-dependent. Hence, the beam direction of serial feed arrays depends strongly on the operating frequency. Compensation is possible using the phase shifters if the signal's fractional bandwidth is low. On the other hand, this effect allows the design of so-called frequency-scanned arrays.

2.3.2 Phase Shifting Networks

Phased arrays are also categorized based on the placement of the phase shift stage. This section presents different approaches and discusses their usage scenarios. The focus here is only on parallel feed networks since they suit a more extensive range of applications.

RF Beamforming

In the Radio Frequency (RF) beamforming architecture, signal control and combination occur in the RF domain. Thus, the phase and amplitude control circuitry must be able to work up to the highest frequencies. This architecture is prevalent since it requires the fewest components and yields the most compact arrays. Ideally, a single Intermediate Frequency (IF) channel suffices without mixers or Local Oscillator (LO) distribution networks. The two cases shown in Fig. 2.5 use RF beamforming.

The main disadvantage of RF beamformers is the control circuits at higher frequencies (e.g., at millimeter wave). If available, they tend to be expensive, inaccurate, or suffer from high losses limiting receiver performance. The phase and amplitude response can also present further challenges.

IF Beamforming

As an alternative, IF beamforming reduces the operating frequency for the phase shifters and combination network. Thus, the available higher-performance components help to improve the array's overall functionality. However, a mixer is required at each antenna element to convert between RF and IF. The mixers require an LO signal demanding an additional distribution network.

Fig. 2.6a shows the topology. The high component count increases system complexity, energy consumption, size, and cost.

LO Beamforming

A mixer is a three-port device that converts an RF signal to IF based on an LO and vice versa. The phase of the RF signal is determined through the summation of LO and IF

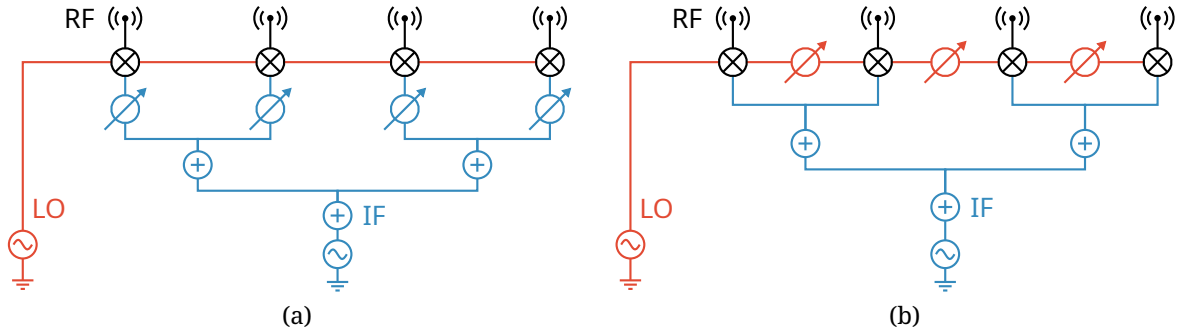

Figure 2.6: Array architecture using (a) IF and (b) LO beamforming. The RF part is marked in —, the IF part in —, and the LO in —.

phase. Unlike IF beamforming, the phase change occurs in the LO path. The signal is combined at IF. This architecture is shown in Fig. 2.6b.

The component count is similar to IF beamforming, but since the LO frequency is usually higher than IF, the phase shifters must operate at a higher frequency close to the RF. Subharmonic mixers can reduce the operating frequency for some use cases. The main advantage of LO beamforming is the absence of the phase shifter from the signal path, reducing loss, noise, and nonlinearities. Furthermore, the requirements on the performance characteristics, such as bandwidth, linearity, and losses of the used phase shifters, are less stringent.

Digital Beamforming

Digital beamforming uses software signal combination in the baseband. Hence, all antenna channels carry a complete processing chain from the RF to the digital domain. In addition to components used in the IF beamformer, a DBF-system must implement a complete IF processing chain including Analog-to-Digital Converter (ADC)/Digital-to-Analog Converter (DAC) in each channel. The concept is illustrated in Fig. 2.7a.

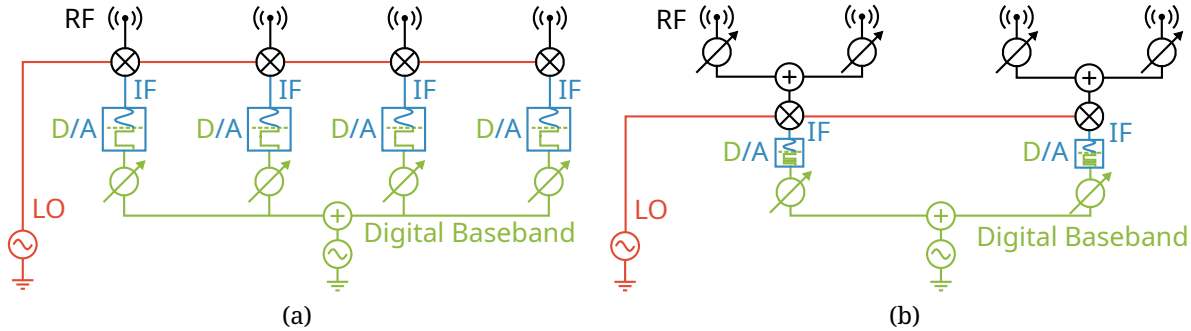

Figure 2.7: Array architecture using (a) Digital and (b) Hybrid beamforming. The RF part is marked in —, the IF part in —, the LO in —, and the digital domain in —.

This topology is the most advanced and complex, suffering from the high cost of extensive circuitry, size requirements, and power consumption. Furthermore, processing and speed requirements on digital hardware can be extreme and require special solutions. In turn, digital beamforming provides unique features and excellent flexibility: It enables an indefinite number of beams, an adaptively generated pattern, flexible nulls to suppress interference, and an instantaneous Direction of Arrival (DOA) estimation.

Hybrid Beamforming

The introduced beamforming approaches can be mixed and combined to obtain hybrid networks. Such hybrid approaches are beneficial for specific applications. Fig. 2.7b illustrates a mixed RF and digital beamforming network, combining (limited) digital beamforming capabilities with fewer components.

2.3.3 Active and Passive Arrays

Although technically sufficient, phased arrays have more active components than just phase shifters. Receiver arrays use LNAs to maximize the SNR. Transmitter arrays require Power Amplifier (PA)s to boost the output signal.

A passive array only uses one central LNA or PA. If, on the other hand, amplifiers are placed at each antenna element, the array is active [18, p. 35]. Passive arrays have significantly lower complexity and require fewer components and less electrical power. One significant advantage of active arrays is reliability since a single failing amplifier does not prevent array operation, but the performance "gracefully degrades". Hybrid approaches are also possible, combining multiple passive subarrays to form a better-performing large array.

Depending on the number of array elements N_{el}, the performance difference between both approaches can be significant. Here, we consider the properties EIRP and G/T and assume an array with an exemplary element spacing of $d = \lambda/2$. PAs with an output power of $P_{\text{Amp}} = 1\,\text{W}$ and LNAs with a noise figure of $F_{\text{LNA}} = 2\,\text{dB}$ are investigated for the Tx case and Rx case, respectively. The total network losses L are estimated, including power combiner and transmission line losses without the phase shifters. The length of transmission lines in a planar parallel fed array is approximately $l = (\sqrt{N_{\text{el}}} - 1)\lambda/2$. A good measure for microstrip lines on low-loss substrates at K_a-band is $0.3\,\text{dB}/\lambda$. For an array with N_{el} elements, a total number of $N_{\text{pd}} = \log_2(N_{\text{el}})$ power dividers are required, each assumed to have a loss of 0.3 dB.

Using Eq. (2.1) and assuming ideally matched components the EIRP is:

$$\text{EIRP} = N_{\text{el}} * \pi * L * P_{\text{Amp}} \qquad \text{(passive case)} \tag{2.18}$$

$$\text{EIRP} = N_{\text{el}}^2 * \pi * P_{\text{Amp}} \qquad \text{(active case) .} \tag{2.19}$$

The EIRP in the active case increases with N_{el}^2, whereas the passive case has only a linear relationship. Although an external PA can generate a much higher output power, the benefits are apparent. Furthermore, the loss term L is omitted in the active case since the individual amplifier gain can compensate for circuit losses. The investigation results are plotted in Fig. 2.8a. Including transmission line losses, the EIRP does not monotonically

increase with the number of elements but reaches a maximum. The maximum defines the largest sensible size of a passive array.

A similar investigation can be made for the G/T assuming an antenna noise temperature of $T_{\text{Ant}} = 100K$:

$$\text{G/T} = \frac{N_{\text{el}} * \pi * L}{T_{\text{Ant}} + (F_{\text{LNA}} * L - 1)T_0} \qquad \text{(passive case)} \tag{2.20}$$

$$\text{G/T} = \frac{N_{\text{el}} * \pi}{T_{\text{Ant}} + (F_{\text{LNA}} - 1)T_0} \qquad \text{(active case) .} \tag{2.21}$$

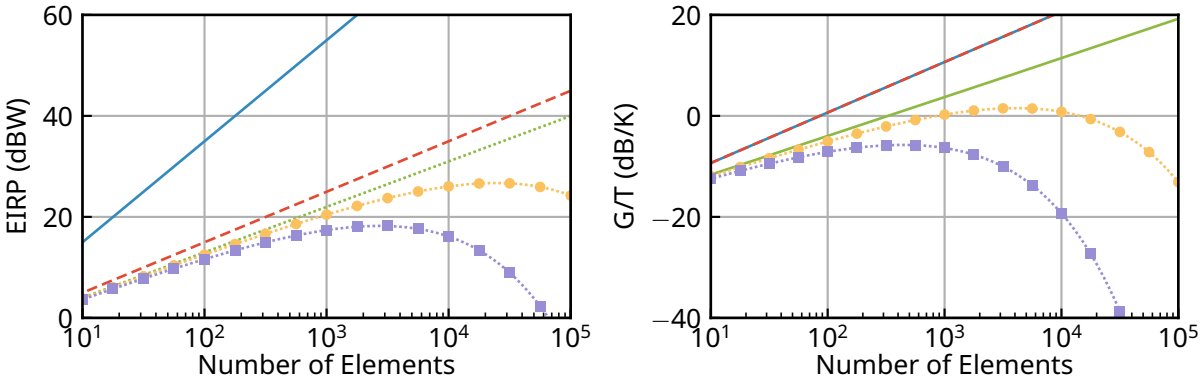

(a) (b)

Figure 2.8: The (a) EIRP and (b) G/T of a square array with element spacing $\lambda/2$. The active array is plotted in ——. The passive array excluding losses is displayed as - - -, with combiner losses as ·····, with combiner and $0.1\,\text{dB}/\lambda$ line losses as ·●·, and with combiner and $0.3\,\text{dB}/\lambda$ line losses as ·■·.

In contrast to the Tx case, the G/T initially increases linearly for both the active and passive cases (cf. Fig. 2.8b). Indeed, the passive lossless and the active cases are quasi-equal. However, due to the additional noise generated in the lossy passive network, the maximum is reached at a smaller element number, and the dropoff is much steeper. Hence, reducing (transmission line) losses is vital for Rx arrays.

2.3.4 Frontend

This work refers to the frontend as the analog part of the signal processing chain, excluding the antennas. The RF frontend includes the mixer and LO distribution network and contains passives (filters, couplers) and active components (amplifiers, phase shifters, Integrated Circuit (IC)s). The frontend design fundamentally influences the overall array size and performance limitations. Organizing frontends in Line Replaceable Unit (LRU)s allows for efficient replacement of malfunctioning ones. Such a LRU or *module* consists of one or multiple channels.

The main challenge in the frontend design process is the integration of active components. They require space, electrical power, cooling, and supply networks [23]. The integration becomes more difficult at higher frequencies because IC packages do not

shrink as much as the available area in the array grid. Moreover, the efficiency of amplifiers decreases, causing even higher power consumption. The resulting high thermal power densities require elaborate cooling solutions.

The two main integration approaches are the so-called “brick” and “tile” architectures [24], [25]. They relate only to “the way the array is assembled, not the organization of the aperture” [18, p. 47].

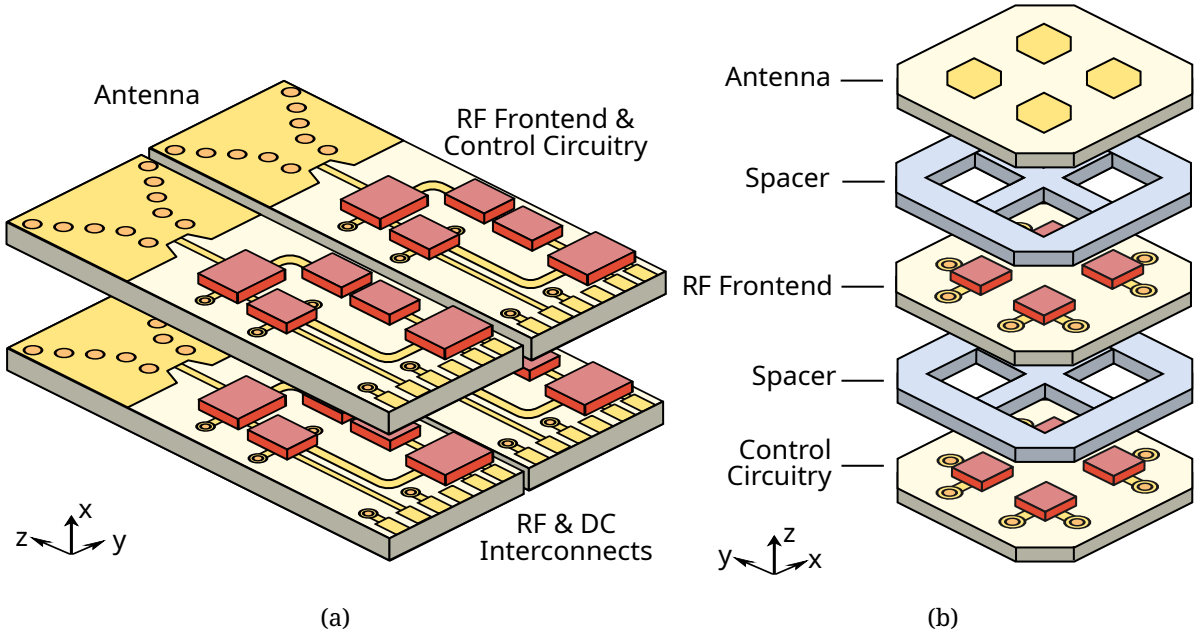

Figure 2.9: 4x4 array in (a) brick and (b) tile architecture.

Examples of both architectures, including the array antennas and the frontends, are depicted in Fig. 2.9. Both arrays are aligned to radiate in the z-direction and are realized in Printed Circuit Board (PCB) technology. The brick construction in Fig. 2.9a is well proven and widely used [26, pp. 161–163]. The available surface for component integration is longitudinally aligned with the radiation direction. It can be easily adjusted by changing the module’s overall depth. In the brick architecture, it is common to integrate only one channel per module [27, p. 26], although multiple channels per module have been demonstrated [28] at millimeter wave frequencies. Besides the scalability, cooling, interconnect design, and maintainability are further advantages of a brick module. Furthermore, many well-known antennas are easily integrable. Examples include waveguide horns, dipoles, and the depicted Substrate Integrated Waveguide (SIW) antennas. The biggest drawback of the brick architecture is the overall module size.

The tile approach is superior for compact designs. Components are integrated into a plane transverse to the radiation direction. Often, patch antennas are used (cf. Fig. 2.9b). Several challenges are involved with tile architectures. A high number of components lead to very dense packaging since the array grid spacing confines the available space. Additional layers can mitigate this problem but require (complex) vertical interconnects [29] and decrease the cooling capability. Furthermore, coupling between components and tightly integrated feed networks decreases performance. Innovative solutions, such

as folded modules [30] or hybrid brick-tile designs [31], are options to overcome these limitations.

2.4 Design for Communications

The focus of this work is on the design of electronically scanned antennas for mobile communications. The underlying requirements differ significantly from radar or other imaging applications. Multiple simultaneous beams and high isolation between Rx and Tx are less critical, whereas low-cost, continuous operation, interference minimization, and high gain are more important. In this section, exemplary satellite communication scenarios are introduced, and their implications on phased array design are discussed. The presented scenarios serve as a reference for the solutions presented in this thesis.

2.4.1 Communication Scenario

Satellite communications have become essential to today's worldwide data networks [32, p. 16]. Particularly in remote areas, satellites are often the only means of communication. The Geostationary Earth Orbit (GEO), located 35,786 km above the equator, is currently the preferred location for communication satellites, as the direction between a satellite and a point on the Earth's surface does not change. GEO communication allows a relatively simple network of fixed earth stations as gateways. In addition, the user terminals for such Fixed Satellite Service (FSS) do not need tracking capabilities. Therefore, many satellites operate in the GEO. The resulting dense orbital spacing requires strict regulation for satellites and terminals alike by organizations such as the ITU and European Telecommunications Standards Institute (ETSI). Consequently, GEO satellites have become increasingly powerful and expensive. Some satellites, such as VIASAT 1, allow total throughputs of more than 100 Gbit/s from a single orbital position.

The available spectrum must be spatially reused to enable such high data rates. Multibeam antennas onboard the satellite generate hundreds of optimally non-overlapping spot beams on the Earth's surface. As shown on the left side of Fig. 2.10, one of four colors is dedicated to each spot beam using the four-color theorem [33]. If each color corresponds to an orthogonal signal, interference is minimal. For Satellite Communications (SatCom), two polarizations (e.g., RHCP and LHCP) along with two frequency bands (e.g., low and high band) represent the four colors. One-quarter of the total achievable data rate is available to users in each spot beam. The total throughput is maximized using many small spot beams on the Earth's surface. As shown on the right side of Fig. 2.10, the spot beams are often shaped to cover populated areas only. To further maximize the throughput, the two-color scheme could be used [34]. The total achievable bandwidth increases to one-half at the expense of more interference problems in beam overlaps.

GEO satellites also have some drawbacks. Due to the significant altitude and dense orbit spacing, the satellites must be very powerful and therefore big and heavy, which increases production and launch costs. Furthermore, the long distance between Earth and the satellite results in a high Free Space Loss (FSL) and a long round trip delay of more than 500 ms. In the polar regions, GEO satellites are below the horizon, making reception impossible. As alternatives, lower orbits such as the Medium Earth Orbit (MEO) or Low Earth Orbit (LEO) illustrated in Fig. 2.11a can be utilized.

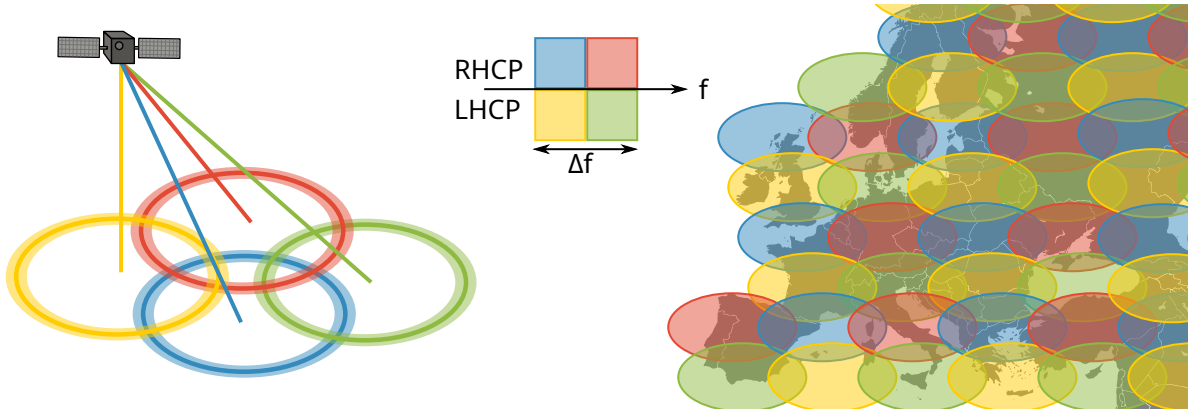

Figure 2.10: Reuse of available resources with minimal interference using the four-color scheme for satellite communications.

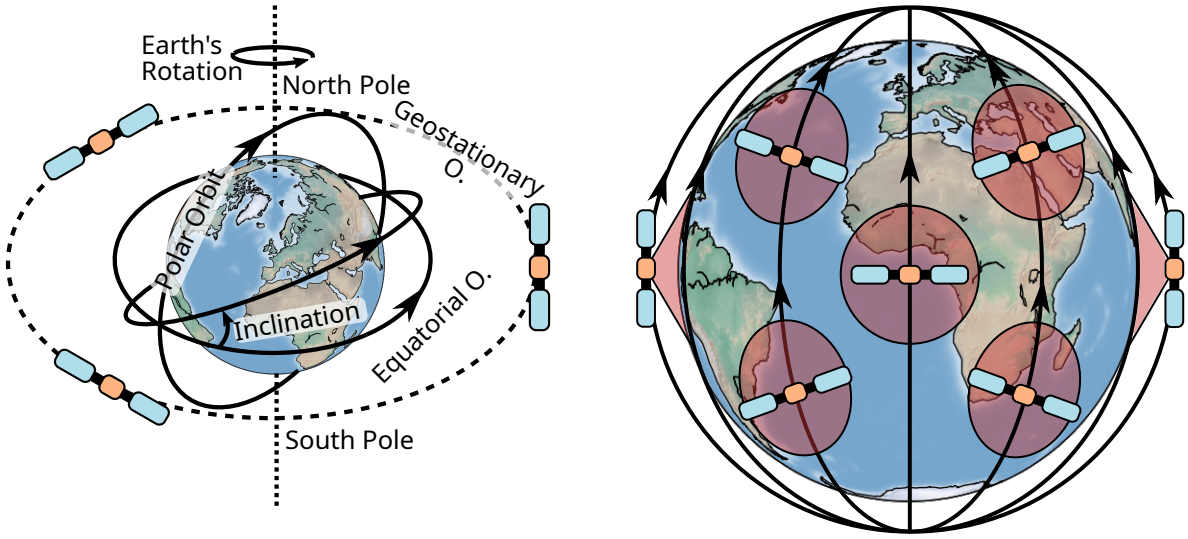

(a) (b)

Figure 2.11: (a) Three satellites in geostationary orbit and different low Earth orbits. (b) Coverage of an exemplary LEO satellite constellation using polar orbits.

Satellites not in the GEO orbit move relative to the Earth's surface. Depending on the inclination (the angle between the orbital and equatorial plane [32, p. 28]), different orbits, such as equatorial and polar, are possible. In particular, the polar orbit is pivotal, as it enables true worldwide satellite coverage [32, 392ff]. Disadvantages of these orbits include the tracking necessity of ground equipment and many satellites to allow permanent global coverage. Another drawback of polar orbits is the required high number of ground stations throughout the desired coverage area. In remote areas, the need for more infrastructure further complicates worldwide operations. A data relay using Inter-Satellite Links (ISL)s can be a solution. Fig. 2.11b shows a constellation of several LEO satellites in a polar orbit.

Constellations with high numbers of LEO satellites have recently attracted significant attention as alternatives to the existing GEO networks. These so-called mega-constellations are currently in development by private companies such as *SpaceX* (Starklink), *OneWeb*, and *Telesat* to participate in the so-called *New Space Economy*. Current network plans include K_u-band-, K_a-band- and even V-band usage with about 100 (Telesat) to more than 10000 (Starlink) satellites in orbits between 500 km and 1500 km. Since 2020 the Starlink constellation has been operational with 3376 satellites in orbit at the end of 2022.

The high number of satellites required for a mega-constellation must be produced and launched on an industrial scale, significantly reducing the build and launch cost compared to a GEO satellite. A LEO satellite can significantly reduce the round trip delay and free space loss, allowing for new applications and compact ground antennas. Smaller spot beams and an improved link budget can increase the available data rate. With reduced network costs, satellite service providers can compete with cable-based ISPs and a ground-independent communication channel. Two main application scenarios are offered: The terminal can directly communicate with the satellite or use a nearby earth station as a gateway. *O3B*-network, which operates in a MEO, uses the gateway scenario. It provides satellite coverage to cheap mobile terminals or smartphones but requires a dense base station network. Therefore, this approach is mostly suitable for populated areas without a proper backbone infrastructure, e.g., in developing countries.

Terminals for LEO communications are ideally inexpensive and compact and must have tracking capability. This work presents such solutions based on electronically scannable antennas. The presented technological innovations are, in principle, applicable to both the mobile user communicating with a GEO satellite and the mobile or fixed user communicating with a moving LEO satellite.

2.4.2 Satellite Constellations

The satellite constellation significantly influences the terminal design and the possible communication scenario. The required number of satellites for continuous global coverage can be estimated using Fig. 2.12. The area a single satellite can illuminate instantaneously depends on the Earth's surface coverage arc γ. This coverage arc depends on the satellite altitude h and the maximal acceptable look angle $\theta_{0,\max}$ of the terminal towards the satellite. $\theta_{0,\max}$ is specified at the Edge of Coverage (EOC) of the satellite beam (typically at the HPBW). If the satellite generates a single beam only, the angle δ is equivalent to the beamwidth of the satellite antenna. r_e is the radius of the Earth. The link length is the distance between the satellite and the terminal. It varies from h in the center of the beam to d at the EOC.

In the case of a GEO satellite with a look angle oriented downward towards the horizon ($\theta_{0,\max} = 90°$), the coverage arc is 162.6°. Therefore, three satellites are required for full coverage of the equator, whereas the polar regions cannot be covered at all. Such a constellation is used in INMARSAT-5 to provide almost worldwide internet access, focusing on the oceans. The minimal look angles to one of the three satellites are plotted in Fig. 2.13.

The three satellites are positioned above the Pacific, Atlantic, and Indian oceans. The look angle remains below 75° on the equator but rises quickly towards the poles. Some regions in Central Europe reach look angles of more than 80°, which are very low above the horizon and are critical for many antenna systems. The satellites are consistently below the horizon in the far North and South. The link distance d also increases for

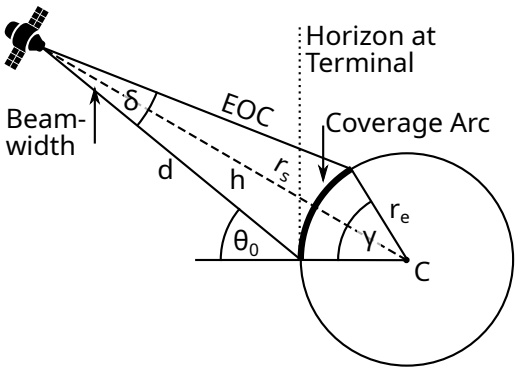

Figure 2.12: Instantaneous coverage arc of one LEO satellite on the Earth.

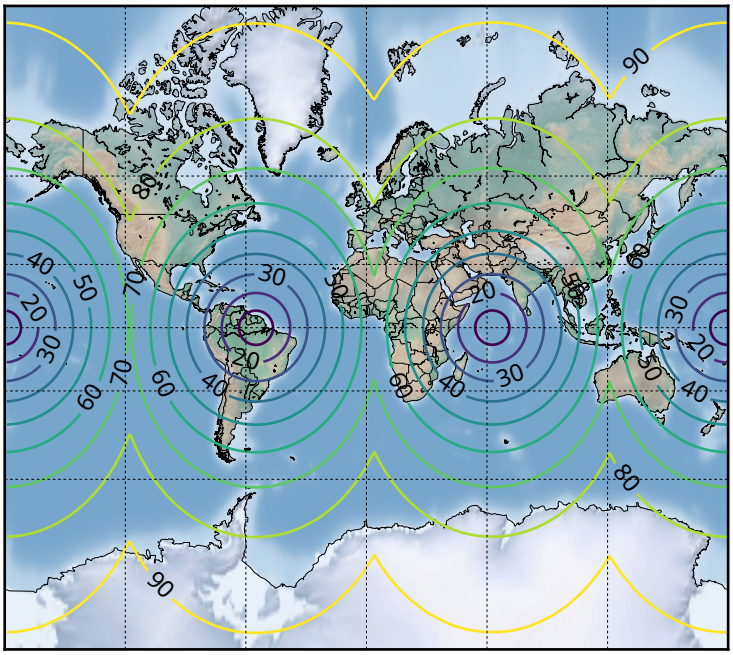

Figure 2.13: Minimal look angles of antenna terminals on the Earth's surface towards the three INMARSAT-5 geostationary satellites at 63° East, 55° West, and 179° East. The map uses a Mercator projection.

regions further away from the sub-satellite point. At $\theta_0 = 90°$ the distance is 41679 km, which is roughly 6000 km more than the shortest path. At K_a-band, this increases the FSL by 1.3 dB.

The satellite position can be altered to improve coverage in Europe. Eutelsat's KA-SAT is positioned at 9° East, which is ideal for covering Europe. As shown in Fig. 2.14 the maximal look angles improve somewhat to less than 70°. Nevertheless, significant parts of Germany and the UK still require angles greater than 60°.

Satellite constellations in a LEO polar orbit can improve the look angle everywhere on Earth. In Fig. 2.11b, not the entire Earth's surface is permanently covered by satellite

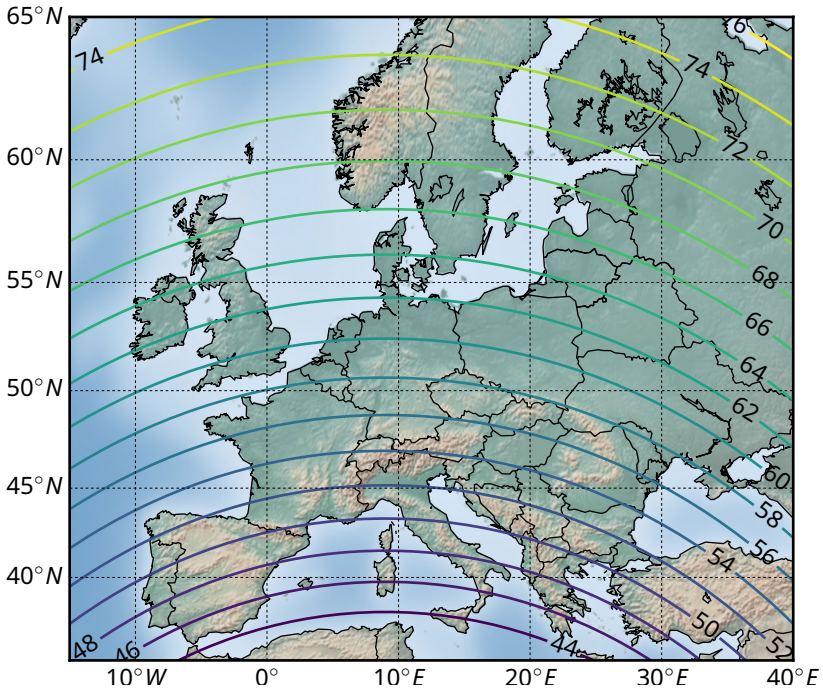

Figure 2.14: Required look angles for satellites communication with the geostationary Eutelsat KA-SAT satellite at 9° East in Europe.

beams. The required number of satellites for continuous coverage can also be estimated using the coverage arc from Fig. 2.12. It is listed in Table 2.1 for LEO satellites operating at 500 km, 750 km, and 1200 km altitude with maximal look angles of 30°, 60°, and 80°. The coverage arc increases significantly for higher orbits and wider satellite beams from 48° with 32 required satellites ($h = 1200\,\mathrm{km}$, $\delta = 112°$) to 4.8° with 2888 required satellites ($h = 500\,\mathrm{km}$, $\delta = 55.2°$).

Table 2.1: Analysis of the minimal number of low Earth orbit satellites in varying altitudes for global coverage and three maximal look angle $\theta_{0,\mathrm{max}}$.

Altitude	$\theta_{0,max}$	**FSL**	**BW** δ	**Gain**	**Coverage Arc** γ	**# Sat.**
500 km	80.0°	172.4 dB	131.9°	2.8 dB	28.1°	91
500 km	60.0°	172.4 dB	106.8°	4.6 dB	13.2°	392
500 km	30.0°	172.4 dB	55.2°	10.3 dB	4.8°	2888
750 km	80.0°	176.0 dB	123.6°	3.3 dB	36.4°	50
750 km	60.0°	176.0 dB	101.6°	5.0 dB	18.4°	200
750 km	30.0°	176.0 dB	53.2°	10.7 dB	6.8°	1431
1200 km	80.0°	180.0 dB	112.0°	4.2 dB	48.0°	32
1200 km	60.0°	180.0 dB	93.6°	5.8 dB	26.4°	98
1200 km	30.0°	180.0 dB	49.8°	11.2 dB	10.2°	648

The results represent only a minimal constellation without any overlaps. If more than one satellite should be visible at any given time and spare satellites must be available,

more satellites are needed. The *OneWeb* constellation is scheduled to begin service with an initial number of 648 satellites at an altitude of 1200 km. Hence, a fixed terminal scanning up to 30° is sufficient to keep one satellite in view. If more satellites are in orbit later in the project, scanning requirements are reduced, and multiple satellites can be used simultaneously.

2.4.3 Scanning Considerations

Section 2.4.2 illustrates the effect of the satellite constellation on the required look angles from the ground terminal to the satellite. While LEO-constellations allow relatively low look angles, they quickly reach more than 60° for GEO-satellite constellations in significant parts of the densely populated and traveled Northern Hemisphere. According to Section 2.2.4, this value is already above the reasonable threshold for a single planar array design, and other solutions are needed.

In addition, mobile terminals further increase the scanning requirement because the orientation between the antenna and the satellite may change through the movements of the mobile platform. Thus, an assessment of typical angular changes is required to determine sensible array designs. Here, we will consider three cases: a ground vehicle, a ship, and an airplane. In principle, the three axes of rotation pitch (nose up and down), roll (circular movement around the forward axis), and yaw (nose moving to the side) must be considered. In many cases, the array boresight coincides with the yaw-axis. In that case, the yaw movement is negligible.

In [35], a car's typical roll and pitch movements in different driving and road conditions are analyzed. During normal driving, roll angles of less than 5° and pitch angles of less than 1° are observed even during spins or on bumpy roads. These values are exceeded for banked or inclined road surfaces. Similar results are reported in [36], where changes in yaw are also investigated.

For maritime applications, roll and pitch angles significantly depend on the vessel size and weather conditions. [37] reports pitch angles of up to 1.9° and roll angles of up to 6.3°. More general considerations are given in [38, Section 2.3.3], reporting pitch angles up to 8° for small and 3° for large container ships. Furthermore, roll angles of up to 10° are reported even for a larger ship, which may reach 45° in extreme conditions.

For planes, available data is somewhat scarce and confidential. An *FAA* statistical analysis of the *Boeing 747-400* airplane provides pitch angles during different flight phases [39]. The pitch angle remains below 15° and 7° for most of the flights during departure and approach, respectively. During cruise flights, only minor (negligible) pitch angles are observed. These results are generally confirmed for a non-commercial plane in [40], where bank (roll) angles of up to 50° are registered. However, the *Airplane Upset Recovery Training Aid* advises maximal banking angles of 45°, nose up pitch angles of 25°, and nose down pitch angles of 10° for a passenger flight to be considered "normal" [41]. Furthermore, bank angles of less than 10–15° are recommended during the cruise phase.

2.4.4 Satellite Links

Historically, the GEO has been widely used for many satellites operating in various frequency bands. GEO satellites operate at a defined altitude above the equator in tightly spaced orbits, sometimes even in the same frequency band. Consequently, satellite terminals undergo strict regulation to minimize interference with neighboring satellites

or services. At K_a-band, ETSI standard EN 303 978 defines such a set of requirements [42]. A significant one is the limitation of the EIRP for in-band off-axis signals emitted by the terminal. Fig. 2.15a shows these limitations for co-polar and cross-polar signals for any 40 kHz band. Since a typical satellite spacing is 2°, no on-axis EIRP limits exist within $\theta = \pm 1°$.

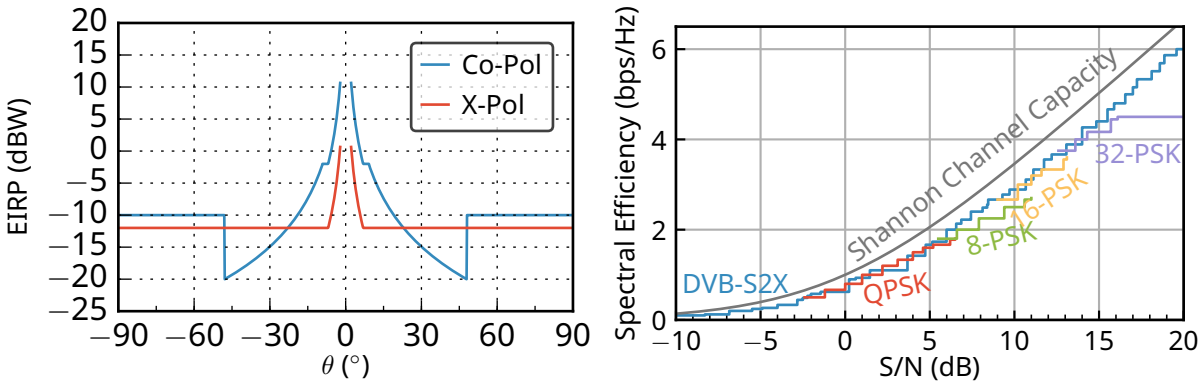

(a) (b)

Figure 2.15: (a) In-band off-axis EIRP requirements for Ka-band satellite terminals according to ETSI standard EN 303 978. (b) Spectral efficiency of satellite links using DVB-S2X.

The achievable data rate is of the greatest importance in evaluating the performance of the radio link. According to the Shannon-Hartley theorem, the channel capacity C of an analog channel with bandwidth B depends only on the SNR:

$$C = B \log_2 \left(1 + \frac{S}{N}\right). \tag{2.22}$$

The channel capacity is the maximal possible error-free data rate of that channel. Practical systems must use high-order modulations and efficient channel coding to maximize the data rate and get close to this upper bound. The improved computing power has enabled the usage of very efficient Low-Density Parity-Check (LDPC) codes [43], [44]. Modern satellite communications use these LDPC codes in standards such as DVB-S2X to maximize the data rate [45]. Since the bandwidth may vary, the spectral efficiency S/B is better suited to compare the effectiveness of coding and modulation. In Fig. 2.15b, the spectral efficiency of DVB-S2X (—) is compared to the modulation used in the older DVB-S2 standard and the Shannon limit. DVB-S2X is very close to the bound and extends DVB-S2 significantly for signal-to-noise ratios S/N below -2 dB and above +16 dB.

To estimate the received carrier power S, the EIRP, the Rx antenna gain, and propagation losses must be determined. Free space loss is the main issue for satellite links. In addition, absorption and scattering in the atmosphere and ionosphere further degrade signal power. These influences are often minor unless precipitation occurs in the propagation path. In particular, liquid water attenuation is crucial. Fig. 2.16a shows the geometry to estimate the influence of rain. The zero-degree isotherm is the melting layer. The water above is frozen and is therefore neglected in the analysis. The altitude of the melting layer changes during the year and depends on the latitude. A worst-case scenario is considered

in Fig. 2.16b to estimate the attenuation [32], [46, p. 509], which depends on the rain rate and the frequency. The rain is light at rates below 2.5 mm/h, whereas convective rain starts at 10 mm/h.

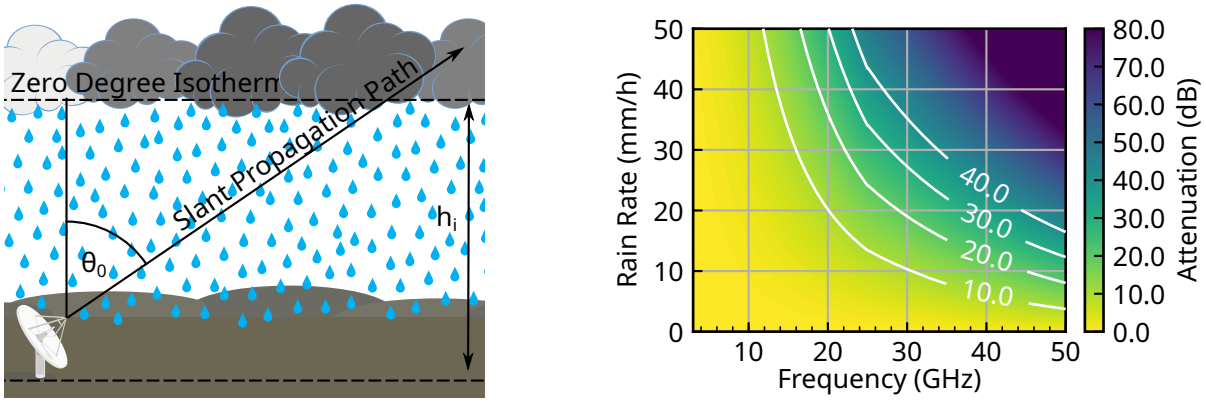

(a) (b)

Figure 2.16: (a) Propagation model of radio waves in rain conditions. (b) Rain rate dependent attenuation.

For frequencies below 10 GHz, the attenuation is generally low but rises quickly with frequency. At a rain rate of 20 mm/h, the rain attenuation is approximately 20 dB at 30 GHz, 9 dB at 20 GHz, and only 3 dB at 1.5 GHz. For high scan angles θ_0, the propagation path through the rain becomes longer, and the attenuation rises further.

An analysis of the receiver system allows to determine the noise power N. Fig. 2.17a shows the schematic of a heterodyne receiver used for many applications. First, the antenna receives an incoming RF signal, which is boosted by an LNA and downconverted to IF in the RF frontend. The IF stage includes filters and amplifiers. The receiver chain ends in the Digital Signal Processor (DSP). Three main causes influence receiver noise performance: background noise, losses, and the LNA. The antenna receives background noise from the ground and also from the sky/space. Background sky noise changes with the scanning angles and strongly depends on the antenna pattern. Ideally, the antenna pattern suppresses noise from the ground, and the antenna does not point toward the sun. Losses in the antenna and RF network at the LNA decrease the SNR further. The LNA increases signal and noise power, but the overall SNR decreases by its noise figure F. If designed correctly, the SNR in the receiver chain stays nearly constant for the rest of the Rx chain.

The noise performance of the Rx frontend mainly depends on the losses and the LNA noise figure. To specify the G/T (c.f. Section 2.2.3), the equivalent Rx noise temperature of the Rx system must be determined. Fig. 2.17b illustrates the influence of the noise figure and losses on the noise temperature. Limits for the noise figure and losses must be carefully observed to keep the noise below the ambient temperature.

All these results are combined to determine the link SNR

$$\frac{S}{N} = \frac{\text{EIRP} * \text{G/T}}{B * \text{Link Losses}}, \tag{2.23}$$

which can be used in combination with Fig. 2.15b to determine the data rate.

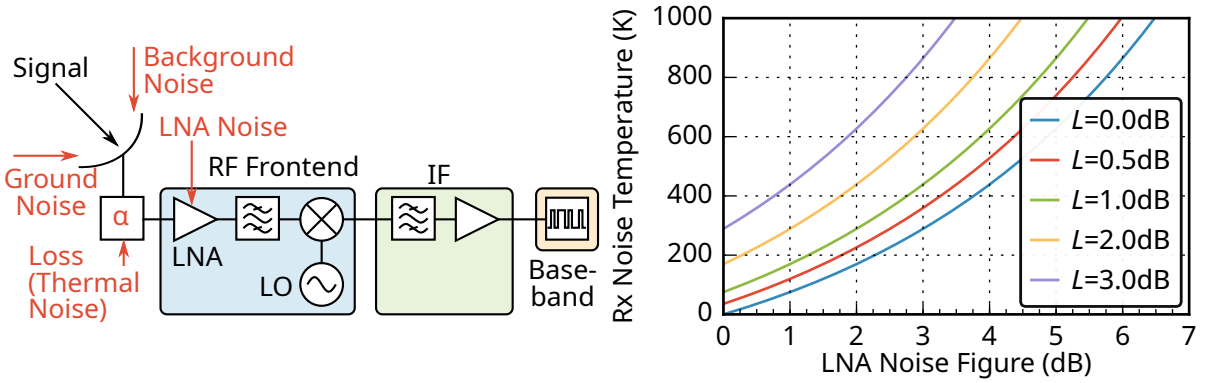

(a) (b)

Figure 2.17: (a) Typical receiver schematic including major noise sources. (b) Influence of RF losses (L) and LNA noise figure on the receiver noise temperature (T_{Rx}.).

2.4.5 Link Budget

Based on the results from Section 2.4.2 and Section 2.4.4, so-called link budgets are calculated for two exemplary cases, a LEO and a GEO constellation at Ka-Band. At Ka-band, the widely used frequency band for the uplink (terminal Tx, satellite Rx) ranges from 29.5 GHz to 30.0 GHz, and for the downlink (terminal Rx, satellite Tx) from 19.7 GHz to 20.2 GHz. The analysis also considers an L-Band LEO uplink as a lower frequency reference. Table 2.2 lists the results.

The uplink bandwidth is smaller than the downlink bandwidth for user terminal links. Typical values are 3 MHz for the uplink and 236 MHz for the downlink. These values are often further reduced for single users by Frequency-Division Multiple Access (FDMA) or Time-Division Multiple Access (TDMA) schemes. The terminal's scanning requirement depends on the constellation. Realistic values are 30° for the LEO and 60° for the GEO.

The FSL of about 210 dB for a K_a-band GEO is the major contributor to the total link loss. For LEO constellations, the FSL is reduced to 180 dB and 160 dB for K_a-band or L-Band links, respectively. Slightly larger values are possible for earth stations located away from the sub-satellite point on the equator.

To determine EIRP and G/T, antenna diameters of 60 cm and 110 cm are assumed for the terminal and satellite, respectively. The satellite transmitter power is 50 W compared to 1 W for the terminal. The assumed system noise temperature of the terminal is 300 K, which is 100 K less than that of the satellite. The satellite's background noise temperature is higher since its antenna points towards the hot Earth. Using this setup with DVB-S2X yields optimal data rates of 18 Mbit/s for the uplink and 1416 Mbit/s for the downlink in all five considered scenarios.

However, actual links have to include margins for precipitation and other effects. In Central Europe, rain rates remain below 22 mm/h for 99.9% of the year [47]. This rain rate results in additional losses of 3.0, 9.3 dB, and 19.8 dB at 1.5 GHz, 20 GHz, and 30 GHz, respectively. In addition, the background temperature of the terminal antenna rises due to the rain. Atmospheric losses (L_{A}) are of less importance but can reach about 1 dB for high scanning angles at K_a-band. Antennas located at the EOC suffer from about 1 dB higher path loss (ΔFSL) and 3 dB lower EIRP from the satellite (ΔEIRP). In addition, scan

Table 2.2: Link budget calculation of three satellite scenario including LEO and GEO satellites at L- and Ka-Band. EIRP and G/T of the satellites are noted at the edge of coverage.

Scenario	**L-Band (LEO)**	**Ka-Band (LEO)**		**Ka-Band (GEO)**	
Terminal	Uplink	Downlink	Uplink	Downlink	Uplink
Frequency (GHz)	1.5	20.0	30.0	20.0	30.0
Bandwidth (MHz)	3.0	236.0	3.0	236.0	3.0
$\theta_{0,\max}$ (°)	30.0	30.0	30.0	60.0	60.0
Link Distance	1200 – 1351 km			35778 – 41671 km	
FSL (dB)	157.6	180.1	183.6	209.5	213.1
Tx Ant. Diameter (m)	0.6	1.6	0.6	1.6	0.6
Tx G_{Ant} (dBi)	19.5	50.6	45.5	50.6	45.5
P_{out} (W)	1.0	50.0	1.0	50.0	1.0
EIRP (dBW)	19.5	67.6	45.5	67.6	45.5
Rx Ant. Diameter (m)	1.1	0.6	1.1	0.6	1.1
Rx G_{Ant} (dBi)	24.6	42.0	50.6	42.0	50.6
Rx T_{Sys} (K)	400.0	300.0	400.0	300.0	400.0
G/T (dB/K)	-1.5	17.2	24.6	17.2	24.6
S/N (dB)	**24.3**	**49.6**	**50.3**	**20.2**	**20.8**
Spectral Efficiency	**6.0**	**6.0**	**6.0**	**6.0**	**6.0**
Date Rate (Mbit/s)	**18.0**	**1416.0**	**18.0**	**1416.0**	**18.0**
ΔEIRP at EOC (dB)	3.0	3.0	3.0	3.0	3.0
ΔFSL at EOC (dB)	1.0	1.0	1.0	1.3	1.3
L_A (dB)	0.1	1.0	1.0	1.0	1.0
Rain(dB)	3.0	9.3	19.8	9.3	19.8
Scan Loss (dB)	1.0	1.0	1.0	3.0	3.0
S/N w. margins (dB)	**16.2**	**34.3**	**24.5**	**2.5**	**-7.3**
Spectral Efficiency	**4.8**	**6.0**	**6.0**	**1.1**	**0.1**
Date Rate (Mbit/s)	**14.4**	**1416.0**	**18.0**	**259.6**	**0.4**

angle-dependent gain reduction and scan loss occur in a planar array. All of these effects combined necessitate a margin of 8 dB for L-band (LEO), 15 dB for K_a-band-band (LEO), and 17 dB at K_a-band GEO.

A reduced SNR leads to a drop in data rate. The K_a-band LEO satellites are least influenced since their antenna gain and SNR are highest. They can still achieve optimal data rates in the uplink and downlink. In contrast, the K_a-band GEO uplink data rate is reduced to 0.4 Mbit/s. The L-Band data rate is only reduced to 14.4 Mbit/s, since this frequency is robust in rain conditions. Starlink satellites operating at an even lower orbital position further enhance the link budget, thereby increasing the advantage over GEO-satellites.

A link budget analysis for differently sized arrays using the approximation from Eq. (2.13) yields a reasonable estimate of the array performance. The G/T is calculated for an active array with equidistant $\lambda/2$ spacing. The results are shown in Fig. 2.18a for the

GEO K_a-band scenario from Table 2.2. As expected, data rate and G/T rise steadily until the data rate reaches the maximum possible with DVB-S2X. For a noise temperature of 200 K, about 3000 elements suffice.

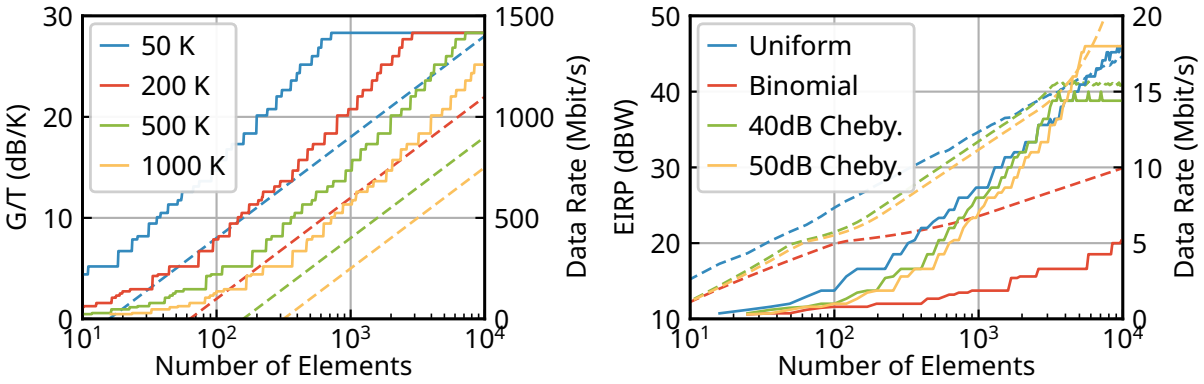

Figure 2.18: (a) Dependence of the G/T —— and data rate - - - of a planar array on the number of elements and noise temperature. (b) Dependence of the EIRP —— and data rate - - - of a planar array on the number of elements and amplitude taper.

For transmit arrays, the EIRP for off-axis in-band signals must comply with ETSI standard EN 303 978. Thus, the maximum possible EIRP depends on the array pattern, especially the beamwidth and sidelobes. The results from the analysis are depicted in Fig. 2.18b for four different amplitude tapers. The uniform taper is most beneficial for a small number of elements since the beamwidth is most critical in this regime. For more than 3000 elements the sidelobes are more critical, and the Chebychev tapers are better suited. However, their performance is also limited since their SLL never decreases below the predefined value. 5000 elements and a 50 dB Chebychev taper are required to achieve optimal performance.

2.5 Challenges

Phased arrays are a technological concept to obtain electronic beam scanning, enabling flexibility and adaptability to various applications. Phased arrays can be based on a variety of architectures and designs, allowing for a multitude of solutions.

The prior sections illustrate the challenges in the design process, including the performance, size, number of elements, and cost. However, there are still more issues, like thermal and power requirements, technology availability, and competition with existing solutions.

In the case of mobile satellite communication, mechanically steered reflector antennas are the prominent alternative. In a GEO scenario, these antennas have significant advantages, most notably their lower cost. In addition, they can be relatively easily scaled to a larger size to compensate for the high free space losses and steer the beam without pattern degradation. As shown in Section 2.4.2, the required scanning range is extensive and not suitable for conventional planar arrays. In a LEO constellation, on the other hand,

the antenna can be much smaller, and scanning requirements are lower. Additionally, constant tracking is necessary. Simultaneous communication with multiple satellites offers a clear benefit by allowing phased arrays to demonstrate their full potential.

Ultimately, the decision remains whether the benefits are worth the extra cost – both in development and production. This work aims to address the issue and provide solutions of lower complexity that allow the use of phased arrays in a broader range of applications.

Chapter 3
Efficient Phased Array Designs

Chapter 2 introduced phased array design principles and the associated challenges. This chapter focuses on technological solutions to efficiently implement such array designs. It begins with an overview of currently available antenna, network, and frontend design technologies and introduces recent developments such as multi-use and reconfigurable designs. Furthermore, an integrated calibration concept for planar patch antenna arrays is discussed.

3.1 Current Fabrication Technologies

Historically, high-performance scanning has been the main driver in phased array design. As explained in Section 2.3.3 and Section 2.4.4, losses in the antennas and distribution networks are significant bottlenecks for high performance. Hence, waveguides are still widely used for phased arrays since they exhibit low losses and yield robust assemblies. Many precision machined components such as antennas, splitters, and phase shifters are available for high power and high sensitivity applications. Their main disadvantages are cost (due to the elaborate fabrication) and size (due to their bulky nature). Over the years, other technologies such as PCBs and ICs have emerged in phased array designs to either complement or replace waveguides. These are briefly introduced in this section.

3.1.1 Printed Circuit Boards

At wavelengths in the low cm and mm range, PCB technology is a viable alternative to waveguides because the dimensions of the electrical structures are in the optimal range limited by process resolution and maximum feature size. PCB can be fabricated in large-scale industrial processes at relatively low cost. A typical substrate panel size for a standard PCB process is 12 by 18 inches and would hence allow producing a 61 x 91 array (5500 elements) at 30 GHz with a $\lambda/2$ element spacing on a single substrate sheet. Multiple panels can be stacked for more complex systems to form multilayer boards. The layer thickness is typically in the range of 0.1 mm to about 1 mm, with thinner and thicker panels available for particular purposes at higher prices. The number of inner layers can be customized according to application requirements. For RF signals, interconnects to and between these inner layers are problematic and limit usability. An RF multilayer with 16 layers and an overall thickness of about 4.8 mm is illustrated in Fig. A.1.

Compared to waveguides for array designs, the benefits of PCB technology are the available (standard) fabrication processes and the overall compactness of good designs. In addition, the integration of electronics is typically straightforward: Packaged ICs are soldered to the top and bottom layer of the PCB in automated processes. Hence, no additional transitions are required, and critical losses such as between LNA and antenna can be avoided. A well-designed large-scale fabricated medium-complex 12 x 18-inch multilayer PCB using high performance RF substrates can be fabricated for less than 1000 EUR per piece. On the downside, the losses of PCB substrates are relatively high, the feature resolution is low (about 100 µm), and fabrication tolerances limit usability.

3.1.2 Integrated Circuits

In addition to the passive components such as antennas and RF networks, phased arrays also require the element control circuitry, often realized using ICs. Thus, the quickly advancing semiconductor technology significantly influences phased arrays' current and future developments. On the one hand, Moore's law has enabled extremely high-speed digital circuits such as Field-Programmable Gate Array (FPGA) and DSPs. These, in turn, enable parallel processing of many channels as required for DBF or MIMO arrays. On the other hand, analog ICs for millimeter wave, so-called Radio Frequency Integrated Circuit (RFIC)s, have significantly gained in performance and thus open new opportunities for array designs.

Typical for all RFICs is that performance (i.e., low losses, gain, and output power) decreases with frequency. Better/advanced technologies with much higher costs are required at higher frequencies. At K_a-band, for example, Gallium Arsenide (GaAs) has been the dominant technology for almost all RFICs such as LNAs, PAs, and phase shifters. GaAs processes are smaller scale, with small wafers, expensive materials, and low-volume production. The fabricated chips are expensive but feature a relatively good performance. More recently, Gallium Nitride (GaN) has been introduced, which is expensive but enables higher power and efficiency [48]. Meanwhile, inexpensive silicon processes also gained performance, and chips are getting ready for the market. Components in Silicon-Germanium (SiGe), which is a bridge process between the mass market Complementary Metal–Oxide–Semiconductor (CMOS) and high performance GaAs, are already commercially available.

A primary advantage of silicon processes is that they are well controlled and hence very replicable since big foundries such as *TSMC* and *Global Foundries* constantly invest and improve their products. Process resolutions are very high, allowing for small and low-cost discrete components. With their large wafers, CMOS processes can yield very low-cost ICs. Furthermore, logic from digital circuits can be integrated with analog hardware to design smart components. A digital bus, control circuits, and processing capability can be merged in an RFIC, allowing easier integration and better system management. Mixed signal ICs are realizable in GaAs processes, but the high cost per unit makes this less feasible.

Today, a variety of RF components in CMOS technology at K_a-band have been introduced, such as high performance LNA [49], phase shifter [50], and T/R-modules for radars [51]. Furthermore, commercial SiGe components specifically for phased arrays are available by *Anokiwave*. These core chips include phase and amplitude control for multiple channels and a digital control interface in a standard solderable Quad Flat No Leads

Package (QFN) package. However, PA and LNA must still be externally connected as proposed in [52]. Even if performance permits its usage, the high initial setup costs of CMOS processes remain. They can easily surpass 1 million euros for a single design run. However, mass fabrication prices of less than one euro per chip are possible when production starts.

3.2 Advanced Technological Approaches

The previously introduced fabrication technologies are well understood and explored for phased array designs. Their achievable performance, limitations, and cost, which are well known, have prevented the development and use of phased arrays in typical consumer products. This section explains new technologies with the potential to reduce cost and thus help to introduce phased arrays in these new markets.

Two main issues require solutions to obtain a low-cost phased array: losses and (phase) tuning. Antenna and transmission line losses severely hamper performance and must be kept minimal. Losses are typically reduced by using traditional waveguides, which are expensive, bulky, and prevent flexible network designs. Hence, two alternative solutions are investigated. In Section 3.2.1, a quasi-air-filled SIW and in Section 3.2.2, a low-cost 3D-printed waveguide are introduced. Section 3.2.3 briefly explains using liquid crystals for (phase) tuning.

3.2.1 Air-filled SIW

SIW technology has attracted much attention in recent decades. It enables the integration of waveguide components in a PCB. PCB designs reduce the cost compared to classical waveguides and enable the design of high-performance components such as filters, combiners, and antennas in a mass fabrication technology. Due to the dielectric core, losses in SIW are higher than in a waveguide. A significant reduction is possible if the SIW is filled with air.

In [53] and [54] air-filled SIW were introduced. The presented approaches use PCB materials but cannot be fabricated using standard PCB processes. [54] does not discuss the bonding process; others rely on soldering. A possible solution is to allow a thin layer of dielectric bonding material inside the waveguide. As shown in Fig. 3.1a, a 25 μm thin sheet of Liquid Crystal Polymer (LCP) available as *Rogers 3850* could be used as the bonding agent, enabling a multilayer construction. LCP features relatively low losses and has seen usage as a quasi-hermetic sealant material in packaging application [55], [56]. It is hence well suited to bond an air-filled cavity in a bonding cycle.

For fabrication, cavities must be milled in the central layer, which will later form the waveguide Fig. 3.1b. The multilayer, including the LCP, is stacked and bonded in the next step. Now, Vertical Interconnect Access (via)s must be drilled and electroplated to create the metallic wall confining the waveguide. A transition similar to [53] can be used to excite the waveguide. Using the proposed process, more complex waveguide structures, such as filters, could be fabricated inside a PCB with low loss (cf.Fig. 3.1b).

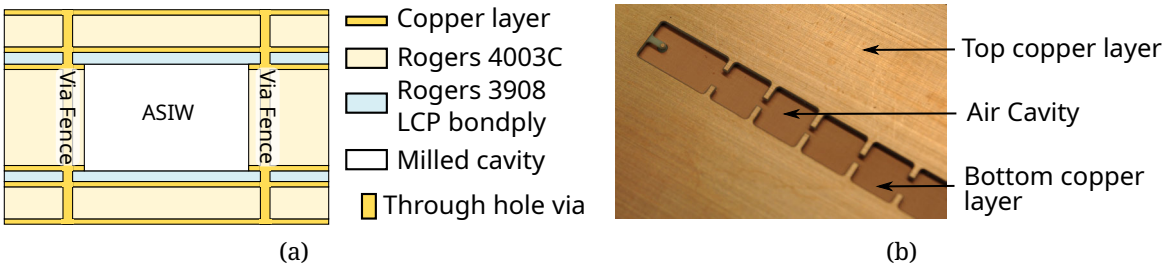

Figure 3.1: (a) PCB stack with LCP layers to construct and air-filled SIW. (b) Milled and etched PCB substrate to construct the SIW.

3.2.2 3D-Printing

The major drawback of rectangular waveguides is the complex and expensive manufacturing that commonly involves milling and brazing solid metal parts. An alternative waveguide fabrication method is a metal coating of plastic parts, thus reducing the weight and production effort [57]. Among different methods of forming plastics, 3D printing is well suited for the cost-efficient fabrication of microwave components on a prototyping or small production scale. Several 3D printed waveguide components were proposed [58], [59] with frequencies reaching W-Band [60] and beyond [61].

Technological advances of Fused Deposition Modeling (FDM) and low-cost Stereolithography (SLA) 3D printers have reduced prices and significantly improved quality. These advances have led to a rapid development of the consumer 3D printer market and a steep decrease in production cost. SLA 3D printers can produce layers as thin as 25 μm, reach build volumes of 15x15x15 cm^3 and cost less than 5000 EUR. FDM printers, on the other hand, can process standard plastics such as ABS, have even larger build volumes and are available for less than 1000 EUR.

Fabrication

In the following, an antenna array is designed at K_a-band using a low-cost consumer SLA printer (*Formlabs* Form1+) and a standard plating procedure for printed circuit boards (PCB) as described in [62]. The fabrication of 3D printed waveguide components, as shown in Fig. 3.2, can be subdivided into three steps. First, a component model is designed for easy manufacturing. This model is printed and subsequently metalized (cf. Fig. 3.2).

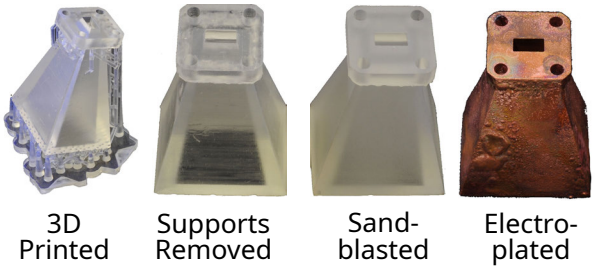

Figure 3.2: Fabrication steps from a 3D printed model to a waveguide horn antenna.

For many 3D prints, a solid support structure stabilizes the part during production. These supports can be seen in the left photo below the horn antenna in Fig. 3.2. After removing the supports, the component's surface is roughened by sandblasting. This step is crucial to improve the adhesion of the metal in the subsequent electroless plating process.

Printing and plating a waveguide component requires careful consideration of the model. High aspect ratios, such as long narrow channels, cannot be fully plated. A split block approach along the E-plane allows fabricating conventional waveguides. Fig. 3.3a depicts manufacturing a 40 mm long waveguide in a split block approach. The assembled component uses a WR-28 flange and operates between 26.5 and 40 GHz.

Measurements of the manufactured waveguide are compared to simulation and a conventional waveguide in Fig. 3.3b. The simulation model includes tolerances of the E-plane cut similar to a 3D print process. All three cases are very similar. The insertion loss of the 3D printed waveguide is only 0.1 dB higher than the reference at K_a-band.

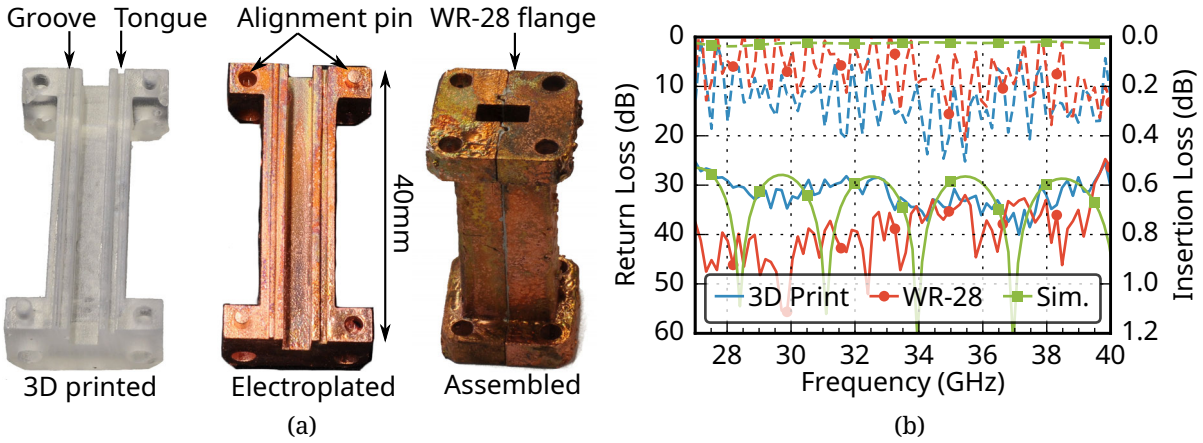

Figure 3.3: (a) Fabrication steps of a 40 mm long waveguide using 3D printing. (b) —— Return loss and - - - insertion loss comparison of conventional and 3D printed waveguides.

Antenna Array

3D printing is a relatively straightforward way to fabricate microwave components. The main limitation is the build volume of the used printer. A Ka-band array with an operating band from 26 to 40 GHz is designed as an example of the possibilities. The array consists of a two-stage E-plane power divider that feeds four horn antennas (cf. Fig. 3.4a). The split-block approach allows fabrication and plating. The internal structure alongside the waveguides is hollow to reduce the weight to about 150 g, including the bolts. Fig. 3.4b shows the complete assembly.

The measured input reflection is shown in Fig. 3.5a and compared to the simulation. The return loss is better than 20 dB and correlates well with the results expected from the simulation. Additionally, two possible assembly methods are compared: In one case, the array is only fixed by bolts, and in the other conductive epoxy adhesive is added between the split-block parts. The minor improvement indicates that no extra adhesive is necessary.

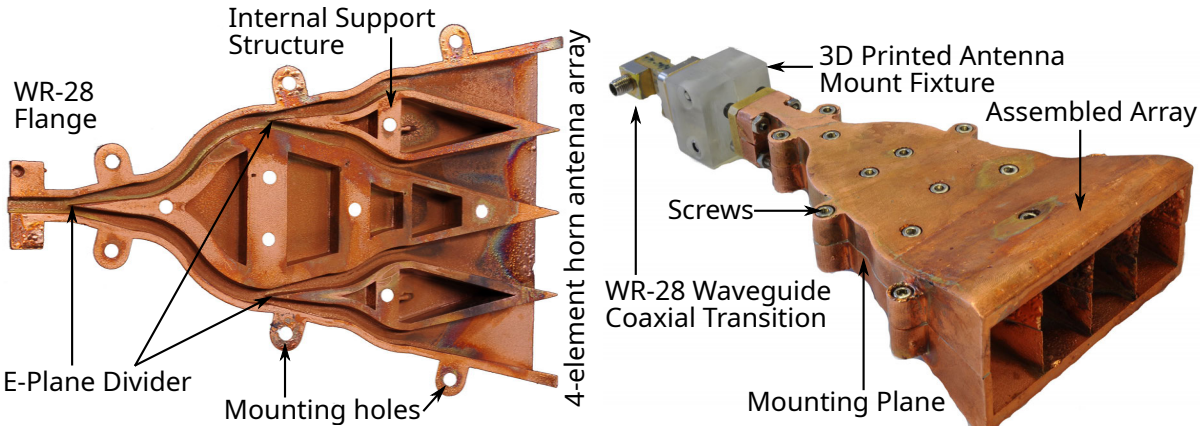

(a) (b)

Figure 3.4: (a) Split-block Ka-band power divider and horn antenna integrated into a single component using 3D printing. (b) Fully assembled 4-element array with a coaxial transition for measurements.

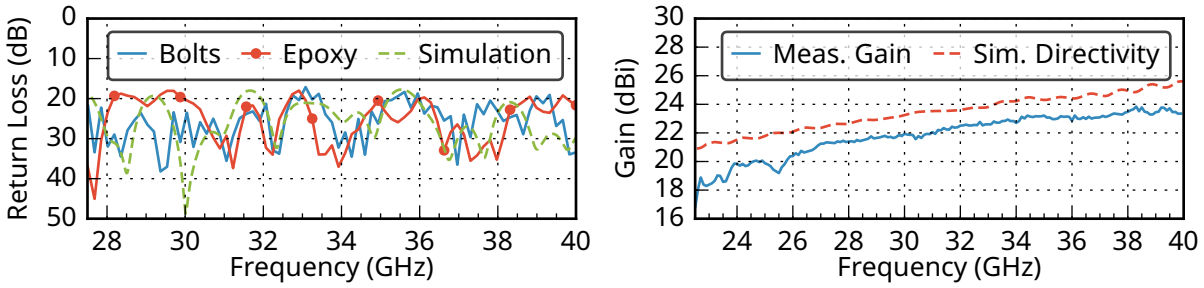

(a) (b)

Figure 3.5: (a) Simulated and measured input return loss of the array. (b) Frequency dependence of the array gain in boresight direction.

The losses in the 3D printed array are estimated by comparing the measured gain to the simulated directivity in boresight direction (cf. Fig. 3.5b). The results agree over the entire frequency range and differ by about 1.5 dB on average. This deviation is mainly attributed to the component's losses and the used coaxial waveguide feed.

The measured normalized radiation pattern of the array in the E-plane at 26.5 GHz is plotted in Fig. 3.6. The beamwidth and the nulls of the simulation and measurement results are in good agreement up to higher elevation angles θ. This validates the high accuracy of the print and the usefulness of this relatively low-cost technology for the design of passive arrays at K_a-band.

3.2.3 Tunable Media

Traditional phased arrays rely on switches to tune the phase and passive tapering for the amplitude. These functionalities were recently joined in a core chip (cf. Section 3.1.2). As an alternative, tunable materials are under active research. Liquid crystals have such tuning properties that enable their usage as a transparent tunable medium mainly used

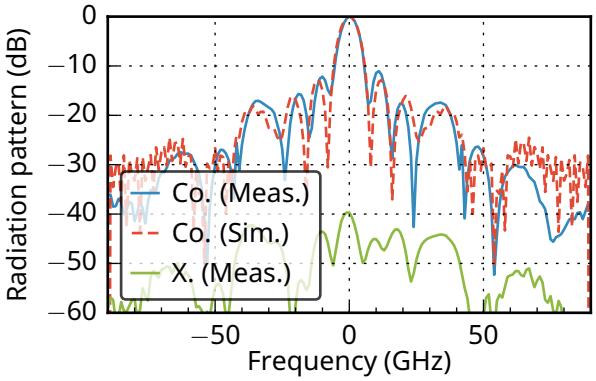

Figure 3.6: Pattern of the horn array at 26.5 GHz.

in displays. As high production capacities are available at a low cost, they have also attracted attention at microwave frequencies. As an alternative to a solid-state phased shifter, liquid crystal-based solutions have been demonstrated [63]. Such solutions can be subsequently used for array designs with integrated tunable liquid crystal layers [64]. Recently, commercial interest in the technology manifested in the startup's foundation *ALCAN Systems*.

The American company *Kymeta* use what they call a holographic array [65]. Compared to a classical phased array, the surface is greatly oversampled with many sub-wavelength elements. These use a tunable metamaterial instead of RF electronics such as amplifiers and phase shifters. The amplitude of these elements can be tuned to modulate the excitation of the entire antenna surface (holographic array). All elements are software controlled and can synthesize a beam with variable direction and polarization. A significant advantage of this approach is that a central feeding point with a single PA and LNA can be used, thus allowing a more straightforward design without power management issues. On the downside, losses introduced in the metamaterial and networks directly impair array performance. One main challenge involved is the realization of the metamaterial antenna surface, which *Kymeta* claims to have solved by using a liquid crystal matrix comparable to a display.

3.3 Multi-Use and Reconfigurable Designs

Technological solutions operating in an ever-growing number of microwave and millimeter wave frequency bands sustain the rapid development of wireless systems. A device operating in as many bands as possible helps to conceal the technological complexity from the user. For example, a modern mobile phone is a single, compact device that can use different services at various frequency bands. In applications such as radar, performance (range, resolution) greatly depends on the chosen frequency band. Bigger maritime vessels operate radar in both S- and X-Band. For weather radars, simultaneous use of a wide range of frequencies from S- to W-band is of interest to optimally detect and classify precipitation based on different scattering characteristics.

Another example of the diversity of wireless systems is modern aviation. Aircraft are equipped with multiple antennas, one for each application (e.g., radar, Global Positioning System (GPS), Aircraft Communications Addressing and Reporting System (ACARS),

SatCom). A multipurpose antenna system would reduce the requirement to integrate multiple separate systems into the fuselage. Although satellite communications links are relatively standardized, a great diversity exists. For optimal coverage, links with a low FSL are often used at L-band frequencies, whereas high throughput services operate with the higher bandwidth available in K_u-band and K_a-band. Different frequencies are in use for up- and downlinks, and the polarization can be either dual circular (RHCP, LHCP) or linear. Additionally, bandwidth specifications can vary depending on the network.

In all these cases, the additional hardware required to operate in multiple bands increases size, weight, and cost. One way to counteract this is to reuse the available resources. Such multipurpose systems can be divided into two groups: Multiplex systems and reconfigurable systems. Multiplex systems operate multiple services simultaneously. Reconfigurable systems use alterable hardware states to adapt to defined applications. Generally, multiplex systems are more flexible but also more complex and costly. Typical multiplex examples include wideband systems and polarization multiplexing, enabling simultaneous reception and processing of different polarizations. A dual polarization multiplex effectively doubles the required circuit complexity, and a wideband design necessitates a high IF and fast sampling. If a single band, single polarization link is sufficient at any given time, multiplex systems represent a significant system overhead. On the other hand, a reconfigurable system also enables dual polarization and multiple band operation but not simultaneously. Multiplexing and reconfigurability can be combined, e.g., by means of a wideband design with a polarization switch.

Since the main scope of this work is to develop efficient designs and reduce the cost of an array system, reconfigurable designs are generally favorable. Since some satellite communication services require dual-band solutions, suitable antenna architectures are introduced as well.

3.3.1 Dual-Band Antennas: Concepts and Challenges

A multi-band antenna can be operated at (greatly) differing frequencies to support multiple applications. Such an antenna can possess a wideband response or operate at multiple discrete bands. Wideband designs can be obtained using dipoles [66], but they are comparatively large and may suffer from a (significantly) frequency-dependent characteristic.

For K_a-band satellite communications, two distinct, relatively widespread frequency bands are used at 20 GHz and 30 GHz. A dual-band design is favorable for a shared Tx and Rx architecture with similar requirements in both bands. Although such a combined antenna is quite rewarding regarding the overall system size, many challenges are involved. One major issue is the array grid which strongly influences the overall pattern. The maximal grid spacing is limited by the wavelength at the highest operating frequency, whereas the individual element size depends on the wavelength at the lowest frequency. Even in optimized grids [67], sufficient space for wideband antennas is unavailable, and inter-element coupling is critical. Since Rx and Tx share the same antenna element, the signals must be split right behind the antenna to prevent overloading the LNA input with the transmit signal and operating the PA with optimal efficiency. The widely spread frequencies allow using diplexers/multiplexers as splitters [68]. A multiplexer is a filter structure with one shared and multiple frequency selective ports. Its intrinsic losses are critical to the overall system's performance since the diplexer is located between the RF frontend and the antenna (cf. Section 2.4.4).

The challenges involved with the high integration density of a dual-band antenna can be mitigated if a larger arrangement is tolerable and a brick design can be used (Section 2.3.4). A brick array layout enables the integration of high-performance (low-loss) waveguide components. From a technological viewpoint, SIW enables the adaption of many well-known waveguide concepts to PCB with the main benefit of size reduction, and an industrial production process [28], [69], [70]. A significant issue of dual-band waveguide design arises for widely spread operating frequencies. The cutoff dictates the lower frequency limit, whereas higher-order modes complicate operation at the upper end.

In principle, a dual-band circularly polarized SIW antenna can be adapted from a standard square horn with a septum polarizer [69]. The polarizer interfaces two linear polarized full-height SIWs and a square circular polarized waveguide. The excitation of the two full-height waveguides from a microstrip or Coplanar Waveguide (CPW) is challenging in SIW technology and requires complex transitions [71].

As an alternative approach, dielectric lens antennas [72] can be used in combination with an SIW to design wideband [73] or dual-band [74] characteristics. The dielectric lens adds a new degree of freedom in the design process, which helps to improve the antenna patterns at the desired frequencies. The resulting antenna element is quite elaborate and challenging to fabricate but can provide good performance even in densely spaced grids.

Another strength of SIW is the easy integration of performant filters. Such filters are a sound basis for the diplexer required to split Rx and Tx [75]. A filter can be realized very compactly using a multilayer SIW approach, enabling the integration of usually very bulky filters in an array with half-wavelength element spacing.

3.3.2 Dual-Band Patch Array Design

Patch antennas are relatively thin compared to SIW and are very beneficial for compact and flat tile arrays. They are often fabricated in PCB-technology and hence allow a high-volume production of relatively large panels containing multiple elements.

However, constructing a dual-band shared transmit and receive array based on dual-polarized microstrip antennas is challenging. The limited element spacing prevents the usage of large antenna elements, and the feed network (2 polarizations per Tx- and Rx-channel) adds complexity. Dual-polarized dual-band antennas have been reported for L- and X-Band in [76] and as a concept for Ka-band in [77]. [78] uses dipole antennas, which are not ideally suited when an extensive scanning range is required [79].

Conventional microstrip patches exhibit a relatively small fractional bandwidth of about 5%-20%. However, a larger bandwidth is needed for wideband designs ranging from 20 GHz to 30 GHz. Specifically designed patch shapes in combination with cutouts permit to influence higher-order TM-modes for an adjustable dual frequency behavior [80], [81]. The excitation of the TM_{30}-mode must be avoided, as this would result in a null in boresight direction. Often, however, this is impossible, yields very narrow bandwidth, or results in geometries not realizable with the resolution available through standard PCB processes.

For this reason, a dual-band and dual-polarized patch array at Ka-Band has been developed and reported in [82], [83] based on the stacked patch approach from [84]. An upper square patch antenna is used for the upper-frequency band, and a square ring is

placed in the layer below, yielding a second resonant frequency lower than an equally sized conventional patch. Fig. 3.7a depicts the arrangement.

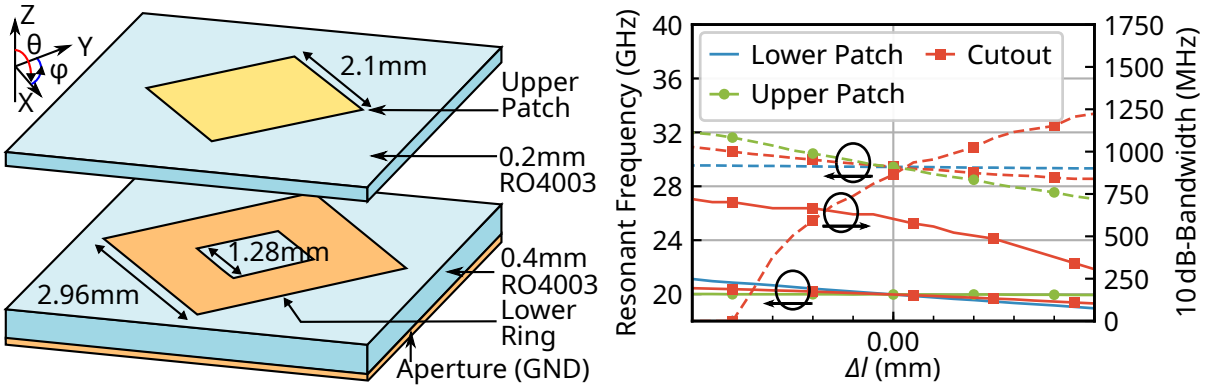

(a) (b)

Figure 3.7: (a) Geometry of the stacked dual-band patch antenna. (b) Dependence of the resonant frequency and 10 dB-bandwidth on antenna dimensions at the lower (——) and the upper band (- - -).

Design Procedure of the Radiating Element

The frequency bands of the dual-band stacked patch must be carefully adjusted to obtain optimal results since the available bandwidth of the design limits the overall performance. The main tuning parameters are the dimensions of the two patches (i.e., the lengths of the top patch, the bottom square ring, and the cutout). The fields are mainly concentrated between the ring and the ground plane in the lower band and between the upper patch and the lower ring/ground at the upper frequency. Changing the cutout thus affects both bands. Fig. 3.7b illustrates how the resonant frequency and the 10 dB-bandwidth are affected by changes Δl of the patch dimensions. Changing the size of the top patch influences the upper resonant frequency only, while the lower resonance remains unchanged. The opposite applies to a change in the size of the square ring. Changing the cutout is more complex, and the bandwidth of the resonance must also be considered. A larger cutout reduces the lower resonant frequency and thus allows a reduction in the antenna size. At the same time, the bandwidth is decreased as the square ring behaves more and more like a ring resonator. The top patch can be easily excited through the bigger opening in the middle, and its bandwidth increases. Thus, a compromise for sufficient bandwidth and low return loss is needed.

The designed radiating element is symmetric and can thus support two linearly polarized modes. Two perpendicular feeds below an appropriate aperture excite both independently. Here, the multilayer feed structure from [85] is adapted to meet the alignment challenges at higher frequencies. The feed lines traverse in the middle of a cross-shaped aperture separated by a thin layer. The ends of the feed are fanned out like a tuning fork to minimize blockage. The arrangement is illustrated in Fig. 3.8a.

In total, five metal layers are required to realize the complete antenna (cf. Fig. 3.8b). The two uppermost contain the patch antennas, the middle one a ground plane with an

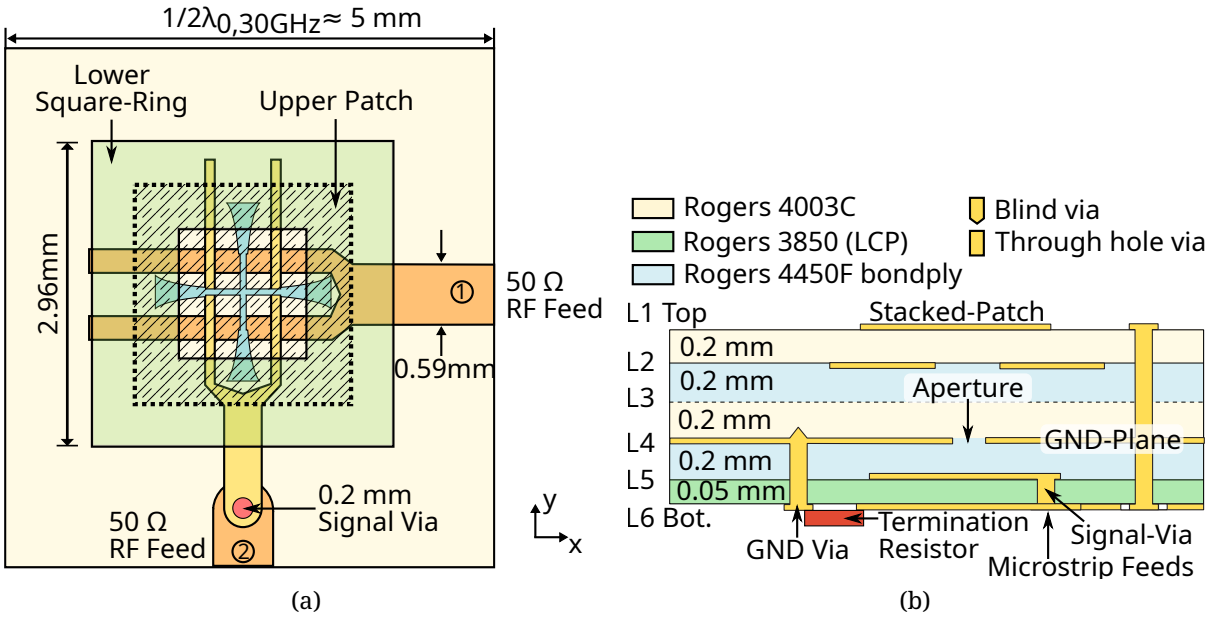

Figure 3.8: (a) Geometry of the stacked dual-band patch antenna with a crossed-feed aperture for dual-polarized operation and (b) the used PCB-stack.

aperture, and the bottom two a crossed-feed structure to excite two orthogonal polarizations. The relatively thick upper substrates help to satisfy the bandwidth requirements. A 50 µm thin sheet of RO3850 Ultralam material provides adequate isolation of the feed lines and still ensures an almost equal coupling of both feeds to the patch.

Antenna Characteristics

The complete antenna's measured and simulated input reflection coefficient is plotted in Fig. 3.9a. Both operational bands can be clearly distinguished, and the input return loss is better than 10 dB throughout the operational bands. Only minor deviations between the two feeds are observed. At the upper band, there is a slight frequency shift between the ports, and the bandwidth is also slightly larger.

A single antenna element in an array setup with surrounding terminated elements is used to assess the radiation characteristics. The far-field measurements are conducted in an anechoic environment with the antenna mounted on a rotatable positioner. The measured data is evaluated through a transmission model containing the free-space loss, cable losses, amplifier gain, and a model of the reference antenna obtained experimentally (three-antenna-method).

Simulation and measurement results of the realized gain are plotted in Fig. 3.9b versus frequency. The simulation results include dielectric and conductor losses occurring in the antenna and losses due to reflections. Simulated and measured data are generally in good agreement. They confirm that the antenna operates in the two specified bands. The realized gain reaches 2 dBi at 20 GHz and 4 dBi at 30 GHz.

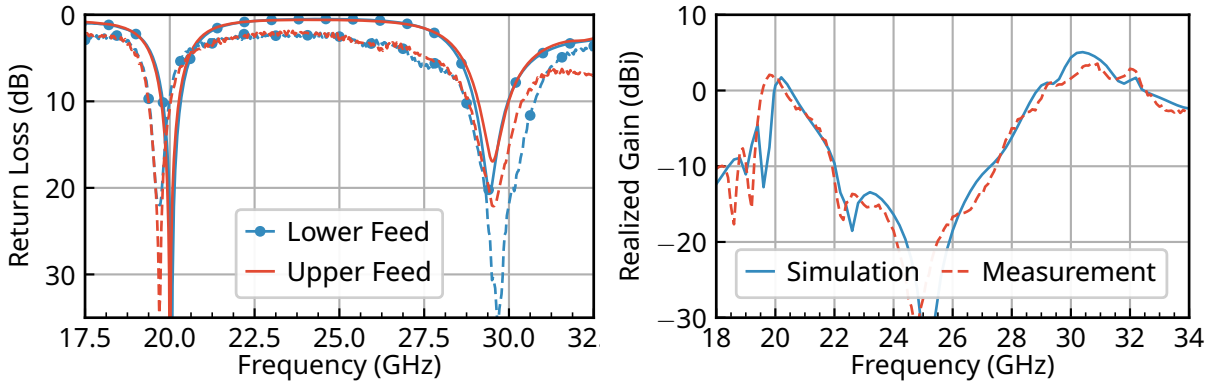

(a) (b)

Figure 3.9: (a) Simulated (——) and measured (- - -) reflection coefficients. (b) Simulated (——) and measured (- - -) frequency dependence of the realized gain in $\theta = 0°$ direction..

Dual-Band Patch Array

An array of patch antennas is required to increase antenna gain and enable beam scanning. Since the overall size of the dual-band element is smaller than half the free-space wavelength at 30 GHz, a rectangular array design is possible without grating lobes in the visible range. However, due to the proximity of the elements, coupling effects between neighboring antennas may occur.

A 4x4 array with a fixed beam is realized to demonstrate the proposed arrangement's functionality. Single polarization is considered only. Dual polarization networks require additional PCB layers, thus increasing the circuit complexity without adding much insight. Twelve elements are placed around a 4x4 array to minimize edge effects. A cascaded wideband power combiner excites the central sixteen elements. The combiner consists of T-junctions with a stepped matching network and exhibits an input reflection below -20 dB from 15 GHz to 35 GHz. Two of the three wideband combiners are asymmetric to tilt the main beam to $\theta = -30°$ at both operating frequencies by introducing a time delay τ. The fabricated array is shown in Fig. 3.10a.

A measured far-field pattern in the yz-cutting plane is plotted in Fig. 3.10b. The array beams are tilted as designed and feature approximately 10 dB gain in both bands. As expected, the sidelobe level increases when the array is scanned. Generally, the simulated and measured patterns are in good agreement, thus demonstrating the suitability of the design for integrating transmit and receive terminals in larger Ka-band communication arrays.

3.3.3 Reconfigurable Antennas

Reconfigurable hardware allows for application-specific adaptions of the system utilizing adjustable or switchable circuits. It allows for greater operational flexibility and reduces subsequent circuits' complexity. On the other hand, switchable elements and their control networks add to the complexity of the reconfigurable hardware itself.

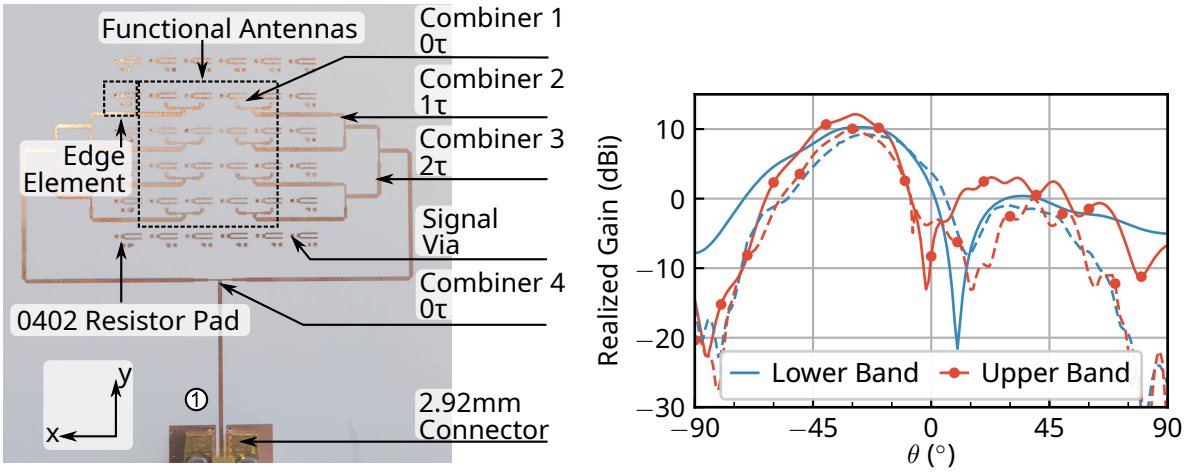

(a) (b)

Figure 3.10: (a) Feed network on the backside of the 4x4 antenna arrays with the main beam in $\theta = -30°$ direction. (b) Simulated (——) and measured (- - -) realized gain at 20 GHz (——) and 30 GHz (—●—) in the yz-cutting plane with the beam pointed to $\theta = -30°$.

In the case of a dual-polarized antenna, two simultaneously active polarization channels double the required circuitry. In many applications, a single but changeable polarization channel is sufficient. This section describes a reconfigurable patch antenna element suitable for an array configuration. It allows switching between polarization states and two neighboring frequency bands [86]. The designed reconfigurable patch antenna element in Fig. 3.11a is based on [87] but substantially modified to better suit an array setup with more compact, aperture-coupled elements.

The antenna is based on a circular patch with a U-shaped slot. A central disc and an outer annular ring constitute the circular patch. Four PIN diodes between the ring and the disc enable frequency agility. When switched off (i.e., the diodes can be ideally replaced by an open), the ring and the disc are not connected. The circumference of the outer ring mainly determines the resonant frequency in this case. When the four diodes are switched on (i.e., the diodes can ideally be replaced by a short), the radiating element behaves like a circular patch, increasing the resonant frequency. The polarization is switched through the two PIN diodes attached to the severed section of the ring. It supports linear polarization (both diodes on or off) and circular polarization (single diode on).

Five carefully placed vias are used to bias and thus control the PIN diodes. As shown in Fig. 3.12b, each via is connected to a simple bias network to ensure decoupling of the Direct Current (DC) network. The antenna element requires only three metal layers (cf. Fig. 3.12a). The uppermost layer contains the antenna, the middle one a ground (GND) plane with the aperture to excite the patch, and the bottom one the radio frequency (RF) and direct current (DC) circuits.

M/A-COM pin diodes MA4AGBLP912 [88] are used for switching. A lumped element model is used in the design procedure to account for losses and parasitic capacitance at the design frequency of 20 GHz. The return loss of the antenna is plotted in Fig. 3.12b. The simulated antenna's upper and lower operating bands cover the desired frequency range

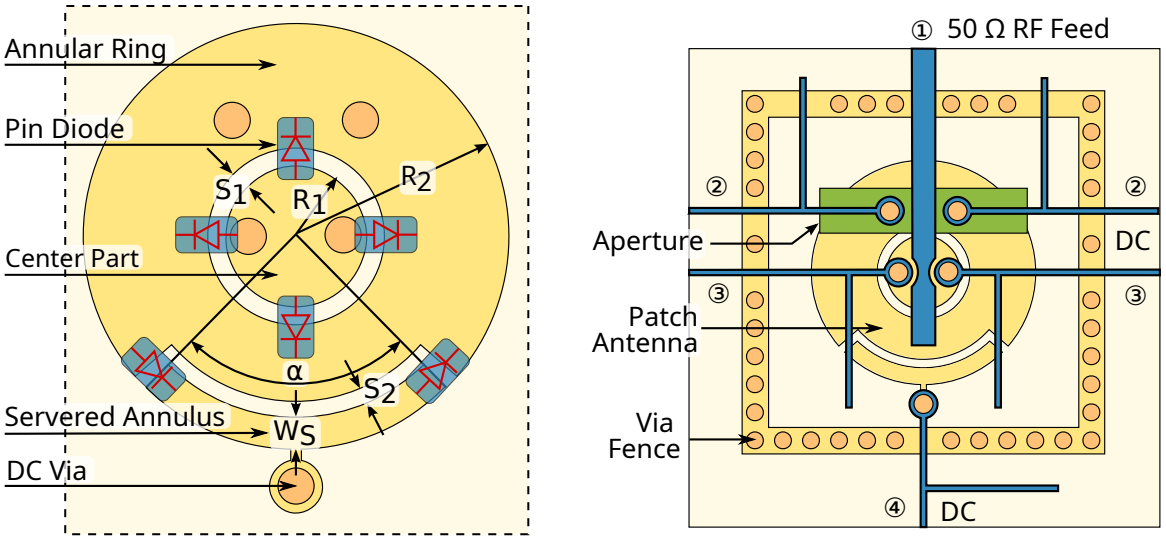

(a) (b)

Figure 3.11: (a) Circular antenna element of the reconfigurable patch antenna with inner disc and outer annular ring. The positions of the PIN diodes and vias are marked. (b) Design of all PCB structures of the reconfigurable patch, including the bias network for the PIN diodes.

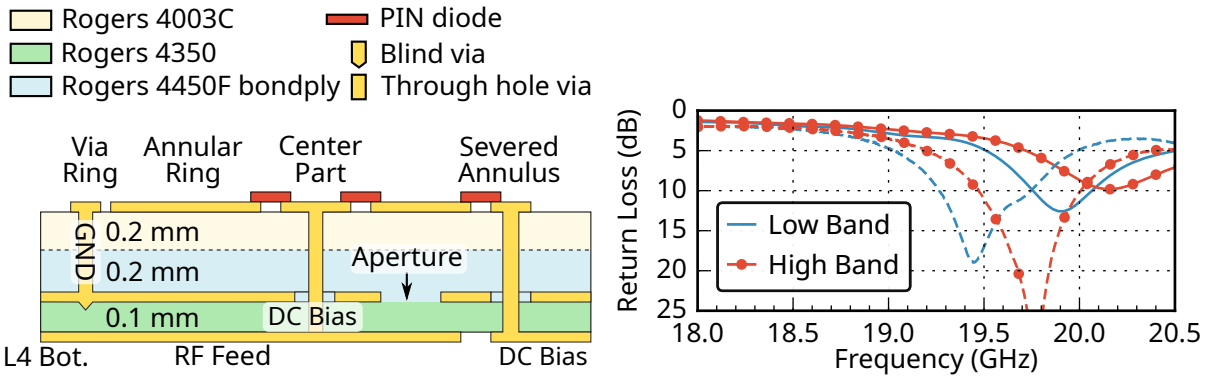

(a) (b)

Figure 3.12: (a) Cut through the multilayer PCB stack of the reconfigurable antenna, including the vias and PIN diodes. (b) Simulated (——) and measured (- - -) return loss of the antenna in the high and low state.

for K_a-band SatCom. The measured antenna exhibits more resonances and a frequency shift. The polarization-switching pin diodes function as expected. Additional information about the antenna pattern and polarization performance is available in [86].

3.3.4 Reconfigurable Filter

The frequency-reconfigurable antenna from Section 3.3.3 can be extended by a switchable image-reject filter for frequency conversion. Such a compact microstrip filter is proposed in [89] based on the well-performing dual-mode meander loop [90]. Four MA4AGBLP912 PIN diodes can switch the filter's frequency response.

Fig. 3.13a shows the design of the proposed switchable meander loop resonator. Two meanders in the loop can be shortcircuited to reduce the circumference. For the realization, two DC control lines connect the loop to a DC bias (not shown in Fig. 3.13a).

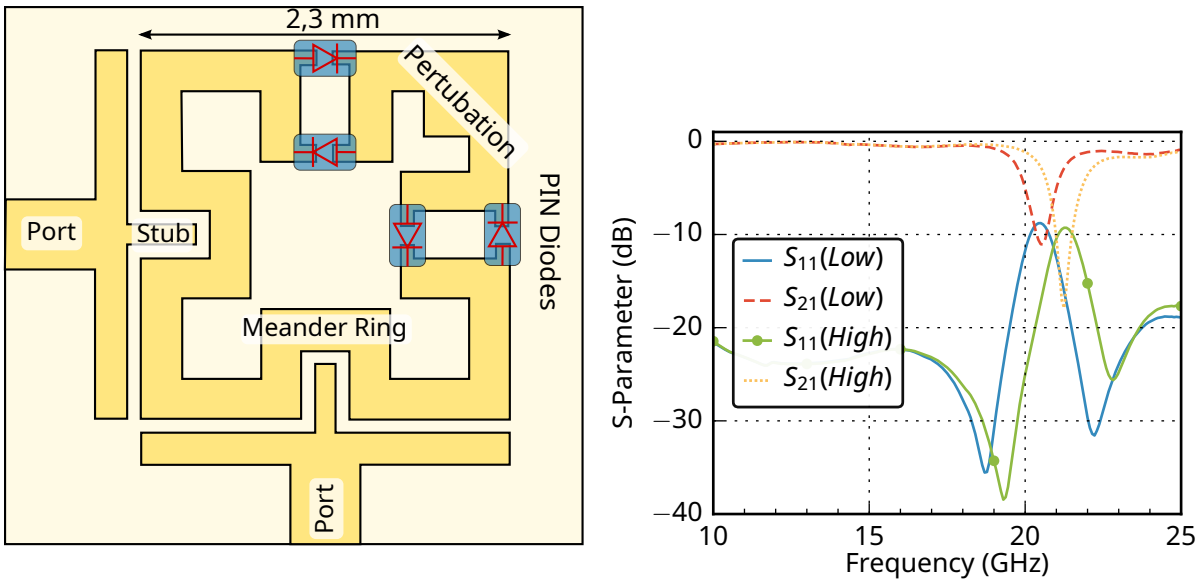

(a) (b)

Figure 3.13: (a) Layout of the switchable meander loop filter. (b) Measured S-parameters in both switching states of the reconfigurable meander loop filter.

Fig. 3.13b shows a plot of the measured S-parameters for both the lower and the upper band state. Similar to the original meander loop [90], this filter features an elliptic filter response with a steep roll-off and distinct nulls. The results validate that frequency tuning of the two closely spaced bands is possible. The observed bandwidth is about 1 GHz in each band. The return loss is better than 10 dB. However, due to the additional ohmic loss and the parasitic capacitance of the diode in the resonant circuit, the insertion loss of about 10 dB is relatively high. Losses are the main disadvantage in many RF reconfigurable circuits. Their use cases are typically limited to applications where losses are less critical.

3.4 Calibration

Tolerances in fabrication and variations during operation lead to deviations in phase and amplitude between channels in a phased array. Especially active arrays with environmentally sensitive electronics can suffer from short and long-term drifts. Uncorrected errors may lead to a rise of sidelobes and even pointing errors. Hence, compensation through

calibration is necessary unless fabrication tolerances are low and the environment and aging influence are well controlled.

3.4.1 Online Calibration

Active arrays can include many RFICs, which may exhibit significant changes in phase and amplitude during operation. Hence, continuous monitoring of channel changes can improve overall performance. Monitoring is not feasible with a conventional offline calibration, where external setups are required. Online calibration, on the other hand, is based on permanently integrated circuitry and allows for permanent monitoring.

Several online calibration techniques are well-studied. An external approach using probe antennas outside the array system is introduced in [91]. The coupling between the probes and each array element is measured, and the calibration coefficients are calculated using a propagation model of the system. Internal networks such as couplers can be used [92] to reduce the size of the calibration network. Though well suited to compensate effects in the active circuitry, they cannot account for antenna array effects such as mutual coupling. The concept of integrated calibration probes for linear patch antennas is thus introduced in [93], [94], which combines the benefits from both methods for linear polarized antennas. This concept can also be used for circularly polarized arrays [95].

3.4.2 Patch with Calibration Probes

The designed 20 GHz antenna is illustrated in Fig. 3.14a from a top view and in Fig. 3.14b from a side view that clarifies the PCB stack. The elementary radiator is chosen as a conventional circularly polarized square patch antenna with truncated corners. It is excited by a microstrip feed line using aperture coupling to allow for easier integration into an array.

Two probes inserted below and beside the microstrip patch symmetrically excite a field pattern that closely replicates the antenna's fundamental mode of operation. The probes are placed at those patch edges, not above the RF feed line, to avoid interference with the antenna feed port. The presented antenna and probe network supports single polarization only.

For the fabrication, a multilayer based on the Rogers 4000 material system is chosen (cf. Fig. 3.14b). Six layers are required, leading to a total height of $\approx 0.6\,\mathrm{mm}$. Each probe consists of two via posts interconnected by a small transmission line section. The calibration signal is fed into one via. The other is terminated with a 50 Ω resistor on the bottom layer (L6). A large distance and bent probe lines are chosen for a low coupling between the patch and probes. (Fig. 3.14a).

The simulated S-parameters are depicted in Fig. 3.15. The antenna feed is well matched in the operating frequency range from 19.7 GHz to 20.2 GHz (S_{11}). Due to the inductive characteristic, the probe suffers from increasing reflections at higher frequencies (S_{33}). The isolation between probes and antenna is higher than 15 dB (S_{31}).

3.4.3 Array with Calibration Probes

Fig. 3.16a illustrates linear four-element arrays designed using the patch antenna with calibration probes as the elementary cell. All four antenna ports are accessible through

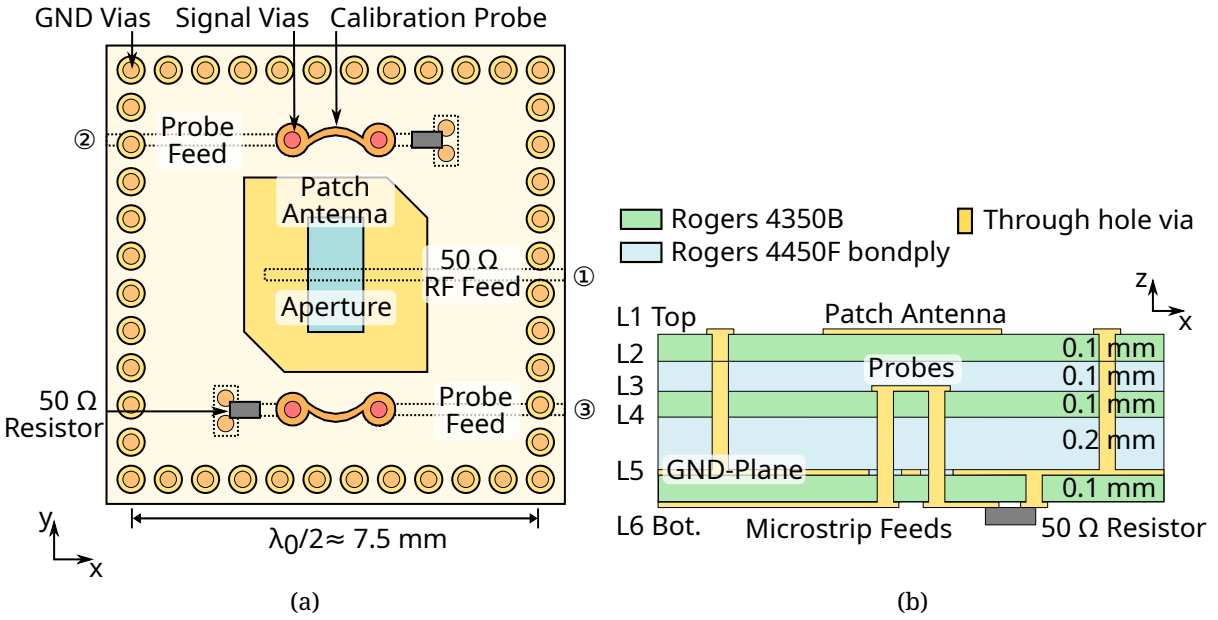

(a) (b)

Figure 3.14: (a) Geometry of the circularly polarized patch antenna with integrated calibration probes viewed from the top. (b) Cut through the multilayer PCB stack of the antenna including the probes.

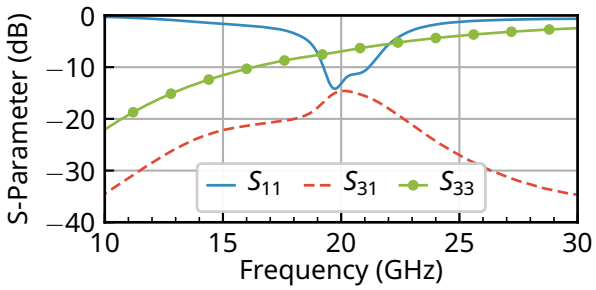

Figure 3.15: Simulated S-Parameters of the circularly polarized antenna with probes.

microstrip lines (Ports 1-4), while the fifth port excites the probes. One probe is placed at each side of the antenna. The red and green colors denote an excitation with opposite phases.

Fig. 3.16b shows the manufactured array from the bottom side. Wilkinson Power Dividers split the calibration signal. Delay lines introduce the required 180° phase shift.

A two-port network analyzer connected to the onboard Sub-Miniature Push-On (Micro) Connector (SMPM) is used for the measurements. All unused ports are terminated with 50 Ω (cf. Fig. 3.16). The coupling between probe and antenna ports is investigated in Fig. 3.17a. All antennas are equally coupled to the probes at about −27 dB. These results coincide well with simulation results, including the distribution network.

The amplitude calibration coefficients are determined using internal probes and an offline calibration as a reference. This approach allows for analyzing the precision of the concept. For the offline calibration, the element amplitudes are equalized based on

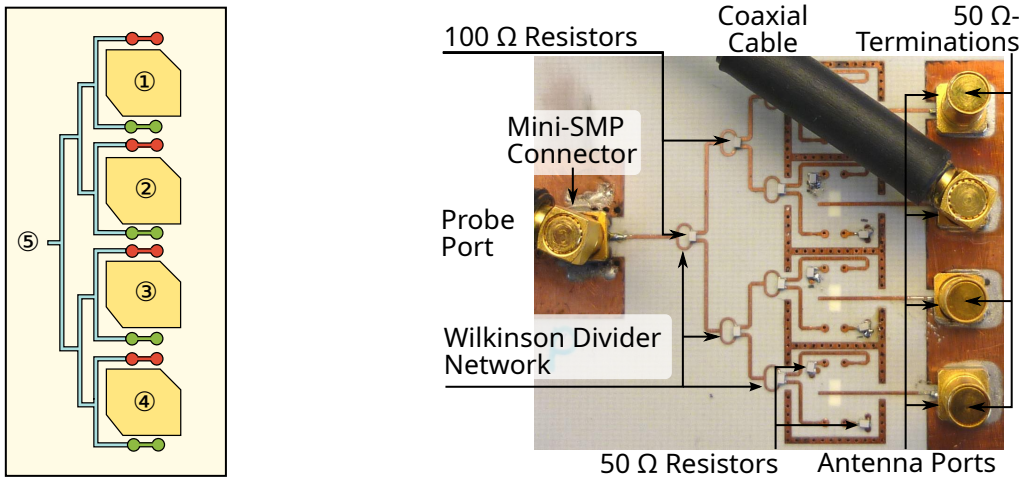

(a) (b)

Figure 3.16: (a) Schematic of the 4x1 antenna array with integrated probes. (b) Bottom view of the manufactured 4x1 antenna array.

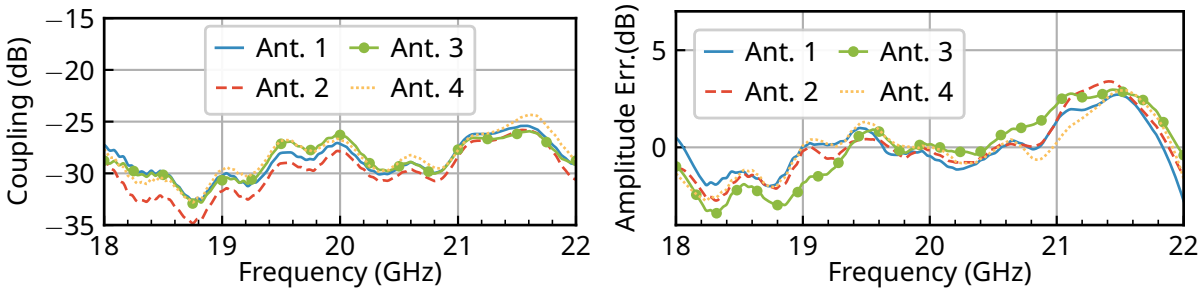

(a) (b)

Figure 3.17: (a) Measured Coupling between probe and the antenna ports. (b) Measured amplitude deviation between far-field and probe calibration.

a far-field measurements in boresight direction. In the case of the probes, the coupling results from Fig. 3.17a are used to calculate calibration coefficients. The deviation between the probe and the reference offline calibration is depicted in Fig. 3.17b. The error varies by $\pm 1\,\mathrm{dB}$ in the operating band and $\pm 2\,\mathrm{dB}$ from $19\,\mathrm{GHz}$ to $21\,\mathrm{GHz}$. A one-time offline calibration can be combined with the continuous monitoring capabilities of the probes to obtain higher accuracy.

3.5 Summary

Fabrication technology is the foundation of all ESA designs. Therefore, PCBs and the fast-evolving RFICs are important tools in today's antenna designs. However, innovative technological approaches may quickly change the state-of-the-art. Air-filled SIW or 3D-printed waveguides offer low-cost, high-performance techniques for future array designs. Furthermore, tunable media may replace the classical phase shifter.

Besides technology, components are also vital for array designs. Reconfigurable and dual-band designs provide more flexibility for applications and allow more compact overall designs. Hence, patch antennas and a filter are realized and validated to demonstrate the approach's feasibility. The promising performance enables to use the designed components for larger arrays. The chapter concludes with an online calibration approach for patch antennas using internal probes.

Chapter 4

Electronically Scanned Reflector Antenna

The solutions discussed in Chapter 3 involve novel technological approaches and architectures to reduce cost and complexity. These concepts are relatively general and adaptable to many use cases. An application-specific design of the electronically scanned array may provide more design freedom for better-suited solutions. Such solutions can drastically improve the economic aspects of the whole system. According to Section 2.2.4, the number of required controls can be drastically reduced, e.g., from about 2500 to 25 if the maximum scanning range is reduced from $\pm 60°$ to $\pm 5°$. A hybrid electronic-mechanical scanning scheme could be a very beneficial solution for such requirements.

4.1 Application Scenario

Today, satellite communications rely on reflector antennas for satellites and Earth stations. Their focusing properties and relatively simple mechanical construction allow for a wide range of applications from very high gain, precision antennas to low-cost consumer terminals for satellite TV. Beam steering is necessary for many operation scenarios, including low Earth orbit satellites or mobile communications. The simplest solution for the terminal is a mechanically rotatable antenna assembly, maintaining similar antenna characteristics throughout the steering range. A typical example is the *Intellian GX60* terminal antenna for K_a-band satellite communication [96]. However, depending on angular velocity, acceleration, and antenna size requirements, the pedestal becomes mechanically complex and bulky. Some systems, such as the *KNS C4 VSAT*, feature up to four axes [97]. A moving feed is an alternative solution. Although this solution might be mechanically less complex, the beam pattern typically deteriorates significantly when the feed is radially offset, thus limiting the available field of view.

In mobile applications like motorized traffic or boating, angular changes are relatively small, and a limited field of view suffices (cf. Section 2.4.3). For these scenarios, the favorable properties of fixed-beam antennas, namely high gain, low-cost, and simplicity, can be combined with agile array antennas to form hybrid electronic/mechanical solutions. The results presented in this chapter are based on the work published in [98] but include more in-depth analysis and greater detail.

One way to realize a hybrid electromechanical antenna is to combine an azimuth positioner with a tilted phased array for electronic scanning in elevation [99]. For low

elevation angles, the effective aperture of the arrays decreases significantly, thus deteriorating both the gain and the SLL. A similar design with an additional elevation positioner is available on the commercial market as so-called *RaySat* antennas by *Gilat Satellite Networks* [100].

Alternatively, an array can also be used as a feed to illuminate a reflector, a so-called AFR. To enable two-dimensional electronic scanning, focal plane arrays are used. Such arrays are positioned in the focal plane of the reflector [101], [102] and offer a relatively wide scanning range [103]. In principle, no mechanics are required for beam scanning, which reduces the cost and complexity of the beamformer. Additionally, the array can generate multiple beams using a single reflector.

Array-Fed-Reflector (AFR) in combination with focal plane arrays are widely used today, especially in radio astronomy [104], [105]. Multiple-feed-per-beam systems onboard satellites rely on the same principle for dense beam spacing and spatial power combining [106]. Furthermore, a focal plane array was successfully used for bistatic radar applications in [107]. A relatively small reflector antenna combined with a circularly polarized array for consumer applications is reported in [108]. Focal plane arrays can also be used for beam scanning in satellite communications [98], [109].

4.2 Hybrid Beamforming Concept

Several applications with limited scanning requirements, such as maritime or land-mobile, exist in mobile communications. For most of the operational time, the pitch and roll movement is relatively low, and a small scanning range of about $\pm 5^\circ$ suffices (cf. Section 2.4.3). According to Section 2.2.4, an electronically scannable antenna with a low number of control elements can fulfill such scanning requirements. One possible solution is to combine the advantageous properties of reflectors with the agility of array antennas to form an AFR with a limited field of view. Relatively simple and inexpensive mechanical positioners allow for extending the scanning range and accommodating slow movements. The electronic scanning capabilities take care of fast movements and vibrations, stabilizing the beam and tracking directional changes.

The AFR-concept can be differentiated by the position of the feed array. The feed can be in front of, behind, or in the focal plane. A position in or relatively close to the focal plane is most suitable for keeping the overall array size small and the element control requirements simple. In this case, neighboring array elements generate independent, closely spaced antenna beams in the reflector far field. Placing an array in front of the plane requires larger arrays to capture the entire incident field in combination with precise phase and amplitude control. One of the main benefits of such a design is a more effective use of the hardware: the power amplifiers could be used simultaneously instead of only one at a time.

The position of the focus relative to the reflector is also critical in the antenna design. It can either be centrally positioned on the optical axis of the reflector (prime focus or front feed) or radially offset. In the offset geometry, neither the feed nor its supporting struts block the reflector aperture. However, the asymmetric setup of an offset reflector results in higher linear cross-polarization or beam squint in case of circular polarization [17, pp 234]. Therefore, compensation techniques such as dual-offset reflector designs or

special arrays ([109]) are necessary for dual-pol applications. A prime focus design helps to simplify the design and minimize blockage effects.

The general operating principle of the investigated AFR is illustrated in Fig. 4.1. A prime focus feed is mounted in the focal plane of a reflector with (rim) radius R and rim height d_z. The array features three elements positioned on the left (——), center (·····), and right (- - -). Raytracing the beams to the reflector surface and the far field indicates a beam shift for radially offset elements along the r-axis, i.e., perpendicular to the z-axis by distance d_r.

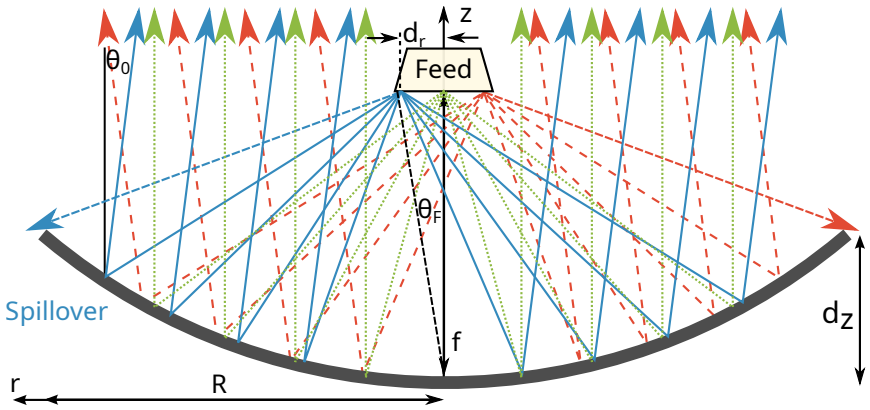

Figure 4.1: Raytracing from a central three-element focal plane array feeding a reflector.

The feed has to incorporate all the electronic circuitry since it functions as the actual beamformer and provides the scanning capability. The resulting circuit complexity and the required compactness pose a significant design challenge. Here, a Tx architecture at 30 GHz is investigated. However, an extension of the Tx-approach is possible to accommodate both Rx and Tx [67].

4.3 Reflector Design

A rotationally symmetric reflector oriented about the principal z-axis (cf. Fig. 4.1) maintains equal beam properties while scanning in different ϕ-directions. The paraboloid of revolution possesses ideal beam collimation properties. Hence, it is the most commonly used shape for reflector antennas. It yields a high gain and features a distinct focal point.

For other applications, spheroids or circular hyperboloids are also in use. The basis of all these shapes are bodies of revolution of conic sections. Various reflector shapes can hence be described and analyzed using a set of parameters governing the characteristics of conic sections.

The reflector diameter is set to $2 * R = 60\,\mathrm{cm}$ for analysis and design since this size represents a good compromise between performance and size for mobile applications at 30 GHz.

4.3.1 Conical Sections

The shape of conical sections can be distinguished by the so-called eccentricity e. It is a measure of the section's deviation from a circle and depends on the length of the section's semi-major axis a and semi-minor axis b. All conical sections have two focus points, and

Table 4.1: Geometrical properties of different conical cuts used in the reflector design.

	Eccentricity (e)	Values (e)	Focal Length (f)
Ellipse (major axis cut)	$\sqrt{1-\frac{b^2}{a^2}}$	$je<0$	N/A
Circle	-	0	a/2
Ellipse	$\sqrt{1-\frac{b^2}{a^2}}$	$(0<e<1)$	$a(1-e)$
Parabola	-	1	$\frac{1}{4a}$
Hyperbola	$\sqrt{1+\frac{b^2}{a^2}}$	$e>1$	$\sqrt{a^2+b^2}$

the sum of the distances between each focus point and every point on the shape is always equal. The focus points are important since an electromagnetic wave emitted in one focal point are collimated at the other. The distance between a focus and the shape center is called linear eccentricity $c = e \cdot a$.

The simplest conical section is the circle. Its eccentricity is $e = 0$, and both focus points coincide at a focal length of $f = a/2$. Eccentricities $0 < e < 1$ describe ellipses and $e > 1$ hyperbolas. The focal lengths are $f = a(1-e)$ and $f = \sqrt{a^2+b^2}$ for ellipse and hyperbola, respectively. Parabolas constitue a special case. They have only one distinct focal point at $f = 1/4a$, whereas the second is located at infinity. This unique property leads to their optimal far-field focusing capability. Table 4.1 summarizes the properties of conical sections.

For practical reflector designs, not complete conical sections but cuts from them are considered. Ellipses cut along the major axis ($a < b$) lose their focus points, and their eccentricity formally turns imaginary. Ellipse cuts with varying eccentricity are depicted in Fig. 4.2a. The z-axis corresponds with the reflector's center axis, whereas the r-axis is oriented from the center radially outwards. All values are normalized to the rim radius R. Hyperbolas are neglected from further analysis since they are typically used to defocus or spread incoming beams as in the Cassegrain reflector. A more comprehensive range of shapes is "superellipses" with even steeper surfaces. An example of a superellipse is a rhombus.

A second important parameter is the rim height d_z, i.e., the z-distance between the rim and the vertex. The height can be normalized to the reflector radius $d_{\mathrm{AR}} = d_z/R$. The following analysis proves that the parameters e, d_{AR}, and r are sufficient to fully qualify an ellipse. They are hence also sufficient to describe a practical reflector design. As shown in Fig. 4.2 the vortex is placed in the origin. The semi-major and semi-minor axes are oriented along z and r, respectively. In this case, the ellipse can be described by:

$$\frac{(z-a)^2}{a^2} + \frac{r^2-0}{b^2} = 1 \tag{4.1}$$

$$\frac{(z-a)^2}{a^2} + \frac{r^2}{a^2(1-e^2)} = 1. \tag{4.2}$$

Inserting the rim height $z = d_z = d_{\mathrm{AR}}R$ at the rim radius $r = R$ in Eq. (4.2), yields an expression for a:

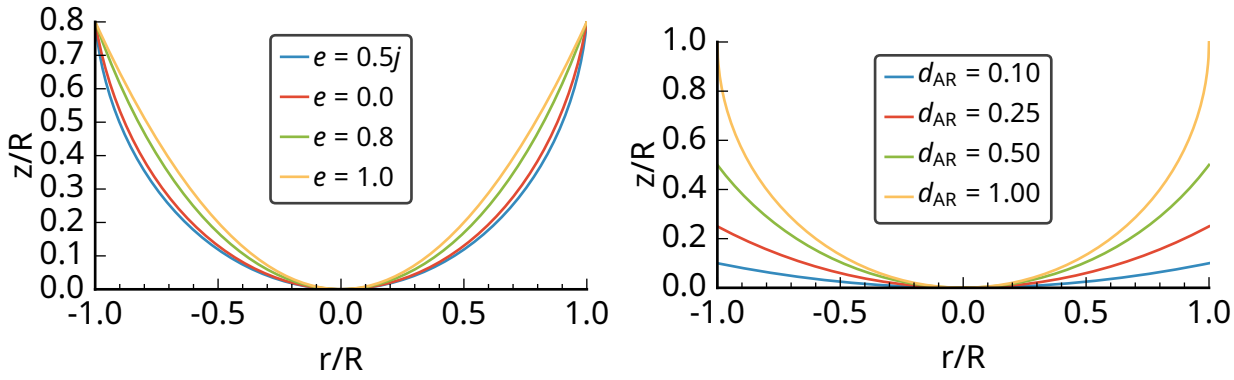

(a) (b)

Figure 4.2: Influence of the parameters aspect ratio d_{AR} and eccentricity e on the ellipse shape for (a) $d_{\mathrm{AR}} = 0.8$ and (b) $e = 0.0$.

$$a = \frac{R + R d_{\mathrm{AR}}^2 (1 - e^2)}{2 d_{\mathrm{AR}} (1 - e^2)}, \qquad d_{\mathrm{AR}} \in (0, 1]. \tag{4.3}$$

Since the ellipse semi-major axis a only depends on the rim radius R, the aspect ratio d_{AR}, and the eccentricity e, the ellipse is fully described. However, care must be taken for ellipse cuts along the major axis since the maximal possible rim height depends on the eccentricity. Indeed, only ellipses with aspect ratios $d_{\mathrm{AR}} < \frac{1}{1-e^2}$ exist for these cuts.

Changes in the aspect ratio effectively flatten the conical section to obtain a broader range of usable reflector geometries. Fig. 4.2b illustrates these cropped sections of an initially bulkier ellipse.

4.3.2 Focal Length and Efficiency

The following sections present the results of a systematic study on elliptical 60 cm-reflectors simulated at 30 GHz with the physical optics software *GRASP* from *TICRA* [110]. The reflector surface is modeled as a perfect electric conductor. The feed pattern is approximated using a Gaussian beam with a taper of 6 dB at an angle of 70°. The cross-polarized field components are zero at boresight without any back radiation. These pattern characteristics stem from approximating a full-wave simulated patch antenna model on an infinite ground plane. This simple model provides realistic results and leads to general conclusions about the reflector without being specific to the feed antenna. Furthermore, the simulation time in *GRASP* for such a model is significantly lower compared to a pattern obtained through simulation or measurements. Field patterns are calculated in elevation-over-azimuth coordinate systems from -15° to 15° and 241 points per axis (58081 total).

The feed antenna is oriented paraxial to the z-axis to radiate toward the reflector vertex. The values for the eccentricity e are set between $1.5j$ to 1.0 to include spheroids and paraboloids. The normalized rim height d_{AR} is varied between 0.2 and 1.0. Lower values correspond to very flat reflectors with long focal lengths f and hence very bulky unpractical strut assemblies. Such designs are not suitable for mobile deployment.

In Section 4.3.1, the geometrical focal length is defined for conical sections. However, this merely geometrical definition is impractical for many reflector setups since a distinct focal point may not necessarily exist. If it does, it depends on the feed and operating frequency. Hence, this work defines the optimal focal length f as the distance between the reflector vertex and the feed aperture, where the boresight gain exhibits a global maximum. This definition applies to all reflector shapes and can include influences from other sources, such as the feed field distribution.

The contour plot in Fig. 4.3 reports the optimal focal length for different reflector geometries. The hatched area (top left) is marked as invalid because in the region $d_{\mathrm{AR}} < \frac{1}{1-e^2}$, the achievable rim height cannot reach the desired value of $d_z = d_{\mathrm{AR}} r$ (cf. Section 4.3.1). Along the white line labeled "Focus Inside" the rim height d_z equals the focal length. Above the line, the feed's aperture plane is inside the reflector, which leads to an overall compact antenna. However, the aperture is not fully illuminated, and similar results could be potentially achieved with a reflector of smaller diameter and different d_{AR}. Below the white line, f is larger than d_z. The resulting spillover degrades the efficiency and, more importantly, collects more ambient noise in the Rx case.

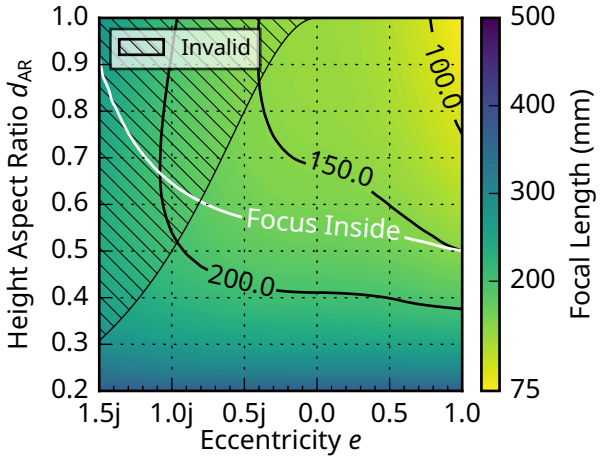

Figure 4.3: Analysis of the optimal focal length f of various elliptical 60 cm-reflectors at 30 GHz illuminated with a Gaussian beam.

The following steps assist in determining the focal length from simulation results. First, the reflector's far-field pattern is simulated at several axial offsets around the geometrical focal length. From the results, the position with a maximal gain is determined and used for a second-stage optimization using a downhill simplex algorithm.

For a given reflector height, parabolic reflectors have the shortest focal length. The focal length generally increases when lowering the eccentricity leading to a bulkier overall arrangement. The eccentricity has less influence for lower d_{AR}, i.e., in flatter reflectors. The reason is that the differences between ellipsoids also vanish for very flat designs. However, very flat reflectors require a longer focal length of more than 300 mm. For $d_{\mathrm{AR}} < 0.2$, the focal length quickly reaches 1000 mm and more.

A different feed antenna may have a displaced phase center, resulting in an optimal distance different from the focal length. For a 30 GHz patch antenna, changes in the order of a few mm are expected and can be taken into account with subsequent simulation. Minor fluctuations are not critical since the reflector radiation pattern does not significantly

change. Hence, the results obtained for the Gaussian beam feed are valid for a relatively general characterization of the reflector shape. The feed aperture is positioned at the optimal focal length from Fig. 4.3 for subsequent investigations.

A longer focal length with a reflector of the same height causes more unwanted spillover from the feed pattern. The spillover efficiency η_{spill} is shown in Fig. 4.4a. As expected, an ideal efficiency of 100% is obtained if the feed aperture is below the reflector rim. Once the feed element is above the reflector, spillover degrades efficiency. At an aspect ratio $d_{\text{AR}} = 0.3$, the spillover efficiency has dropped to less than 75%, the lower bound for the tolerable spillover. At this value, 1.25 dB Tx power is lost, and a significant part of the noisy background is in the visible range of the receiver. A feed antenna with a narrower beam would be required to counteract the high spillover.

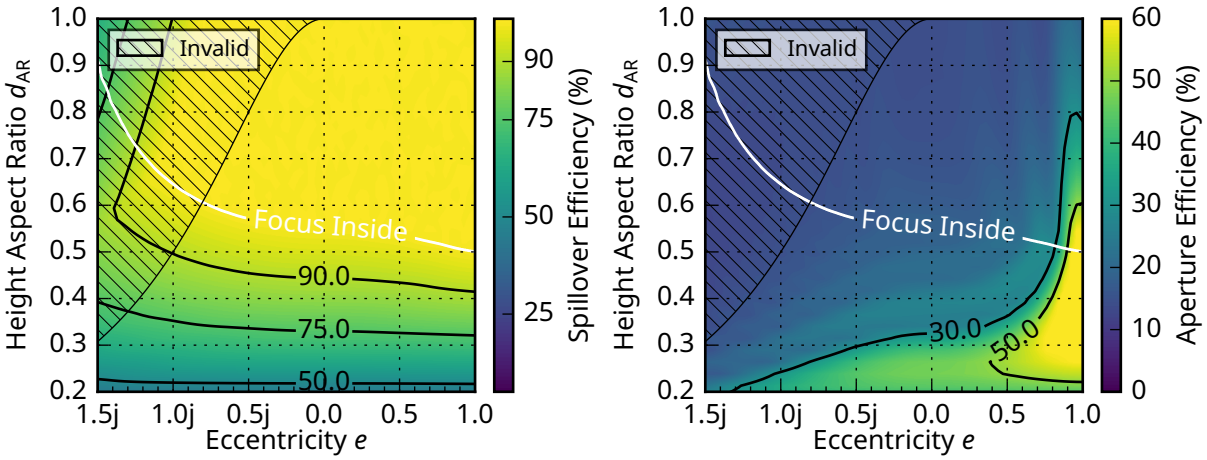

(a) (b)

Figure 4.4: (a) Spillover and (b) aperture efficiency of various elliptical 60 cm-reflectors at 30 GHz.

Fig. 4.4b depicts the simulated aperture efficiency, i.e., the ratio of effective and physical antenna size [17, p. 58]. The aperture efficiency is a good measure of how effective the antenna surface is used for beam focusing. Feed and strut blockage is not included in the simulation. As expected, the paraboloid reflectors feature the highest efficiencies ($> 50\%$), whereas most spherical and elliptical reflectors reach between 20% and 30%.

4.3.3 Scanning

For mobile applications, the possible scanning range is crucial. The feed is radially displaced from its central position to change the beam direction. Investigations on the scanning capability of paraboloids by moving the feeds are also investigated in [111], [112]. A radial displacement reduces the gain and causes comatic aberrations, which increase the sidelobes. Similar effects are expected for other reflector shapes and are investigated in the following sections.

The feed is radially shifted in the focal plane, i.e., at a constant distance in the z-direction from the reflector's vertex, to evaluate the scanning performance. The scan-angle θ_0 for a radial feed offset of $d_r = 25\,\text{mm}$ is plotted in Fig. 4.5a. From ray optics, it is evident that

for this case, θ_0 depends mainly on the focal length f and the resulting incidence angle. Reducing the focal length in the setup of Fig. 4.1 results in a larger scan angle. The results in Fig. 4.5a confirm these findings: The high d_{AR} parabolic reflectors scan the beam to about $\pm 10°$, whereas only $\pm 4°$ are achievable using flat reflectors with high focal lengths.

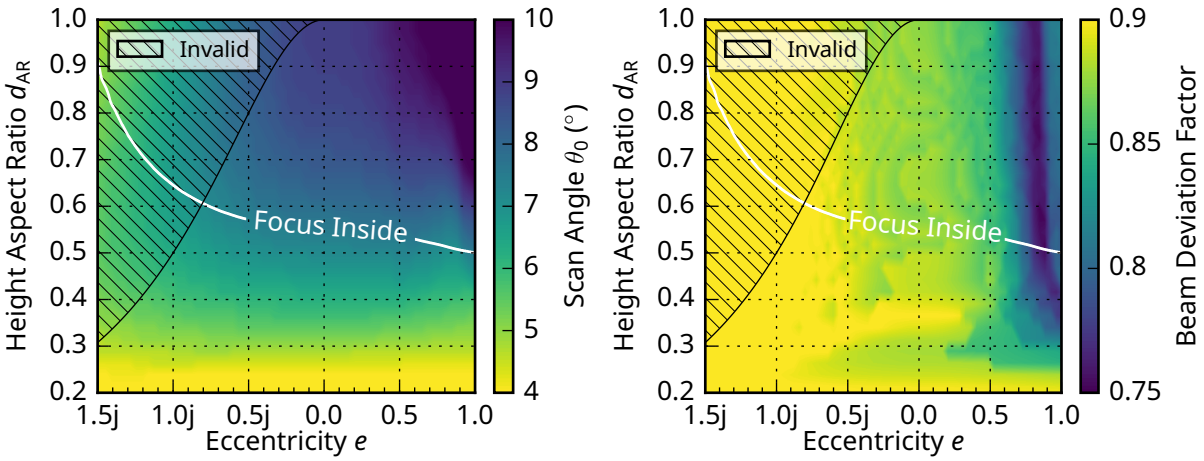

(a) (b)

Figure 4.5: (a) Scan angle θ_0 and (b) beam deviation factor using a radial feed offset of $d_r = 25\,\mathrm{mm}$ and various elliptical 60 cm-reflectors at 30 GHz

Another import figure of merit is the Beam Deviation Factor (BDF) [111], [113]:

$$\mathrm{BDF} = \frac{\theta_0}{\theta_F}, \tag{4.4}$$

where θ_F is the angle of incidence. It is helpful to determine the influence of the actual reflector shape only and eliminate the effect of the focal distance on the scan angle. As shown in Fig. 4.1, the BDF corresponds to the angle between the feed antenna and the reflector's optical axis and depends on f and the radial feed offset d_r: $\theta_F = \arctan(\frac{d_r}{f})$. The BDF is depicted in Fig. 4.5b. The factor varies between 0.75 and 0.9 for the different reflector shapes and mainly depends on the eccentricity. A low eccentricity yields a higher factor and hence a larger scan angle at a given feed offset and focal length. Indeed, the reflectors with low eccentricity are less curved in the center (cf. Fig. 4.2a) and are hence very similar to a flat mirror, which has a BDF of 1. In contrast to their high scanning angles found in Fig. 4.5a, the BDF of paraboloids is relatively low.

4.3.4 Gain, Beamwidth, and Sidelobes

The most important performance characteristic of a reflector antenna is its gain. Only the parabolic reflector features a distinct focal point and optimal beam collimation, which result in a high gain. This relation is observable in Fig. 4.6a, where the boresight gain is plotted for various reflector shapes. As expected, the gain is maximal for the parabola and exceeds 43 dBi for $d_{\mathrm{AR}} < 0.6$. The elliptical reflectors suffer from aberrations: the waves originating from a point source in the focus are scattered on the reflector and do not form plane waves in the far field. As a result, the beam slightly widens, and sidelobes rise. In

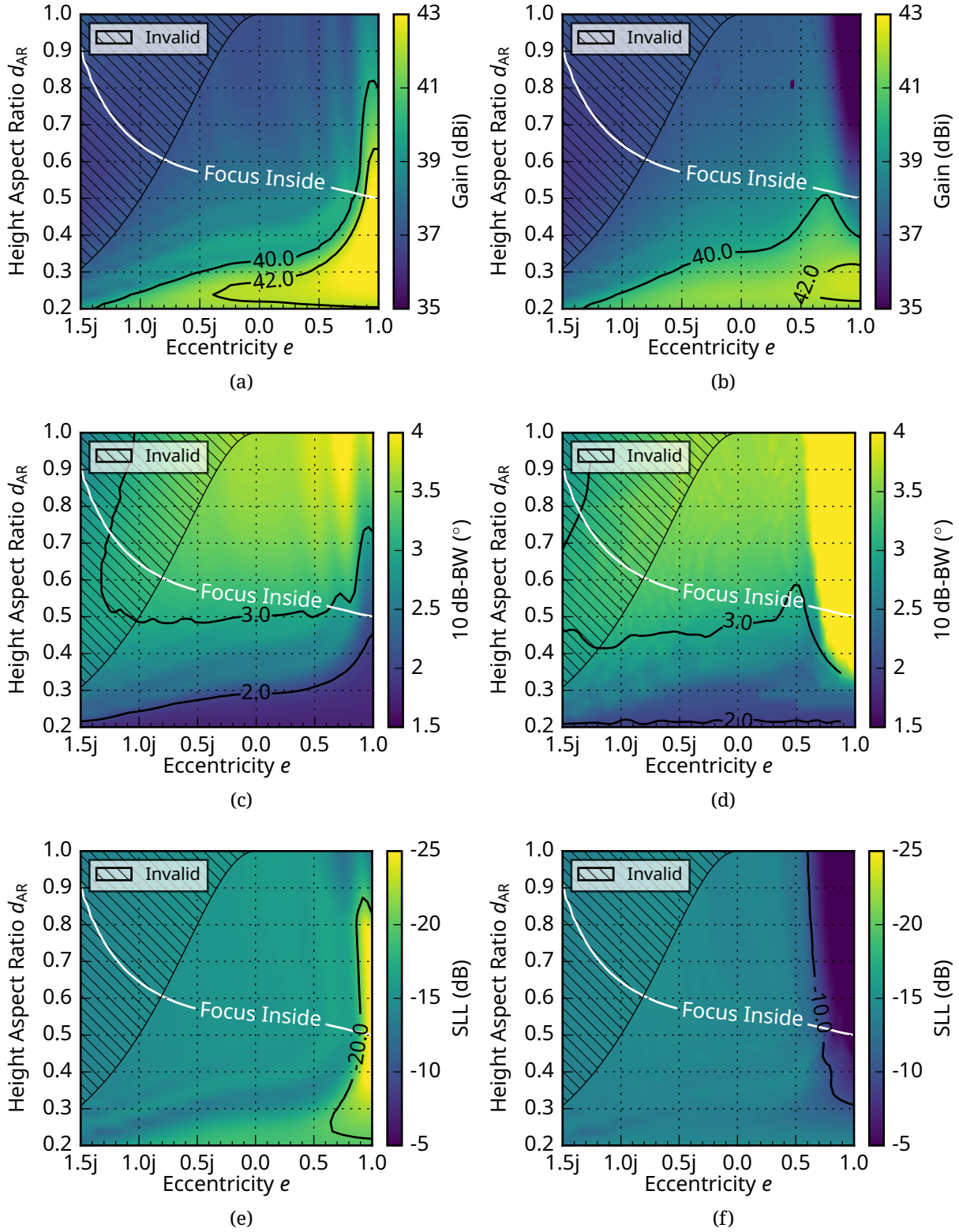

Figure 4.6: Investigation of different beam parameters for various elliptical 60 cm-reflectors at 30 GHz: gain with a radial offset of (a) $d_r = 0\,\mathrm{mm}$ and (b) $d_r = 25\,\mathrm{mm}$, 10 dB-beamwidth with a radial offset of (c) $d_r = 0\,\mathrm{mm}$ and (d) $d_r = 25\,\mathrm{mm}$, SLL with a radial offset of (e) $d_r = 0\,\mathrm{mm}$ and (f) $d_r = 25\,\mathrm{mm}$.

the case of spheroids, this effect is known as spherical aberration. Different techniques are used in optical systems to minimize the effect [114, pp. 401-409].

The resulting decrease in gain with lower eccentricities is also visible in Fig. 4.6a. Most elliptical reflectors exhibit a gain in the range of 39-40 dBi. Higher values can be reached for flat shapes with a $d_{\mathrm{AR}} < 0.3$, but spillover rises as well. If the focus is inside the reflector, the effective aperture is reduced, resulting in a drop in gain.

These results change significantly if the feed is radially or laterally moved away from the center axis to scan the beam. The simulated gain at a radial offset of 25 mm is depicted in Fig. 4.6b. The most significant difference is visible for reflectors with an eccentricity close to 1, where the gain can drop below 35 dBi. This effect is smaller for flat reflectors since the longer focal length leads to an almost paraxial beam. For reflectors with $d_{\mathrm{AR}} > 0.4$, a maximum occurs at $e \approx 0.7$. Reflectors with a low eccentricity show almost no change in gain when the feed is displaced, making them particularly useful for scanning applications.

The beamwidth is another critical parameter. In SatCom, narrow pencil beams are required to cope with strict ETSI regulation. The beamwidth is inverse to the gain and can be approximated for standard reflectors [115, p. 78]. The most commonly used measure is the HPBW or 3 dB-beamwidth. Determining the 3 dB-beamwidth is problematic here because the angular resolution of the simulation is set to 0.15° to keep simulation times reasonable. Since the expected HPBW is close to 1°, inaccuracies would lead to unreliable results. Therefore, the 10 dB-beamwidth is used, which is more robust to slight angular uncertainties.

The paraxial and radially displaced feed results are plotted in Fig. 4.6c and Fig. 4.6d, respectively. The beamwidth is the smallest for the parabolic reflector, low d_{AR}, and no radial feed offset. For reflectors with the feed aperture above the reflector rim, a 10 dB-beamwidth below 3° is achieved. The beam is only slightly widened for the scanned case and elliptical reflectors. For paraboloids, the beamwidth increases to more than 4°, which is not tolerable for many use cases.

The SLL is a good measure of how much field is radiated outside the wanted main beam. For SatCom, strict regulation applies to minimize interference. In the case of the unscanned beam, the simulated SLL is shown in Fig. 4.6e. It is generally between -15 dB and -20 dB, with slightly better results for flatter reflectors. The parabolic reflectors suppress sidelobes to levels below -25 dB. This good result reverses when the feed antenna is moved off-axis (cf. Fig. 4.6f). Due to the comatic aberrations, the sidelobes of the paraboloids increase to values of more than -10 dB. On the contrary, SLL of the more spherical-shaped reflectors remains almost unchanged.

4.3.5 EIRP, and G/T

The radiation characteristics of Tx-antennas are subject to strict regulations (cf. Section 2.4.4). At $\mathrm{K_a}$-band, ETSI defines restrictions in EN 301 459 [116]. The EIRP, which includes many pattern effects discussed in Section 4.3.4 such as beam widening, higher sidelobes, and gain reduction, is a good indicator of antenna performance in this respect.

The maximal achievable EIRP for an on-axis and a 25 mm radially displaced feed is depicted in Fig. 4.7a and Fig. 4.7b, respectively. In the former case, a parabolic reflector enables the highest EIRP at about 40 dBW. Low d_{AR}-values are also beneficial since they result in maximal gain and generally low sidelobes. For paraboloid reflectors, a radially offset feed causes a rise in sidelobes and a reduced ETSI-compliant output power. As

shown in Fig. 4.7b, the EIRP drops to 15 dBW, whereas it remains almost unchanged at about 20 to 25 dBW for most elliptical reflectors.

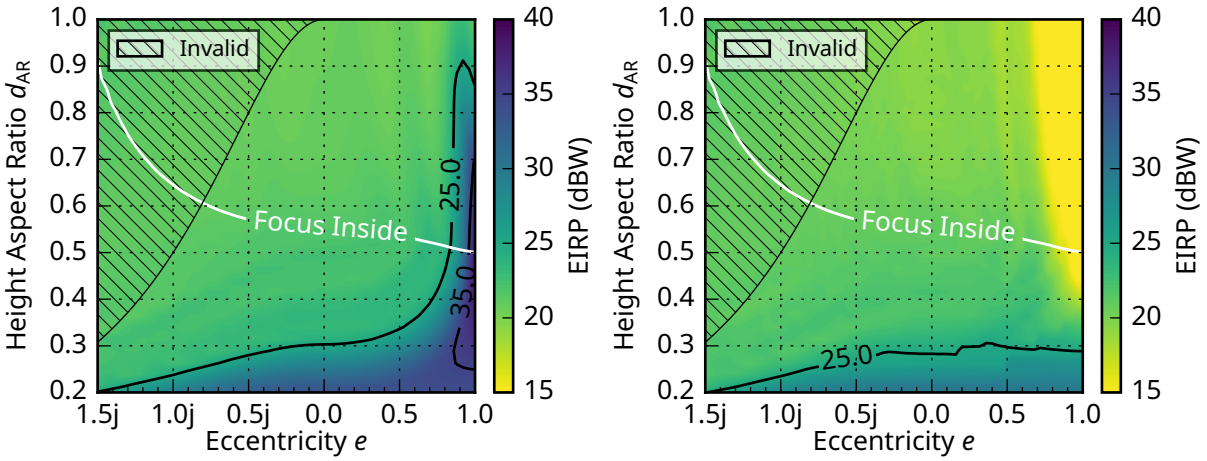

(a) (b)

Figure 4.7: Contour plots of the maximal permissible EIRP in compliance with ETSI EN 301 459 in a 40 kHz-band using a radial feed offset of (a) $d_r = 0\,\mathrm{mm}$ and (b) $d_r = 25\,\mathrm{mm}$ for various elliptical 60 cm-reflectors at 30 GHz

The required total amplifier output power depends on the tolerable EIRP and the gain. If the entire 3 MHz uplink bandwidth of *KA-SAT* is considered (instead of the 40 kHz used in ETSI regulation), the total permissible EIRP is increased by about $3\,\mathrm{MHz}/40\,\mathrm{kHz} = 19\,\mathrm{dB}$ compared to Fig. 4.7. Fig. 4.8 shows the calculated amplifier power. A power amplifier with more than 10 dBW is required to fully use the maximal EIRP for an axially centered feed and a parabolic reflector (cf. Fig. 4.8a). In many applications, amplifiers operate in back-off to guarantee linearity. Amplifiers with sufficiently high output powers are currently not commercially available in small packages and would require complex thermal management. For an elliptical reflector, the maximal allowable power is decreased to about 0 to 5 dBW. As shown in Fig. 4.8b, these power levels are slightly lower for scanned beams. For a parabolic reflector, a power level of 0-5 dBW suffices in the scanned case.

For an Rx-antenna, antenna gain over system noise temperature G/T is the most crucial figure of merit. The G/T calculation includes spillover as it affects the Rx-antenna noise temperature T_A. In the worst case, i.e., when the spillover is entirely directed towards the Earth, T_A is approximately:

$$T_\mathrm{A} = \eta_\mathrm{spill} T_\mathrm{A,0} + (1 - \eta_\mathrm{spill}) T_\mathrm{earth}, \tag{4.5}$$

where η_spill is the spillover efficiency, $T_\mathrm{earth} = 290\,\mathrm{K}$ the earth surface temperature, and $T_\mathrm{A,0}$ the background brightness temperature [117]. $T_\mathrm{A,0}$ is the noise temperature the antenna would see if no spillover would occur ($\eta_\mathrm{spill} = 1$).

A typical brightness temperature at Ka-band $T_\mathrm{A,0}$ is 15 K [118]. For $\eta_\mathrm{spill} = 75\%$, T_A increases to 85 K. The G/T for the case $T = T_\mathrm{A}$, including the noise temperature rise due to spillover, is plotted in Fig. 4.9a. The reflector is tilted to $\theta = 30°$ for the analysis, which results in a brightness temperature $T_\mathrm{A,0} \approx 30\,\mathrm{K}$. These values do not include antenna losses

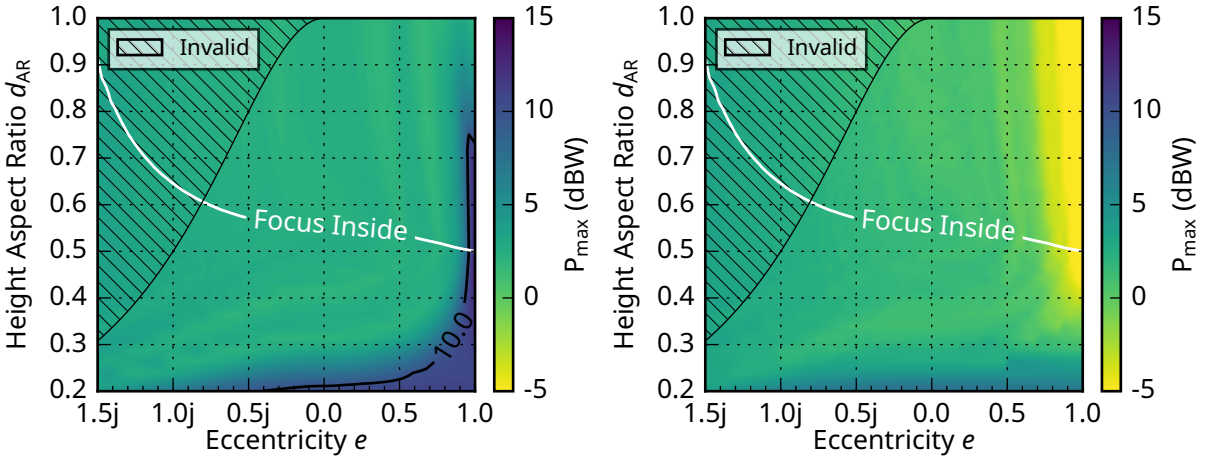

(a) (b)

Figure 4.8: Contour plots of the maximal allowable amplifier power using a radial feed offset of (a) $d_r = 0\,\mathrm{mm}$ and (b) $d_r = 25\,\mathrm{mm}$ and various elliptical 60 cm-reflectors at 30 GHz

or further degradation in the array network due to mismatch or electronic components. However, they provide means to investigate the influence of the reflector shape.

The highest G/T of 25 dB/K occurs if the feed is just about inside an ellipsoid reflector with high eccentricity. If the focal distance increases, spillover occurs and the G/T decreases. Hence, d_{AR} should be close to the "Focus Inside" line to obtain a good Rx antenna. Flat reflectors with high gain and EIRP are ideally suited for transmitters and not particularly good for the receiver. Thus, a well-considered compromise is essential for a combined transmit and receive antenna. Here, $d_{\mathrm{AR}} = 0.38$ is chosen.

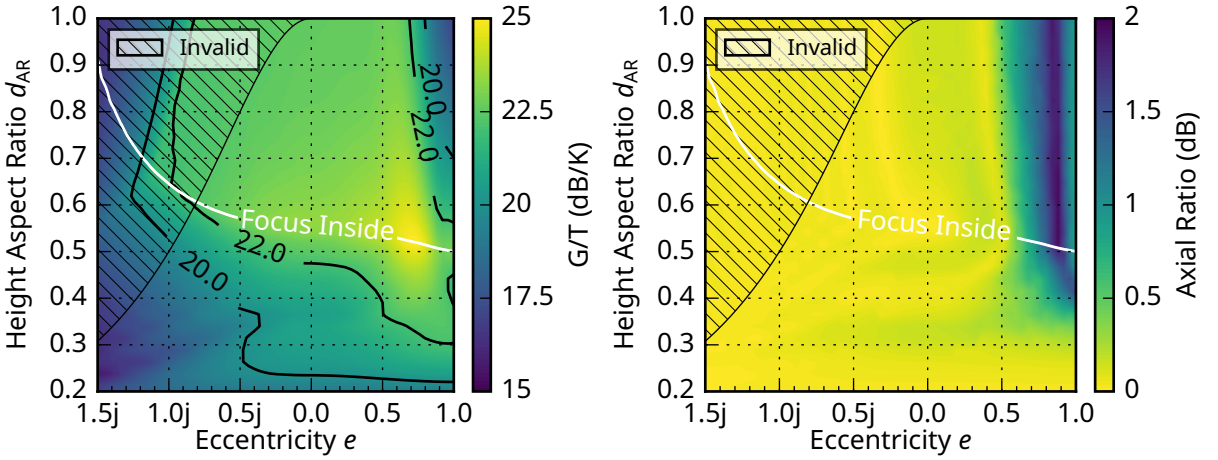

(a) (b)

Figure 4.9: (a) G/T at $\theta = 30°$ and (b) boresight Axial Ratio (AR) using a radial feed offset of $d_r = 25\,\mathrm{mm}$ and various elliptical 60 cm-reflectors at 30 GHz

Fig. 4.9b shows the axial ratio in the boresight direction of an off-axis feed antenna. The deviance from 0 in the plot stems from the reflector since the Gaussian beam used for the feed features a very high XPD. The most extensive degradation in polarization occurs for reflectors with an eccentricity higher than 0.5. The reason is the so-called beam squint that occurs if circular polarization is used with paraboloid reflectors and off-axis feeds [17, pp 234].

4.3.6 Final Design Considerations

The scanning performance is further investigated to determine the optimal reflector eccentricity for the desired application. In the simulation setup, the reflector rim height remains fixed at $d_z = 11.4\,\mathrm{cm}$ in combination with four eccentricities at 1.0j, 0.0, 0.5, and 1.0. The feed is radially offset by up to 50 mm. The achieved scan angles are reported in Fig. 4.10a. All four reflectors exhibit a very similar scan range, the maximum difference of 1° occurring between the cases with $e = 1.0$ and $e = 1.0j$ for 50 mm offset.

The directivity is substantially different (Fig. 4.10a). For low radial offsets, it varies between 44 dBi ($e = 1$) and 38 dBi ($e = 1.0j$). However, a higher eccentricity also leads to a fast drop-off. At about 25 mm offset, the spheroid ($e = 0$) has the maximal directivity, which starts to drop at about 40 mm offset.

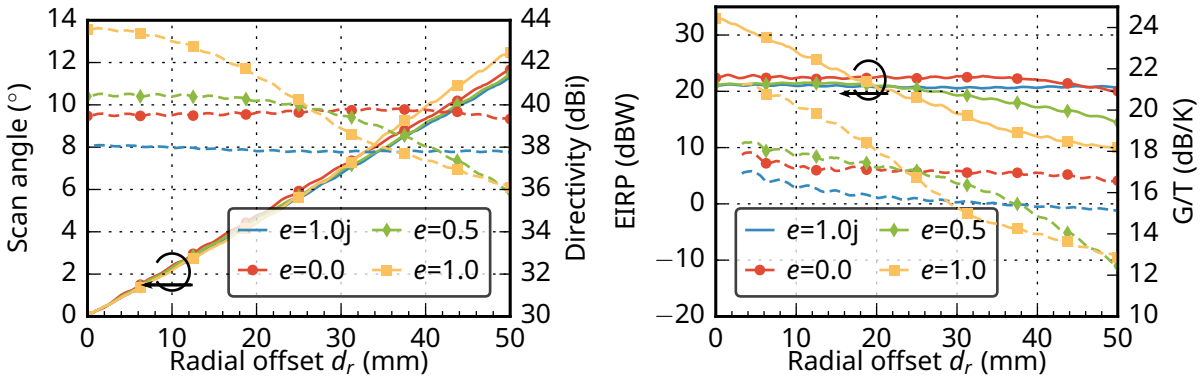

(a) (b)

Figure 4.10: (a) Dependence of the scan angle (——) and directivity (- - -) on the radial feed offset. (b) Dependence of the EIRP (——) and G/T (- - -) on the radial feed offset.

The influence of eccentricity and radial offset on EIRP and G/T is shown in Fig. 4.10b. Due to the fast rise in side lobes, the paraboloid's achievable EIRP decreases even faster than its directivity. Hence, the spheroid performs best for radial offsets of more than 20 mm. This effect is not as pronounced for G/T, where the same happens at about 24 mm. Generally, the spheroid and the major-axis-cut ellipsoid show the lowest changes throughout the scanning range.

For the considered use-case, the required scanning range of ±6° results in a feed offset of about 25 mm. In this case, the spheroid performs best as it also features the smallest dependence on offset. Hence, a spherical reflector design with a rim height d_z of 11.4 mm offers the best compromise.

4.4 Feed design

Section 4.3 only focuses on the reflector design. The feed is considered a single ideal source that has to be radially displaced to obtain scanning. Since the mechanical movement of the feed is unwanted, an antenna array is proposed here as a solution. This setup is often referred to as a focal plane array.

Several tasks are involved in designing such a reflector feed array. First, an element spacing has to be selected such that the scanned pattern does not vary more than a threshold value (cf. Section 4.4.1, Section 4.4.2). Second, a distribution network topology is needed to allow control of each element (cf. Section 4.4.3). Third, the required components must be designed (cf. Section 4.5). This thesis focuses on the design of a 30 GHz Tx array. However, some insight is provided on implementing a dual-band Rx-/Tx-architecture.

4.4.1 Array Grid

Array elements can be arranged in different grids, most notably rectangular and triangular ones [67]. This working principle is well known for traditional direct radiating arrays. In a feed array, the design criteria are different and homogeneous scanning, low element count, and power combining are most important. In [119], focal plane array grids and their excitation are analyzed. A hexagonal structure is found to arrange “the elements space-efficiently and evenly across the rotationally symmetric feed area”. Hence, a hexagonal grid is immensely beneficial to obtain a relatively homogeneous power distribution of the scanned beam.

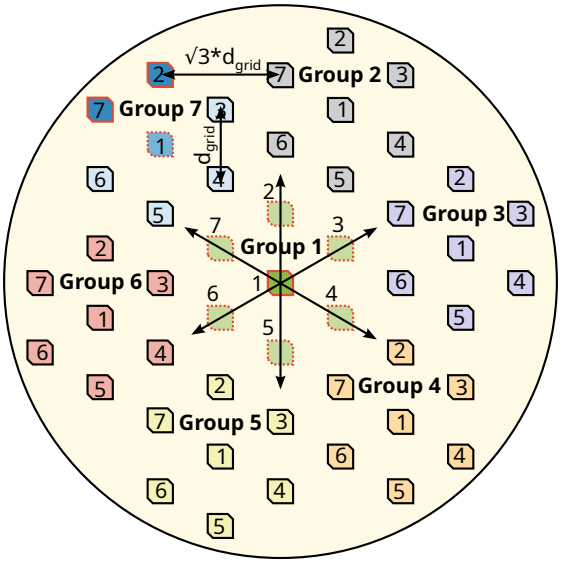

Figure 4.11: Proposed 49-element triangular array design using seven subgroups of seven elements each. Also shown are the grid spacing, main axes, and analyzed excitation groups of the array.

A grid of 61 elements provides good homogeneous scanning coverage and approximates a circle [119]. The realization of such an array is challenging. Due to the hexagonal

arrangement, ordering 61 elements in subgroups is complex, and the routing of the feed network gets challenging. Hence, a different approach is used here: a 49-element array on a triangular grid is arranged in 7 subgroups. As depicted in Fig. 4.11, each subgroup consists of seven elements. This approach provides a relatively well-filled circular array and simple network design with reusable subgroup designs.

Besides the grid arrangement, the power variation when scanning strongly depends on the element density/spacing. Main grid axes can be defined, originating from the center element of each subgroup. The distance between elements along these axes is called grid spacing d_{grid}. Between main axes, the element distance increases to $\sqrt[3]{d_{grid}}$.

A larger grid spacing (cf. Fig. 4.11) reduces the number of elements required to achieve the desired scanning range but increases the power variations. To analyze the effect of the grid spacing, the reflector design from Section 4.3.6 is simulated in conjunction with single discrete feed antennas positioned on the array grid. A two-step approach helps to determine the achievable directivity in each spatial direction. First, the antenna element providing the maximum contribution is determined. Second, the directivity is simulated, and the results are plotted in Fig. 4.12.

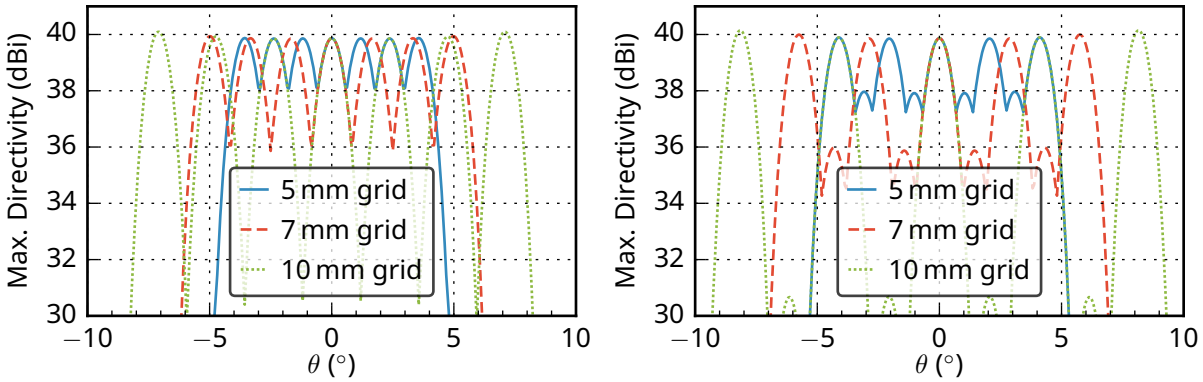

Figure 4.12: (a) Maximal achievable directivity using a single element along a cut in a main array axis for different grid spacings. (b) Maximal achievable directivity using a single element between two main axes for different grid spacings.

The maximum achievable directivity along one of the main axes is analyzed to determine the grid spacing. In the case of the 49-element array, up to seven elements are on these axes. The resulting directivity is shown in Fig. 4.12a for three different grid spacing (5 mm, 7 mm, and 10 mm). Each element causes a single distinct maximum in the plot. The minima are significantly reduced for denser grids at the expense of a lower achievable angular coverage.

> As expected, the directivity varies the least (about 2 dB) for the 5 mm grid spacing and the most (about 10 dB) for the 10 mm grid. It is lowest halfway between two maxima. A cut along the main grid axis yields the best possible results since the elements are exactly the grid spacing apart. If a 30° off-axis cut is investigated, the element distance increases by $\sqrt{3}$ and hence also

the amplitude variation. The resulting maximal difference for the 7 mm grid increases from 4 dB to about 5.5 dB [c.f. Fig. 4.12b].

[Fig. 4.12a] 13 also illustrates the maximal available scanning range, which ranges from about ±4° for the 5 mm grid to about ±8° for the 10 mm grid. Here, the 7 mm grid is chosen, since it yields a reasonable scanning range and tolerable directivity variations. The maximal available gain of such a 49-element array on an angular elevation-over-azimuth grid is depicted in [Fig. 4.13b]. The scan range and the directivity variations are clearly visible. They are less pronounced along a grid main axis (e.g., azimuth=0°) compared to an off-axis-cut (e.g., elevation=0°). [98]

As a reference, Fig. 4.13a also includes the results for the 5 mm grid. The maximal directivity is more evenly distributed for the same number of elements, but the achievable scanning range is significantly reduced.

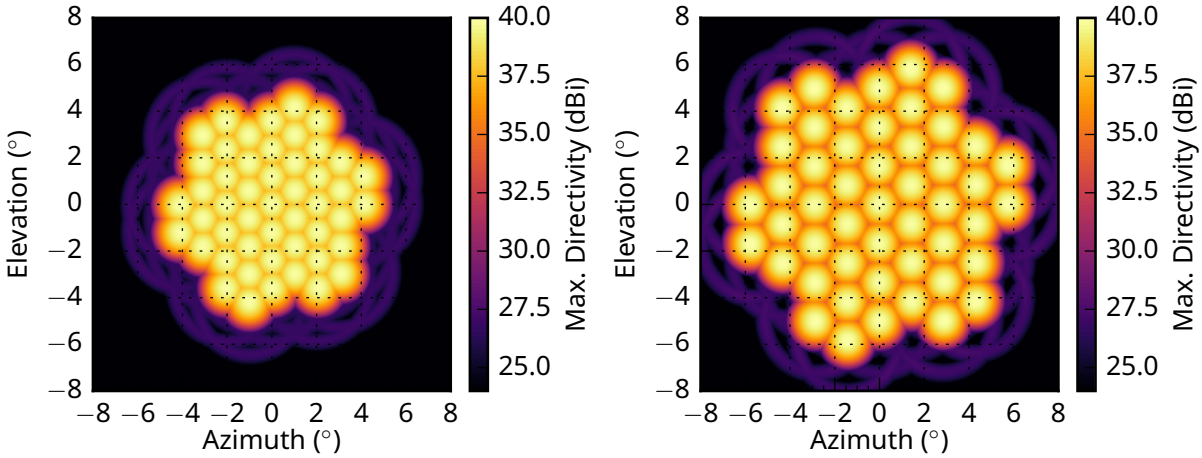

(a) (b)

Figure 4.13: (a) 2D-Plot of the maximal achievable directivity for a grid using a 5 mm- and (b) 7 mm-grid spacing.

4.4.2 Array Excitation

The analysis in Section 4.4.1 is carried out with a single active element. Since the core of the feed is an array, multiple elements can be switched on simultaneously. Furthermore, the phase and amplitude of each element can be individually adjusted. These additional degrees of freedom in the excitation of the array can be used to improve the radiation pattern, such that an optimized excitation scheme mitigates the observed gain change of 5.5 dB for the 7 mm grid spacing proposed in Section 4.4.1.

Fig. 4.14a shows the simulated results of a single active element, which is positioned on the outside of the array (Group 7 'blue', Element 7, c.f.Fig. 4.11). The maximum is visible and corresponds to a scan angle of $\theta \approx 5.8°$ and $\phi = 330°$-direction. The concentric lines around the center are the sidelobes of the beam. A cut through the maximum in $\phi = 330°$-direction is plotted in Fig. 4.15a (——). This scan angle represents the best possible

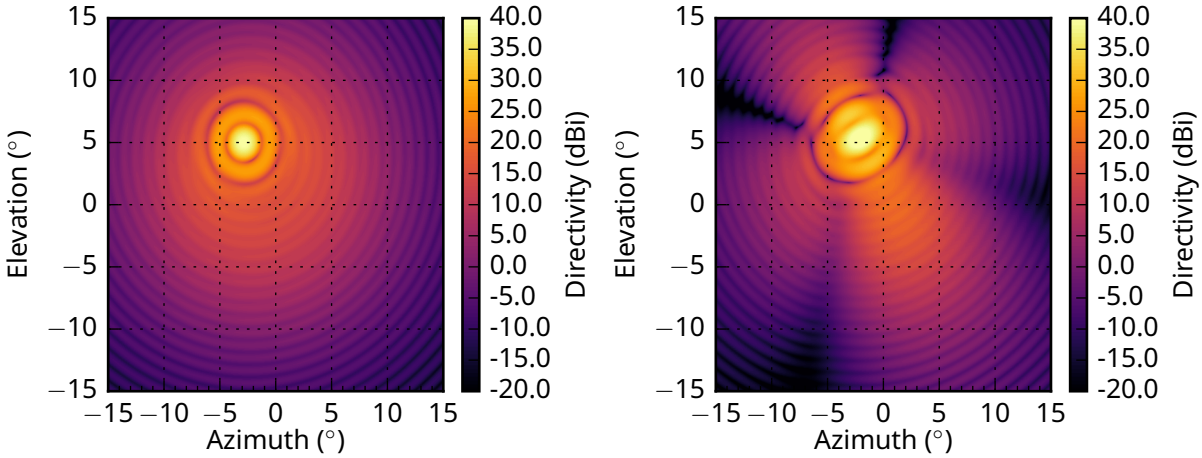

(a) (b)

Figure 4.14: Simulated far field patterns in elevation-over-azimuth coordinates. In (a), a single element on the outside of the grid (Group 7 'blue', Element 7 in Fig. 4.11) is switched on. In (b), three active elements with different amplitudes on the outside of the grid (Group 7 'blue', Element 1, 2, and 7 in Fig. 4.11) are turned on to mitigate a grid minimum.

case, whereas a beam scanned between two elements (e.g., in $\phi = 338°$-direction) results in the worst case (—●— in Fig. 4.15a). The difference in the maxima between both curves corresponds to the 5.5 dB calculated in Section 4.4.1.

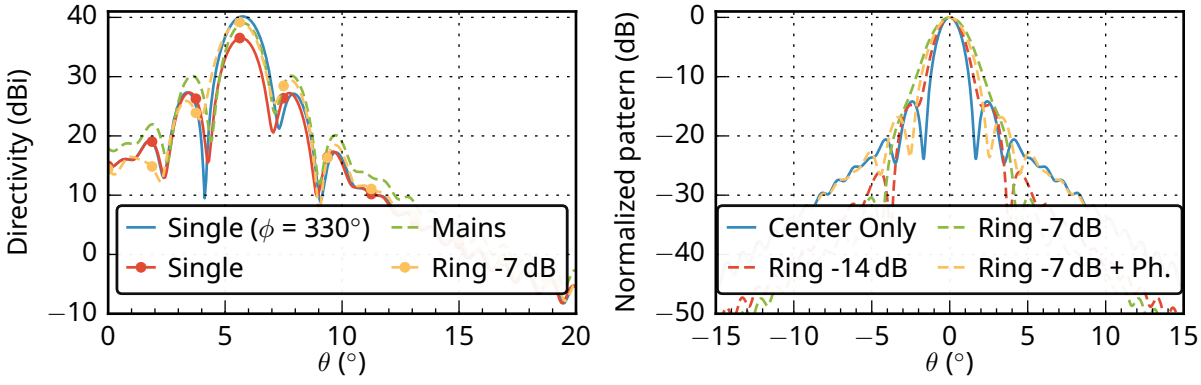

(a) (b)

Figure 4.15: Simulated far-field cuts of different array excitation schemes to show (a) the beam scanning and (b) the changes of the beam pattern.

The results can be significantly improved by switching on a second element (Group 7, Element 2) with the same power as the first one (cf. - - - in Fig. 4.15a). The directivity improves, but the beam widens, and sidelobes increase. A further improvement in the sidelobes is possible by switching on another element (Group 7, Element 1) at an amplitude reduced by 7 dB. As shown in Fig. 4.15a (-●-), the beam widens more, but the

inner sidelobe is reduced by about 5 dB. An azimuth-over-elevation plot of the resulting far-field pattern is depicted in Fig. 4.14b. The beam is now broader but centered midway between the main elements. Additionally, sidelobes are reduced in certain directions.

To estimate the effect of these results for practical use, the ETSI requirements (cf. Section 2.4.4) are considered. The maximal tolerable EIRP values in a 25 kHz band are calculated for all three cases with the theoretical receiver positioned at $\theta = 5.8°$, $\phi = 338°$. For a single active element, the maximal tolerable EIRP is about 16.6 dBW, for two main elements 18.7 dBW and for the three-element excitation 19.9 dBW – an improvement of more than 3 dB. Further simulations indicate that similar results are feasible for all positions.

So far, the benefit of exciting multiple elements is the increased performance for beams scanned in insufficiently covered directions. The pattern of an ideal, unscanned beam is analyzed in the next step. Fig. 4.16a shows the far field pattern of the array element in the very center of the array (Group 1 'green', Element 1). If the surrounding elements (Elements 2-7) are excited with a reduced amplitude (7 dB), the pattern changes (cf. Fig. 4.16b). The shape of the main beam and its beamwidth are altered. Furthermore, large black areas are visible in the plot indicating reduced sidelobes.

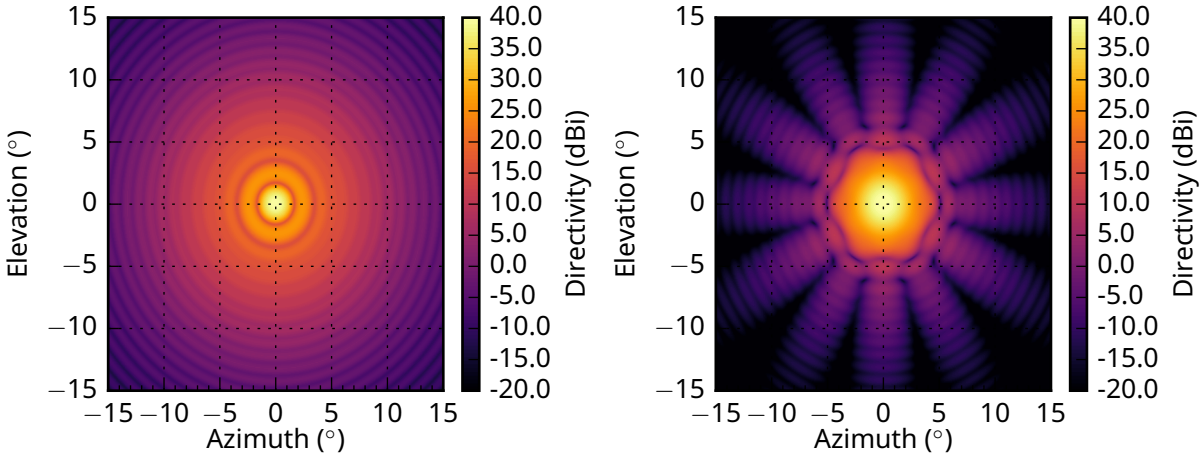

(a) (b)

Figure 4.16: Simulated far field patterns in elevation-over-azimuth coordinates for elements in Group 1 'green'. (a) only the center element (Element 1 in Fig. 4.11) is activated and (b) all surrounding elements (Element 2-7) are activated with an ampltitude reduced by 7 dB.

A far field cut in Fig. 4.15b along the $\phi = 0°$-direction delivers further insight. The beam is indeed widened, and far-end sidelobes are reduced. Only a slight improvement is possible within $\theta \pm 4°$. Thus, the amplitude of the excited ring elements is reduced to -14 dB. As expected, the beamwidth decreases while the far-end sidelobes remain at low values. Some marginal improvements can be made if the phase of the ring elements is adjusted. Again, the ETSI requirements are considered, and the EIRP is calculated. However, improvements are only marginal (≈ 0.1 dB), and the main benefit is the reduced power requirement for the PA due to spatially combined power from multiple elements.

4.4.3 Distribution Networks

Different array excitations that improve the radiation pattern are analyzed in Section 4.4.2. Multiple beams have to be excited simultaneously to enable such schemes. Thus, some sort of signal distribution network is necessary.

Similar to classical phased arrays, different network topologies are possible. Advanced architectures like DBF or phase shifting networks are unnecessary since simulations indicate only marginal improvements using phase-adjusted excitations. Hence, a network with amplitude control elements suffices.

A typical realization of such a distribution network is a switch matrix. As illustrated in Fig. 4.17a a Single Pole, Double Throw (SPDT)-switch connects a central source to all antenna elements. A significant difference from direct radiating arrays is that transmitter and receiver have to be colocated at the same array element to scan the beam in the same direction. Therefore, every array element is equipped with a combined Rx/Tx-frontend, separating input and output signals through diplexers. To connect more than two antenna elements SPDT-switches have to be cascaded, which increases circuit and control complexity. For the proposed 49-element array, a six-stage network (with 64 output ports) would be required, which would cause significant losses at microwave frequencies ($\approx 2\,\mathrm{dB}$ per cascaded switch).

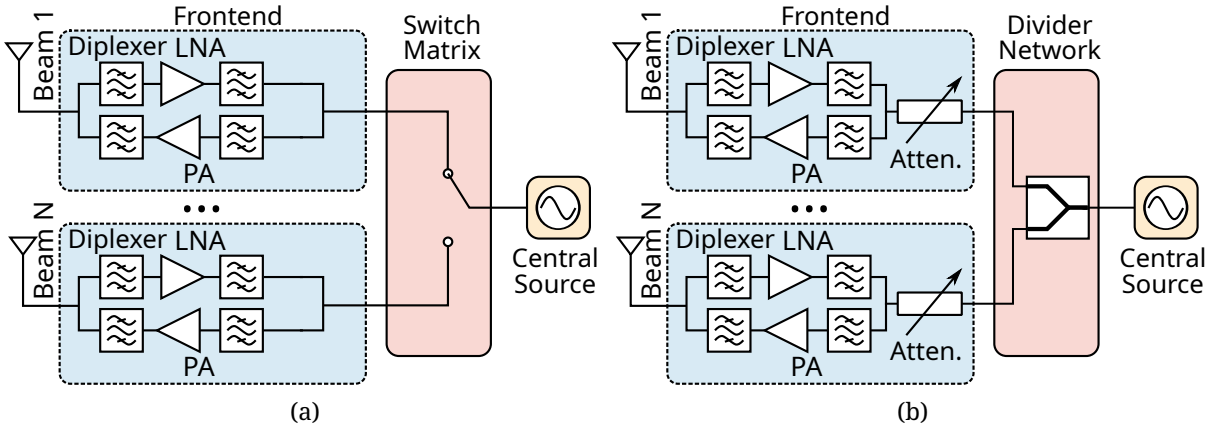

Figure 4.17: Schematics of the array distribution network, enabling the proposed excitation scheme using (a) SPDT-switches and (b) a combination of power dividers and attenuators.

A complex switching matrix is required if multiple beams must be excited simultaneously, posing a significant design challenge. Hence, a different solution is proposed: A power divider network distributes the signal from a central source with equal phase and amplitude to all antenna elements. Each element has a tunable attenuator that provides amplitude control and the ability to “switch off” individual channels. A schematic of this approach is shown in Fig. 4.17b. Due to its relatively simple topology and high flexibility, the feed is based on this network topology. Phase control is also feasible by inserting an additional phase shifter.

4.4.4 Final Design Considerations

The main goal of the initial design is to verify the AFR-concept and to demonstrate the proposed beam scanning schemes. Integration of a dual-band Rx/Tx frontend would add unnecessary complexity. Hence, a 30 GHz Tx frontend is designed for the proposed 49-element feed. The input signal is distributed to the antennas using two cascaded 7-way radial dividers ([120], cf. Section 4.5.3). A schematic is depicted in Fig. 4.18. Tunable attenuators and switchable amplifiers (driver and PA) are placed in the frontends to switch the beams on and off. The attenuator also provides the required matching for the radial dividers in the off-state. An output amplifier boosts the input signal and compensates for losses in the network and attenuator.

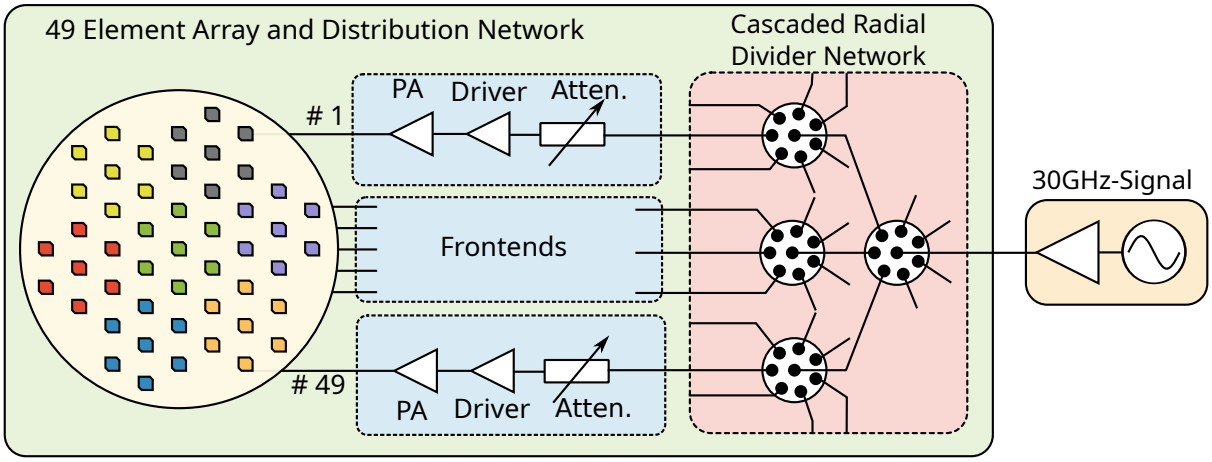

Figure 4.18: Schematic drawing of a 49-element feed array including transmitter frontends with variable attenuator and PA. The input signal is distributed through cascaded 7-way radial dividers.

The realization is carried out in PCB technology using a ten-layer multilayer approach (cf. Fig. 4.19). The Rogers 4003 material system is chosen because of its relatively good performance in the Ka-band and mostly FR4-compatible fabrication process.

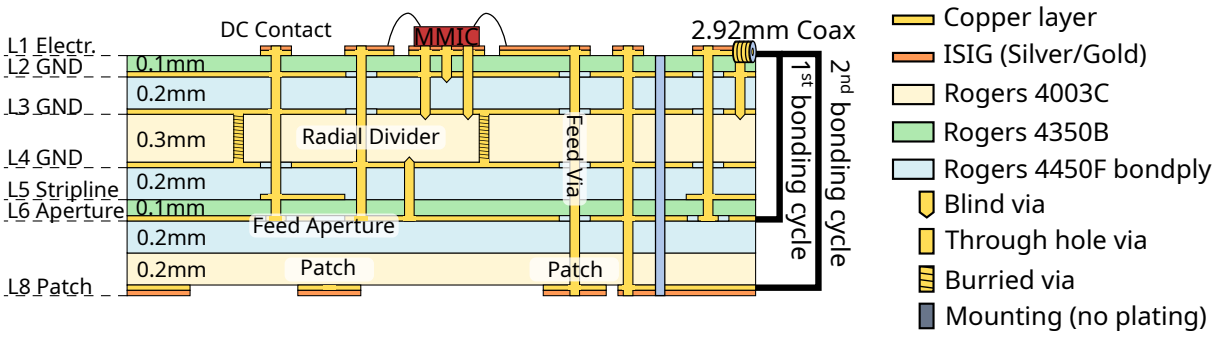

Figure 4.19: Multilayer PCB-stack for the active reflector feed network.

The bottommost layer (L7) accommodates the antennas illuminating the reflector. Patch antennas are used since they are efficiently designed and manufactured on a PCB. Layers L4-L6 contain a stripline routing network. So-called radial dividers are integrated between L3 and L4 to connect all elements to a single input. The remaining two topmost layers, L1 and L2, are used for coplanar transmission lines and component placement. All active circuitry (attenuators and amplifiers), as well as DC- and RF-interconnects, are positioned on L1.

The design of all individual components of the frontend is described in Section 4.5.

4.5 Feed Components

The feed consists of different interconnected microwave components. The design procedures of the individual PCB-components are discussed in this section. These are

- vertical via transitions (Section 4.5.1),
- patch antenna (Section 4.5.2),
- radial power divider (Section 4.5.3), and
- subgroup design including the active circuitry (Section 4.5.4).

The section concludes with a discussion of the complete feed design in Section 4.5.5.

4.5.1 Vertical Transitions

Vertical Transitions are essential to realizing RF interconnects between circuits on different layers of a PCB, e.g., to access the 50 Ω -stripline on Layer 5 from the CPW on the top layer containing all the components (cf. Fig. 4.19). Such a transition based on vias is illustrated in Fig. 4.20. The design parameters are listed in Table 4.2 and a 3D-cross-sectional view is depicted in Fig. 4.21a.

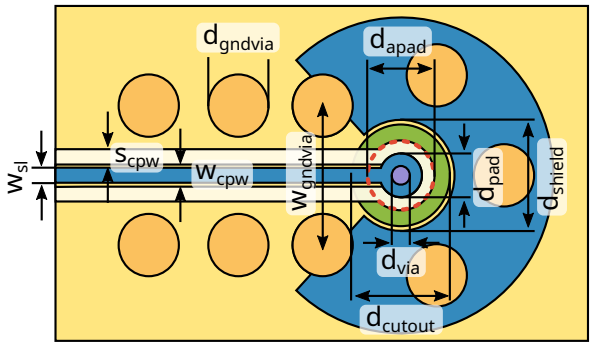

Figure 4.20: Top view of the vertical transition from CPW to stripline.

Par.	Value	Par.	Value
$\mathbf{d_{via}}$	0.150 mm	$\mathbf{d_{gndvia}}$	0.500 mm
$\mathbf{d_{pad}}$	0.350 mm	$\mathbf{w_{gndvia}}$	1.120 mm
$\mathbf{d_{apad}}$	0.550 mm	$\mathbf{w_{sl}}$	0.120 mm
$\mathbf{d_{cutout}}$	0.816 mm	$\mathbf{w_{cpw}}$	0.180 mm
$\mathbf{d_{shield}}$	0.892 mm	$\mathbf{s_{cpw}}$	0.120 mm

Table 4.2: Geometrical properties of the vertical transition using a via.

A major challenge in the design of the transitions is the via. Due to the production process, the via extends from L1 to L6, resulting in a parasitic via stub and pad on L6. The via pad diameter d_{pad} has to be kept as small as possible to minimize the capacitance and excitation of waves in the lower layers of the dielectric. The Ground (GND)-cutout d_{cutout}

on L6 and GND-shield around the via on L5 can also be adjusted to improve the matching. Additional vias are placed around the signal via to minimize the excitation of parallel plate modes on crossed layers.

To measure the S-parameters of the transitions, standard Vector Network Analyzer (VNA) calibration techniques such as Short Open Load Through (SOLT) are not suitable [121]. They are mainly used for coaxial cables since they require precise well-known calibration standards not easily and reliably realized in PCB-technology. A back-to-back transition can be measured using SOLT with limited validity for a single transition. Through Reflect Line (TRL) calibration offers an alternative [122], [123] using more flexible standards. Furthermore, on some VNA, a so-called Unkown Open Short Match (UOSM) calibration is implemented [124]. It is relatively easy to use and allows for shifting the reference plane using suitable calibration standards. However, care must always be taken when using these calibration techniques, since unreliable calibration standards may cause unexpected errors. Fig. 4.22a shows the fabricated standards for a TRL- and UOSM-calibration of the vertical transition.

In addition to a suitable calibration approach, a coaxial connection between PCB and measurement equipment is needed. Most laboratory equipment uses coaxial cables with 2.92 mm connectors for frequencies of up to 40 GHz. The *Rosenberger 02K80A-40ML5* connects the PCBs to the equipment. It is solderless, precision-aligned, and fixed by a pair of screws. However, the connector is rather bulky and requires a counterpart for the screws on the backside of the PCB. Thus, an SMPM connector is a compact alternative for some components.

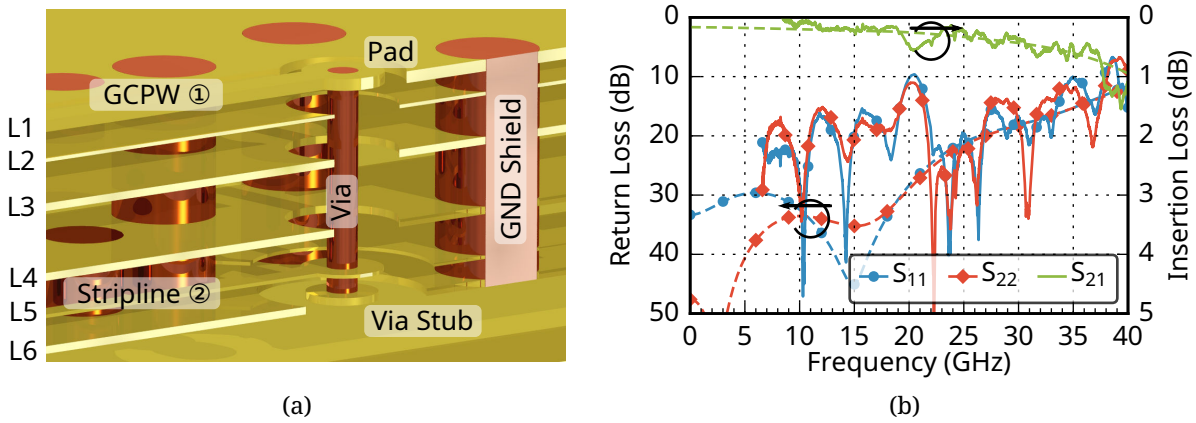

(a) (b)

Figure 4.21: (a) 3D-cross-sectional view of the designed vertical transitions between top layer CPW and burried stripline. (b) Measured (——) and simulated (- - -) S-Parameters of the vertical transition.

The S-parameters of the vertical transition are plotted in Fig. 4.21b. In the simulation, the reflection is less than -15 dB up to a frequency of 35 GHz, and the insertion loss remains below 0.5 dB. The transition is measured using UOSM calibration. Reflections are higher than in simulation, especially below 20 GHz. The image of a fabricated transition in Fig. 4.22b shows the main reason for these reflections: The drilled via and the pad on the top layer are misaligned. The via and surrounding ground were initially connected, and manual removal was required to get some separation. Such misalignments are a

problem for all feed components since they have all been fabricated in a single production run. The measured insertion loss agrees with the simulation, with the most significant deviation occurring due to the parasitic reflections at about 20 GHz. The transition is relatively wideband and would allow dual-band operation at 20 and 30 GHz.

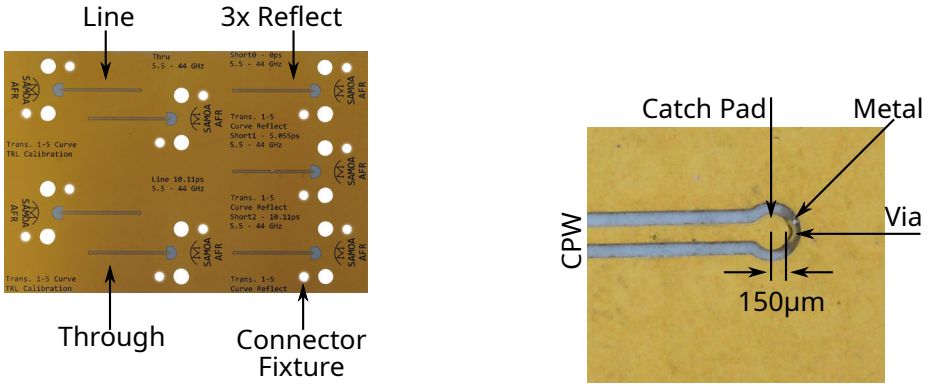

(a) (b)

Figure 4.22: (a) Fabricated PCB TRL and UOSM calibration standards for the vertical transition and *Rosenberger 02K80A-40ML5* connectors. (b) Fabricated transitions with visible defects in the fabricated PCB.

4.5.2 Patch Antennas

To illuminate the reflector, PCB-antennas are needed. The main requirements for the antenna are the center frequency (29.75 GHz), bandwidth (500 MHz), circular polarization, and space requirements on the PCB. All requirements allow a standard patch design. Since the antenna is connected directly to the frontend on the opposite side of the PCB, a "via-feed" patch design is chosen. Truncated patch corners generate circular polarization. The overall design is shown in Fig. 4.23, and the design parameters are listed in Table 4.3. The patch antenna is fed by a grounded CPW-transmission line with ground vias on the top layer (L1). The via connecting the CPW and patch crosses the complete PCB stack.

A single patch antenna is fabricated on a finite substrate to evaluate the performance. The simulated and measured directivity in the $\phi = 0°$-cutting plane is shown in Fig. 4.24a. The measurement results are in good agreement with the simulation. The additional ripples are mainly due to finite ground plane effects.

A densely spaced patch array is required to use the excitation schemes proposed in Section 4.4.2. For such arrays, mutual coupling between adjacent array elements can significantly reduce the performance. Hence, the active reflection coefficient [125] is calculated using simulation and measurement results of a 7-element subgroup. The results are depicted in Fig. 4.24b. If only a single element is excited (Γ), matching in both simulation and measurements is better than -15 dB in the operating frequency band. Due to the high tolerances in the manufacturing process, the simulated results are about 10 dB lower. The active reflection coefficient (Γ_{act}) strongly depends on the desired excitation scheme. If three elements on the outside are used ("blue" scheme from Fig. 4.11), $\Gamma_{\text{act,3}}$ does not deviate significantly from the single element case. If all surrounding elements

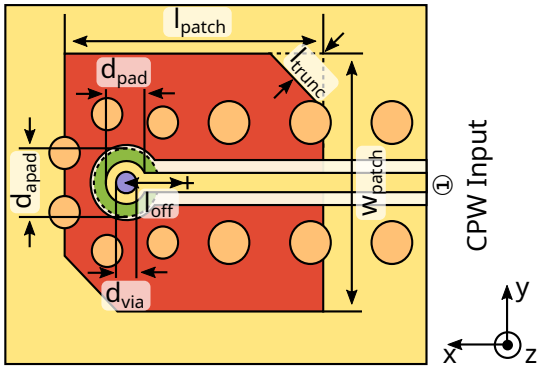

Figure 4.23: Top view of the patch antenna with CPW port.

Circular patch	
Parameter	**Value**
$\mathbf{d_{via}}$	0.200 mm
$\mathbf{d_{pad}}$	0.400 mm
$\mathbf{d_{apad}}$	0.636 mm
$\mathbf{l_{patch}}$	2.540 mm
$\mathbf{w_{patch}}$	2.406 mm
$\mathbf{l_{trunc}}$	0.367 mm
$\mathbf{l_{off}}$	0.788 mm

Table 4.3: Geometrical properties of the circularly polarized patch with via feed.

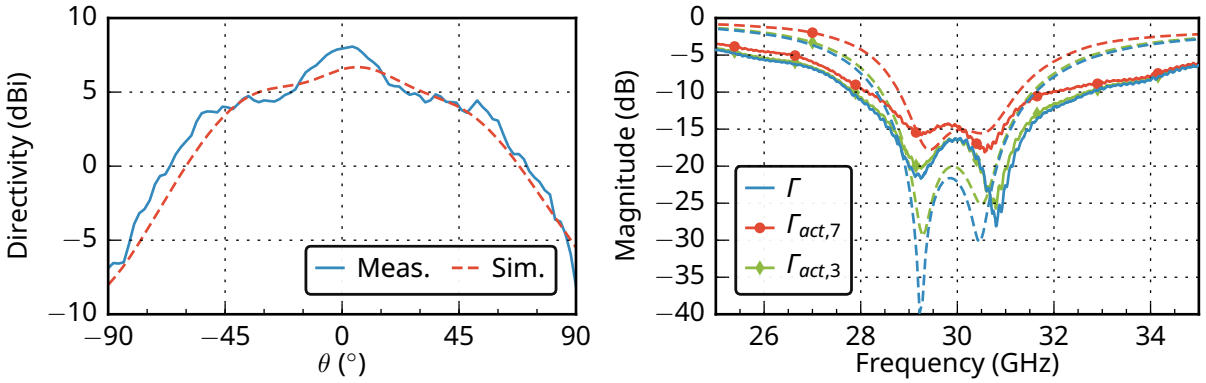

(a) (b)

Figure 4.24: Measurement (——) and simulation (- - -) results of the via-feed patch antenna. (a) Directivity in the $\phi = 0°$-cutting plane of a single element. (b) Active reflection coefficients of a 7-element subgroup.

(Element 2-7) are activated ("green" scheme from Fig. 4.11), the simulated and measured $\Gamma_{\text{act,7}}$ degrades to about 15 dB, which is still sufficient for operation.

4.5.3 Power Divider

Power dividers (or combiners) are a central design element of the feed's distribution network (cf. Section 4.4.3). A divider connects one common port to multiple ports. The most straightforward power divider is the T-junction [126, pp. 316-317], which connects a single input with two outputs. The T-junction is not matched/isolated at all ports. The Wilkinson divider (also known as the resistive divider) [12] is a matched but lossy alternative. It is widely used at microwave frequencies but requires discrete resistors, which occupy space on the PCB and are increasingly difficult to fabricate at higher frequencies. Planar microwave dividers can be extended from 2-way to N-way dividers [127].

Recently the reflective radial power divider known from waveguide technology [120], [128] has been adapted to PCB-technology using SIW [129]–[131]. In [132], a 7-port radial divider is developed for applications at 20 GHz. The presented divider features low loss and is very compact.

These properties match the requirements set by the array grid and distribution network. Each subgroup can be designed around a radial divider with a single input and seven output ports. Since a single compact divider suffices per subgroup, the much-needed surface area is freed on the PCB. Two cascaded radial dividers distribute the input signal to all 49 elements. The dividers are referred to as the first-stage (at the input of the feed) and second-stage (subgroup divider).

The following discusses the design of both the first- and second-stage dividers. They differ since they are engineered to be a divider and vertical transition simultaneously, meaning that inputs and outputs are on different PCB-layers. The input of the first-stage design is on the top layer (L1) since the input coaxial connector is mounted here (cf. Fig. 4.19). The output is located on the stripline layer (L5) to allow easier routing between the cascaded dividers. The second-stage dividers are reversed to connect a stripline input to a CPW output to feed the patch antennas.

A radial divider generally consists of a cylindrical cavity excited by a central input feed. The outputs are symmetrically placed around this feed. In planar technology, the cavity can be realized using two adjacent GND layers and a circular via fence. In the utilized multilayer (Fig. 4.19), the cavity is integrated between L3 and L4. The via fence is realized using buried vias with a diameter of d_{via}, and the spacing is adapted to minimize field leakage. A top view of such a divider is visible in Fig. 4.25. The resonator radius r_{res} must be adjusted to change the cavity's resonant frequency.

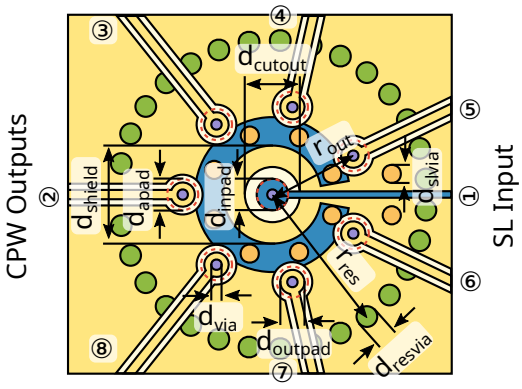

Figure 4.25: Top view of the radial divider with the stripline input port and CPW output ports.

Par.	Value	Par.	Value
$\mathbf{d_{via}}$	0.200 mm	$\mathbf{d_{shield}}$	1.894 mm
$\mathbf{d_{inpad}}$	0.468 mm	$\mathbf{d_{slvia}}$	0.350 mm
$\mathbf{d_{outpad}}$	0.604 mm	$\mathbf{d_{resvia}}$	0.400 mm
$\mathbf{d_{apad}}$	0.600 mm	$\mathbf{r_{out}}$	1.734 mm
$\mathbf{d_{cutout}}$	1.066 mm	$\mathbf{r_{res}}$	2.981 mm

Table 4.4: Geometrical properties of the radial divider with CPW outputs.

Radial Divider with CPW Output Ports - Subgroup Divider

The radial divider from Fig. 4.25 is for the second stage in the subgroup since the input transmission line ① is routed as a stripline on L5. The stripline ends in a via. The via starts on L6 and goes up centrally through the circular cavity, where it is grounded on L3.

The via functions as a simple current probe to excite the resonator. The used design is similar to the transition from Section 4.5.1 and suffers from its drawbacks.

Seven current probes (outputs) are placed symmetrically on a circle around the input feed to couple energy out of the cavity. The radius of this circle r_{out} must be adjusted depending on the cavity diameter and required bandwidth. The output vias start on L1 and are grounded on L4. On the top layer (L1), a CPW is used as a transmission line at the output ports (②-⑧). Antipads of diameter d_{apad} are placed between the input/output vias and all crossing ground planes. The diameter is set to the technological minimum. The diameter of the input and output via pads d_{inpad} and d_{outpad} is adjusted to reduce reflections at the port. The parameters used for the divider (Fig. 4.25) are listed in Table 4.4.

A cross-sectional view of the stripline to 7-port CPW divider is depicted in Fig. 4.26a. The dielectric between the layers is removed for a better view. The input stripline starts on the right and leads to the input via. The output CPW lines are on the top layer and reach into the cylindrical cavity, bounded by a fence of buried vias. The fabricated test circuit is shown in Fig. 4.26b. The connectors are not attached yet, so the footprint and mounting holes remain visible. The input CPW starts on the right side and leads to a curve and a stripline transition (cf. Section 4.5.1). The radial divider is a tiny part in the center, only noticeable by the seven CPW outputs.

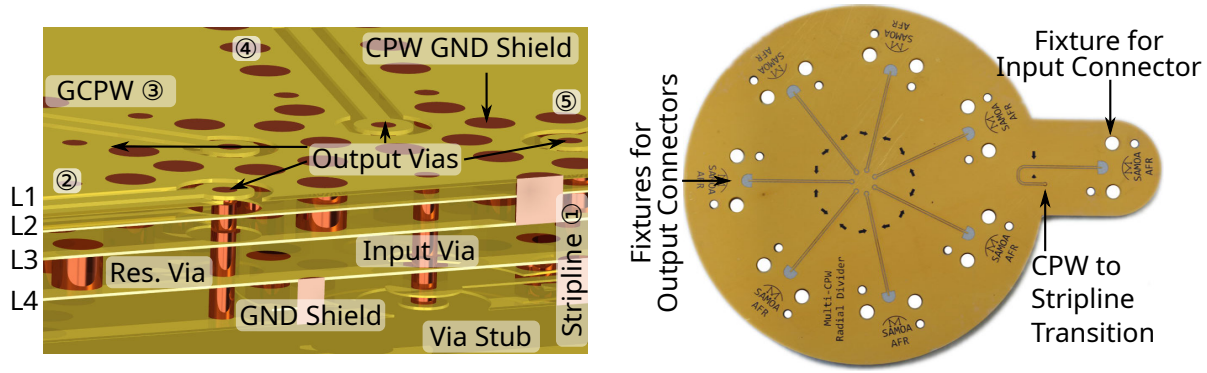

(a) (b)

Figure 4.26: (a) Cross-section of radial divider with CPW outputs and (b) fabricated divider without attached connectors.

The simulated and measured S-parameters are shown in Fig. 4.27. As the divider is a reflective, non-isolating component, only the reflection coefficient of the input port and the transmission coefficients between the input and output ports are shown. Power inserted into a single output port is strongly reflected and transmitted to the input and all other outputs. Achieving matching requires equal excitation of all ports (phase and amplitude, even mode). This behavior is uncritical for the chosen design approach because reflections are absorbed in the next stage attenuators, and additional amplifiers can compensate for power loss (cf. Section 4.4.4).

Fig. 4.27a shows the magnitude of the measured and simulated S-parameters. The input reflection is minimal in the frequency band of interest at about 30 GHz and does not exceed -30 dB in simulation. In the measurements, ripples occur that remain below -15 dB. These can be mainly attributed to the additional vertical transitions (Section 4.5.1) that are not

de-embedded in the measurement results. Furthermore, inaccuracies and a misalignment in the fabrication process as well as a non-ideal transition to the coaxial connectors cause additional reflections at the output ports. The 10 dB-band, which reaches from 23 to 39 GHz in simulation, is widened and shifted to lower frequencies in the measurements. One reason is uncertainties in the effective permittivity of the used substrate Rogers 4000 material, but higher losses, as visible in the transmission coefficients S_{m1}, are also a factor.

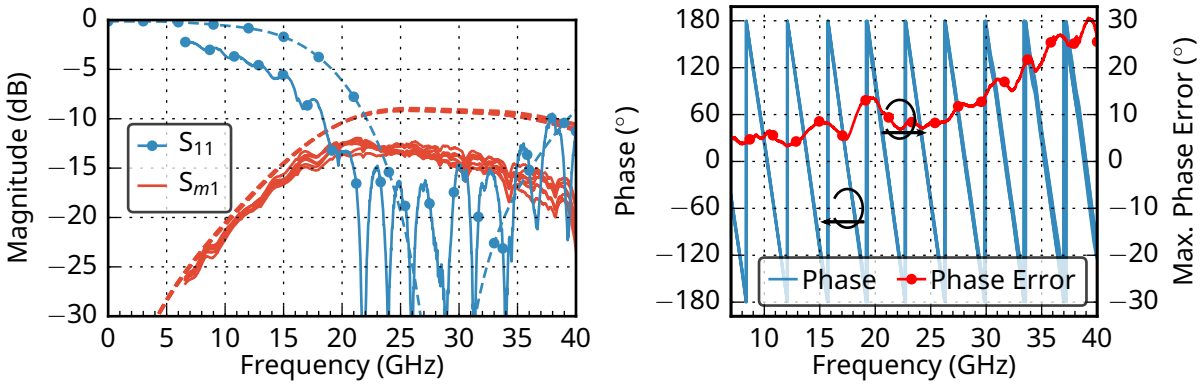

(a) (b)

Figure 4.27: (a) Magnitude of the measured (——) and simulated (- - -) S-parameters of the radial divider with CPW outputs. (b) Measured phase and phase differences at the output ports of the divider.

In simulation, the transmission coefficient of the seven-port divider is close to the theoretical optimum of 8.5 dB. The amplitude differences are less than 1 dB in simulation and reach 2.5 dB in the measurements. Both results can be calibrated using the attenuator.

To equally excite all subgroup elements, the output phase is also essential. The phase is measured sequentially with only two ports at a time, while the other six ports terminate in matched loads. This measurement technique causes some uncertainties since the test set cable is operated at different bend angles, and different PCB-connectors are involved in the measurements. The test setup is similar to the first-stage design shown in Fig. 4.29b. The measured results are plotted in Fig. 4.27b. The phases of all six S_{m1}-transmission coefficients vary linearly with frequency and are quite similar. The maximal error between the seven measurements is plotted as well to provide further insight. As expected, the phase error increases with frequency. In the frequency band of interest, the maximal phase error is about 10°, which is in the range of the measurement uncertainty of the setup and tolerable without requiring a phase shifter.

Radial Divider with Stripline Output Ports - Input Divider

The first-stage divider uses a reversed design, where the input is CPW, and the outputs are stripline. A schematic drawing is shown in Fig. 4.28, and the parametric values of the design are listed in Table 4.5. A miniaturized version of the transition from Section 4.5.1 is used at the output ports. The design procedure and size are similar to those of the second-stage divider.

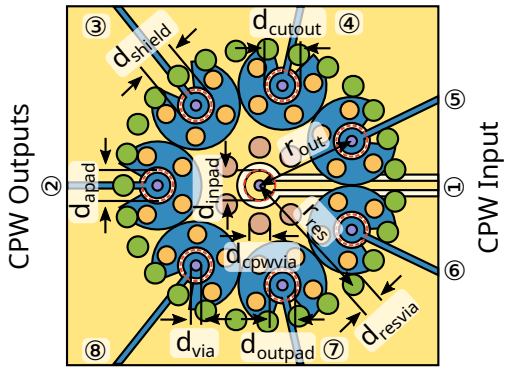

Figure 4.28: Top view of the radial divider with CPW input and stripline output ports.

Par.	Value	Par.	Value
$\mathbf{d_{via}}$	0.200 mm	$\mathbf{d_{shield}}$	0.700 mm
$\mathbf{d_{inpad}}$	0.572 mm	$\mathbf{d_{slvia}}$	0.350 mm
$\mathbf{d_{outpad}}$	0.492 mm	$\mathbf{d_{resvia}}$	0.400 mm
$\mathbf{d_{apad}}$	0.600 mm	$\mathbf{r_{out}}$	1.976 mm
$\mathbf{d_{cutout}}$	0.700 mm	$\mathbf{r_{res}}$	2.732 mm

Table 4.5: Geometrical properties of the radial divider with stripline outputs.

A cross-sectional view of the divider is shown in Fig. 4.29a. The input Grounded Coplanar Waveguide (GCPW) (port 1) starts on the right and leads to the input via. The output vias lead from the resonator cavity to the stripline. Fig. 4.29b shows the measurement setup. CPW-transitions (cf. Section 4.5.1) are needed to access the transmission line on the lower layer.

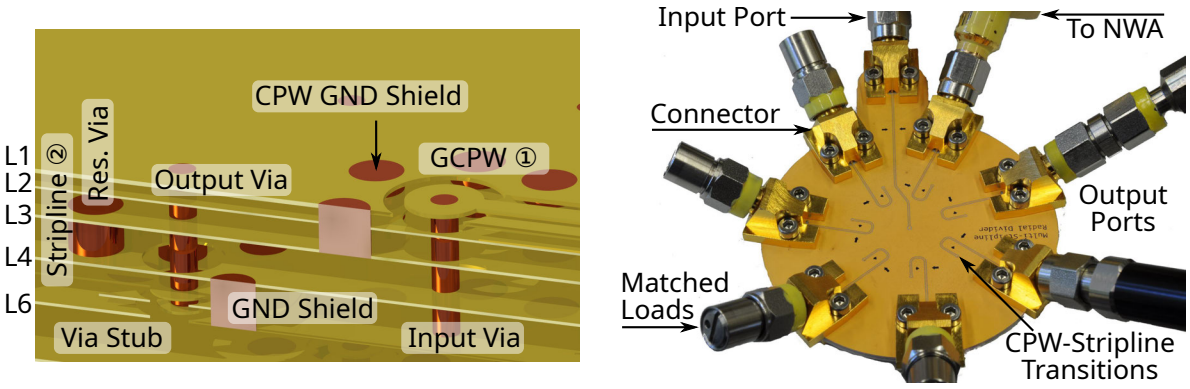

(a) (b)

Figure 4.29: (a) Cross-section of radial divider with stripline outputs and (b) fabricated divider with matched load and Network Analyzer (NWA) connected for measurements.

The measured S-parameters are plotted in Fig. 4.30a and are very similar to those of the second-stage divider. Due to the transitions at the outputs, the measured input reflection in Fig. 4.30a is slightly higher. It remains below -15 dB in the operational band. The magnitude of the transmission coefficients is comparable to the results in Fig. 4.27a. The maximal difference is about 2 dB and 10° in phase (cf. Fig. 4.30b).

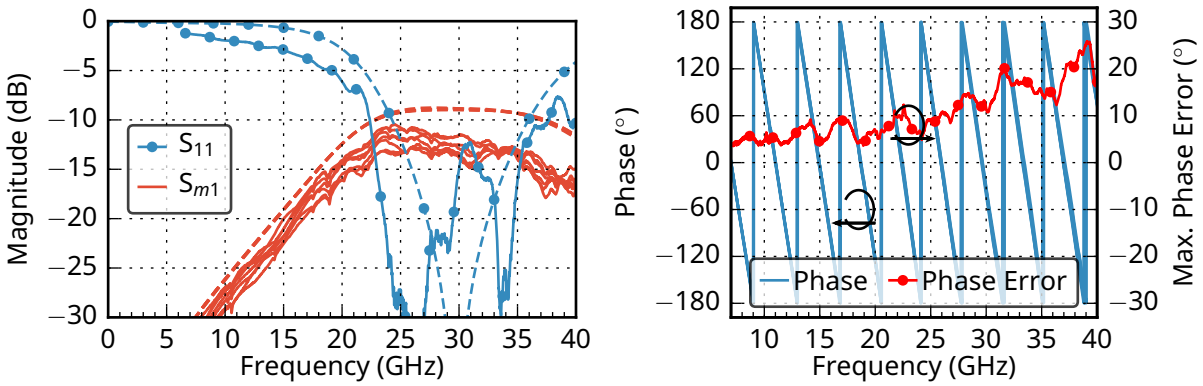

(a) (b)

Figure 4.30: (a) Magnitude of the measured (—) and simulated (- - -) S-parameters of the radial divider with stripline outputs. (b) Measured phase and phase differences at the output ports of the divider.

Wideband Radial Divider

The presented first- and second-stage dividers perform well but do not provide enough bandwidth for a combined Rx and Tx design. The main limiting factor is the vertical via transition embedded into the design. Thus, a wideband design is developed as a proof of concept. As shown in Fig. 4.31, a CPW is used for both input and output.

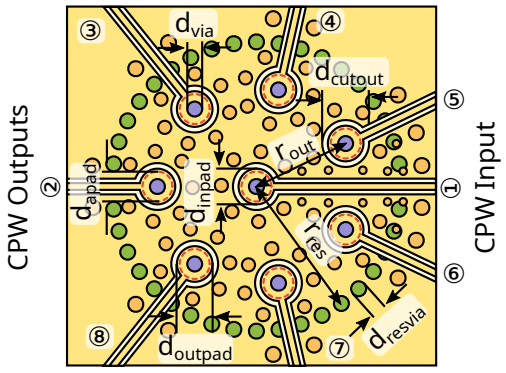

Figure 4.31: Top view of the wideband radial divider with CPW input and output ports.

Wideband		Dual-Band	
Par.	**Value**	**Par.**	**Value**
$\mathbf{d_{via}}$	0.400 mm	$\mathbf{d_{via}}$	0.400 mm
$\mathbf{d_{inpad}}$	0.957 mm	$\mathbf{d_{inpad}}$	0.900 mm
$\mathbf{d_{outpad}}$	0.953 mm	$\mathbf{d_{outpad}}$	0.900 mm
$\mathbf{d_{apad}}$	0.800 mm	$\mathbf{d_{apad}}$	0.800 mm
$\mathbf{d_{cutout}}$	1.257 mm	$\mathbf{d_{cutout}}$	1.200 mm
$\mathbf{r_{out}}$	1.894 mm	$\mathbf{r_{out}}$	2.495 mm
$\mathbf{r_{res}}$	3.868 mm	$\mathbf{r_{res}}$	4.010 mm
$\mathbf{d_{resvia}}$	0.400 mm	$\mathbf{d_{resvia}}$	0.400 mm

Table 4.6: Geometrical properties of dual-band/wideband radial divider with CPW ports.

The cavity size is increased by 1.5 to shift the frequency response to lower frequencies. Tuning the via diameters and pads allows a flexible frequency response adjustment based on application-specific requirements, such as a dual-band or wideband characteristic. Table 4.6 lists the geometrical parameters for such designs. The following presents the wideband design with an input matching of more than 10 dB from 14-34 GHz (83% fractional bandwidth).

Fig. 4.32 depicts the simulated and measured S-parameters of the wideband design. The magnitude of the S_{11} and S_{m1} parameters is plotted in Fig. 4.32a. Simulation and measurement results are generally in good agreement. Input matching is better than 10 dB at both 20 and 30 GHz. The losses are about 2 dB higher in the measurements, and the amplitude variation increases for frequencies above 25 GHz. Due to the removed stripline port, the results are significantly more consistent than the other presented dividers. The measured phase deviation between channels remains below 20° throughout the frequency bands of interest (cf. Fig. 4.32b).

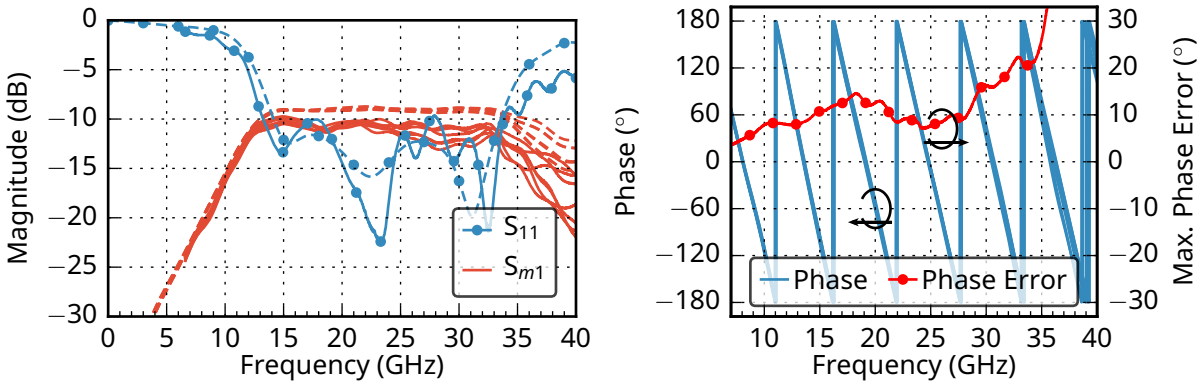

(a) (b)

Figure 4.32: (a) Magnitude of the measured (——) and simulated (- - -) S-parameters of the wideband radial divider with CPW outputs. (b) Measured phase and phase differences at the output ports of the divider.

4.5.4 Subgroup Design

The 7-element subgroups are designed around the second-stage radial power divider in the center. The outputs of the divider are connected to the active frontend. The length of the CPW transmission lines is carefully adjusted using curves and meanders to ensure an equal phase at each element. Due to the small available area, it is not feasible to design lines with an equal total length. Hence, an electrical length difference of multiples of 2π at the center frequency of 29.75 GHz is used. The active components are placed at the end of the CPW, followed by the via-fed patch antenna from Section 4.5.2. The complete arrangement is illustrated in Fig. 4.33, and the top-view of the manufactured subgroup is shown in Fig. 4.37b.

The active frontend from Section 4.3.6 consists solely of an attenuator and an amplifier. Here, Monolithic Microwave Integrated Circuit (MMIC)s are used since they are very compact. For the attenuator, a *UMS* CHT4694 is utilized. It offers an adjustable attenuation range of about 20 dB and requires an analog control voltage. Since 14 dB suffices for the desired excitation schemes (Section 4.4.2), enough buffer remains for channel calibration. The attenuator offers a relatively good matching, which minimizes unwanted reflections back into the divider. The output amplifier is a relatively low-cost AMMC-6232 by *Avago*. It features about 30 dB gain and about 20 dBm output power. Switching it off adds another 30 dB of isolation between input and output. In principle, a more expensive, higher-output

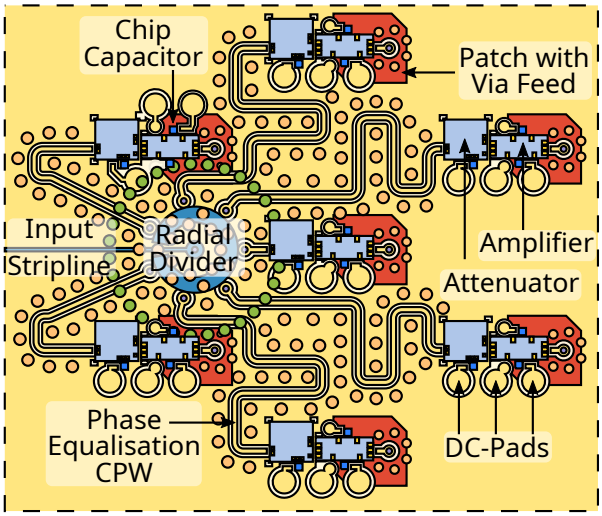

Figure 4.33: Schematic drawing of a 7-element subgroup including the central radial divider and active components.

power amplifier could be integrated to increase the EIRP. The integration requires an adapted network topology to allow for the larger amplifiers and place additional strain on the thermal management.

Wideband Subgroup Design

The subgroup is well suited for the proposed single band Tx antenna. However, for an integrated Rx and Tx antenna, the different electrical lengths of the CPWs would lead to unequal phases for the 20 GHz signal. Feasible solutions include integrating phase shifters or choosing a different network design. Since a phase shifter is a significant challenge at K_a-band, the network is reworked. The phase equalization CPWs are replaced with striplines buried on Layer 5. The designed (passive) dual-band network is depicted in Fig. 4.34a.

The input CPW is routed to the wideband radial divider in the center of the layout. Its output lines lead radially outward, providing equal space for each channel's electronic circuitry. Following the transmission line, a vertical transition (Section 4.5.1) leads to the stripline layer. Enough space is available to design a network with equal electrical length. The stripline feeds a (single band) patch antenna using aperture coupling. This design frees up valuable space on the top layer, allowing for integrating the bulkier wideband divider from Section 4.5.3 and additional components.

As a proof of concept, a dual-band subgroup design is used to integrate larger active components. Fig. 4.34b shows a photograph of the fabricated Tx module, which includes packaged 4 W High Power Amplifier (HPA)s. The module is not further investigated, since the thermal management of the HPA proved challenging. However, it demonstrates that the simultaneous integration of Rx and Tx components is feasible for a dual-band feed using the patch antennas from Section 3.3.2.

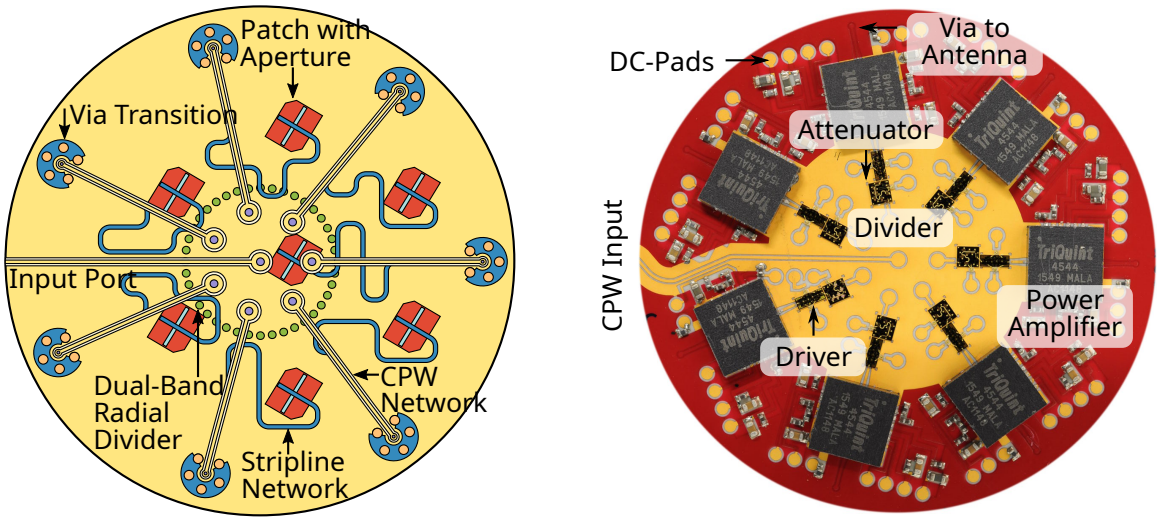

(a) (b)

Figure 4.34: (a) Illustration of a passive 7-element subgroup design for dual-band operation. (b) Realized Dual-Band subgroup.

4.5.5 Complete Feed Design

The complete 49-element feed design is illustrated in Fig. 4.35. The PCB material is removed in the figure to allow a view of all relevant layers. On the bottom, the input CPW transmission line leads to the first-stage radial divider (cf. Section 4.5.3) with stripline output ports on L5. The output signals are subsequently routed to the seven subgroups (cf. Section 4.5.4). The meandering stripline is designed to excite the second-stage radial dividers with equal phases. Vias (not shown in the illustration) are placed around the stripline to minimize the excitation of parallel plate modes at discontinuities.

Fig. 4.36 shows the fabricated Tx-feed. Fig. 4.36a shows the topside, including all the electronics. The seven subgroups are also clearly visible in the photograph. A compact SMPM-connector is used to connect an external RF source to the input of the feed. The 49 antenna elements are placed on the backside of the feed in Fig. 4.36b.

Spring-loaded pins supply the voltages for the active array (cf. Fig. 4.37a). The connection with these pins is non-permanent and assured only by the mechanical pressure applied to the pins – no soldering or gluing is involved. Connected components can thus be easily separated. The springs are required to compensate for an uneven surface of the PCB. The relatively small footprint is a significant benefit of the spring-loaded pins compared to other DC connectors. As visible in Fig. 4.37b, small DC pads close to the MMICs suffice for the required biasing.

All feed electronics fit into an aluminum cylinder with a total height of 90 mm, which serves as housing and thermal reservoir for the power amplifier management. The housing is shown in Fig. 4.37a. The interposer board is integrated into the housing. Six equally spaced pairs of pins are used to ensure a precise alignment between the spring-loaded pins and the RF electronics on the array PCB. The M3 threads are needed to fix the array to the housing and apply the mechanical pressure required to ensure reliable connections of the spring-loaded pins.

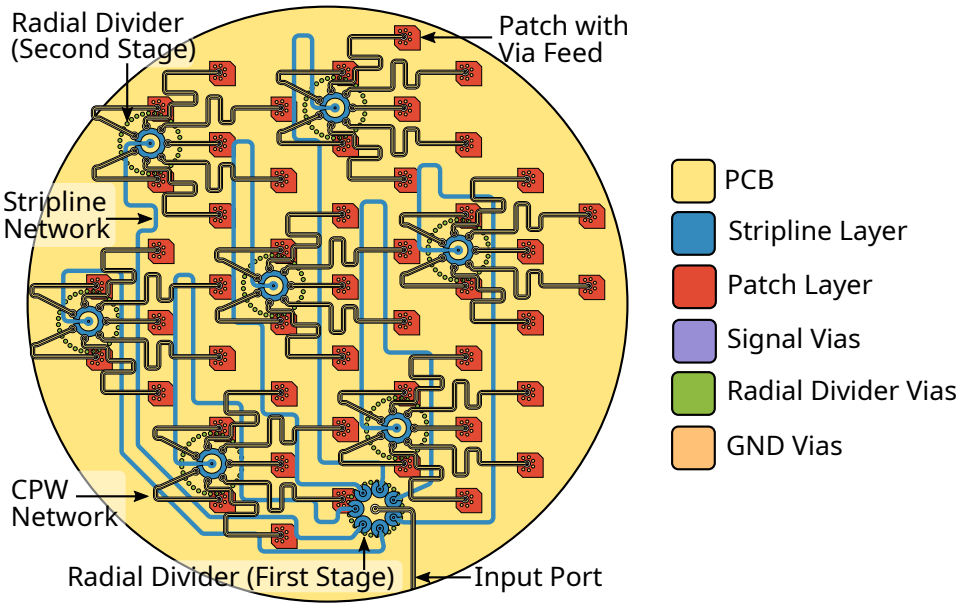

Figure 4.35: Illustration of the full 49-element array setup without active components. It consists of seven subgroups with seven elements each.

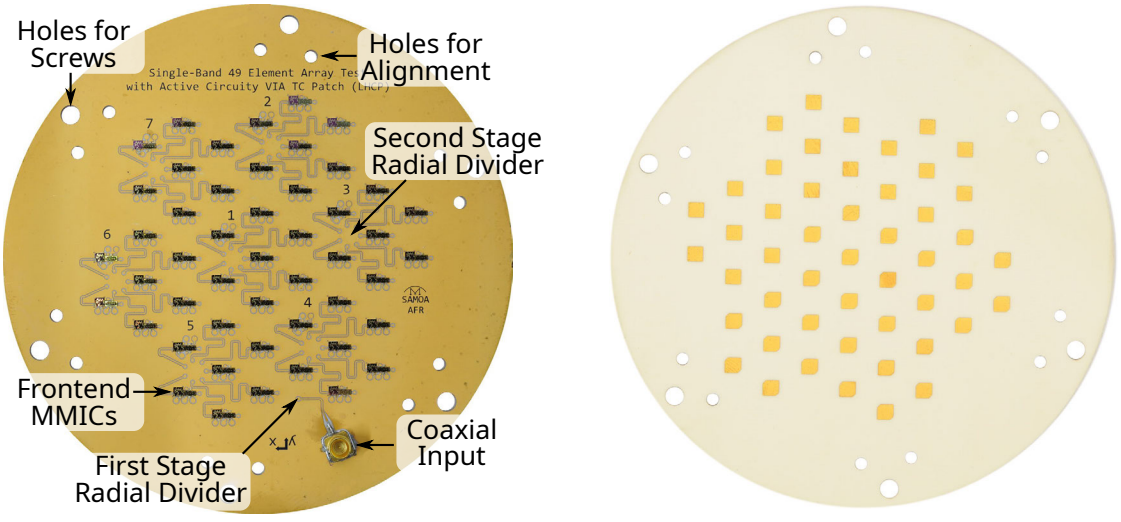

Figure 4.36: (a) Topside of the fabricated 49-element array with mounted electronics and connector. (b) Backside of the array with the patch antennas.

To digitally control the beam scanning, additional circuitry is required to set the attenuators' analog control voltage and the amplifiers' bias. Here, DACs and DC switches are used. As shown in Fig. 4.38a, a small control board is designed for each subgroup.

The boards consist of an 8-channel DAC to supply the analog control voltage for the attenuators and an 8-bit shift register. The registers are connected to an integrated gate voltage controller to switch off unused amplifiers. If the proposed excitation schemes

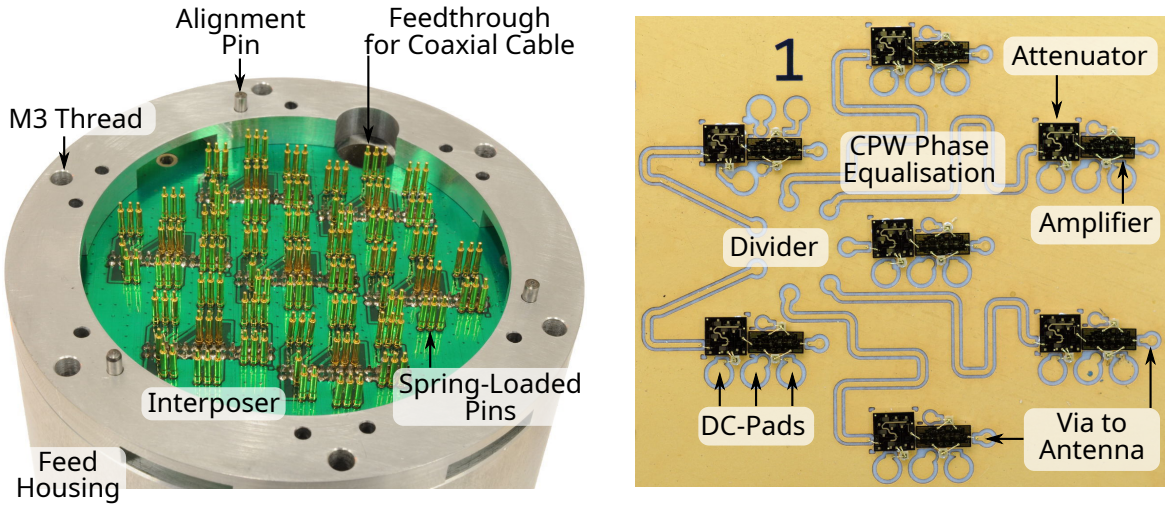

(a) (b)

Figure 4.37: (a) Interposer with springloaded pins in feed housing. (b) Top-view of a manufactured subgroup equipped with attenuators and amplifiers.

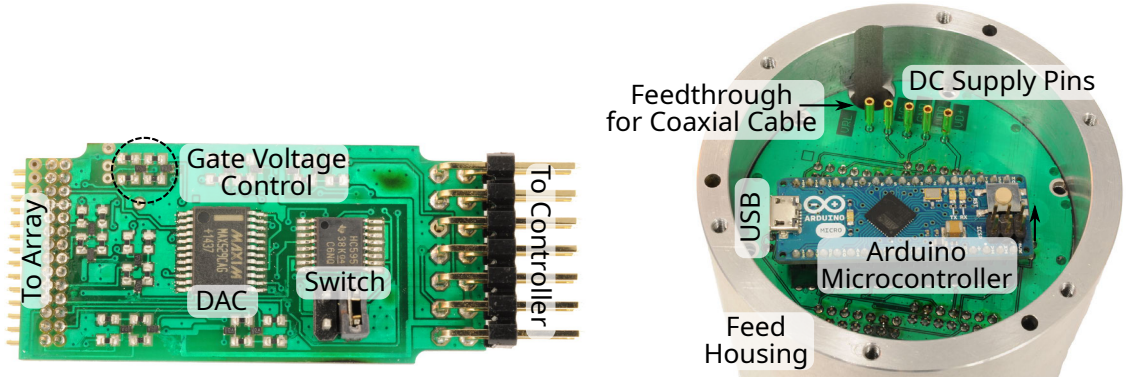

(a) (b)

Figure 4.38: (a) DC control board for the attenuators and amplifiers. (b) Mounted *Arduino Micro* used as the controller for the beam forming.

are used, up to seven elements are switched on simultaneously. Switching all others off significantly reduces power consumption and eases thermal power management. If high-speed beam scanning is required, additional elements may have to be enabled to ensure the amplifiers are ready when needed.

A compact *Arduino Micro* microcontroller suffices to digitally control the DACs and shift registers. It is connected to a host computer by a USB interface, providing the required electrical power. This simple setup allows controlling the complete beam-scanning of the design. Fig. 4.38b shows the mounted controller on the backside of the feed alongside the pins for the amplifier bias. All feed components are integrated within a solid aluminum

housing. Drilled holes inside the housing allow inserting heat pipes to transfer excess heat to a heat spreader and fans on the backside of the feed.

The assembled feed without the housing is shown in Fig. 4.39. On the bottom, the PCB with the microcontroller is connected to seven DC control boards. The interposer with the spring-loaded pins is mounted on top of the control boards. At the very top, the 49-element array is visible. The holes in the array PCB are required to insert alignment pins and screws to fix the board to the housing around the interposer (cf. Fig. 4.37a).

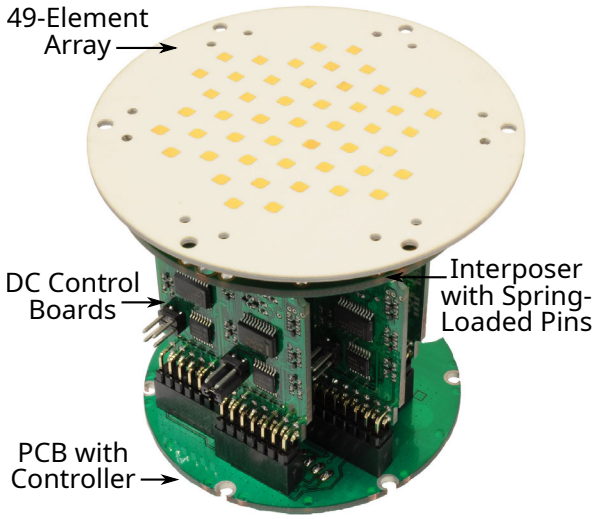

Figure 4.39: Complete setup of the feed network, including the active array and control circuitry without the feed housing.

4.6 System Performance

The AFR consists of the two main functional components, the reflector (Section 4.3) and the array feed (Section 4.4). In addition, the overall design also includes a mechanical fixture to join both components. The fixture must be sufficiently stable and ensure precise alignment between the feed and reflector. This complete setup is shown in Fig. 4.40.

The reflector is precision machined from solid aluminum. For the mechanical feed fixture, aluminum struts are used. Mechanical simulation using *Autocad Inventor* indicates that a single 10 mm cylindrical strut can significantly deform if a heavy feed is attached. A weight of 1 kg can displace the feed up to 1 mm, which results in a deviating beam direction and deteriorating beam properties. Hence, three equally spaced rectangular aluminum struts are attached to the reflector rim and connected to the backside of the feed. Simulations indicate that the expected maximal displacement of the setup is negligible.

The struts are attached to the backside of the reflector. This arrangement allows a simple distance adjustment between the feed and reflector. In Fig. 4.40, the feed housing is transparent to visualize the electronics inside. Additionally, three fans are attached to the back for cooling.

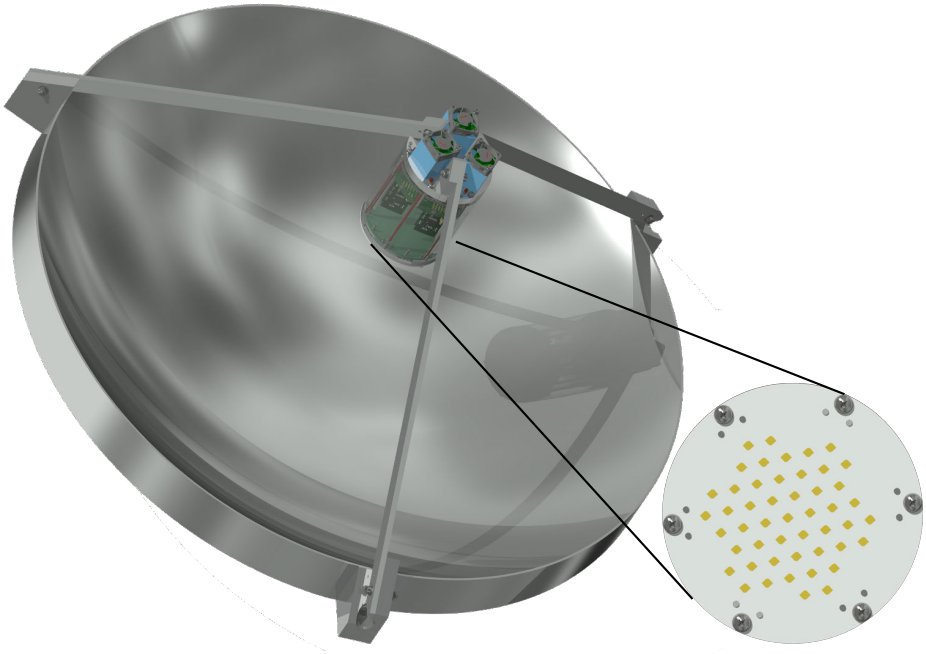

Figure 4.40: Illustration of the designed electronically scanned reflector antenna. The 49-element array feed is attached to the spherical reflector by three struts. Reflector with feed attached

4.6.1 Blockage

The feed and struts of a prime focus reflector always cover part of the aperture. Rays emanating from the feed are absorbed or reflected/scattered in an unwanted direction. The effect is twofold: the gain is reduced, and sidelobes are increased. Both effects are frequently subsumed as blockage. The influence of blockage is analyzed using a simulation model that includes blockage effects due to feed and strut. The results are depicted in Fig. 4.41, for an ideal (unblocked) antenna (——), a reflector with a feed only (·····), and a reflector with struts only (- - -).

The feed blockage mainly increases sidelobes close to the main beam. Due to the circular shape of the feed, they are concentric around the center. On the other hand, strut blockage has a more significant influence for higher θ-angles, where the sidelobes significantly increase. A 2D pattern analysis indicates that the sidelobes are highest at the ϕ-angles aligned with the struts. Since blockage is unavoidable, a minimal feed and struts size are desirable. If a more extensive scanning range is required, the feed diameter must also be increased, which deteriorates the overall performance.

4.6.2 Measurement Setup

The university's antenna test facility is used to evaluate the reflector system's far-field characteristics and scanning capability. As shown in Fig. 4.42a, the AFR is mounted to a roll-azimuth positioner in an anechoic chamber. The spherical near-field measurements are conducted on a 0.4° grid to collect enough data for a near-field-to-far-field transformation. Measurements at 0 and 90° probe antenna polarization allow calculating the reflector's

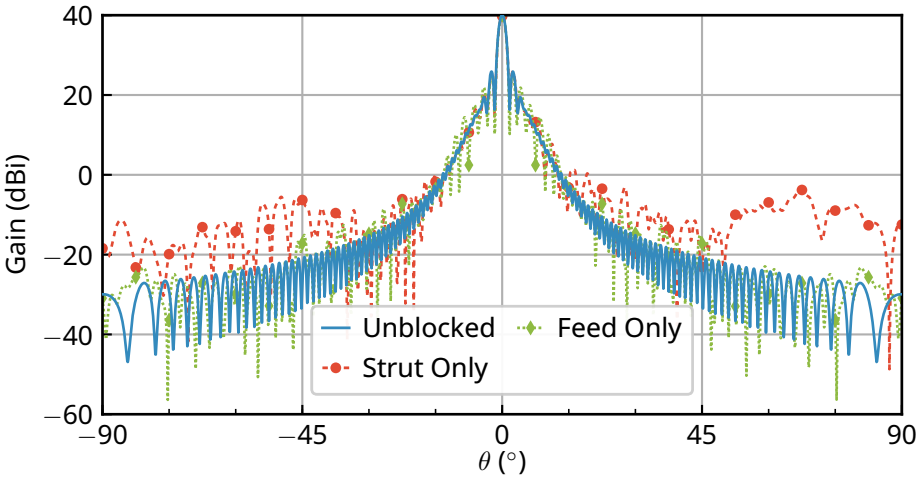

Figure 4.41: Influence of blockage on the antenna pattern.

circular polarization properties. In the final post-processing step, the measured data is time-gated to reduce parasitic reflections from the chamber, and the far field is calculated. Currently, absolute gain measurements cannot be carried out. The measured data is hence normalized to the simulated one.

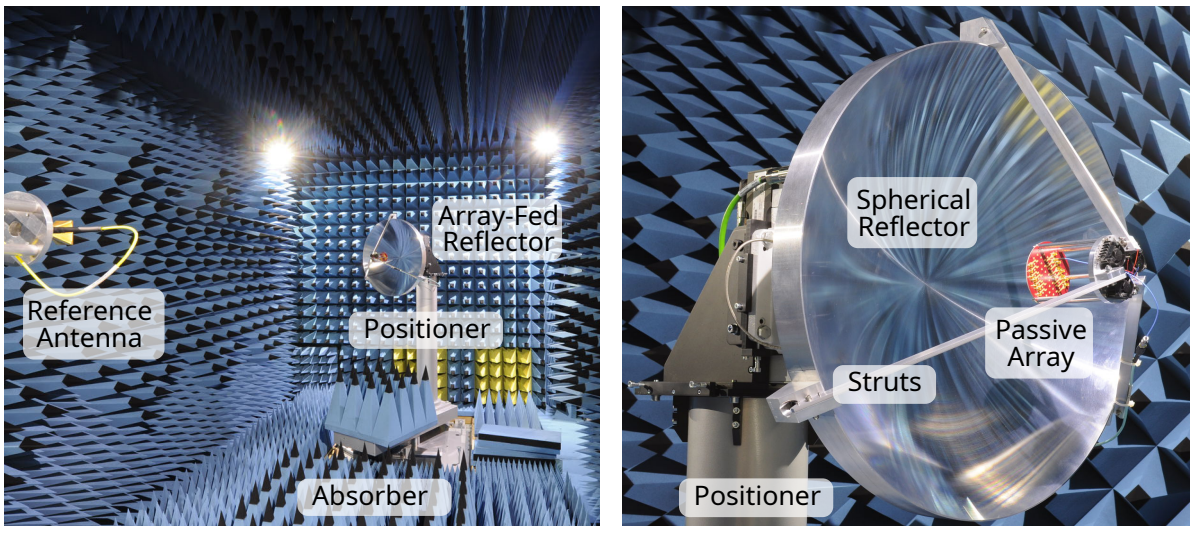

(a) (b)

Figure 4.42: (a) AFR in antenna test facility. (b) Assembled passive AFR on positioner.

4.6.3 Central Beam

Three scenarios are investigated. First, the setup is simulated in *GRASP* using a full-wave simulated feed model and including blockage effects from the feed and struts. Next, a passive array is measured, where all array elements are accessible through coaxial connectors [cf. Fig. 4.42b]. Finally, the active array

is investigated, where the array element is selected through the attenuator and amplifier voltage. For a good comparison, the central element is excited, which generates a beam along the reflector's main axis. A one-element-per-beam excitation is used for all measurements and simulations. The obtained θ-cuts are depicted for an angular range of $\theta = \pm 10°$ in [Fig. 4.43a] and $\theta = \pm 30°$ [Fig. 4.43b]. The θ-direction of the active array is compensated by 0.4° since the array center is slightly displaced by 1.5 mm on the feed fixture.

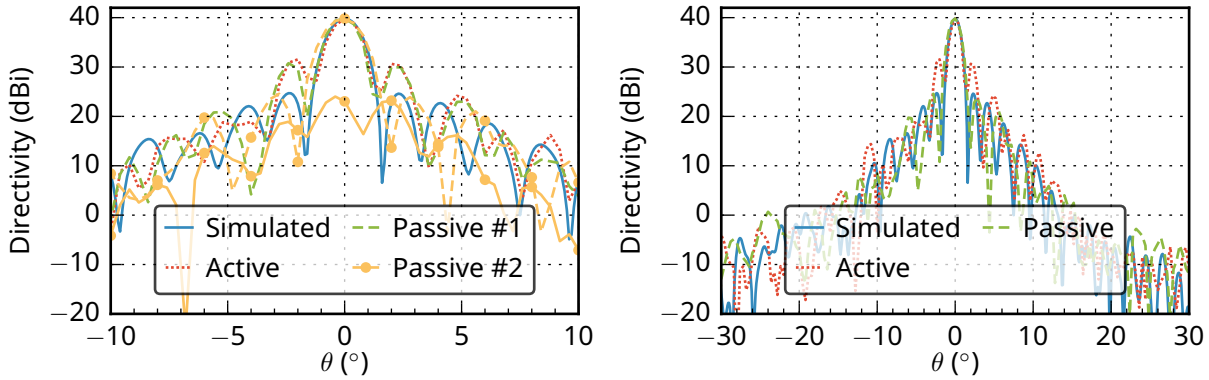

Figure 4.43: Simulated and measured far-field θ-cuts close to the main beam at $\phi = 0°$, when the central element is excited for an angular range of (a) $\theta = \pm 10°$ and (b) $\theta = \pm 30°$ to the main beam. —•— shows the cross-polarization.

The results in [Fig. 4.43a] show a good agreement between all plotted patterns with respect to beamwidth and directivity, but significant deviations in the level of the first side lobe. Passive (#1) and active array measurements, however, behave very similar for all angles, which validates the proposed beamforming approach. A closer investigation of the possible causes for the higher side lobe level [SLL] revealed that the focal length was inaccurately set in the mechanical setup. An adjustment in the passive setup (#2) yields much improved results. The remaining differences can be attributed to the inaccurate feed model and blockage effects such as multiple reflections that were not taken into account [133]. [Fig. 4.43a] also shows the cross-polarization, which is almost 20 dB below the co-polarization in the main beam.

The agreement between simulation and measurements is also good for higher $\theta-$angles [see Fig. 4.43b]. From the active measurements[, it] can be clearly seen that the focal length must be correctly set for optimal results. The measured far-field contour of the passive [and active] array using the adjusted focal length is plotted in [Fig. 4.44a and Fig. 4.44b, respectively]. [98]

4.6.4 Scanned Beam

To demonstrate the beam scanning, an off-center element (element 4 in group 3 from [Fig. 4.11] at the edge of the array is excited. The results for the simulated

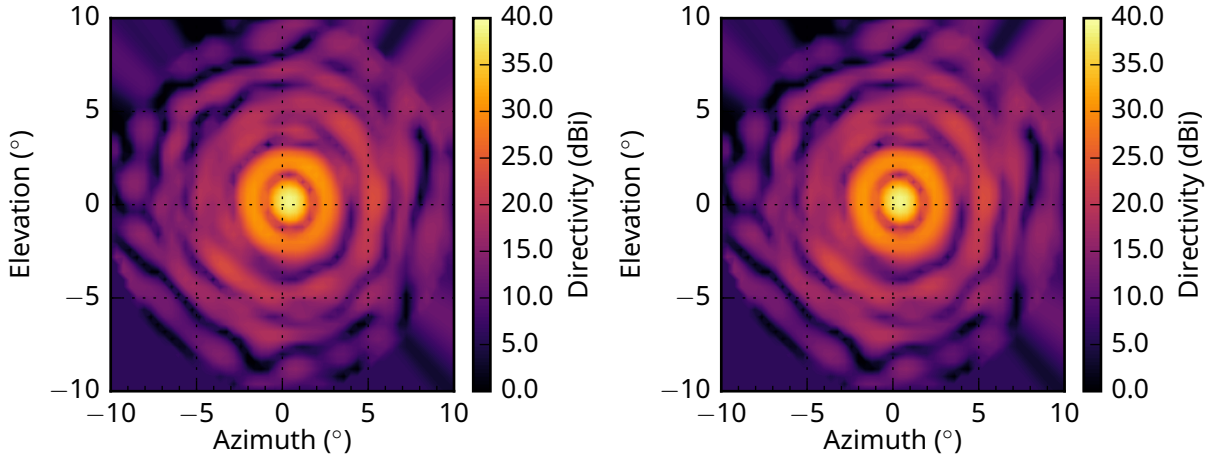

(a) (b)

Figure 4.44: Measured far field in elevation-over-azimuth coordinates if the central element is excited in (a) the passive and (b) the active array.

and adjusted passive setup are shown in [Fig. 4.45a]. The θ-direction of the measured data is again compensated by 0.4°, since the array center is displaced by 1.5 mm on the feed fixture.

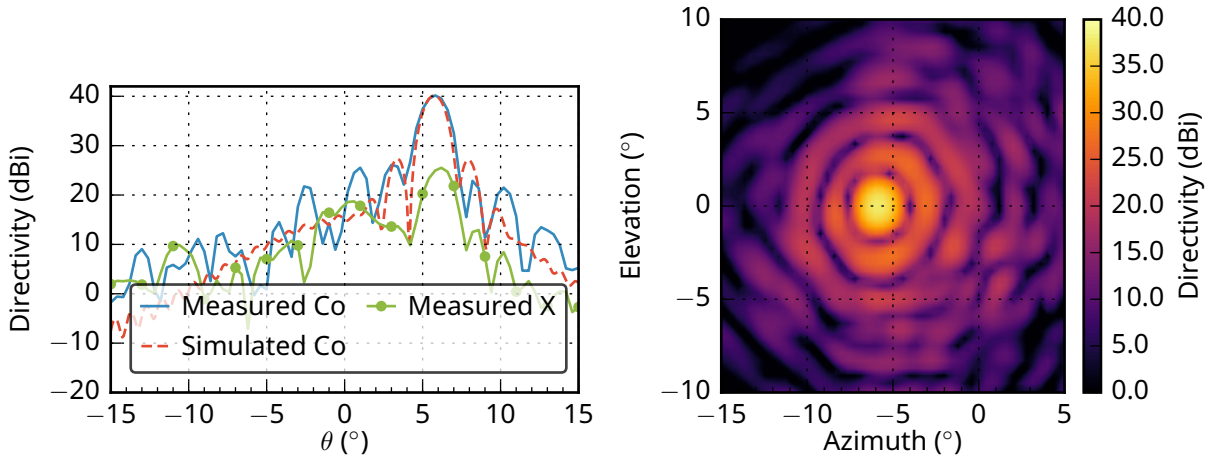

(a) (b)

Figure 4.45: (a) Simulated and measured far-field (θ-cuts at $\phi = 0°$), when an offset element is excited to obtain a scanned beam. (b) Measured far field in elevation-over-azimuth coordinates if an outer element is excited in the passive array.

The main beam pattern, scan angle, and SLL show good agreement between simulation and measurements. The measured data exhibit significantly more ripple. One reason is that the used *GRASP*-model for the scanned beam did not include any blockage effects. Cross-polarization levels are more than

> 15 dB lower in the main lobe. In comparison to the unscanned case plotted in [Fig. 4.43a], the directivity [remains] almost constant.
>
> A contour plot of the measured array is shown in [Fig. 4.45b]. It can be seen that the beam is scanned to an azimuth of -6°, which is as expected from the simulation. The calculated directivity is 38 dBi is close to the expected value of 39 dBi for a spherical reflector [...]. Beamwidth and SLL are also in the expected range and similar to the results in [Fig. 4.44a] of the central beam. [98]

The maximal EIRP in compliance with ETSI [42] allows estimating the performance of such an antenna. In the case of the scanned beam, an EIRP of up to 36 dBW is possible. Using the calculated link budget of a geostationary satellite from Section 2.4.5 and Table 2.2, an uplink data rate of about 6.4 Mbit/s can be achieved if a 30 dBm output amplifier is used.

4.7 Summary

The array-fed reflector presented in this chapter demonstrates that electronic beam scanning with a limited field of view is possible with a relatively low number of control elements. Indeed, the presented electronically scannable reflector system utilizes only 49 active elements to achieve a scanning range of $\pm 6°$, which is sufficient for many applications. Combining the setup with a simple mechanical positioning system enables a wide field of view. The implementation of such a combined electromechanical scanning system has yet to be further investigated.

The AFR uses a spherical reflector combined with a customized feed system to maintain consistent performance throughout the scanning range. An innovative distribution network approach is implemented, which enables multiple beams using a simple architecture. These extra beams allow for reduced sidelobes and compensate minima between adjacent beams.

The measurement results prove the feasibility of the approach, but some technical limitations remain. For instance, the output power of the currently used amplifiers is not optimal, and amplifiers with an output power of 1 W or more are necessary to boost uplink performance. These would require more sophisticated thermal management, which is challenging to implement using the proposed planar patch array.

Switching from tile to brick architecture (cf. Section 2.3.4) would yield more design freedoms to facilitate the extra components. A brick design is possible without reduced performance since a larger size is not an issue for a reflector design as long as the blockage is not increased. A brick design also helps to implement a dual-band integrated Rx/Tx frontend. Indeed, many of the required components have already been designed using SIW-technology [73], [75], [134]–[137]. Instead of SIW, the usage of 3D-printed components could also reduce loss and increase system performance (cf. Section 3.2.2).

Chapter 5

Heterodyne Frequency-Controlled Phased Array

Electronically scannable arrays rely on the means of phase and amplitude control of the elements to point the antenna beam in a desired direction. Realizing these controls is one of the most challenging tasks in the array design process. The available surface area is scarce, whereas the components and circuitry are relatively complex, bulky, and potentially expensive. In the case of phased arrays, vector modulators or phase shifters are used as control elements. To minimize cost and size, they are available as an IC or "core chip" (cf. Section 3.1.2). Low-cost, mass-market semiconductor processes such as standard CMOS or higher-performance GaAs are used depending on the frequency band and performance requirements. In many frequency bands, core chips or phase shifters are not commercially available but require a custom design, which is only feasible for large markets or very high-priced systems.

To protect the fragile semiconductor die and improve the handling, ICs are commonly packaged. A typical commercial package is an 8x8 QFN measuring 5x5 mm^2 and, thus, it complies with the wavelength constraints in 30 GHz antenna arrays. In addition, circuitry for biasing, analog or digital control, and the RF input and output transmission lines are required. Hence, such a packaged IC is too large for tile architectures at frequencies beyond 30 GHz. To use such a large chip, a brick architecture could be used or active circuitry for multiple channels incorporated into a single package. Nevertheless, the packaging density and the circuit complexity remain very high.

Alternative approaches without the need for core chips or phase shifters could enable novel or extensively improved solutions for applications where electronic beamforming is desirable, but the required components are not available, too expensive, or too challenging to integrate. In this chapter, a heterodyne technique is introduced. It does not require active phase shifters and allows for effortless beam-pointing control.

5.1 Frequency-Controlled Scanning

A straightforward and efficient way to scan an antenna beam is so-called frequency scanning, as shown in Fig. 5.1. A mixer minimizes the tuning requirements in the data source frequency (which commonly operates at a predefined constant frequency). A serial feed architecture realizes the actual frequency scanning with a constant transmission delay τ between adjacent elements. τ is chosen such that the phase difference $\Delta\phi = \omega\tau$

between elements is a multiple of 2π at the center frequency f_0. For this case (and frequency multiples), the beam is directed in boresight direction ($\theta_0 = 0\,\mathrm{deg}$).

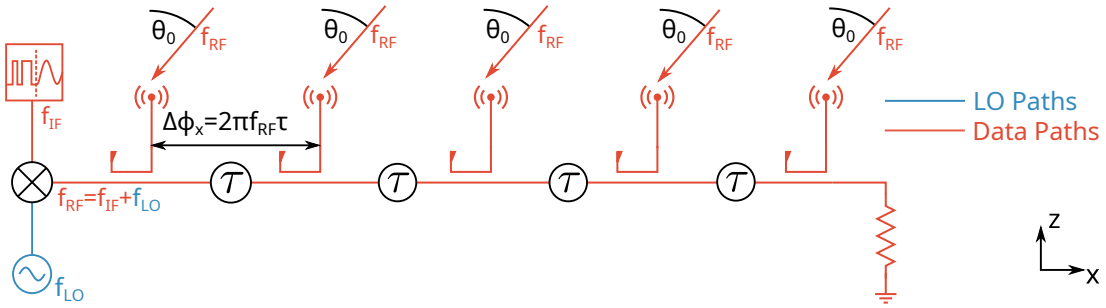

Figure 5.1: Serial array topology for frequency scanning.

If the operating frequency f_{Rx} is tuned away from f_0, $\Delta\phi$ and the beam direction θ_0 change. Increasing and decreasing the frequency allows for scanning in both directions. The frequency sensitivity of the beam direction is proportional to τ. A high sensitivity decreases the necessary frequency band for a full scan but requires longer delays which, in turn, result in larger and lossier electrical circuits. Since the data signal is serially fed to the antennas, losses are critical, and amplification might be needed to compensate for losses through the delay lines and coupler.

Although this approach is simple and effective, the direct relationship between operating frequency f_{Rx} and beam direction is a major drawback. In most wireless scenarios, strict frequency limits are imposed through regulation, network design, and current usage by other services or users. Indeed, frequency is a highly scarce resource, and efficient use is of paramount importance. Hence, the beam direction must be independent of the carrier frequency in a wireless communication system, which is impossible using classical frequency scanning. Furthermore, changing the frequency f_{Rx} allows only beam scanning in one dimension. There is no means to independently scan the beam of a planar array in two dimensions, with only one degree of freedom.

Fortunately, the concept of frequency scanning is extendable to enable an independent frequency-direction relationship and 2D-scanning. In the next Sections, a different concept called Heterodyne BeamForming (HBF) is introduced [138]–[142]. As the name suggests, the concept is based on mixers and frequency conversion to introduce more degrees of freedom. In principle, such a heterodyne beamforming network can be implemented up to very high frequencies since mixers based on Schottky diodes are available up to the Terahertz range.

5.1.1 Heterodyne Beam Scanning

The heterodyne scanning technique is illustrated in Fig. 5.2. Compared to Fig. 5.1, each antenna element is connected to a mixer. The LO-signal is now serially fed through the delay lines, whereas a divider-based parallel feed architecture is used for the data signal (denoted by a "+"). Losses in the delay line circuits are now less critical since the data signal is only attenuated by a single mixer instead of multiple delay lines, significantly improving the link budget.

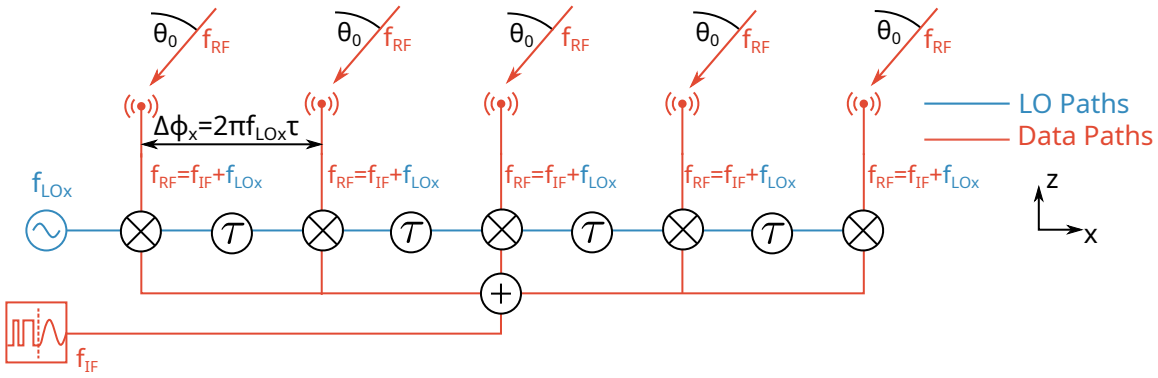

Figure 5.2: Basic HBF array architecture with a single mixer per element using a serial feed for the LO and parallel feed for IF.

Beam scanning in the xz-plane is performed by changing the frequency of the LO source (f_{LOx}, x for scanning in the xz-plane). The basic principle stays the same as in the introduced frequency scanning concept. However, the frequency at the antenna f_{Rx} can now be kept constant by adjusting f_{IF} to counteract changes in f_{LOx}.

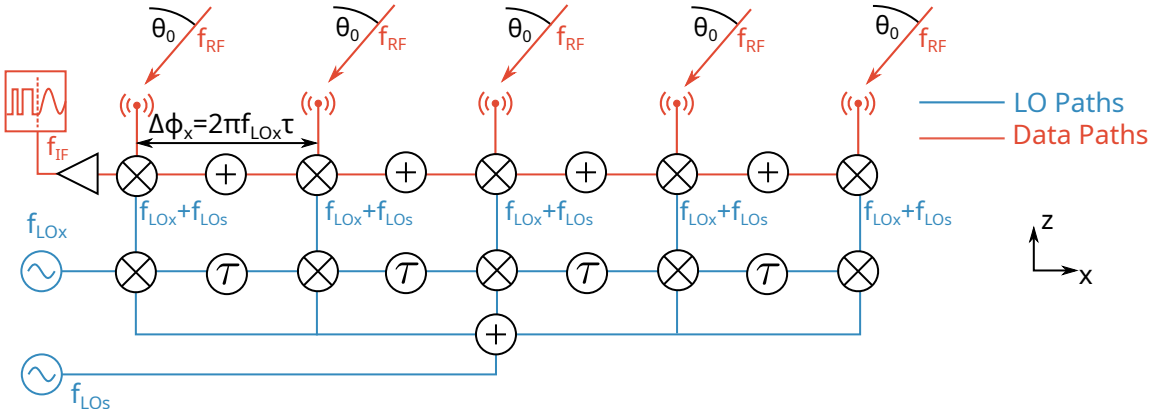

Figure 5.3: Extended HBF array architecture with two mixers per element with constant IF frequency.

Changing the IF as in [138]–[142] is, however, less than ideal since the required changes of the IF-frequency might be substantial and a wideband data source is much more challenging. The introduction of an additional LO-source (f_{LOs}, s for stabilizing) in combination with another mixer allows to keep the IF-frequency constant. It introduces a second degree of freedom to independently set f_{IF} and f_{LOx}. Path losses increase if the second mixer stage is placed in the IF. Thus, the architecture illustrated in Fig. 5.3 is proposed. One mixer is added to each antenna element. Although the component count increases, the data signal still undergoes only one mixer stage. Furthermore, this specific architecture allows greater flexibility to choose the intermediate frequencies in the LO-channels.

The proposed architecture is essentially an extension of the LO-beamforming network from Fig. 2.6b. Indeed, the signal path for the data signal is equal to classical LO-beamforming and so are the link budget implications. The modifications occur only in the LO-signal path, where the phase shifter is replaced with a second mixer driven by both LO-sources. The LO-signal at f_{LOx} is used to set the phase difference $\Delta\phi_{\mathrm{x}}$ between adjacent antenna elements by means of the delay τ:

$$\Delta\phi_{\mathrm{x}} = 2\pi f_{\mathrm{LOx}}\tau \ . \tag{5.1}$$

A serial feed architecture keeps the circuitry simple by eliminating the need for long delay lines. Since the RF frequency $f_{\mathrm{RF}} = f_{\mathrm{LO}} + f_{\mathrm{IF}}$ must remain constant, f_{LO} must not change during beam scanning. This can be achieved by adjusting f_{LOs} when f_{LOx} is changed for scanning such that $f_{\mathrm{LOs}} = f_{\mathrm{LO}} - f_{\mathrm{LOx}}$.

This relatively simple approach does not require any active control circuitry on the array and no additional components apart from the mixers. The scanning is entirely controlled by changing the frequency of the (external) LO-sources. The only requirement is a phase-lock of the LO-signals, realized by a common reference clock.

5.1.2 Mixers for Phase Shifting

The fundamental component of the heterodyne beamformer is the mixer. A phase shift in one of the mixer's input signals must be preserved and propagated to the output for the heterodyne principle to work. It is well understood that a mixer operates linearly for small signals in the presence of a large signal. However, two general signals (at least one large signal) and their relationship must be considered here.

For a brief analysis, two harmonic signals $v1(t) = V_1\cos(\omega_1 t+\phi_1)$ and $v2(t) = V_2\cos(\omega_2 t+\phi_2)$ are considered. Superimposing and applying them to a nonlinear device (e.g., a mixer) yields mixing products at $n\cdot f_1 + m\cdot f_2$, where n and m are integers.

A mixer can be described through its nonlinear current-voltage relationship. For the analysis, this relationship is expanded into a Taylor series:

$$i(v) = a_1 v + a_2 v^2 + a_3 v^3 + \ldots \text{, where } a_i \in \mathbb{R}. \tag{5.2}$$

First-order terms $i_1(v) = a_1 v$ are not of interest and can be filtered along all higher-order harmonics. Investigation of the second order terms $i_2(v) = a_2 v^2$ yields:

$$i_2(v1+v2) = a_2(V_1\cos(\omega_1 t+\phi_1) + V_2\cos(\omega_2 t+\phi_2))^2 \tag{5.3}$$

$$\begin{aligned} &= a_2(V_1^2\cos^2(\omega_1 t+\phi_1) + V_2^2\cos^2(\omega_2 t+\phi_2) \\ &\quad + V_1V_2\cos(\omega_1 t+\phi_1)\cos(\omega_1 t+\phi_1)) \ . \end{aligned} \tag{5.4}$$

Using trigonometric identities Eq. (5.4) can be simplified:

$$\begin{aligned} i_2(v1+v2) = a_2\Bigg(&\frac{V_1^2}{2}(1+\cos(2\omega_1 t+2\phi_1)) + \frac{V_2^2}{2}(1+\cos(2\omega_2 t+2\phi_2)) \\ &+ V_1V_2\cos((\omega_1+\omega_2)t + (\phi_1+\phi_2)) \\ &+ V_1V_2\cos((\omega_1-\omega_2)t + (\phi_1-\phi_2))\Bigg) \ . \end{aligned} \tag{5.5}$$

If the harmonics from Eq. (5.5) are filtered, only the sum and difference frequencies remain. Furthermore, the original phase from each of the input signals is preserved. Phases are added in the case of the sum signal and subtracted for the difference signals. This relationship holds even for two large signals. As a result, an ideal mixer with a maximal rejection of higher-order harmonics is the perfect building block for the heterodyne beamformer.

5.2 Array Design

The design of an HBF array requires careful planning. Frequencies for the local oscillator need to be specified, a technology for the array chosen, and the essential components must be designed. Some of the designs used for the HBF array are based on results from [143].

Here, a linear array with N elements is designed as depicted in Fig. 5.3. The beamformer requires at least $2N$ mixers, N couplers for the LOx signal, $N-1$ delay networks, and two power combiners with N ports (one for each LO and IF). K_a-band Rx satellite communication is chosen as the reference scenario, with a center RF frequency of 20 GHz and 500 MHz of bandwidth. The IF is centered at 1 GHz to provide sufficient bandwidth and reasonable component cost and performance.

A $\lambda_0/2$-element spacing avoids visible grating lobes when scanning the beam. In consequence, the high component count strongly limits the available space. A custom RFIC design could significantly reduce these limitations but is neither feasible nor instrumental to demonstrate the HBF principle. As a low-cost alternative, a brick architecture (cf. Section 2.3) offers enough flexibility to house high component counts.

The realization of a linear array using PCB technology in a brick architecture at 30 GHz is proposed in [70], [144] using SIW. This approach is adopted here since it provides exceptional flexibility to incorporate components and dual-polarization capability. At 20 GHz, the required thickness of the PCB for dual-polarized SIW horn antennas is critical and very close to the maximum typically available in commercial processes.

A linear array size with eight elements is chosen to demonstrate the beamforming and scanning principle. The top side of the designed 8-element array module is illustrated in Fig. 5.4. The interconnects for the LO and IF signals are visible at the top of the image. Below are the distribution networks for IF and LO_S. The center part of the module contains the frontend, including the HBF beamformer and all its required components. At the bottom of the image are the dual-polarized SIW antennas. The underside of the module contains a mirror image of the top. These extra eight channels are required for the second polarization and are independently controllable. The component and frontend design is further explained in Section 5.3 and Section 5.4, respectively.

The module is based on the PCB multilayer stack shown in Fig. A.1 using Rogers 4000 as substrate material. The total thickness of the PCB is about 4.8 mm, and it incorporates 16 metal layers, primarily included for the SIW. Layer 8 contains the quasi-symmetry plane and separates the topside and the underside. The outer layers are used for signal routing and contain microstrip and CPW transmission lines. An additional signal layer is available (top: Layer 3, bottom: Layer 14) for stripline circuits used for LO_S signal. DC bias lines are also routed on this layer. Top layer metal surfaces are coated with Immersion Silver/Immersion Gold (ISIG) for low losses and relatively high robustness.

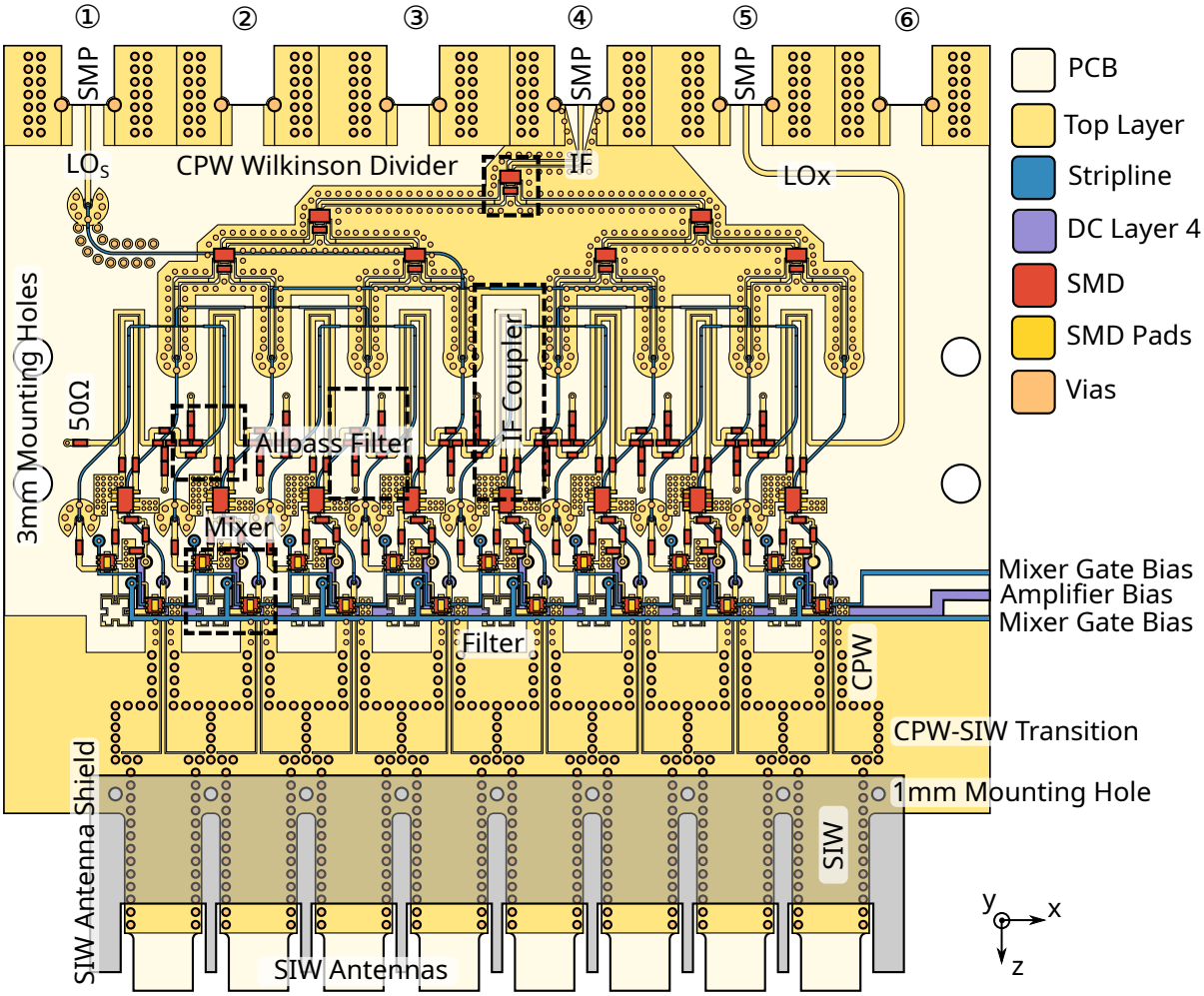

Figure 5.4: Dual-polarized 8-element array module for heterodyne beamforming using an SIW antenna concept.

Another critical design criterion is the operating frequency of the LO_x tuning network containing the delay elements. To ensure maximum design flexibility, the progressive phase shift $\Delta\phi$ between elements must be adjustable from $-180°$ to $+180°$. An untilted beam requires a progressive phase shift of integer multiples M of 2π between elements to ensure constructive interference. Consequently, the necessary delay between elements τ_x can be expressed as a function of the center frequency of LO_x using Eq. (5.1): $\tau_x = M/f_{LOx,0}$.

Increasing M results in a higher phase slope and hence a lower required tuning bandwidth for the LO to achieve the same phase change. At $M = 1$, the required bandwidth BW for a $\pm 180°$ phase change is $BW = f_{LOx,0}$, which decreases linearly to, e.g., $BW = f_{LOx,0}/4$ for $M = 4$. On the downside, circuit complexity, size, and losses increase similarly, so $M = 2$ is a good compromise for the desired application.

f_{LOx} should be lower than f_{RF} to minimize losses and reduce the mixer operating frequency. Since the space for the delay networks is limited, the frequency f_{LOx} is set significantly lower to allow for lumped network elements. The center frequency is at

2 GHz, resulting in a tuning band from 1.5 GHz– 2.5 GHz. Table 5.1 in Section 5.7.2 provides an overview of all used frequency ranges.

5.3 Components

Several components and circuits must be designed to construct an array based on the specifications from Section 5.2. This section introduces the major components involved and their performance.

5.3.1 Passive Delay Networks

The delay lines are one of the fundamental building blocks for the heterodyne beamformer since the frequency-dependent phase characteristic is exploited to scan the beam. The realization of delay lines depends on the frequency, the available technology, and space. Here, the primary goal is to obtain passive and compact delay elements for integration on a PCB at the chosen center frequency of 2 GHz.

The simplest form of a delay element is a simple transmission line. A higher permittivity yields a shorter line but requires specific materials. Furthermore, a transmission line can be meandered, although parasitic effects such as cross-coupling or reflections in the turns limit this approach. For decades, such slow wave structures have been researched to obtain compact designs or to match beam velocity in vacuum electronics [145], [146].

Compared to the array spacing, the resulting wavelengths at the operating frequencies of the delay network are long. A distributed transmission line-based delay network is hence not feasible in standard PCB technology. As an alternative, lumped elements are usable for the chosen frequency band. In general, a lossless delay line can be considered as a type of all-pass circuit. It features a constant group delay and a constant gain transfer function for all frequencies:

$$H(j\omega) = |A|\mathrm{e}^{-j\varphi(\omega)} = \mathrm{e}^{-\tau\omega}. \tag{5.6}$$

This exponential characteristic cannot be realized by an RLC-network but can be approximated [147, pp. 267–268]. Since the LO signals are Continuous Wave (CW), dispersion is not an issue, and components do not have to exhibit a constant group delay. Thus, so-called Zobel-networks[1] can be used. In a Zobel-network, the input and output impedances are independent of the transfer function, allowing for an easy cascade of multiple such sections (so-called constant-impedance lattices).

The most widely used implementation of a Zobel network is a bridged-T as shown in Fig. 5.5a. The bridged-T network is symmetrical if input and output impedance are equal and purely reactive in the case of an all-pass filter, as shown in the figure. A design procedure is presented in [147, pp. 263–265].

A microstrip implementation of two cascaded bridged-T all-pass sections is illustrated in Fig. 5.5b. Each section exhibits a 180° phase shift between the two designed corner frequencies, here set to 1.5 GHz and 2.5 GHz. Hence, two sections have to be used to achieve full 360°.

[1] Zobel-networks are named after Otto Zobel, who published a fundamental paper on filter theory in 1923 [148]

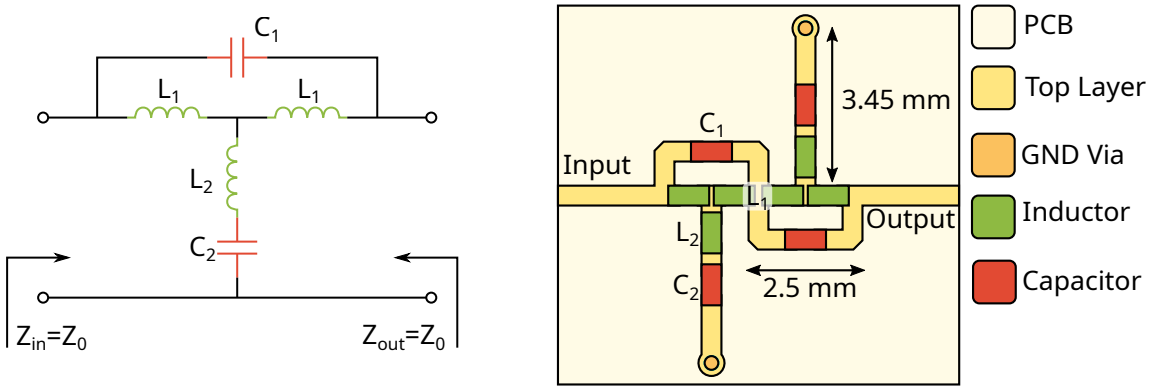

(a) (b)

Figure 5.5: (a) Schematic of a second order Bridged-T all-pass filter with matched in- and output ports and (b) illustration of a 2-element filter using lumped Surface Mounted Device (SMD)-elements in microstrip technology.

The fabricated filter is shown in Fig. 5.6a and manifests outer dimensions of 7 mm x 5 mm, only about 1/30 of the wavelength at 2 GHz. Table A.1 lists all used components.

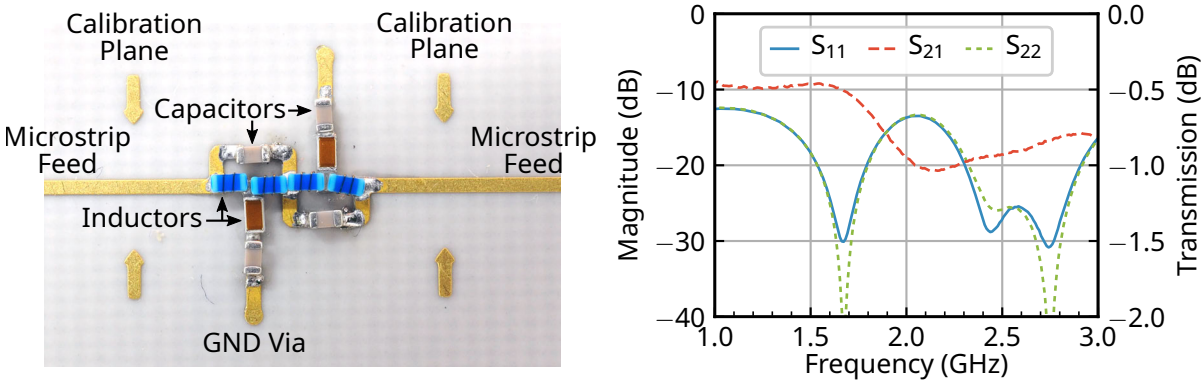

(a) (b)

Figure 5.6: (a) Fabricated all-pass filter consisting of two second-order bridged-T networks and (b) measured S-Parameters of the the allpass filter.

The filter relies on lumped SMD capacitors and inductors. Particularly the inductors must be chosen carefully to minimize parasitic effects at 2 GHz. Still, the filter's performance is impaired by intrinsic losses and element tolerances. The measured S-Parameters are depicted in Fig. 5.6b. The input and output matching is almost symmetrical and better than 12 dB. However, a significant resonance occurs in the center, increasing the insertion loss from 0.5 dB to about 1 dB.

The measured transmission phase $\varphi(S_{21})$ is plotted in Fig. 5.7a. The total phase change between 1.5 and 2.5 GHz is close to 360°. The filter works as expected, successfully verifying the design.

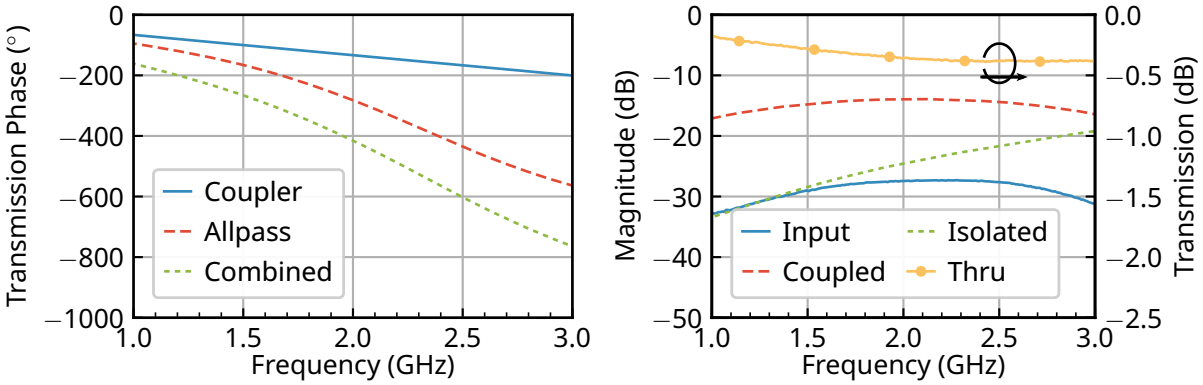

(a) (b)

Figure 5.7: (a) Measured phase delay of the all-pass filter, coupler, and the sum of both components. (b) Measured S-parameter of the meandered microstrip coupler.

5.3.2 Coupler

For the serial LO feed network, couplers allow diverting only a fraction of the total signal power. The design is based on a simple backward-wave microstrip coupler, requiring two closely spaced quarter-wave sections. It is illustrated in Fig. 5.8a. The coupler is folded to fit the quarter-wave sections in the tight array spacing.

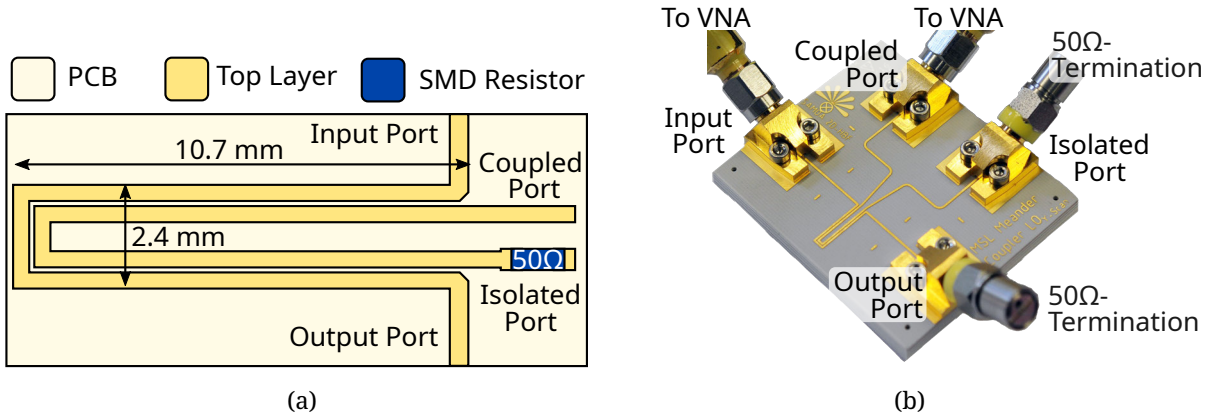

(a) (b)

Figure 5.8: (a) Illustrated and (b) realized LO-coupler for the serial feed.

The PCB process limits the line spacing to a minimum of 100 µm. Nevertheless, this meander line design amounts to a total width of only 2.4 mm. The fabricated coupler is shown in Fig. 5.8b. Several two-port S-parameter measurements are combined to assess the performance. TRL-calibration and 50 Ω terminations at unused ports ensure reliable results. The measured S-parameters are plotted in Fig. 5.7a and Fig. 5.7b, for phase and magnitude, respectively.

The coupling varies between -14 and -13 dB in the operating band. The insertion loss is lower than 0.5 dB, and input matching is better than 20 dB. Isolation is unimportant since the isolated port is unused and can be terminated in the design. As plotted in Fig. 5.7a, the

coupler thru signal exhibits a phase change of about 90° in the operating band (observed at the reference planes). As shown in the figure, this can be added to the result from the all-pass filter to get the total combined phase shift of the delay network.

5.3.3 Bandpass Filter

The proposed heterodyne beamformer uses a two-stage mixer design. In the first mixer stage, two large signals (LO_x, LO_s) are superimposed, potentially generating many unwanted spurious mixing signals (cf. Fig. 5.3). These, in turn, could cause unwanted signal content at the RF due to the second mixing stage.

Since the sum frequency $f_{LOx} + f_{LOs}$ is constant (at 19.0 GHz), a band-pass filter suppresses unwanted signals. The relatively high frequency enables a microstrip filter design. A very compact, second-order design is the meander loop [90]. This type of filter uses a dual-mode ring resonator to obtain a second-order elliptic filter response. The fabricated filter with an edge length of only 2.5 mm is shown in Fig. 5.9a.

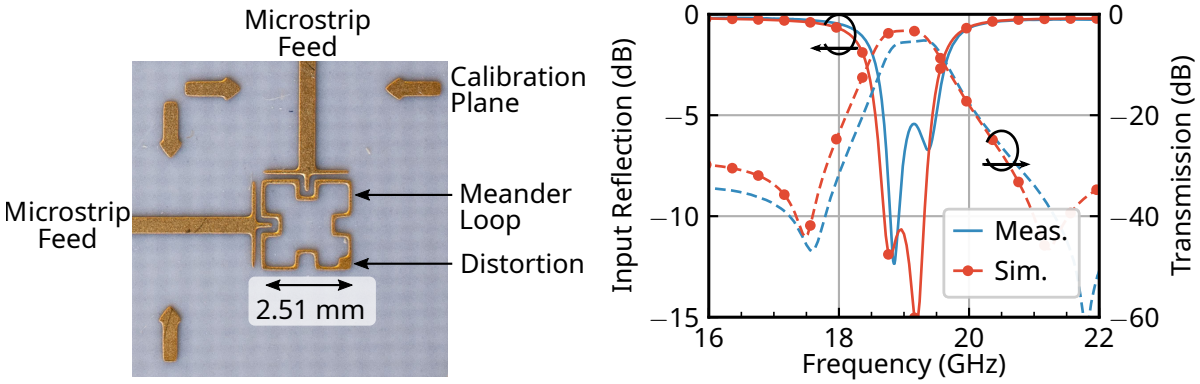

Figure 5.9: (a) Fabricated meander loop band-pass filter and (b) simulated and measured magnitude of the input reflection (S_{11}, ——) and transmission (S_{21}, - - -).

The simulated and measured S-parameters are plotted in Fig. 5.9b. The dual-mode characteristics can be seen in the input reflection coefficient, whereas the elliptic filter response with its distinct nulls is observable in the transmission. In general, simulation and measurements are in good agreement. However, the measured filter response is slightly shifted to higher frequencies, and the input reflection is higher. One cause is the significant underetching from the fabrication, which is also visible in Fig. 5.9a.

5.3.4 Vertical Transition

To implement the heterodyne beamformer, three signal distribution networks (IF, LO_x, and LO_s) have to be routed to the two mixers. Unfortunately, these networks require much space and also need some crossings. Hence, not all signal paths can be routed on outer layers, and, as mentioned in Section 5.2, some networks have to be designed on an inner layer as a stripline. Since connectors and SMD components have to be placed on outer layers, vertical signal transitions are required. These are particularly problematic at

higher frequencies. The designed vertical transition is depicted in Fig. 5.10 and Fig. 5.11a from a cross-sectional and top view, respectively.

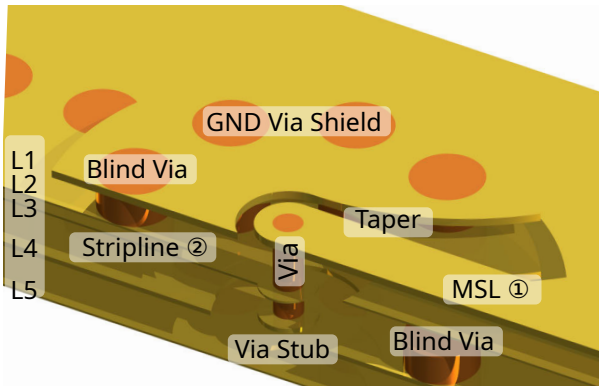

Figure 5.10: Cross-sectional view of a vertical transition from microstrip to stripline.

The microstrip line on the outer (Top) layer leads to a via, which connects the microstrip to the stripline. The via diameter is set to the process minimum of 200 µm to minimize the parasitic inductance. Antipads are present in each GND-layer. Due to the stack (cf. Fig. A.1), the via cannot terminate on the stripline layer but continues to the next GND layer, where a pad and antipad are placed around it. This parasitic via-stub significantly hampers higher frequency performance. GND-vias are placed around the stripline and the via to minimize the excitation of parallel plate modes. Since the via transition works better for CPW than microstrip, a short taper at the via functions as microstrip-CPW transition.

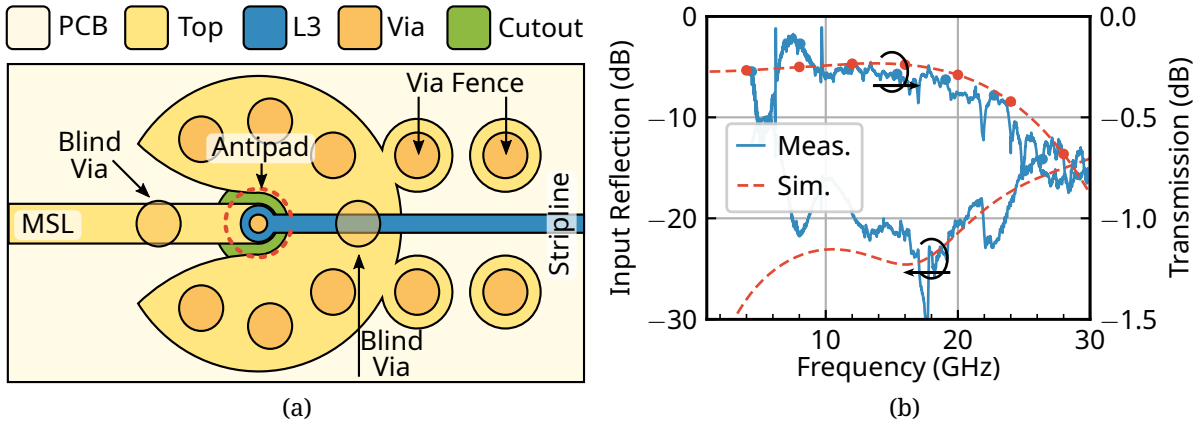

Figure 5.11: (a) Illustrated top and (b) de-embedded measurement results of the vertical transition.

The simulated and measured results are depicted in Fig. 5.11b. Data below 10 GHz is omitted since the higher frequencies are the limitation for this transition. The simulated input reflection is lower than -20 dB up to 20 GHz. Simultaneously, the insertion loss remains below 0.5 dB. The degradation at higher frequencies is mainly caused by the unwanted via stub, which increases the mismatch and leaks energy into lower layers.

The measured results are obtained by de-embedding measurement data from three stripline shorts of varying lengths. Calibration standards similar to those in Fig. A.2 are used. The spikes in the data are caused by this de-embedding technique. The advantage is, however, that no back-to-back transition measurements are necessary. The results verify the vertical transition obtained from the simulation.

5.3.5 CPW-SIW Transition

Substrate integrated waveguides are a method to implement a waveguide in a standard PCB process. The substrate fills the waveguide, while the outer metallization forms the top and bottom walls. The conductive sidewalls of the waveguide are formed by a periodic via fence [149]. For a specific frequency range, SIW can be modeled as a standard waveguide using an equivalent width [150] mainly depending on the periodic via structure.

Here, SIW is used to design a dual-polarized horn antenna. Thus, the waveguide requires square cross-sectional dimensions. In the first step, it is sufficient to consider a full-height waveguide, i.e., one where the ratio between width and height is 2:1. Such SIW can be considered electrically thick. Typically used wideband transitions from microstrip or CPW to SIW [151] do not work correctly for this configuration since a significant part of the CPW fields is concentrated close to the conductors on the substrate surface.

In [152], a via based transition from CPW to SIW is proposed. This design is illustrated in Fig. 5.12a and adapted to the 20 GHz full-height design required here. It requires a central via in the CPW, which effectively works as a current probe exciting the waveguide.

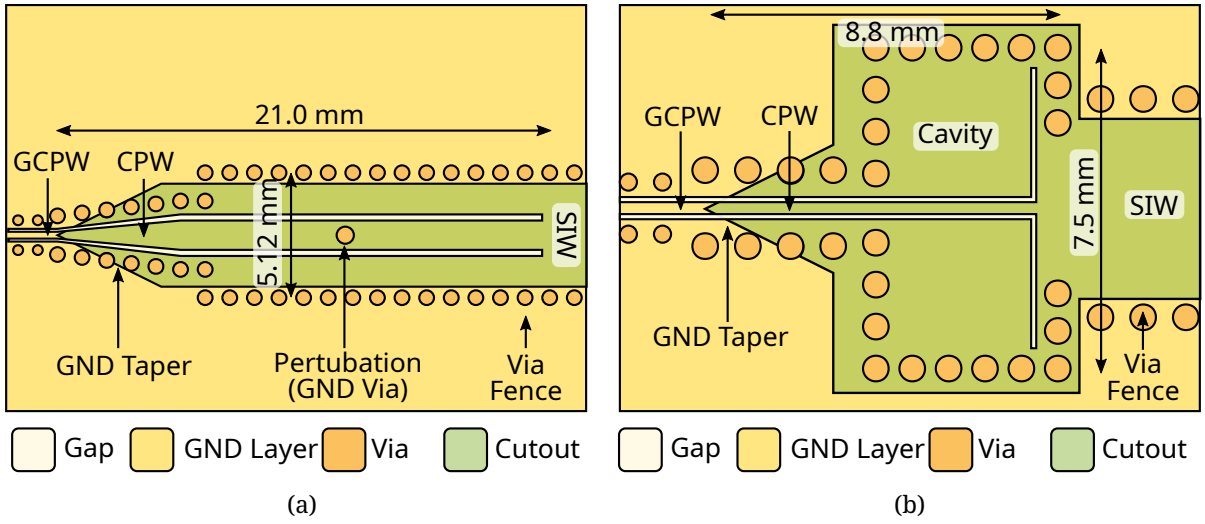

Figure 5.12: Transition from CPW to SIW using (a) a GND-via pertubation and (b) a cavity design.

Alternatively, a cavity-based transition from [153] is depicted in Fig. 5.12b. This design uses a simple SIW resonator cavity with an adjustable iris to couple into the waveguide. Since this significantly wider design requires the full width of the array grid, via fences between neighboring elements have to be shared. On the upside, the overall length is shortened from 21 mm to 8.8 mm from the via to the cavity transition.

Both designs start with a compact GCPW, which is subsequently tapered to CPW. For the via-transition, the inner CPW conductor has to be wider to incorporate the via. Hence a second taper to widen the CPW must be included.

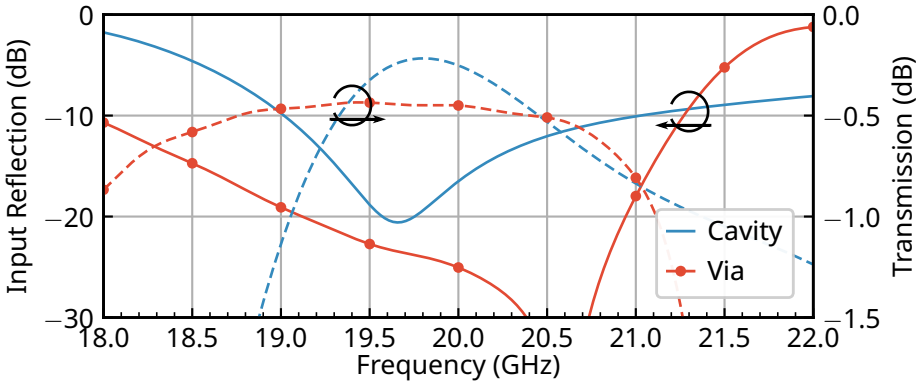

Figure 5.13: Simulated S-Parameters for the two designed transitions from CPW to SIW.

Simulation results for both CPW-SIW-transitions are plotted in Fig. 5.13. In general, the via transition is better matched and offers a broader 10 dB-bandwidth reaching from 18.0 to 21.3 GHz compared to 19 to 21 GHz for the cavity transition. In the operating band around 20 GHz both work well, but the cavity design's insertion loss is significantly lower. The higher losses can be attributed to the much longer transmission line in the via-case.

5.3.6 Circular Polarized SIW Antenna

The central building block of every array are the antenna elements. Here, SIW antennas are used, since they are well suited for a brick architecture and can be fabricated in a PCB process. The design is based on the 30 GHz array design from [69], [70].

The antenna is illustrated in Fig. 5.14. The cross-section shown in Fig. 5.14a represents a cut along the symmetry plane of the multilayer on Layer 8 (cf. Fig. A.1). Above and below are two full-height substrate-integrated waveguides separated by a metal plane on the layer. These SIWs form the two polarization ports of the antenna. In the central part, a stepped transition (septum) removes the metal plane and forms a square-SIW capable of supporting two polarization [154]. If properly designed, the two input SIW ports are well decoupled, generating 90° phase shifted TE_{01}- and TE_{10}-modes, respectively, in the square section for circular polarization.

The square SIW is not fully symmetric for both TE-modes since the used dielectric is often anisotropic, and the waveguide wall is a solid metal shield for two sides and a periodic via fence on the others. The asymmetry results in slightly different propagation constants of the two modes. The square section behind the polarizer is kept short to maintain good circular polarization. It ends in a square dielectric slab. As shown in Fig. 5.14b, a metallic choke is placed around the structure to improve matching and minimize backward radiation (and subsequently coupling in an array setup) [155, 185ff]. The choke is an externally mounted component. Fig. 5.15a shows the fabricated antenna.

The antenna consists of an RF connector, followed by a short CPW section. The via based CPW-SIW-transition is included in the design. The externally mounted, centrally split choke can be seen on the right side of the image. It is aligned with precision pins and

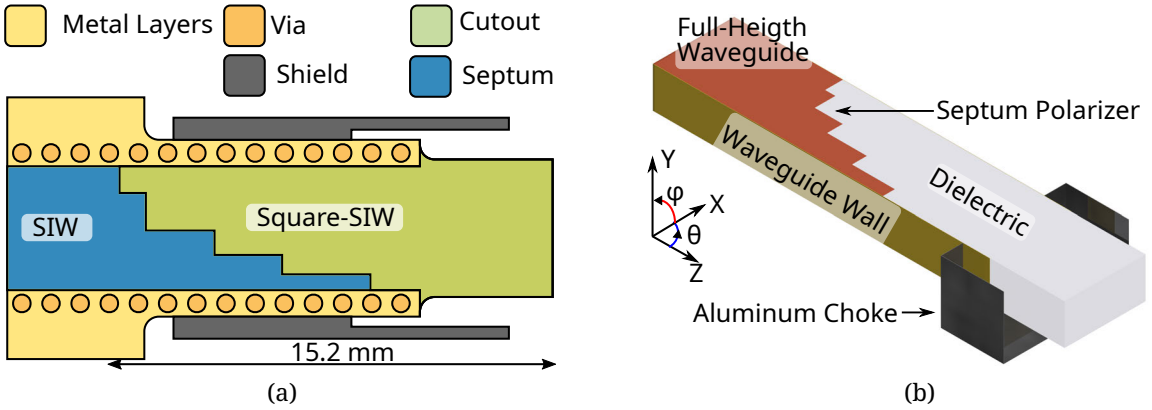

Figure 5.14: (a) Illustrated cross-sectional top and (b) three-dimensional view of the used dual-polarized SIW-horn-antenna including a septum polarizer and a metallic shield.

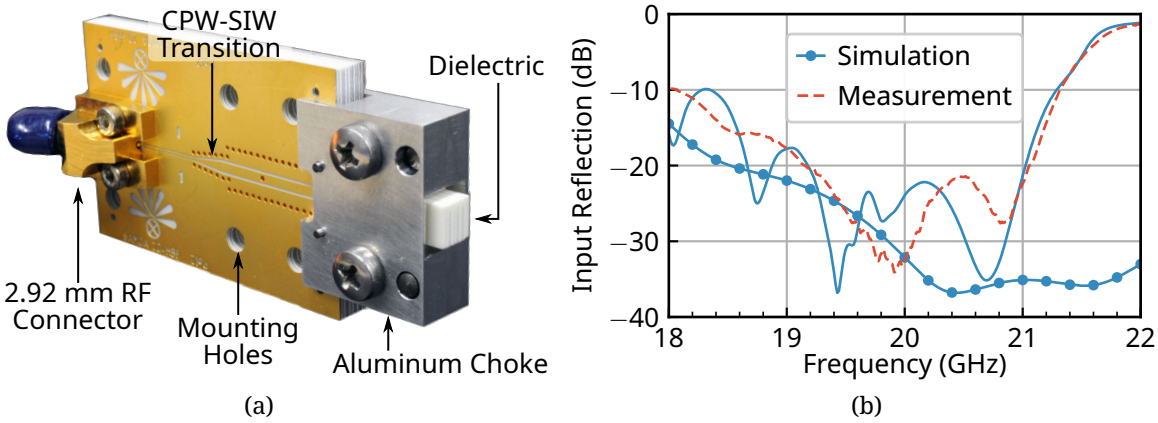

Figure 5.15: (a) Fabricated SIW-antenna including the external choke. (b) Simulated and measured reflection coefficient (— includes the transition and —•— is the antenna only).

fixed with two screws. The PCB dielectric slightly protrudes from the choke. The backside of the antenna reproduces the visible front side and excites the other polarization.

The simulated and measured reflection coefficient is plotted in Fig. 5.15b. Two simulations are conducted, one with and one without the transition. The results are relatively close for lower frequencies but diverge, starting at about 20.5 GHz, when the transition fails to work. The antenna itself is intrinsically more wideband. The measurements verify the results, which correspond well with the simulated data. The input matching is better than 20 dB in the desired operating band, around 20 GHz.

Far-field measurements allow for evaluating the antenna performance. The simulated and measured results for one polarization in two different cuts, the xz-plane ($\phi = 0°$) and the yz-plane ($\phi = 90°$), are shown in Fig. 5.16a and Fig. 5.16b, respectively. The simulated and measured directivity are in relatively good agreement in both cases.

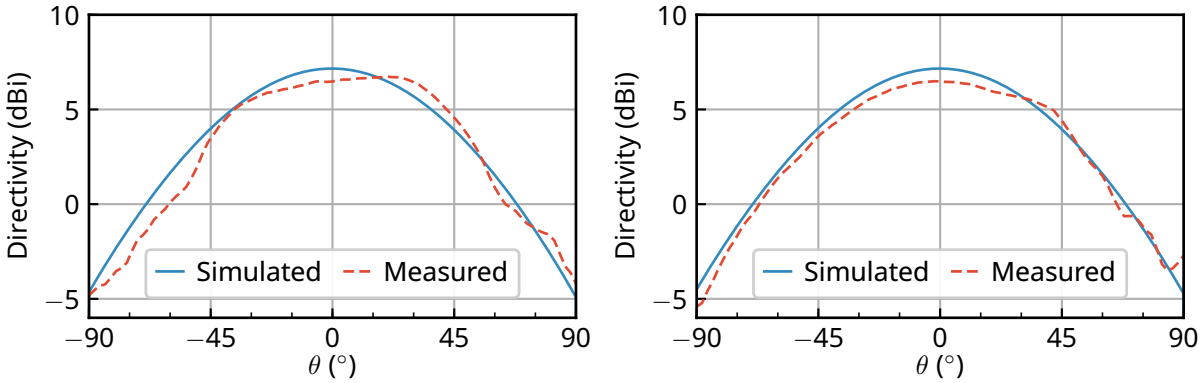

Figure 5.16: Simulated and measured SIW-antenna pattern cuts for a single polarization in (a) the xz-plane ($\phi = 0°$) and (b) the yz-plane ($\phi = 90°$).

5.4 Frontend

The beamformer is the central part of the designed HBF frontend. Additional components required for practically usable frontends, such as LNAs or image-reject filters, are neglected since they are not required for a proof of concept. Their integration is straightforward in brick architecture.

In Section 5.3, essential components such as the all-pass filters and the couplers are examined. In the worst case, the insertion losses from both components add up to 1.5 dB. Since these components are repeatedly used in a serial feed architecture, the subsequent power loss quickly becomes critical. A significant, unwanted LO amplitude taper would result. Hence, countermeasures must be taken to avoid influencing the RF power level.

One possible solution is to operate the second (RF) mixer stage with a high input power so that a change of LO power has only a minor influence on the conversion loss. However, for an 8-element array, about 10 dB of dynamic range would have to be covered. In addition, the output power of the first mixer stage (LO_x+LO_S) is relatively low. Hence, an equalization of LO_x-signal is proposed. Equalization is attainable through a simple, low-cost gain block amplifier (*AVAGO AVT-51663*). The test circuit in Fig. 5.17a shows the designed 4-channel evaluation board.

The input LO_x signal is fed into port ① at the first coupler. Most of the signal continues along the microstrip to the first all-pass filter, and only a fraction is coupled to the newly introduced LO-amplifier. The output of the amplifier forms port ②. This setup is repeated for port ③ through ⑤. The last coupler is terminated by 50 Ω .

The amplifiers are operated in saturation to equalize the output power of all channels. For the S-parameter measurements in Fig. 5.17b, an LO_x drive level of 15 dBm is used. The input matching deteriorates when compared to the results from Fig. 5.17b and Fig. 5.7b of the all-pass filter and coupler, respectively. The additional input reflection also results in ripples of the transmission parameters S_{x1}. However, all four channels' gain closely matches at about -1 dB in the frequency band of interest. Thus, the equalization characteristic of the circuit is successfully demonstrated. The results correspond well with the expected datasheet value for the saturated output power of slightly more than 13 dBm.

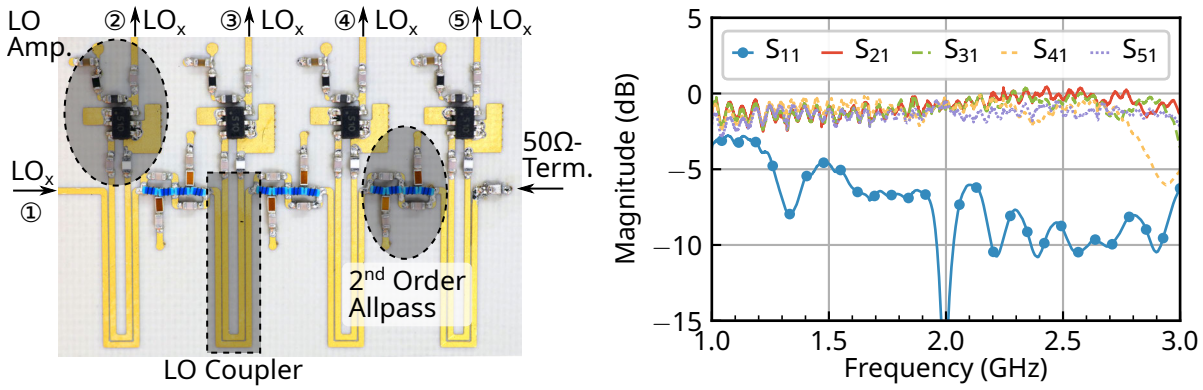

Figure 5.17: (a) Fabricated, active LO delay line circuit for the HBF array including the coupler and an LO-amplifier. (b) Measured S-Parameters at an input LO drive level of 15 dBm.

Operating an amplifier in saturation results in nonlinear effects. Since phase stability is critical for the design, conducted power sweeps help to validate the approach. The results shown in Fig. 5.18 are obtained by sweeping the input power of the evaluation board from -10 to 20 dBm at a constant frequency of 1.5 GHz.

All four channels' gain change is plotted in Fig. 5.18a. At a low input power level, all four amplifiers operate in the linear regime, and the gain is constant. The gain differences between the channels are mainly due to delay network losses and varying amplifiers. These are the deviations needing equalization. At about 5 dBm the amplifier's compression point is reached, and at about 12 dBm all are saturated at maximum output power. As desired, all four channels' gain and output power are equal.

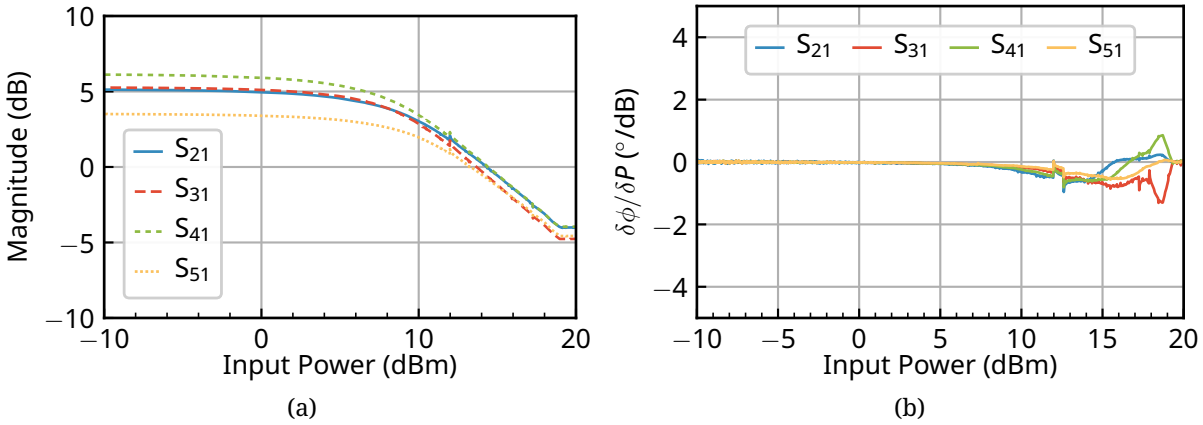

Figure 5.18: Measured results from a power sweep of the input LO drive level at 1.5 GHz. (a) shows the gain characteristics and (b) the differential phase change at the four output ports.

Fig. 5.18b depicts the differential phase change ($\delta\phi/\delta P$) with varying input power. $\delta\phi/\delta P$ remains constant until the amplifiers reach saturation and changes start to occur. These are relatively small with less than 1° phase change per dB power change and have a similar trend in all four channels up to about 15 dBm input power.

The input power is set to a constant 15 dBm, and the phase is measured to investigate the influence in realistic operation. The results are plotted in Fig. 5.19a. As expected, all four channels have a negative phase slope, which increases with every delay section.

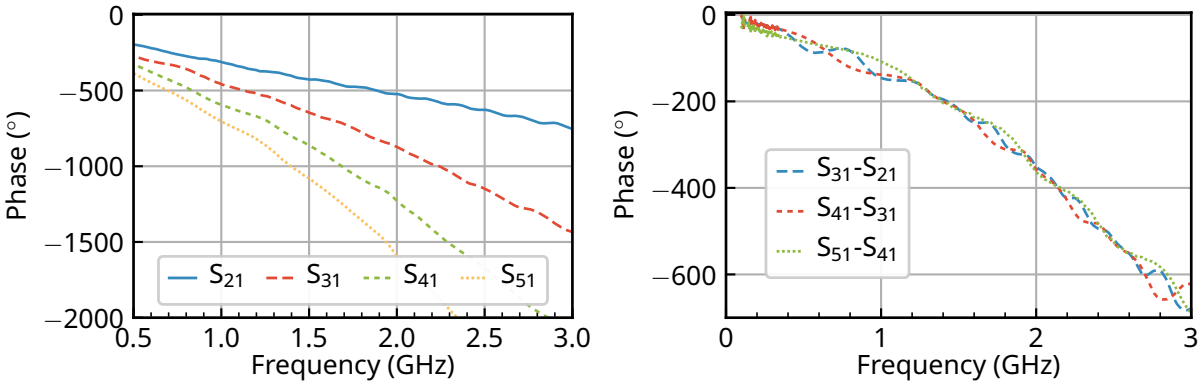

(a) (b)

Figure 5.19: (a) Measured phase of the active LO delay line network at an input LO drive level of 15 dBm. (b) Progressive phase differences ($\Delta\varphi$) of adjacent channels.

Since the absolute phase value is not of importance for the HBF-principle, the relative phase change between adjacent channels is plotted in Fig. 5.19b. All three difference curves exhibit almost equal characteristics, with a maximal deviation of less than $\pm 5°$ in the operating band. These results prove the approach's feasibility, including both the delay network and the equalization amplifier.

The complete frontend design is illustrated in Fig. 5.20. Its central part is the active delay network which occupies about $^2/_3$ of the total surface area. Two full channels are shown in the image. The first mixer directly follows the LO amplifier. The $\mathrm{LO_s}$ also connects to this mixer through the vertical transition from Section 5.3.4. Capacitors on the microstrip line block rectified DC currents from the mixers.

The output of the first-stage mixer is routed to the meander loop band-pass filter to block unwanted mixing products. The second mixer stage follows next. The RF is converted to the desired IF. The IF is routed through the inner stripline layer. Due to the relatively low intermediate frequency, a very compact and straightforward vertical transition close to the mixer is used. A gate bias is applied to both mixers to reduce the required LO drive level for optimal conversion loss. The RF port of the second stage mixer constitutes the input of the frontend. The following CPW connects directly to the antennas.

The IF distribution networks on the left-hand side of Fig. 5.20 are not part of the frontend but are also visible in the image. The IF power combiner network is designed using CPW transmission lines and lumped SMD power dividers on the top layer. A vertical transition connects the top CPW to the stripline on an inner layer.

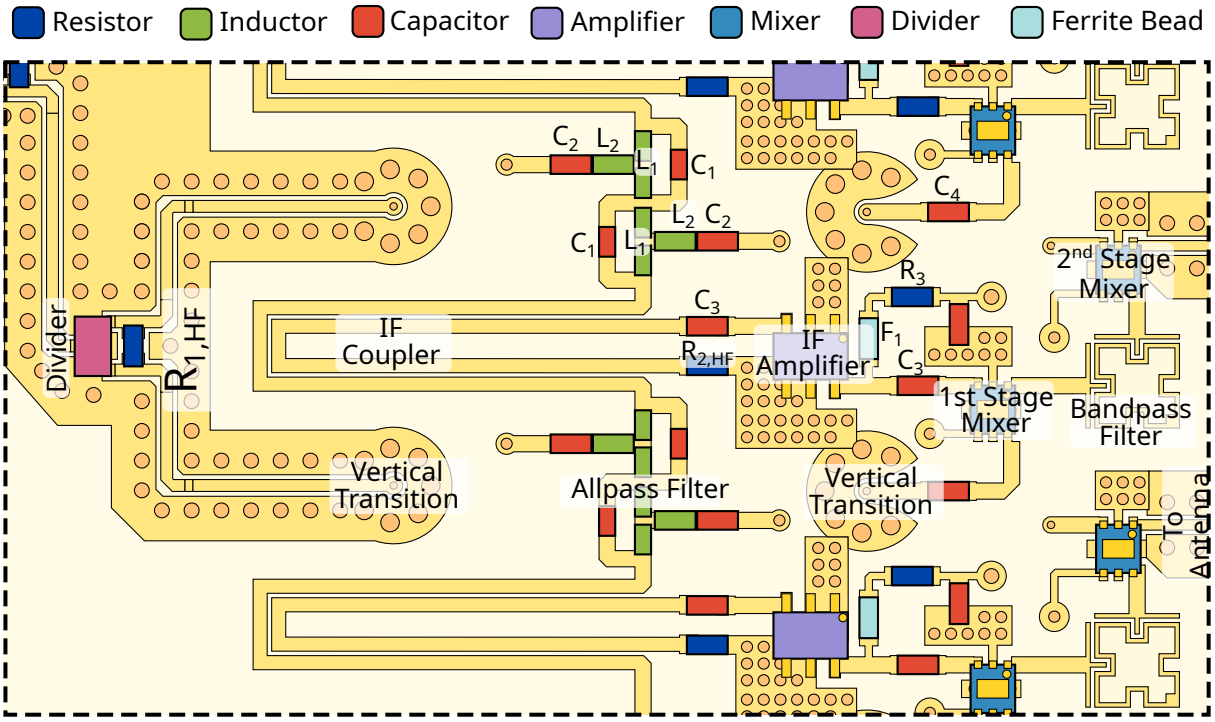

Figure 5.20: Closeup of the heterodyne beamformer's frontend circuitry.

5.5 Module

The designed modules each contain a dual-polarized linear 8-element array. As illustrated in Fig. 5.21, the center part of the module is the heterodyne beamformer design from Section 5.4. The RF port of the frontend is followed by a via-based CPW-SIW transition (cf. Section 5.3.5). The actual radiator is the circularly polarized SIW-antenna design explained in Section 5.3.6. The design is fully scalable as long as the power levels of LO_x suffice.

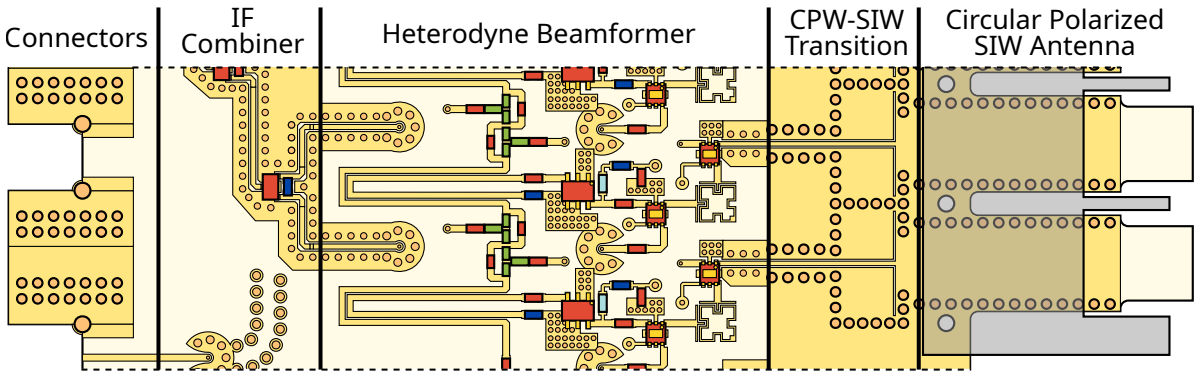

Figure 5.21: Structural design of two channels/elements of the HBF-array .

The left side of the module is reserved for interconnects. Here, Sub-Miniature Push-On Connector (SMP) connectors are used for the high-frequency signals IF, LO_x, and LO_s. These connectors perform sufficiently well up to 20 GHz, and provide flexibility for fabrication and soldering tolerances. A total of six SMP-connectors are required per module to feed independent signals for both polarizations. LO_x and LO_s on the top and bottom could be joined if both polarizations were to be scanned in the same direction.

The IF combiner lies between the connectors and the beamformer. It is a simple cascaded design, which would result in a slightly longer brick if more elements were integrated into the same module. Also visible in the lower part of the IF combiner section of Fig. 5.21 is the routing of the LO_s-signal. Behind the connector, a vertical transition changes the microstrip to a stripline. The LO signal is subsequently split for the eight channels utilizing simple T-section stripline dividers (not visible).

A fabricated module is shown in Fig. 5.22 without mounted antenna chokes. The outer dimensions are 113.0 mm by 80.5 mm with a total thickness of 4.8 mm. With mounted chokes, the total module thickness would increase to 7.5 mm, corresponding to $\lambda_0/2$. Thus, in y-direction, multiple such modules could be placed next to each other and maintain the array grid spacing.

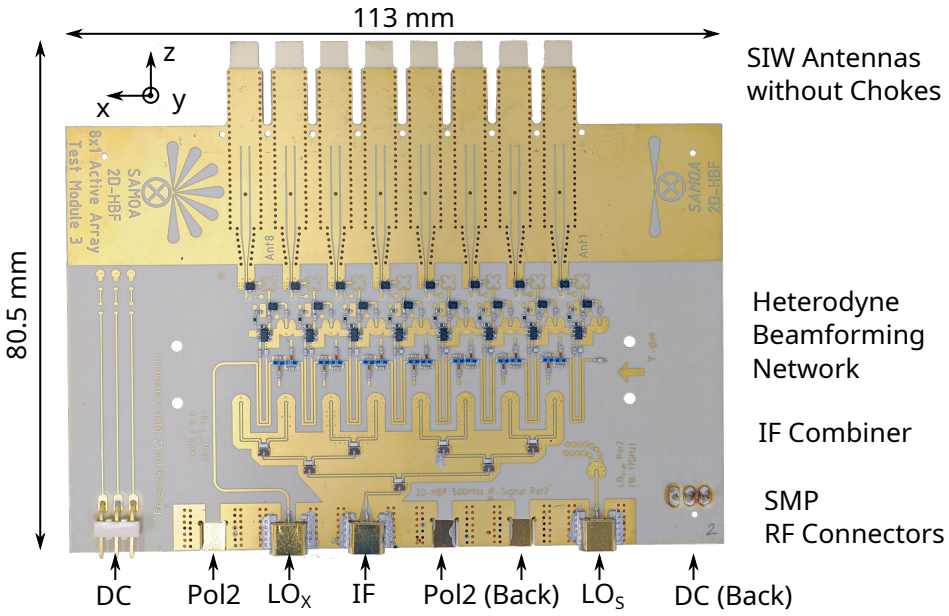

Figure 5.22: 8-element HBF-array module with all electronic components but without the SIW-antenna chokes.

In addition to the RF interconnects, three DC pins are also placed on the side of the module. These provide the gate voltages for the mixers and the bias for the LO-amplifiers. The SMP connectors function as the DC return path.

5.6 Array Performance

Far-field measurements are conducted to assess the scanning performance of the designed linear HBF array. Fig. 5.23 shows a fully equipped module mounted to the positioning

system in the anechoic chamber at *TUHH*. The positioner allows for a module rotation in θ- and ϕ-direction, allowing measurements of the entire antenna pattern.

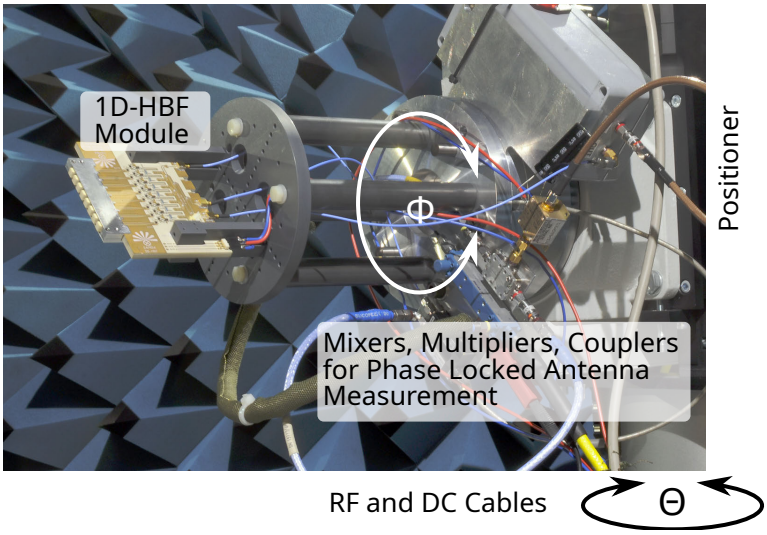

Figure 5.23: Heterodyne beamforming array undergoing antenna measurements.

The measurement setup is rather complex, including external mixers, multipliers, and couplers to enable phase-locked measurements (not only phase locked LO-signals). The required three high frequency and DC signals prevent the usage of the available rotary joint and require a careful rotation in ϕ-direction. Fortunately, a module rotation in θ-direction suffices to analyze the beam scanning.

The frequency f_{LOx} is changed for every measurement and compensated through f_{LOs} to keep $f_{\mathrm{RF}} - f_{\mathrm{IF}}$ constant. The transmitted RF frequency is swept during each measurement between 19.7 and 20.3 GHz. The IF is evaluated on a VNA.

The measured array patterns at 20 GHz in the xz-plane ($\phi = 0°$) are plotted in Fig. 5.24. For a better comparison, the gain for each curve is normalized to the maximum value. Seven distinct $\mathrm{LO_x}$ frequencies between 1.7 and 2.3 GHz are shown. As desired, the beam θ-direction changes from about -30 to +30°. At the center frequency of 2.0 GHz, the boresight direction is very close to the z-axis ($\theta = 0°$), which coincides well with the design goal of the delay network explained in Section 5.3.1. At about 12 dB, the central beam's SLL agrees well with the expectations. However, the SLL rises significantly for scanned beams. Hence, scanning angles of more than $\pm 30°$ are not feasible with the designed antennas and are not shown in the plot.

Fig. 5.25 highlights the HBF-scanning principle. The boresight direction of the array beam (θ_0) is evaluated for different frequencies f_{LOx} at three constant RF frequencies 19.7, 20.0, and 20.3 GHz. The results verify the concept by demonstrating a continuously rising, almost linear relationship between the scan angle and the LO-frequency. Furthermore, the beam directions for all three plotted RF frequencies are almost equal, proving that the scan angle is independent of f_{RF}.

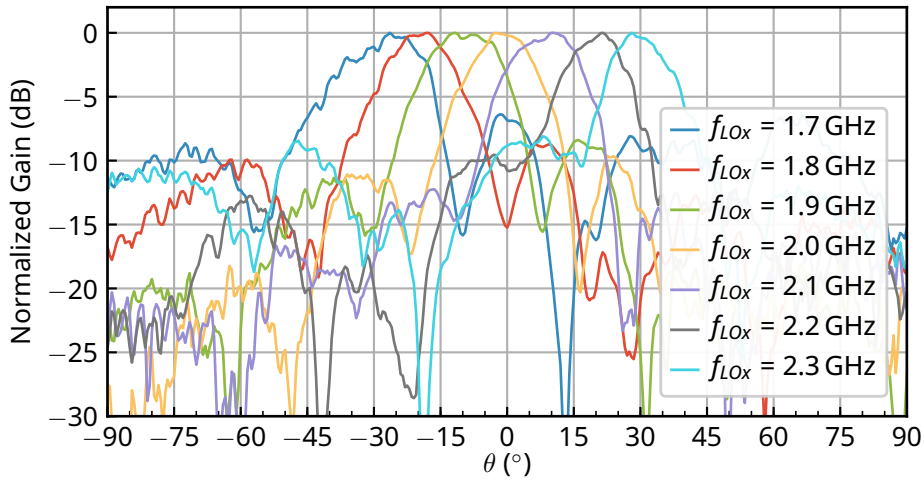

Figure 5.24: Scanned array patterns at 20 GHz for various LO_x-frequency in $\phi = 0°$-plane.

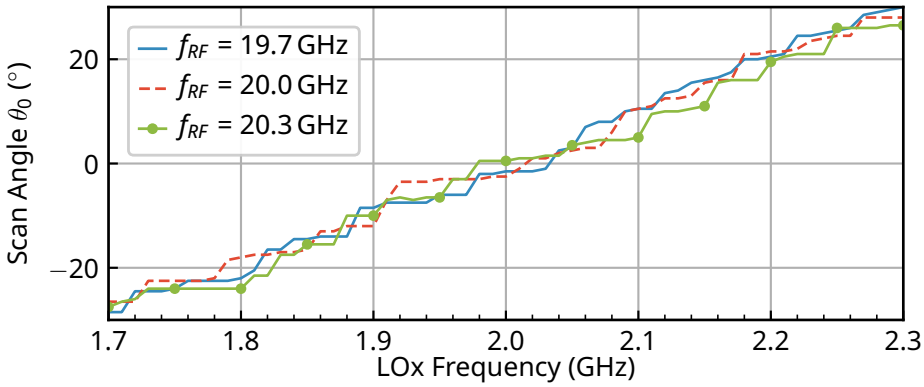

Figure 5.25: Dependence of the array pointing direction at 19.7 GHz, 20.0 GHz, and 20.3 GHz on the LO-frequency.

5.7 2D-HBF-Beamforming

The heterodyne beamformer proposed in Section 5.1.1 has many upsides but lacks the ability to scan the beam along the second principal direction. 2D-beam scanning is a fundamental requirement in many applications and must be implemented. This section develops a concept for such a planar HBF array.

5.7.1 2D-Heterodyne Beam Scanning

Generally, 2D-beam scanning with the linear array from Section 5.5 could be achieved by aligning multiple modules in a serial feed architecture and interconnecting each with a phase shifter in any one of the three signal paths LO_x, LO_s, or IF. The phase shifters could then set a progressive phase shift between the modules, resulting in a tilted beam. Though feasible, this approach conflicts with the general goal of an HBF system to work without phase shifters and their required control circuitry.

In [156], a general but complex architecture is presented to obtain a 2D-scannable HBF phased array. It is based on the less advantageous single mixer architecture discussed in Section 5.1.1. Thus, the proposed linear array from Section 5.5 is used to develop a 2D scanning concept.

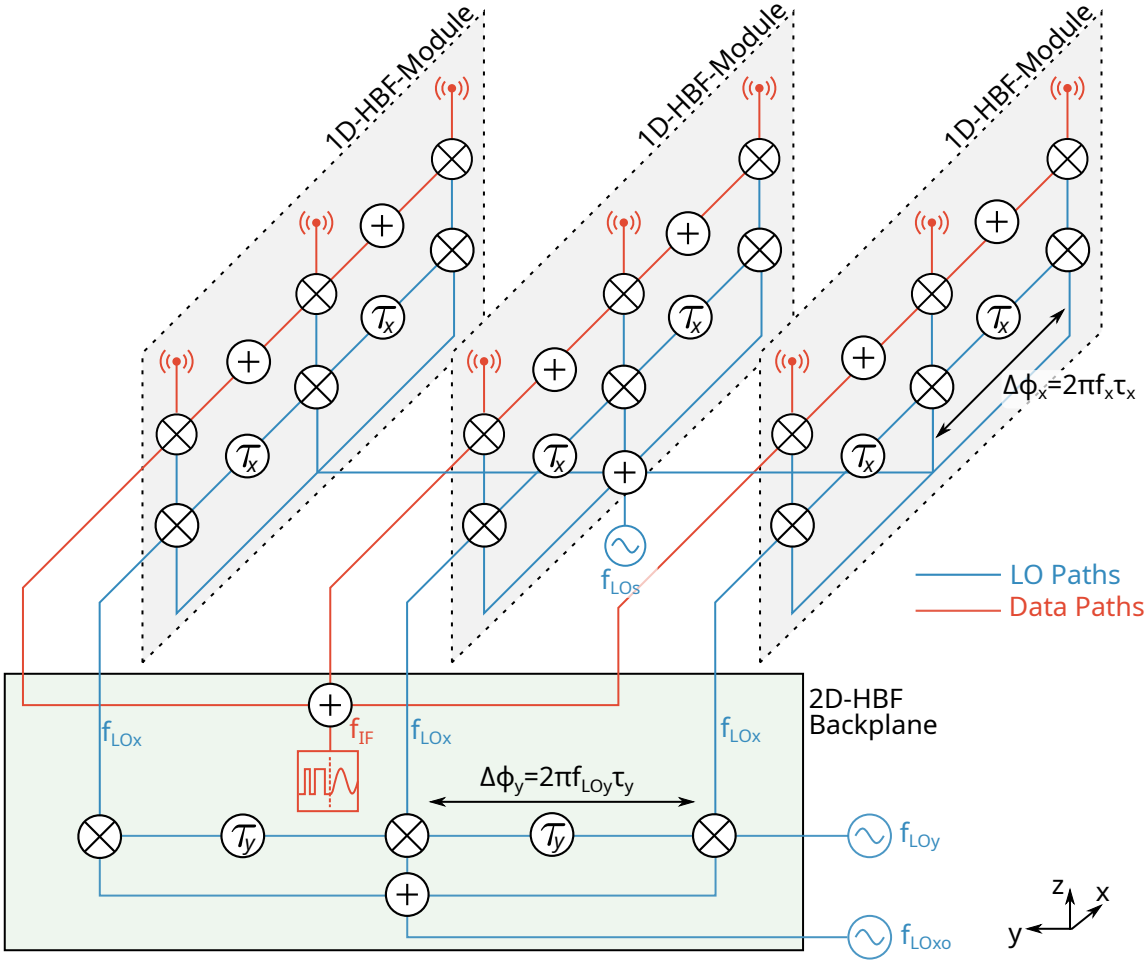

Figure 5.26: 2D-HBF architecture for independent beam scanning in two principal directions.

Fig. 5.26 depicts the proposed architecture. The linear arrays are placed adjacent to each other and are used to scan the beam in the xz-plane. The required input signals for the beamformer are the same as before: the data signal IF, the LO_x for the scanning in xz-direction, and the LO_s for compensating the introduced frequency changes and to keep the RF frequency constant. The subsequent phase shift between elements in the x-direction is $\Delta\varphi_x = 2\pi f_{LOx}\tau_x$.

The linear arrays are connected to a backplane, which incorporates distribution networks and a second independent heterodyne beamformer. This beamformer is oriented in the y-direction and is responsible for beam scanning in the yz-plane. It requires an additional independent signal source LO_y, a serial delay network with delays of length τ_y, and one additional mixer per linear array. The frequency-dependent phase shift in the y-direction is $\Delta\varphi_y = 2\pi f_{LOy}\tau_y$.

The output signal from the mixers on the backplane is connected to the linear array's LO_x channel. Changing f_{LOy} to scan in the y-direction would also affect f_{LOx} and the scanning in the x-direction. To compensate, the signal source LO_{xo} must take this effect into account. The frequencies required to scan the beam in a desired direction with phase progressions $\Delta\varphi_x$ and $\Delta\varphi_y$ can be calculated as follows:

$$f_{LOy} = \frac{\Delta\varphi_y}{2\pi\tau_y} \tag{5.7}$$

$$\begin{aligned} f_{LOxo} &= f_{LOx} \pm f_{LOy} \\ &= \frac{1}{2\pi}\left(\frac{\Delta\varphi_x}{\tau_x} \pm \frac{\Delta\varphi_y}{\tau_y}\right) . \end{aligned} \tag{5.8}$$

The sign in Eq. (5.8) depends on whether an up- or downconversion mixer is used. The selection should be based on the desired frequency range for the delay lines and mixers. As explained in Section 5.2, lower frequencies might yield some advantages.

5.7.2 Heterodyne 2D-Beam Forming Array

A backplane board with the novel beamformer has to be designed to realize a 2D-array based on the module from Section 5.5. In the first step, the frequencies f_{LOy} and f_{LOxo} have to be determined. To design a lumped component delay line circuit as presented in Section 5.3.1, an operating frequency below f_{LOx} is necessary for f_{LOy}. For a single all-pass filter section design, a frequency range from 250 – 2250 MHz is appropriate.

Name	Tuning Range
IF	1.0 GHz
RF	20.0 GHz
f_{LOx}	1.5 GHz–2.5 GHz
f_{LOs}	16.5 GHz–17.5 GHz
f_{LOy}	250 MHz–750 MHz
f_{LOxo}	750 MHz–2250 MHz

Table 5.1: Frequencies used in the proposed heterodyne beamformer.

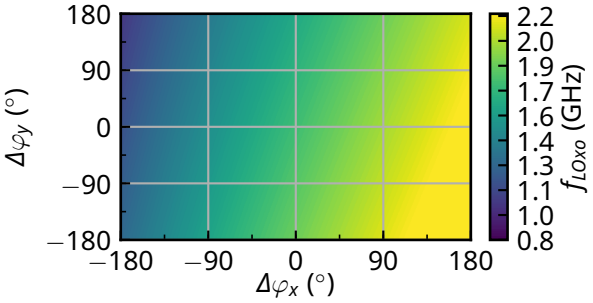

Figure 5.27: Tuning of f_{LOxo} in dependence of $\Delta\varphi_x$ and $\Delta\varphi_y$.

Using Eq. (5.8), the required tuning range of f_{LOxo} is calculated to be between 750 and 2250 MHz. The required frequencies for all signals in the 2D-HBF-array are listed in Table 5.1.

To evaluate realistic tuning requirements of the additional LO_{xo}, its frequency dependence on the phase shift settings $\Delta\varphi_x$ and $\Delta\varphi_y$ is evaluated. The phase-frequency relationship from Fig. 5.19 is included as a reference. The results are shown in Fig. 5.27 and highlight the dependence of f_{LOxo} on both scan directions. However, the results are very smooth, and no problems are expected.

Multiple linear array modules would be placed next to each other to realize such an array. The total thickness of one module, including the choke, is 7.5 mm, allowing such a

module placement even with the $\lambda_0/2$-constraints of the array grid. A concept for an 8x8 element planar HBF-array is illustrated in Fig. 5.28.

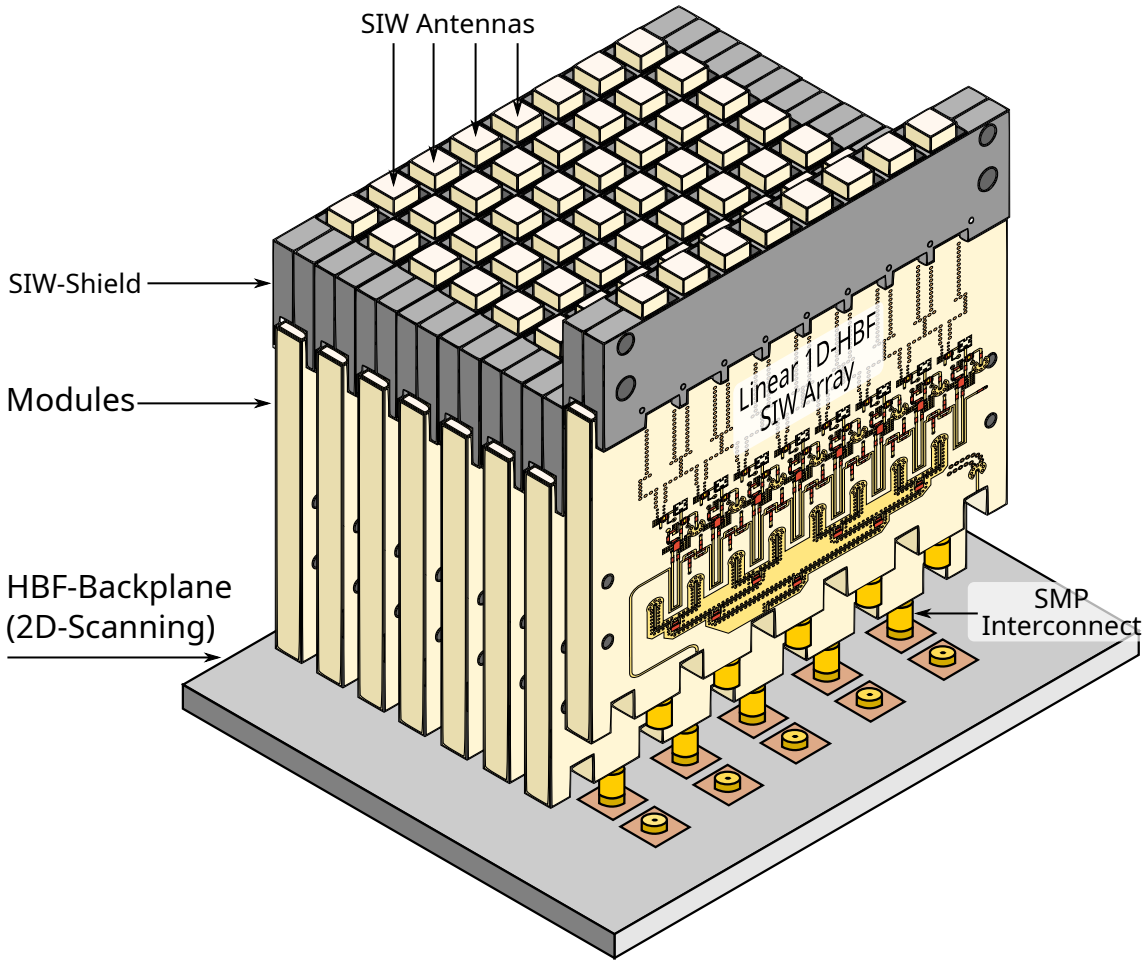

Figure 5.28: Concept for a 2D-HBF-array setup with 8x8 elements based on the introduced 8-element modules.

The eight modules are attached to a backplane using the same SMP-connectors as before. The backplane contains the heterodyne beamformer for the scanning in the y-direction. LO_X is an output signal from the backplane and must be routed to each linear module. Furthermore, distribution networks for LO_S and IF must be designed to ensure equal signal phase at all modules. Phase variations are critical since they directly influence the scanning in the y-direction. Low frequencies are again desirable to keep the influence of PCB fabrication tolerances on the phase at a minimal level.

5.8 Summary

Efficient and simple beam scanning is a necessity for low-cost systems. The heterodyne beamforming technique presented in this chapter enables such phased array designs without the need for phase shifters or complex control circuitry. Instead, mixers and

simple delay lines are used and beam control is possible through frequency changes of a local oscillator or another signal source.

The presented dual-polarized linear phased array demonstrates the principle at 20 GHz in a standard PCB-process. Application-specific improvements, including LNAs or different antenna elements, are possible without voiding the concept.

As an outlook, a planar array design for two-dimensional beam scanning is presented based on the designed modules. A significant size reduction of the delay line circuits would be required to obtain smaller, more compact modules in a tile architecture. One possible approach could be to exploit waveguides' dispersive characteristics close to the cutoff. Another way would be to design custom RFICs for the beamformer. Such an RFIC would, however, contradict the taken low-cost approach.

Chapter 6
Conclusions

Electronically scannable antennas are advanced electronic systems with a unique feature set. One of their most prominent abilities is to change the beam direction without physically moving the antenna. Since the limitations of mechanical drive systems do not apply, instantaneous direction changes are possible. Additionally, an array antenna allows the adjustment of critical beam properties such as the sidelobes, beamwidth, or null positions during operation. It is even possible to excite multiple beams simultaneously from a single aperture.

Arrays typically constitute the basis for electronic beam scanning. They consist of multiple combined elements to form a shared aperture. Depending on the application requirements, these elements can be (widely) separated or densely packed. Such arrays enable more reliable operation since they commonly do not have a single point of failure and gracefully degrade over time. Additionally, very flat or conformal array designs enable low-profile systems with high gain.

The high scanning performance and wide functional range are unmatched but ultimately lead to complex circuits and high costs. A standard reflector often presents a much more economical solution in most high-gain applications. Thus, phased arrays are mainly used in military (radar) applications. However, technological progress and new concepts might change the status quo towards a broader use.

This thesis discusses various aspects of electronically scannable antennas, starting with the basics and ending with innovative solutions. In Chapter 2, essential properties of arrays are presented, such as the number of required control elements to achieve the desired scanning range. This fundamental relationship is vital to understanding the complexity of many arrays while illustrating that unique solutions are possible with reduced requirements. Planar arrays are particularly problematic if high scan angles are required. Other topics discussed in this chapter include various beamforming topologies and their specific advantages and disadvantages. Classical beamforming relies on the signal combination in RF-stage, but IF-, LO-, or even DBF-combining are other options. DBF is a prime example of the flexibility and power of electronic scanning but also of the complexity and challenges involved. Besides the beamformer, the choice of an active or passive array also significantly influences the system's performance. The presented satellite communication scenarios in GEO and LEO orbit are ideal for understanding the requirements of antenna systems. Hence, key performance figures for a communication scenario such as EIRP, G/T, and data rates are analyzed.

Chapter 3 focused on technology and essential components for phased arrays. It includes a summary of current technology, an outlook on recent advances, and new concepts/ideas. The main emphasis of the chapter is on efficient designs to reduce cost and complexity. Air-filled SIWs and 3D-printed waveguides are technological concepts that allow manufacturing low-loss components. Such components could help facilitate passive arrays with good performance. In addition, 3D-printing technology enables new degrees of freedom in design and production. Low-cost waveguide components can be designed and integrated into a multilayer architecture. Another promising idea is dual-band arrays, which integrate a receiver and transmitter operating at different frequencies into a single aperture. However, dual-band designs lead to a very high integration density. In applications that do not require a simultaneous operation, reconfigurable designs can be a viable alternative. The presented reconfigurable components use switches to change characteristics such as the frequency response or polarization, but other methods, such as tunable materials, also exist. Another critical issue in phased array operation is calibration. Sufficiently accurate calibration of the elements is necessary to guarantee and maintain performance. Here, a microstrip patch design with integrated probes allows for online calibration. A reference signal is injected into the array and enables constant monitoring of array changes.

Besides technology and components, beamforming array systems are the main focus of the thesis. These systems often utilize planar arrays with a wide scanning range to offer flat, high-performance, but also expensive solutions. In many applications, the physical size of the system is not a significant issue, and the occurring angular changes are minor. For these use cases, hybrid solutions can be an ideal fit. Chapter 4 discusses a high-gain reflector combined with an electronically controllable array to enable fast scanning with a limited field of view. The reflector shape and the resulting beam and system properties are comprehensively analyzed. These results allow obtaining a reflector geometry based on application requirements. This thesis considers a satellite communication scenario requiring constantly high gain, EIRP, and G/T over a limited scanning range. In this case, a spherical reflector constitutes the best compromise. A custom-designed transmitter feed for the reflector maximizes system performance. A custom array grid spacing and a specialized excitation scheme are central to the feed architecture. This grid and excitation combination helps to keep the number of elements low and maintains a satisfactory performance for scanned beams. Simple microstrip patch antennas function as radiators. The beamformer utilizes a relatively simple design based on attenuators and radial dividers. It allows great flexibility to excite advanced schemes and even multiple simultaneous beams. Measurement results of the manufactured array feed and reflector verify the concept. The antenna system highlights that application-specific designs can significantly reduce complexity and cost.

Chapter 5 discusses another challenge in phased array designs. To control the excitation of the array elements, phase shifters or RFICs (core chips) are needed. These essential building blocks must be small, efficient, and ideally low-cost. However, new IC designs are involved, time-consuming, and extremely expensive. They are often only available at frequencies with significant enough commercial interest. In other bands, phase shifters are either not available at all or only as bulky, expensive general-purpose components. Thus, the development of a different type of phase-shifting network is crucial. The proposed “heterodyne beamforming” solution combines the frequency-dependent phase response of components with a network of simple mixers. The name heterodyne stems

from signal mixing and emphasizes its importance. The explanation of the underlying principle provides essential insight into designing an 8-element dual-polarized linear array based on SIW-technology. Distributed and lumped components form the core of the beamformer at 20 GHz. An introduction to the individual component's functionality provides an understanding to assess their simulated and measured performance. Finally, an SIW-array module is manufactured and tested. The result demonstrates that heterodyne beamforming does indeed work as expected. It allows for an effortless way to scan the beam without high requirements on components or digital circuitry. The chapter concludes by proposing an advanced heterodyne beam scanning concept. It extends the principle used for the linear array to planar arrays to enable 2D scanning.

This thesis introduces several components and concepts that can significantly benefit electronic beam scanning systems. Concepts such as the array-fed reflector are already quite sophisticated. However, the hybrid reflector system, e.g., suffers from relatively high sidelobes caused by beam blockage. To improve performance, a better blockage model can help to understand and mitigate the problem. Redesigning the reflector with an offset feed is a possibility as a last resort. Additionally, the current scanning range of the system is limited, and an extension to complete hemispherical scanning is possible through a simple mechanical drive. Software is the greatest challenge in such a combined electrical and mechanical solution. However, integrating the receiver into the feed is critical for practically using the reflector system. Dual-band components and additional electronics require costly real estate on the PCB. Furthermore, integrating higher power amplifiers is necessary to use the design's reserves fully. Thus, a switch from tile to brick architecture is advisable. Many good SIW components are already available or are adaptable for this purpose. Alternatively, a 3D-printed feed using high-performance waveguides is an ideal fit for the reflector.

The heterodyne beamformer is an innovative scanning architecture requiring further effort to exploit its potential fully. An extension to planar arrays has been presented but requires practical validation. In addition, the used arrays are relatively small, and a full-scale adaptation might cause unexpected problems. Although the front end includes electronics, the presented array is passive without a signal LNA or PA. An active design, including a calibration option, is desirable to increase performance.

Overall, electronic beam scanning remains an advanced, high-performance technique with many benefits. New technologies and concepts have steadily advanced the state of the art in electronic beam scanning for over 100 years. For now, the military and scientific communities are still the primary users, but subsequent development steps may provide the final breakthrough of this exciting technology.

Appendix A

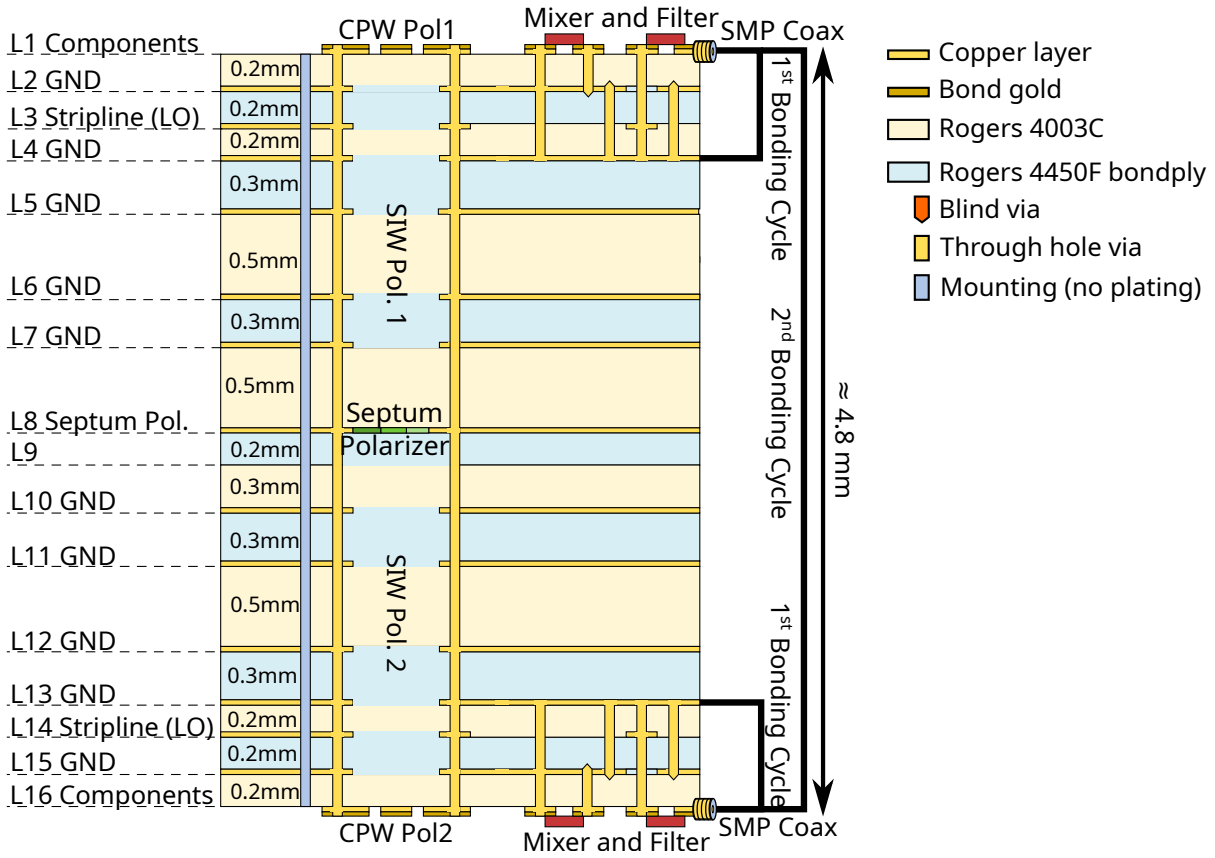

Figure A.1: Multilayer stack used for the fabrication of the 8-element SIW-array.

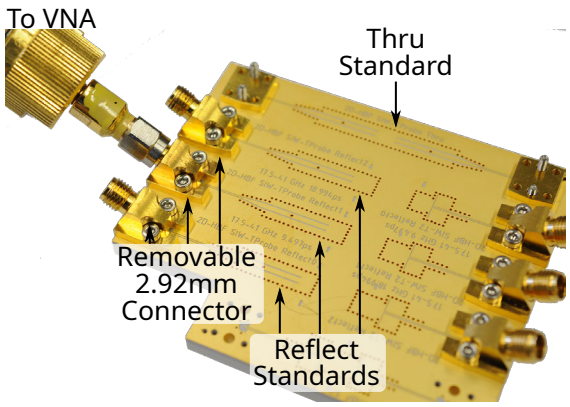

Figure A.2: Standards used for VNA-calibration of SIW-components.

Table A.1: Electronic components used in the frontend of the heterodyne beamformer.

Name	**Type**	**Value**	**Package**
SMP	Molex 0734153591	Coaxial connector	SMP
Amplifier	Avago AVT-51663	20 dB amplifier	SOT-363
Mixer	MACOM MAMX-011021	Mixer (5–35 GHz)	TDFN 6-lead
Divider	Anaren PD0409J5050S2HF	IF Divider	0805
$R_{1,\mathrm{HF}}$	Vishay FC0603E1000BST1	100 Ω RF resistor	0603
$R_{2,\mathrm{HF}}$	Vishay FC0402E50R0BST1	50 Ω RF resistor	0402
R_3	Panasonic ERJ-2RKF30R0X	30 Ω	0402
F_1	Murata BLM15GG471SN1D	470 Ω Ferrite Bead	0402
C_1	Murata GJM1555C1HR90WB01	0.9 pF RF capacitor	0402
C_2	Murata GJM1555C1H2R0WB01	2.0 pF RF capacitor	0402
C_3	Kemet CBR04C101F3GAC	100.0 pF DC block	0402
C_4	Murata GJM1555C1H1R0BB01D	1.0 pF DC block	0402
C_5	Murata GRM155R71C104KA88J	100 nF bypass capacitor	0402
L_1	Murata LQW15AN2N5B00	2.5 nH RF inductor	0402
L_2	Murata LQP15MN1N0W02	1.0 nH RF inductor	0402

Bibliography

[1] A. Sumits, *The History and Future of Internet Traffic*, Sep. 2015. [Online]. Available: https://blogs.cisco.com/sp/the-history-and-future-of-internet-traffic (visited on Mar. 1, 2023).

[2] Cisco, "Cisco Visual Networking Index: Forecast and Trends, 2017–2022," White Paper, 2019, pp. 1–38. [Online]. Available: https://blogs.cisco.com/sp/the-history-and-future-of-internet-traffic (visited on Mar. 1, 2023).

[3] ITU, "Measuring digital development Facts and Figures 2022," Tech. Rep., 2022. [Online]. Available: https://www.itu.int/dms_pub/itu-d/opb/ind/d-ind-ict_mdd-2022-pdf-e.pdf (visited on Mar. 1, 2023).

[4] R. L. Haupt and Y. Rahmat-Samii, "Antenna Array Developments: A Perspective on the Past, Present and Future," *IEEE Antennas Propag. Mag.*, vol. 57, no. 1, pp. 86–96, Feb. 2015, ISSN: 1558-4143. DOI: 10.1109/MAP.2015.2397154.

[5] G. Marconi, "On methods whereby the radiation of electric waves may be mainly confined to certain directions, and whereby the receptivity of a receiver may be restricted to electric waves emanating from certain directions," *Proc. R. Soc. London A*, vol. 77, no. 518, pp. 413–421, Apr. 1906, ISSN: 2053-9150. DOI: 10.1098/rspa.1906.0036.

[6] K. F. Braun, "Electrical oscillations and wireless telegraphy," *Nobel Lecture, December*, vol. 11, no. 1909, pp. 226–245, 1909.

[7] S. J. Stone, "Directive antenna array," 1643323A, 1927. [Online]. Available: https://patents.google.com/patent/US1643323A/en.

[8] Chaddy, *Aerial photograph of USASA Field Station Augsburg*, 2010. [Online]. Available: https://commons.wikimedia.org/wiki/File:BND-Au%C3%9Fenstelle_Gablingen.jpg (visited on Mar. 3, 2023).

[9] C. L. Dolph, "A Current Distribution for Broadside Arrays Which Optimizes the Relationship between Beam Width and Side-Lobe Level," *Proc. IRE*, vol. 34, no. 6, pp. 335–348, Jun. 1946, ISSN: 2162-6634. DOI: 10.1109/JRPROC.1946.225956.

[10] J. Spradley, "A volumetric electrically scanned two-dimensional microwave antenna array," in *1958 IRE International Convention Record*, vol. 6, IEEE, Mar. 1966, pp. 204–212. DOI: 10.1109/IRECON.1958.1150684.

[11] G. A. Deschamps, "Microstrip microwave antennas," in *Proceedings of the Third Symposium on the USAF Antenna Research and Development Program, Oct*, 1953, pp. 18–22.

[12] E. J. Wilkinson, "An N-Way Hybrid Power Divider," *IRE Transactions on Microwave Theory and Techniques*, vol. 8, no. 1, pp. 116–118, Jan. 1960, ISSN: 0097-2002. DOI: 10.1109/TMTT.1960.1124668.

[13] R. Munson, "Microstrip phased array antennas," in *1973 EIC 11th Electrical Insulation Conference*, IEEE, 1973, pp. 281–283.

[14] A. Wootten and A. R. Thompson, "The Atacama Large Millimeter/Submillimeter Array," *Proc. IEEE*, vol. 97, no. 8, pp. 1463–1471, Jun. 2009, ISSN: 1558-2256. DOI: 10.1109/JPROC.2009.2020572.

[15] Research and Markets, "Global Flat Panel Antenna Market 2022," Mar. 2022. [Online]. Available: https://www.researchandmarkets.com/reports/5560066/flat-panel-antenna-market-with-covid-19-impact-by?utm_source=GNOM&utm_medium=PressRelease&utm_code=2fh7xx&utm_campaign=1677246+-+Global+Flat+Panel+Antenna+Market+(2022+to+2027)+-+Demand+for+High+Data+Rate+Transmission+Presents+Opportunities&utm_exec=jamu273prd (visited on Mar. 11, 2023).

[16] A. Geise, A. F. Jacob, K. Kuhlmann, *et al.*, "Smart Antenna Terminals for Broadband Mobile Satellite Communications at Ka-Band," in *2007 2nd International ITG Conference on Antennas*, IEEE, Mar. 2007, pp. 199–204. DOI: 10.1109/INICA.2007.4353962.

[17] C. A. Balanis, Ed., *Modern Antenna Handbook*, English, 1st ed. Hoboken, NJ: Wiley-Interscience, Sep. 2008, ISBN: 978-0-470-03634-1.

[18] R. J. Mailloux, *Phased Array Antenna Handbook, Second Edition*, English, 2nd ed. Boston: Artech Print on Demand, Mar. 2005, ISBN: 978-1-58053-689-9.

[19] J. Carr and G. Hippisley, *Practical Antenna Handbook*, English, 5th ed. New York, NY: McGraw-Hill Education TAB, Nov. 2011, ISBN: 978-0-07-163958-3.

[20] C. A. Balanis, *Antenna Theory: Analysis and Design*, English, 4th ed. Wiley, Feb. 2016, ISBN: 978-1-118-64206-1.

[21] "IEEE Standard for Definitions of Terms for Antennas," *IEEE Std 145-2013 (Revision of IEEE Std 145-1993)*, pp. 1–50, Mar. 2014. DOI: 10.1109/IEEESTD.2014.6758443.

[22] G. F. Masters and S. F. Gregson, "Coordinate System Plotting for Antenna Measurements," in *Antenna Measurement Techniques Association Symposium (AMTA 2007)*, St Louis, Missouri, USA, Mar. 2007.

[23] P. A. Claridge, W. G. Gates, W. J. M. Grfham, P. Hazeldine, M. D. R. Tench, and R. Young, "Design of a Phased Array Antenna using Solid State Transmit/Receive Modules," in *1989 19th European Microwave Conference*, Sep. 1989, pp. 1131–1140. DOI: 10.1109/EUMA.1989.334120.

[24] S. Sanzgiri, D. Bostrom, W. Pottenger, and R. Q. Lee, "A Hybrid Tile Approach for Ka Band Subarray Modules," *IEEE Transactions on Antennas and Propagation*, vol. 43, no. 9, pp. 953–959, Sep. 1995, ISSN: 0018-926X. DOI: 10.1109/8.410212.

[25] A. Stark, A. Dreher, H. Fischer, *et al.*, "SANTANA: Advanced electronically steerable antennas at Ka-Band," in *2009 3rd European Conference on Antennas and Propagation*, Mar. 2009, pp. 471–478.

[26] N. Fourikis, *Advanced Array Systems, Applications and RF Technologies*. Elsevier Science, 2000, ISBN: 978-008049870-6.

[27] K. Kuang and R. Sturdivant, *RF and Microwave Microelectronics Packaging II*. Springer, 2017, ISBN: 978-3-319-51696-7. DOI: 10.1007/978-3-319-51697-4.

[28] K. Kuhlmann, B. Rohrdantz, and A. F. Jacob, "Performance Assessment and Optimization of an Active Ka-Band Antenna Array with Polarization Multiplexing," in *44th European Microwave Conference (EuMC 2014)*, Oct. 2014, pp. 239–242. DOI: 10.1109/EuMC.2014.6986414.

[29] L. C. Stange, *Integrationstechnik und Aufbauarchitekturen für aktive Antennensysteme im Millimeterwellenbereich*. Cuvillier Verlag, 2005, ISBN: 978-386537542-1.

[30] A. Geise and A. F. Jacob, "Flex-rigid Architecture for Active Millimeter-Wave Antenna Arrays," in *2009 IEEE MTT-S International Microwave Symposium Digest (IMS 2009)*, Jun. 2009, pp. 809–812. DOI: 10.1109/MWSYM.2009.5165820.

[31] T. Buning, W. Ren, G. Yongxin, L. Yan, C. Muren, and G. Guangding, "A hybrid array architecture for space-based highly integrated phased array antenna," in *2016 IEEE International Workshop on Electromagnetics: Applications and Student Innovation Competition (iWEM)*, May 2016. DOI: 10.1109/iWEM.2016.7504869.

[32] T. Pratt, C. W. Bostian, and J. E. Allnutt, *Satellite Communications*. Wiley, Oct. 2002, ISBN: 978-047137007-9.

[33] K. I. Appel and W. Haken, *Every Planar Map is Four Colorable* (Contemporary Mathematics). Providence, RI, USA: American Mathematical Society, Oct. 1989, vol. 98, ISBN: 9780821854310. DOI: 10.1090/conm/098.

[34] Y. Couble, C. Rosenberg, E. Chaput, J. Dupé, C. Baudoin, and A. Beylot, "Two-Color Scheme for a Multi-Beam Satellite Return Link: Impact of Interference Coordination," *IEEE J. Sel. Areas Commun.*, vol. 36, no. 5, pp. 993–1003, May 2018, ISSN: 0733-8716. DOI: 10.1109/JSAC.2018.2832784.

[35] J. Oh and S. B. Choi, "Vehicle roll and pitch angle estimation using a cost-effective six-dimensional inertial measurement unit," *Proceedings of the Institution of Mechanical Engineers, Part D: Journal of Automobile Engineering*, vol. 227, no. 4, pp. 577–590, Oct. 2012, ISSN: 0954-4070. DOI: 10.1177/0954407012459138.

[36] J. Ryu and J. C. Gerdes, "Estimation of Vehicle Roll and Road Bank Angle," *Proceedings of the 2004 American Control Conference*, vol. 3, Jun. 2004. DOI: 10.23919/ACC.2004.1383772.

[37] G. K. Hibbert, G. R. Lesser, *et al.*, "Measuring Vessel Motions Using a Rapid-Deployment Device on Ships of Opportunity," in *Coasts and Ports 2013: 21st Australasian Coastal and Ocean Engineering Conference and the 14th Australasian Port and Harbour Conference*, Engineers Australia, 2013, p. 376.

[38] *Container Handbook*, Feb. 2006. [Online]. Available: http://www.containerhandbuch.de/chb_e/stra/index.html?/chb_e/stra/stra_02_03_03.html (visited on Oct. 28, 2019).

[39] "Statistical Data for the Boeing-747-400 Aircraft in Commercial Operations," Office of Aviation Research, Federal Aviation Administration, Final Report DOT/FAA/AR-06/11, Nov. 2006. [Online]. Available: http://www.tc.faa.gov/its/worldpac/techrpt/ar04-44.pdf (visited on Oct. 28, 2019).

[40] J. Grauer, E. Morelli, and D. Murri, "Flight-Test Techniques for Quantifying Pitch Rate and Angle-of-Attack Rate Dependencies," *Journal of Aircraft*, vol. 54, pp. 1–11, Jun. 2017. DOI: 10.2514/1.C034407.

[41] "High Altitude Operations - Supplement #1 to the Airplane Upset Recovery Training Aid," Flight Safety Foundation, Training Aid, Oct. 2008. [Online]. Available: https://flightsafety.org/wp-content/uploads/2016/09/AP_UpsetRecovery_Book.pdf (visited on Oct. 28, 2019).

[42] European Telecommunications Standards Institute, ETSI, *Satellite Earth Stations and Systems (SES); Harmonized EN for Earth Stations on Mobile Platforms (ESOMP) transmitting towards satellites in geostationary orbit in the 27,5 GHz to 30,0 GHz frequency bands covering the essential requirements of arcticle 3.2 of the R&TTE Directive*, ETSI EN 303 978 V1.1.0 (Draft), Sophia-Antipolis Cedex, France, Jul. 2012, [Online]. Available: https://www.etsi.org/deliver/etsi_en/303900_303999/303978/01.01.00_20/en_303978v010100c.pdf (visited on Aug. 18, 2016).

[43] R. Gallager, "Low-Density Parity-Check Codes," *IRE Trans. Inf. Theory*, vol. 8, no. 1, pp. 21–28, Jan. 1962, ISSN: 0096-1000. DOI: 10.1109/TIT.1962.1057683.

[44] D. J. C. MacKay and R. M. Neal, "Near Shannon Limit Performance of Low Density Parity Check Codes," *Electron. Lett.*, vol. 33, no. 6, pp. 457–458, Mar. 1997, ISSN: 0013-5194. DOI: 10.1049/el:19970362.

[45] European Telecommunications Standards Institute, ETSI, *Digital Video Broadcasting (DVB); Second generation framing structure, channel coding and modulation systems for Broadcasting, Interactive Services, News Gathering and other broadband satellite applications; Part 2: DVB-S2 Extensions (DVB-S2X)*, ETSI EN 302 307-2 V1.1.1 (Draft), Sophia-Antipolis Cedex, France, Oct. 2014, [Online]. Available: http://www.etsi.org/deliver/etsi_en/302300_302399/30230702/01.01.01_20/en_30230702v010101a.pdf (visited on Aug. 18, 2016).

[46] W. L. Stutzman and K. M. Yon, "A simple rain attenuation model for earth-space radio links operating at 10-35 GHz," *Radio Science*, pp. 65–72, Feb. 1986. [Online]. Available: https://ntrs.nasa.gov/search.jsp?R=19860036768 (visited on Oct. 24, 2016).

[47] International Telecommunication Union, ITU, *Characteristics of precipitation for propagation modelling*, ITU-R P.837-1 (Recommendation), Geneva, Italy, 1992, [Online]. Available: https://www.itu.int/dms_pubrec/itu-r/rec/p/R-REC-P.837-1-199408-S!!PDF-E.pdf (visited on Aug. 18, 2016).

[48] C. Friesicke, R. Quay, B. Rohrdantz, and A. F. Jacob, "A Linear 4W Power Amplifier at K-Band using 250nm AlGaN/GaN HEMTs," in *European Microwave Integrated Circuits Conference (EuMIC 2013)*, Oct. 2013, pp. 157–160.

[49] C. Li, O. El-Aassar, A. Kumar, M. Boenke, and G. M. Rebeiz, "LNA Design with CMOS SOI Process-l.4dB NF K/Ka band LNA," *IEEE MTT-S International Microwave Symposium - (IMS 2018)*, pp. 1484–1486, Jun. 2018, ISSN: 2576-7216. DOI: 10.1109/MWSYM.2018.8439132.

[50] B. Min and G. M. Rebeiz, "Ka-Band BiCMOS 4-Bit Phase Shifter with Integrated LNA for Phased Array T/R Modules," *2007 IEEE/MTT-S International Microwave Symposium*, pp. 479–482, Jun. 2007, ISSN: 0149-645X. DOI: 10.1109/MWSYM.2007.380511.

[51] B. Min and G. M. Rebeiz, "A Ka-Band BiCMOS T/R Module for Phased Array Applications," *2008 IEEE Compound Semiconductor Integrated Circuits Symposium*, pp. 1–4, Oct. 2008, ISSN: 1550-8781. DOI: 10.1109/CSICS.2008.24.

[52] G. M. Rebeiz and L. M. Paulsen, "Advances in SATCOM phased arrays using silicon technologies," *IEEE MTT-S International Microwave Symposium (IMS 2017)*, pp. 1877–1879, Jun. 2017. DOI: 10.1109/MWSYM.2017.8059022.

[53] F. Parment, A. Ghiotto, T. Vuong, J. Duchamp, and K. Wu, "Broadband transition from dielectric-filled to air-filled Substrate Integrated Waveguide for low loss and high power handling millimeter-wave Substrate Integrated Circuits," *IEEE MTT-S International Microwave Symposium (IMS2014)*, pp. 1–3, Jun. 2014, ISSN: 0149-645X. DOI: 10.1109/MWSYM.2014.6848524.

[54] F. Parment, A. Ghiotto, T. Vuong, J. Duchamp, and K. Wu, "Air-Filled Substrate Integrated Waveguide for Low-Loss and High Power-Handling Millimeter-Wave Substrate Integrated Circuits," *IEEE Transactions on Microwave Theory and Techniques*, vol. 63, no. 4, pp. 1228–1238, Apr. 2015, ISSN: 0018-9480. DOI: 10.1109/TMTT.2015.2408593.

[55] M. J. Chen, A.-V. H. Pham, N. A. Evers, *et al.*, "Design and Development of a Package Using LCP for RF/Microwave MEMS Switches," *IEEE Transactions on Microwave Theory Techniques*, vol. 54, no. 11, pp. 4009–4015, Nov. 2006, ISSN: 0018-9480. DOI: 10.1109/TMTT.2006.884639.

[56] M. Huang, C. Chu, and F. Lim, "Development of Hermetic LCP for Electronic Device Packages," *2012 IEEE 14th Electronics Packaging Technology Conference (EPTC)*, pp. 415–419, Dec. 2012. DOI: 10.1109/EPTC.2012.6507119.

[57] E. G. Geterud, P. Bergmark, and Jian Yang, "Lightweight waveguide and antenna components using plating on plastics," in *7th European Conference onAntennas and Propagation (EuCAP)*, 2013, pp. 1812–1815.

[58] Y. Arbaoui, V. Laur, A. Maalouf, and P. Queffelec, "3D printing for microwave: Materials characterization and application in the field of absorbers," in *IEEE MTT-S International Microwave Symposium (IMS 2015)*, 2015, pp. 1–3. DOI: 10.1109/MWSYM.2015.7166769.

[59] R. Bahr, L. Perregrini, T. Le, *et al.*, "Additive manufacturing of 3D substrate integrated waveguide components," *Electronics Letters*, vol. 51, no. 18, pp. 1426–1428, 2015, ISSN: 0013-5194. DOI: 10.1049/el.2015.2298.

[60] M. D'Auria, W. J. Otter, J. Hazell, *et al.*, "3-D Printed Metal-Pipe Rectangular Waveguides," *IEEE Transactions on Components, Packaging and Manufacturing Technology*, vol. 5, no. 9, pp. 1339–1349, 2015, ISSN: 2156-3950. DOI: 10.1109/TCPMT.2015.2462130.

[61] A. v. Bieren, E. d. Rijk, J.-P. Ansermet, and A. Macor, "Monolithic metal-coated plastic components for mm-wave applications," in *39th International Conference on Infrared, Millimeter, and Terahertz waves (IRMMW-THz)*, 2014, pp. 1–2. DOI: 10.1109/IRMMW-THz.2014.6956222.

[62] B. Rohrdantz, C. Rave, and A. F. Jacob, "3D-Printed Low-Cost, Low-Loss Microwave Components up to 40 GHz," *IEEE MTT-S International Microwave Symposium (IMS 2016)*, pp. 1–3, May 2016. DOI: 10.1109/MWSYM.2016.7540122.

[63] F. Goelden, A. Gaebler, M. Goebel, A. Manabe, S. Mueller, and R. Jakoby, "Tunable Liquid Crystal Phase Shifter for Microwave Frequencies," *Electronic Letters*, vol. 45, no. 13, pp. 686–687, Jun. 2009, ISSN: 0013-5194. DOI: 10.1049/el.2009.1168.

[64] Y. Zhao, C. Huang, A. Qing, and X. Luo, "A Frequency and Pattern Reconfigurable Antenna Array Based on Liquid Crystal Technology," *IEEE Photonics J.*, vol. 9, no. 3, pp. 1–7, Jun. 2017, ISSN: 1943-0655. DOI: 10.1109/JPHOT.2017.2700042.

[65] M. C. Johnson, S. L. Brunton, N. B. Kundtz, and J. N. Kutz, "Sidelobe Canceling for Reconfigurable Holographic Metamaterial Antenna," *IEEE Transactions on Antennas and Propagation*, vol. 63, no. 4, pp. 1881–1886, Apr. 2015, ISSN: 0018-926X. DOI: 10.1109/TAP.2015.2399937.

[66] C. Rave, T. Jaschke, B. Rohrdantz, and A. F. Jacob, "A Curved-Edge Dipole Antenna for UWB Applications," in *European Microwave Conference (EuMC 2013)*, Oct. 2013, pp. 648–651.

[67] T. Jaschke, B. Rohrdantz, H. K. Mitto, and A. F. Jacob, "Rx/Tx Integration Concepts for Ground Segment SatCom Antenna Arrays," in *2016 German Microwave Conference (GeMiC)*, Mar. 2016, pp. 27–30. DOI: 10.1109/GEMIC.2016.7461547.

[68] A. Sieganschin, T. Jaschke, D. Safi, and A. F. Jacob, "On the design of active Rx/Tx-diplexers with wide frequency spread," in *2018 11th German Microwave Conference (GeMiC)*, IEEE, Mar. 2018, pp. 315–318. DOI: 10.23919/GEMIC.2018.8335093.

[69] K. Kuhlmann, K. Rezer, and A. F. Jacob, "Far Field Measurement on Ka-band Substrate-Integrated Waveguide Antenna Array with Polarization Multiplexing," in *IEEE MTT-S International Microwave Symposium Digest (IMS 2008)*, Jun. 2008, pp. 1337–1340. DOI: 10.1109/MWSYM.2008.4633024.

[70] K. Kuhlmann, K. Rezer, and A. F. Jacob, "Circularly Polarized Substrate-Integrated Waveguide Antenna Array at Ka-Band," in *German Microwave Conference (GeMIC 2008)*, Mar. 2008, pp. 1–4.

[71] T. Jaschke, B. Rohrdantz, W. M. Gitzel, and A. F. Jacob, "Modeling and design of stepped transitions for substrate-integrated waveguides," in *2016 German Microwave Conference (GeMiC)*, Mar. 2016, pp. 124–127, ISBN: 9783981266870. DOI: 10.1109/GEMIC.2016.7461572.

[72] T. Jaschke, B. Rohrdantz, and A. F. Jacob, "A Flexible Surface Description for Arbitrarily Shaped Dielectric Lens Antennas," *Frequenz*, vol. 69, no. 1-2, pp. 29–37, 2014, ISSN: 2191-6349. DOI: 10.1515/freq-2014-0124. [Online]. Available: http://www.degruyter.com/view/j/freq.2015.69.issue-1-2/freq-2014-0124/freq-2014-0124.xml (visited on Apr. 24, 2016).

[73] T. Jaschke, B. Rohrdantz, H. K. Mitto, and A. F. Jacob, "Ultrawideband SIW-Fed Lens Antenna," *IEEE Antennas and Wireless Propagation Letters*, vol. 16, pp. 2010–2013, 2017, ISSN: 1536-1225. DOI: 10.1109/LAWP.2017.2693179.

[74] T. Jaschke, H. K. Mitto, and A. F. Jacob, "An SIW fed dual-band and dual-polarized lens antenna at K/Ka-band," in *2017 47th European Microwave Conference (EuMC)*, Oct. 2017, pp. 62–65. DOI: 10.23919/EuMC.2017.8230799.

[75] T. Jaschke, B. Rohrdantz, J.-P. Mohncke, and A. F. Jacob, "A Ka-band substrate-integrated waveguide diplexer with wide frequency spread," in *2016 46th European Microwave Conference (EuMC)*, IEEE, Oct. 2016, pp. 779–782. DOI: 10.1109/EuMC.2016.7824459.

[76] D. M. Pozar and S. D. Targonski, "A Shared-Aperture Dual-Band Dual-Polarized Microstrip Array," *IEEE Transactions on Antennas and Propagation*, vol. 49, no. 2, pp. 150–157, Feb. 2001, ISSN: 0018-926X. DOI: 10.1109/8.914255.

[77] F. Greco, G. Amendola, E. Arnieri, L. Boccia, and A. I. Sandhu, "A Dual-Band, Dual-Polarized Array Element for Ka Band Satcom on the Move Terminals," in *8th European Conference on Antennas and Propagation (EuCAP 2014)*, Apr. 2014, pp. 2432–2435. DOI: 10.1109/EuCAP.2014.6902309.

[78] A. B. Smolders, R. M. C. Mestrom, A. C. F. Reniers, and M. Geurts, "A Shared Aperture Dual-Frequency Circularly Polarized Microstrip Array Antenna," *IEEE Antennas and Wireless Propagation Letters*, vol. 12, pp. 120–123, 2013, ISSN: 1536-1225. DOI: 10.1109/LAWP.2013.2242427.

[79] K. Kuhlmann and A. F. Jacob, "Scanning Range of Circularly Polarized Antenna Arrays with Sequential Rotation," in *German Microwave Conference (GeMIC 2014)*, Mar. 2014, pp. 1–4.

[80] R. Lelaratne and R. J. Langley, "Dual-Band Patch Antenna for Mobile Satellite Systems," *IEE Proceedings on Microwaves, Antennas and Propagation*, vol. 147, no. 6, pp. 427–430, Dec. 2000, ISSN: 1350-2417. DOI: 10.1049/ip-map:20000864.

[81] K.-P. Yang and K.-L. Wong, "Dual-Band Circularly-Polarized Square Microstrip Antenna," *IEEE Transactions on Antennas and Propagation*, vol. 49, no. 3, pp. 377–382, Mar. 2001, ISSN: 0018-926X. DOI: 10.1109/8.918611.

[82] B. Rohrdantz, T. Jaschke, F. K. H. Gellersen, and A. F. Jacob, "A Dual-Frequency and Dual-Polarized Patch Antenna at Ka-Band," in *European Radar Conference (EuRAD 2015)*, Sep. 2015, pp. 473–476.

[83] B. Rohrdantz, T. Jaschke, F. K. H. Gellersen, A. Sieganschin, and A. F. Jacob, "Ka-band antenna arrays with dual-frequency and dual-polarized patch elements," *International Journal of Microwave and Wireless Technologies*, vol. 8, no. 6, pp. 963–972, Sep. 2016, ISSN: 1759-0787. DOI: 10.1017/S1759078716000830.

[84] P. Bafrooei and L. Shafai, "Characteristics of Single- and Double-Layer Microstrip Square-Ring Antennas," *IEEE Transactions on Antennas and Propagation*, vol. 47, no. 10, pp. 1633–1639, Oct. 1999, ISSN: 0018-926X. DOI: 10.1109/8.805910.

[85] J.-K. Lee, C.-H. Ahn, and K. Chang, "Broadband Circularly Polarized Aperture-Coupled Microstrip Antenna with Dual-Offset Feedlines," in *IEEE International Symposium on Antennas and Propagation (APSURSI 2011)*, Jul. 2011, pp. 1127–1130. DOI: 10.1109/APS.2011.5996481.

[86] B. Rohrdantz, C. Luong, and A. F. Jacob, "A Frequency and Polarization Reconfigurable Patch Antenna at K-Band," in *44th European Microwave Conference (EuMC 2014)*, Oct. 2014, pp. 49–52. DOI: 10.1109/EuMC.2014.6986366.

[87] B. Kim, B. Pan, S. Nikolaou, Y.-S. Kim, J. Papapolymerou, and M. M. Tentzeris, "A Novel Single-Feed Circular Microstrip Antenna With Reconfigurable Polarization Capability," *IEEE Transactions on Antennas and Propagation*, vol. 56, no. 3, pp. 630–638, Mar. 2008, ISSN: 0018-926X. DOI: 10.1109/TAP.2008.916894.

[88] M/A-Com Technology Solutions, *Datasheet MA4AGBLP912 - AlGaAs beamlead PIN diode*, M/A-Com Technology. [Online]. Available: https://www.macomtech.com/.

[89] B. Rohrdantz, V. Schmidt, and A. F. Jacob, "Microstrip Ring Resonator Based Frequency Reconfigurable Band-Pass Filters at K-Band," in *20th International Conference on Microwaves, Radar, and Wireless Communication (MIKON 2014)*, Jun. 2014, pp. 1–4. DOI: 10.1109/MIKON.2014.6899907.

[90] J. S. Hong and M. J. Lancaster, "Microstrip Bandpass Filter using Degenerate Modes of a Novel Meander Loop resonator," *IEEE Microwave and Guided Wave Letters*, vol. 5, no. 11, pp. 371–372, Nov. 1995, ISSN: 1051-8207. DOI: 10.1109/75.473539.

[91] H. Pawlak and A. F. Jacob, "An External Calibration Scheme for DBF Antenna Arrays," *IEEE Transactions on Antennas and Propagation*, vol. 58, no. 1, pp. 59–67, Jan. 2010, ISSN: 0018-926X. DOI: 10.1109/TAP.2009.2036195.

[92] X.-l. Yu, D.-n. Ni, Y.-x. Wu, and F.-S. Zhang, "Design of a Calibration Network for Circular Smart Antenna Array," in *Asia-Pacific Microwave Conference Proceedings (APMC 2005)*, vol. 3, Dec. 2005, 3 pp.—. DOI: 10.1109/APMC.2005.1606679.

[93] A. Stark, U. Johannsen, and A. F. Jacob, "In-Situ Probes for Antenna Array Calibration," in *European Microwave Conference (EuMC 2010)*, Sep. 2010, pp. 465–468.

[94] A. Stark, B. Rohrdantz, U. Johannsen, and A. F. Jacob, "In-Situ Probes for Patch Antenna Array Calibration," *International Journal of Microwave and Wireless Technologies*, vol. 3, no. Special Issue 03, pp. 273–280, 2011. DOI: 10.1017/S1759078711000316.

[95] B. Rohrdantz, A. Stark, E. Hawamdah, and A. F. Jacob, "A Circularly Polarized Antenna Array with Integrated Calibration Probes," in *2014 Asia-Pacific Microwave Conference (APMC 2014)*, Nov. 2014, pp. 462–464.

[96] *Intellian Adds To Their GX Antenna Family*, Aug. 2020. [Online]. Available: https://news.satnews.com/2020/08/10/intellian-adds-to-their-gx-antenna-family (visited on Mar. 12, 2023).

[97] *KNS C4 VSAT*. [Online]. Available: https://electromarinaservice.com/kns-c4-vsat (visited on Mar. 12, 2023).

[98] B. Rohrdantz, T. Jaschke, T. Reuschel, S. Radzijewski, A. Sieganschin, and A. F. Jacob, "An Electronically Scannable Reflector Antenna Using a Planar Active Array Feed at Ka-Band," *IEEE Transactions on Microwave Theory and Techniques*, vol. 65, no. 5, pp. 1650–1661, Mar. 2017. DOI: 10.1109/TMTT.2017.2663402.

[99] J. Biosca, D. Llorens, and M. C. Viganó, "Side-lobe reduction with overlapped beam-forming network for Ku-band hybrid antenna array," in *2016 10th European Conference on Antennas and Propagation (EuCAP)*, Apr. 2016, pp. 1–5. DOI: 10.1109/EuCAP.2016.7481542.

[100] *RaySat SR300*. [Online]. Available: https://www.gilat.com/technology/raysat-sr300 (visited on Mar. 12, 2023).

[101] J. Huang and Y. Rahmat-Samii, "Fan Beam Generated by a Linear-Array Fed Parabolic Reflector," *IEEE Transactions on Antennas and Propagation*, vol. 38, no. 7, pp. 1046–1053, Jul. 1990, ISSN: 0018-926X. DOI: 10.1109/8.55616.

[102] P. F. Goldsmith, C. Hsieh, G. R. Huguenin, J. Kapitzky, and E. L. Moore, "Focal Plane Imaging Systems for Millimeter Wavelengths," *IEEE Transactions on Microwave Theory and Techniques*, vol. 41, no. 10, pp. 1664–1675, Oct. 1993, ISSN: 0018-9480. DOI: 10.1109/22.247910.

[103] C. M. Rappaport and W. P. Craig, "High Aperture Efficiency Symmetric Reflector Antennas with up to 60 deg Field of View," *IEEE Transactions on Antennas and Propagation*, vol. 39, no. 3, pp. 336–344, Mar. 1991, ISSN: 0018-926X. DOI: 10.1109/8.76331.

[104] M. A. W. Verheijen, T. A. Oosterloo, W. A. van Cappellen, L. Bakker, M. V. Ivashina, and J. M. van der Hulst, "Apertif, a Focal Plane Array for the WSRT," in *The Evolution of Galaxies Through the Neutral Hydrogen Window*, R. Minchin and E. Momjian, Eds., ser. American Institute of Physics Conference Series, vol. 1035, Aug. 2008, pp. 265–271. DOI: 10.1063/1.2973599. eprint: 0806.0234. [Online]. Available: https://arxiv.org/abs/0806.0234 (visited on Oct. 30, 2016).

[105] M. V. Ivashina, O. Iupikov, R. Maaskant, W. A. van Cappellen, and T. Oosterloo, "An Optimal Beamforming Strategy for Wide-Field Surveys With Phased-Array-Fed Reflector Antennas," *IEEE Transactions on Antennas and Propagation*, vol. 59, no. 6, pp. 1864–1875, Jun. 2011, ISSN: 0018-926X. DOI: 10.1109/TAP.2011.2123865.

[106] C. Leclerc, M. Romier, H. Aubert, and A. Annabi, "Ka-Band Multiple Feed per Beam Focal Array Using Interleaved Couplers," *IEEE Transactions on Microwave Theory and Techniques*, vol. 62, no. 6, pp. 1322–1329, Jun. 2014, ISSN: 0018-9480. DOI: 10.1109/TMTT.2014.2320697.

[107] P. Cooke, M. Trinkle, H. Hansen, and J. Palmer, "Ku-Band Phased Array Reflector Array for Bistatic Radar Experiments," in *2008 International Conference on Radar*, Sep. 2008, pp. 193–196. DOI: 10.1109/RADAR.2008.4653916.

[108] M. Nagasaka, S. Nakazawa, and S. Tanaka, "Prototype of a Dual-Circularly Polarized Parabolic Reflector Antenna with Microstrip Antenna Array for 12-GHz Band Satellite Broadcasting Reception," in *2016 10th European Conference on Antennas and Propagation (EuCAP)*, Apr. 2016, pp. 1–5. DOI: 10.1109/EuCAP.2016.7481691.

[109] A. Zamanifekri and A. B. Smolders, "Beam Squint Compensation in Circularly Polarized Offset Reflector Antennas Using a Sequentially Rotated Focal-Plane Array," *IEEE Antennas and Wireless Propagation Letters*, vol. 14, pp. 815–818, 2015, ISSN: 1536-1225. DOI: 10.1109/LAWP.2014.2386308.

[110] TICRA, *GRASP - Reflector antenna design software*. [Online]. Available: https://www.ticra.com/software/grasp (visited on Mar. 12, 2023).

[111] J. Ruze, "Lateral-Feed Displacement in a Paraboloid," *IEEE Transactions on Antennas and Propagation*, vol. 13, no. 5, pp. 660–665, Sep. 1965, ISSN: 0018-926X. DOI: 10.1109/TAP.1965.1138514.

[112] W. Imbriale, P. Ingerson, and W. Wong, "Large Lateral Feed Displacements in a Parabolic Reflector," *IEEE Transactions on Antennas and Propagation*, vol. 22, no. 6, pp. 742–745, Nov. 1974, ISSN: 0018-926X. DOI: 10.1109/TAP.1974.1140910.

[113] Y. Lo, "On the beam deviation factor of a parabolic reflector," *IRE Trans. Antennas Propag.*, vol. 8, no. 3, pp. 347–349, May 1960, ISSN: 1558-3643. DOI: 10.1109/TAP.1960.1144854.

[114] F. B. Wright, "Theory and Design of Aplanatic Reflectors Employing a Correcting Lens," in *Amateur Telescope Making*, A. G. Ingalls, Ed., Scientific American, 1959.

[115] D. Minoli, *Satellite Systems Engineering in an IPv6 Environment*. CRC Press, Feb. 2009, ISBN: 9781420078695.

[116] European Telecommunications Standards Institute, ETSI, *Satellite Earth Stations and Systems (SES); Harmonized EN for Satellite Interactive Terminals (SIT) and Satellite User Terminals (SUT) transmitting towards satellites in geostationary orbit in the 29,5 GHz to 30,0 GHz frequency bands*, ETSI EN 301 459 V1.4.1 (Harmonized European Standard), Sophia-Antipolis Cedex, France, Jun. 2007, [Online]. Available: http://www.etsi.org/deliver/etsi_en/301400_301499/301459/01.04.01_60/en_301459v010401p.pdf (visited on Aug. 18, 2016).

[117] M. L. Livingston, "The Effect of Antenna Characteristics on Antenna Noise Temperature and System SNR," *IRE Transactions on Space Electronics and Telemetry*, vol. SET-7, no. 3, pp. 71–79, Sep. 1961, ISSN: 0096-252X. DOI: 10.1109/IRETSET.1961.5008770.

[118] International Telecommunication Union, ITU, *Radio Noise*, ITU-R P.372-12 (Recommendation), Geneva, Italy, Jul. 2015, [Online]. Available: https://www.itu.int/dms_pubrec/itu-r/rec/p/R-REC-P.372-12-201507-I!!PDF-E.pdf (visited on Aug. 18, 2016).

[119] T. Reuschel, "Electronically Scannable Reflector Antennas Fed by Microstrip Patch Arrays for High Performance Satellite Links," M.S. thesis, Technische Universität Hamburg-Harburg, 2013.

[120] A. Appelbaum, P. Cloud, E. Daly, and L. Parad, "A Flat-Feed Technique for Phased Arrays," *IEEE Transactions on Antennas and Propagation*, vol. 20, no. 5, pp. 582–588, Sep. 1972, ISSN: 0018-926X. DOI: 10.1109/TAP.1972.1140264.

[121] W. Kruppa and K. F. Sodomsky, "An Explicit Solution for the Scattering Parameters of a Linear Two-Port Measured with an Imperfect Test Set (Correspondence)," *IEEE Transactions on Microwave Theory and Techniques*, vol. 19, no. 1, pp. 122–123, Jan. 1971, ISSN: 0018-9480. DOI: 10.1109/TMTT.1971.1127466.

[122] G. F. Engen and C. A. Hoer, "Thru-Reflect-Line: An Improved Technique for Calibrating the Dual Six-Port Automatic Network Analyzer," *IEEE Transactions on Microwave Theory and Techniques*, vol. 27, no. 12, pp. 987–993, Dec. 1979, ISSN: 0018-9480. DOI: 10.1109/TMTT.1979.1129778.

[123] H. J. Eul and B. Schiek, "A Generalized Theory and New Calibration Procedures for Network Analyzer Self-Calibration," *IEEE Transactions on Microwave Theory and Techniques*, vol. 39, no. 4, pp. 724–731, Apr. 1991, ISSN: 0018-9480. DOI: 10.1109/22.76439.

[124] A. Ferrero and U. Pisani, "Two-port Network Analyzer Calibration Using an Unknown 'Thru'," *IEEE Microwave and Guided Wave Letters*, vol. 2, no. 12, pp. 505–507, Dec. 1992, ISSN: 1051-8207. DOI: 10.1109/75.173410.

[125] M. V. Ivashina, R. Maaskant, and B. Woestenburg, "Equivalent System Representation to Model the Beam Sensitivity of Receiving Antenna Arrays," *IEEE Antennas and Wireless Propagation Letters*, vol. 7, pp. 733–737, 2008, ISSN: 1536-1225. DOI: 10.1109/LAWP.2008.2006917.

[126] D. M. Pozar, *Microwave Engineering*, 3rd ed. Wiley, Feb. 2005, ISBN: 978-0-471-44878-5.

[127] A. A. M. Saleh, "Planar Electrically Symmetric N-Way Hybrid Power Dividers/Combiners," *IEEE Transactions on Microwave Theory and Techniques*, vol. 28, no. 6, pp. 555–563, Jun. 1980, ISSN: 0018-9480. DOI: 10.1109/TMTT.1980.1130118.

[128] M. E. Bialkowski and V. P. Waris, "A Systematic Approach to the Design of Radial-Waveguide Dividers/Combiners," in *Asia-Pacific Microwave Conference (APMC 92)*, vol. 2, Aug. 1992, pp. 881–884. DOI: 10.1109/APMC.1992.672280.

[129] K. Song, Y. Fan, and Y. Zhang, "Radial Cavity Power Divider Based on Substrate Integrated Waveguide Technology," *Electronics Letters*, vol. 42, no. 19, pp. 1100–1101, Sep. 2006, ISSN: 0013-5194. DOI: 10.1049/el:20062012.

[130] K. Song, Y. Fan, and Y. Zhang, "Eight-Way Substrate Integrated Waveguide Power Divider With Low Insertion Loss," vol. 56, no. 6, pp. 1473–1477, Jun. 2008, ISSN: 0018-9480. DOI: 10.1109/TMTT.2008.923897.

[131] Y.-P. Hong, Y.-J. An, and J.-G. Yook, "Differential Radial Power Combiner Using Substrate Integrated Waveguide," *Electronics Letters*, vol. 46, no. 24, pp. 1607–1608, Nov. 2010, ISSN: 0013-5194. DOI: 10.1049/el.2010.8624.

[132] C. Rave and A. F. Jacob, "A Wideband Radial Substrate Integrated Power Divider at K-band," in *German Microwave Conference (GeMiC 2015)*, Mar. 2015, pp. 84–87. DOI: 10.1109/GEMIC.2015.7107758.

[133] O. A. Iupikov, R. Maaskant, M. V. Ivashina, A. Young, and P. S. Kildal, "Fast and Accurate Analysis of Reflector Antennas With Phased Array Feeds Including Multiple Reflections Between Feed and Reflector," *IEEE Transactions on Antennas and Propagation*, vol. 62, no. 7, pp. 3450–3462, Jul. 2014, ISSN: 0018-926X. DOI: 10.1109/TAP.2014.2320529.

[134] T. Jaschke, B. Rohrdantz, and A. F. Jacob, "Dual-Band Stepped-Impedance Transformer to Full-Height Substrate-Integrated Waveguide," in *45th European Microwave Conference (EuMC 2015)*, Sep. 2015, pp. 367–370. DOI: 10.1109/EuMC.2015.7345776.

[135] A. Sieganschin, B. Tegowski, T. Jaschke, and A. F. Jacob, "Compact Diplexers With Folded Circular SIW Cavity Filters," *IEEE Transactions on Microwave Theory and Techniques*, vol. 69, no. 1, pp. 111–118, Dec. 2020, ISSN: 1557-9670. DOI: 10.1109/TMTT.2020.3039545.

[136] T. Jaschke and A. F. Jacob, "A Dual-Polarized SIW Lens Antenna Array for Rx-/Tx-Integration at K/Ka-Band," *IEEE Transactions om Antennas Propagation*, p. 1, Jan. 2023, ISSN: 1558-2221. DOI: 10.1109/TAP.2023.3235006.

[137] T. Jaschke, "Substrate integrated waveguide technology for Rx/Tx integrated array antennas," doctoralThesis, Technische Universität Hamburg, 2021. DOI: 10.15480/882.3648. [Online]. Available: http://hdl.handle.net/11420/9874.

[138] M. Kim, J. B. Hacker, A. L. Sailer, and J. H. Hong, "A Heterodyne-Scan Phased-Array Antenna," *IEEE Microwave and Guided Wave Letters*, vol. 9, no. 12, pp. 535–537, Dec. 1999. DOI: 10.1109/75.819423.

[139] T. Nishio, Y. Wang, Y. Qian, and T. Itoh, "A novel K-band frequency-controlled beam-steering quasi-Yagi array with mixing frequency compensation," in *IEEE MTT-S International Microwave Symposium Digest (IMS 2002)*, vol. 2, Jun. 2002, 1345–1348 vol.2. DOI: 10.1109/MWSYM.2002.1011918.

[140] T. Nishio, Y. Wang, and T. Itoh, "A Frequency-Controlled Beam-Steering Array with Mixing Frequency Compensation for Multichannel Applications," *IEEE Transactions on Antennas and Propagation*, vol. 52, no. 4, pp. 1039–1048, Apr. 2004. DOI: 10.1109/TAP.2004.825674.

[141] T. Nishio, H. Xin, Y. Wang, and T. Itoh, "A Frequency-Controlled Active Phased Array," *IEEE Microwave Wireless Components Letters*, vol. 14, no. 3, pp. 115–117, Mar. 2004. DOI: 10.1109/LMWC.2004.825188.

[142] J. D. Roque, G. S. Shiroma, and W. A. Shiroma, "A full-duplex, single-frequency-controlled phased array," in *IEEE MTT-S International Microwave Symposium Digest (IMS 2006)*, Jun. 2006, pp. 453–456. DOI: 10.1109/MWSYM.2006.249589.

[143] V. Schmidt, "Ein heterodynes Strahlschwenkverfahren für zweidimensionale Gruppenstrahler im Ka-Band," M.S. thesis, Technische Universität Hamburg-Harburg, 2015.

[144] K. Kuhlmann and A. F. Jacob, "Active 30 GHz Antenna Array for Digital Beamforming and Polarization Multiplexing," in *2010 IEEE MTT-S International Microwave Symposium Digest (IMS 2010)*, May 2010, pp. 1276–1279. DOI: 10.1109/MWSYM.2010.5514863.

[145] S. Seki and H. Hasegawa, "Cross-Tie Slow-Wave Coplanar Waveguide on Semi-Insulating GaAs Substrates," *Electronics Letters*, vol. 17, no. 25, pp. 940–941, Dec. 1981. DOI: 10.1049/el:19810657.

[146] H. Hasegawa and H. Okizaki, "M.I.S. and Schottky Slow-Wave Coplanar Striplines on GaAs Substrates," *Electronics Letters*, vol. 13, no. 22, pp. 663–664, Oct. 1977. DOI: 10.1049/el:19770471.

[147] O. Wing, *Classical Circuit Theory*. Springer Science & Business Media, Sep. 2008, ISBN: 978-038709740-4.

[148] O. J. Zobel, "Theory and Design of Uniform and Composite Electric Wave Filters," *The Bell System Technical Journal*, vol. 2, no. 1, pp. 1–46, Jan. 1923. DOI: 10.1002/j.1538-7305.1923.tb00001.x.

[149] J. Hirokawa and M. Ando, "Single-Layer Feed Waveguide Consisting of Posts for Plane TEM Wave Excitation in Parallel Plates," *IEEE Transactions on Antennas and Propagation*, vol. 46, no. 5, pp. 625–630, May 1998. DOI: 10.1109/8.668903.

[150] D. Deslandes and K. Wu, "Accurate Modeling, Wave Mechanisms, and Design Considerations of a Substrate Integrated Waveguide," *IEEE Transactions on Microwave Theory Techniques*, vol. 54, no. 6, pp. 2516–2526, Jul. 2006, ISSN: 0018-9480. DOI: 10.1109/TMTT.2006.875807.

[151] D. Deslandes and K. Wu, "Integrated Microstrip and Rectangular Waveguide in Planar Form," *IEEE Microwave and Wireless Components Letters*, vol. 11, no. 2, pp. 68–70, Feb. 2001. DOI: 10.1109/7260.914305.

[152] D. Deslandes and K. Wu, "Analysis and Design of Current Probe Transition from Grounded Coplanar to Substrate Integrated Rectangular Waveguides," *IEEE Transactions on Microwave Theory and Techniques*, vol. 53, no. 8, pp. 2487–2494, Aug. 2005. DOI: 10.1109/TMTT.2005.852778.

[153] A. Patrovsky, M. Daigle, and K. Wu, "Millimeter-Wave Wideband Transition from CPW to Substrate Integrated Waveguide on Electrically Thick High-permittivity Substrates," in *2007 European Microwave Conference*, IEEE, Oct. 2007, ISBN: 978-2-87487-001-9. DOI: 10.1109/EUMC.2007.4405145.

[154] M. Chen and G. Tsandoulas, "A Wide-Band Square-Waveguide Array Polarizer," *IEEE Transactions on Antennas and Propagation*, vol. 21, no. 3, pp. 389–391, May 1973. DOI: 10.1109/TAP.1973.1140486.

[155] A. D. Olver, P. J. B. Clarricoats, and A. A. Kishk, *Microwave Horns and Feeds* (IEE Electromagnetic Waves Series). Institution of Engineering and Technology, Jan. 1994, ISBN: 978-085296809-3. DOI: 10.1049/PBEW039E.

[156] M. K. Watanabe, R. N. Pang, B. O. Takase, J. M. Akagi, G. S. Shiroma, and W. A. Shiroma, "A 2-D Phase-Detecting/Heterodyne-Scanning Retrodirective Array," *IEEE Transactions on Microwave Theory and Techniques*, vol. 55, no. 12, pp. 2856–2864, Dec. 2007. DOI: 10.1109/TMTT.2007.909883.

Glossary

4G Short form for fourth generation of mobile telecommunications technology, with standards Mobile Worldwide Interoperability for Microwave Access (WiMAX) and Long Term Evolution (LTE) data rates up to 1 Gbit/s. 1

5G Short form for the fifth generation of mobile telecommunications technology, which provides data rates up to 10 Gbit/s. 1

K_a-band Frequency range from 26.5 to 40 GHz; For satellite communications 17.7–21.2 GHz (downlink) and 27.5–31 GHz (uplink). 15, 20, 21, 24, 26–28, 31, 33–35, 37, 43, 49, 58, 79, 93

K_u-band Frequency range from 12 to 18 GHz; For satellite communications 10.7–12.7 GHz (downlink) and 12.75–17.8 GHz (uplink). 20, 37

L-band Frequency range from 1 to 2 GHz. 37

W-band Frequency range from 75 to 110 GHz. 36

Wi-Fi Term for local wireless networks originally used by the Wi-Fi foundation for IEEE 802.11b networks. 1, 3

Acronyms

ACARS Aircraft Communications Addressing and Reporting System. 36

ADC Analog-to-Digital Converter. 14

AFR Array-Fed-Reflector. 50, 51, 68, 83–85, 88

ALMA Atacama Large Millimeter/submillimeter Array. 3

AR Axial Ratio. 60

BDF Beam Deviation Factor. 56

CMOS Complementary Metal–Oxide–Semiconductor. 31, 32

CPW Coplanar Waveguide. 38, 69–80, 93, 99–101, 105, 106

CW Continuous Wave. 95

DAC Digital-to-Analog Converter. 14, 81, 82

DBF Digital Beam Forming. 4, 14, 31, 67, 114

DC Direct Current. 42, 44, 80–83, 93, 105, 107, 108

DOA Direction of Arrival. 15

DSL Digital Subscriber Line. 1

DSP Digital Signal Processor. 25, 31

EIRP Equivalent Isotropic Radiated Power. 10, 15, 16, 24, 26–28, 58–61, 66, 79, 88, 114, 115

EOC Edge of Coverage. 20, 26, 27

ESA Electronically Scanned Antenna. 2, 47

ETSI European Telecommunications Standards Institute. 18, 24, 58, 59, 66, 88

FDM Fused Deposition Modeling. 33

FDMA Frequency-Division Multiple Access. 26

FPGA Field-Programmable Gate Array. 31

FSL Free Space Loss. 18, 21, 26, 27, 37

FSS Fixed Satellite Service. 18

FTTH Fiber to the Home. 1

G/T Antenna Gain-to-Noise-Temperature. 10, 15, 16, 25–28, 59–61, 114, 115

GaAs Gallium Arsenide. 31

GaN Gallium Nitride. 31

GCPW Grounded Coplanar Waveguide. 76, 101

GEO Geostationary Earth Orbit. 2, 18–20, 23, 26–28, 114

GND Ground. 69, 70, 73, 99, 100

GPS Global Positioning System. 36

HBF Heterodyne BeamForming. 90, 91, 93, 103–112

HPA High Power Amplifier. 79

HPBW Half-Power Beamwidth. 6, 20, 58

IC Integrated Circuit. 16, 30, 31, 89, 115

IF Intermediate Frequency. 13, 14, 25, 37, 91, 93, 98, 105, 107, 108, 110, 112, 114

ISIG Immersion Silver/Immersion Gold. 93

ISL Inter-Satellite Links. 19

ISP Internet Service Provider. 1, 20

ITU International Telecommunication Union. 1, 18

LCP Liquid Crystal Polymer. 32, 33

LDPC Low-Density Parity-Check. 24

LEO Low Earth Orbit. 2, 18–23, 26–28, 114

LHCP Left-Handed Circular Polarization. 7, 18, 37

LNA Low Noise Amplifier. 10, 15, 25, 26, 31, 32, 36, 37, 103, 113, 116

LO Local Oscillator. 13, 14, 16, 90–95, 97, 103–105, 107–109, 114

LOS Line-of-Sight. 2

LRU Line Replaceable Unit. 16

LTE Long Term Evolution. 133

MEO Medium Earth Orbit. 18, 20

MIMO Multiple-Input and Multiple-Output. 3, 31

MMIC Monolithic Microwave Integrated Circuit. 78, 80

NWA Network Analyzer. 76

PA Power Amplifier. 15, 31, 32, 36, 37, 66, 68, 116

PCB Printed Circuit Board. 17, 30–33, 38, 40, 43, 45–47, 68–73, 75, 80, 83, 93, 95, 97, 100–102, 112, 113, 116

QFN Quad Flat No Leads Package. 31

Radar Radio Detection and Ranging. 2

RF Radio Frequency. 13, 14, 25, 26, 30, 31, 36, 37, 44, 80, 92, 93, 98, 101, 103, 105–108, 114

RFIC Radio Frequency Integrated Circuit. 31, 45, 47, 93, 113, 115

RHCP Right-Handed Circular Polarization. 7, 18, 37

Rx Receive. 7, 10, 15, 16, 18, 24–27, 37, 38, 51, 59, 60, 62, 67, 68, 77, 79, 93

SatCom Satellite Communications. 18, 37, 43, 58

SiGe Silicon-Germanium. 31

SIW Substrate Integrated Waveguide. 2, 17, 32, 33, 38, 47, 73, 88, 93, 94, 100–103, 106, 107, 115, 116, 118

SLA Stereolithography. 33

SLL Sidelobe Level. 9, 12, 28, 50, 57, 58, 86–88, 108

SMD Surface Mounted Device. 96, 98, 105

SMP Sub-Miniature Push-On Connector. 107, 112

SMPM Sub-Miniature Push-On (Micro) Connector. 46, 70, 80

SNR Signal-to-Noise Ratio. 1, 15, 24, 25, 27

SOLT Short Open Load Through. 70

SPDT Single Pole, Double Throw. 67

TDMA Time-Division Multiple Access. 26

TEM Transverse ElctroMagnetic. 6

TRL Through Reflect Line. 70, 71, 97

Tx Transmit. 7, 15, 16, 18, 26, 27, 37, 38, 51, 55, 58, 62, 67, 68, 77, 79, 80

UOSM Unkown Open Short Match. 70, 71

via Vertical Interconnect Access. 32, 45, 69–71, 73, 76, 77, 99–101

VNA Vector Network Analyzer. 70, 108, 118

VSWR Voltage Standing Wave Ratio. 7

WiMAX Worldwide Interoperability for Microwave Access. 133

XPD Cross-polar Discrimination. 7, 61